J. Hydrol. Hydromech., 66, 2018, 2, 129–132
DOI: 10.1515/johh-2017-0060

Thematic Issue on HYDRUS Software Applications to Subsurface Fluid Flow and Contaminant Transport

Jiří Šimůnek[1*], Martinus Th. van Genuchten[2, 3], Radka Kodešová[4]

[1] Department of Environmental Sciences, University of California, Riverside, CA, USA.
[2] Center for Environmental Studies, CEA, São Paulo State University, UNESP, Rio Claro, SP, Brazil.
[3] Department of Earth Sciences, Utrecht University, Netherlands.
[4] Department of Soil Science and Soil Protection, Czech University of Life Sciences, Prague, Czech Republic.
[*] Corresponding author. E-mail: Jiri.Simunek@ucr.edu

INTRODUCTION

This thematic issue documents selected presentations given at the Fifth International Conference on "HYDRUS Software Applications to Subsurface Flow and Contaminant Transport Problems," held in Prague, Czech Republic, March 30–31, 2017, as well as several other papers by authors who did not attend the conference. Previous conferences in the HYDRUS series were held in Utrecht in 2005, in Tokyo in 2008, and in Prague in 2008 and 2013. The conferences focused on the development and application of advanced numerical models simulating fluid flow, heat transport, and/or the transport of various contaminants or other solutes (such as nutrients, pesticides, heavy metals, radionuclides, and pathogenic microorganisms) in variably-saturated soils and groundwater. The conferences were designed to bring together users of the HYDRUS family of codes, as well as of related software, to review and exchange information on various aspects of the codes, future enhancements of the software, and their application to a broad range of soil, environmental, hydrological, ecological, and agricultural problems.

Since the first conference in 2005, the community of HYDRUS users has been growing continuously as evidenced by the number of downloads (over 10,000 times each of the past several years) and visits to the HYDRUS web pages (several hundred on average each day). Hundreds of journal articles have been published in which the HYDRUS codes have been used (see the review by Šimůnek et al., 2016). Feedback from users such as those attending the HYDRUS conferences has been extremely important in terms of identifying particular strengths and weaknesses of the codes, defining additional processes or features that should be included in the models, or identifying key challenges and new perspectives in modeling a multitude of interacting soil physical, chemical, and biological processes (Vereecken et al., 2016).

Although the HYDRUS codes are now widely used for modeling biogeochemical processes in the vadose zone, a large number of alternative subsurface flow and transport models can be used for similar applications. Popular existing codes (such as MODFLOW-SURFACT, STOMP, SWAP, VS2DI, and TOUGH2) are discussed in detail in a special 2008 issue "Vadose Zone Modeling" of Vadose Zone Journal (Šimůnek and Bradford, 2008), while a more extensive inventory of available models is provided in the Encyclopedia of Hydrological Sciences (Šimůnek, 2005). Steefel et al. (2015) further provided a review of more comprehensive reactive transport codes for subsurface environmental simulations. We refer readers to these additional resources for more information about alternative subsurface flow and transport models.

HYDRUS DEVELOPMENT AND APPLICATIONS

This special issue contains 12 contributions from HYDRUS software users, covering a range of topics from the very fundamental to important practical applications. The leading paper by Šimůnek et al. (this issue) describes new features that will be available in Version 3 of the HYDRUS (2D/3D) computer software package. Several important new features have been implemented recently in the standard computational module of Version 3. The most important additions relate to root growth and the use of a reservoir boundary condition. While HYDRUS-1D allowed users to prescribe a time-variable rooting depth, using either the logistic growth function or some tabulated form upon input, HYDRUS (2D/3D) thus far assumed that the spatial distribution of roots in the root zone remained constant during the simulations. Šimůnek et al. (this issue) discuss multiple adaptations to overcome this shortcoming. Also, earlier versions of HYDRUS (2D/3D) required pressure heads at boundaries representing external water bodies, such as pumping wells or agricultural furrows, to be specified as an external input, without any feedback that would relate possible changes in their water level in response to flow processes within the subsurface (such as infiltration or exfiltration). The upcoming new HYDRUS version has now an option to account for such interactions using a new reservoir boundary condition. The new root growth and reservoir boundary features were requested by many HYDRUS users; they should undoubtedly extend the applicability of the code to a much broader range of applications. Additionally, the GUI of HYDRUS (2D/3D) has been completely rewritten to ensure compatibility with new Windows operating systems and the development of more efficient software in the near future (Šimůnek et al., this issue). Multiple new tools, such as Manipulator, Clipper, and Slicer, as well as the use of 3D streamlines, were developed for Version 3 of HYDRUS (2D/3D) and are discussed briefly by the authors.

The remaining papers in the thematic issue can be divided into two groups. The first group of papers uses existing standard HYDRUS modules and describes their application to a wide range of problems. Applications range from evaluations of a) the effects of temporal averaging of meteorological data on predictions of groundwater recharge (Batalha et al., this issue), b) flow in capillary barriers (Berger, this issue), c) the Hyprop evaporation method for estimating the unsaturated soil hydraulic properties (Bezerra Coelho et al., this issue), d) the effects of soil water repellency on the unsaturated soil hydraulic properties (Filipović et al., this issue), e) the impact of stones in actual field soils of the High Tatras mountains in Slovakia on soil water storage and recharge (Hlaváčiková et al., this issue), f) how changes in cropping patterns at a large scale can produce

water savings and social gains (Karimov et al., this issue), to g) ^{137}Cs transport from the Goiânia Radioactive Waste Repository in Brazil towards groundwater (Pontedeiro et al., this issue). These applications quite nicely demonstrate the breadth of possible applications of the HYDRUS software packages.

The second group of papers focuses either on applications of existing special add-on modules of HYDRUS, such as HPx for multicomponent contaminant transport (Jacques et al., this issue) and the Wetland module (Pucher and Langergraber, this issue), or on coupling the HYDRUS code with DSSAT (Shelia et al., this issue) or the SWI2 package of MODFLOW (Szymkiewicz et al., this issue). DSSAT is a suite of field-scale, process-based crop models that simulate the phenological development of crops to obtain detailed information about various yield components from emergence till maturity on the basis of crop genetic properties, environmental conditions (soil, weather) and management options (Jones et al., 2003). MODFLOW is the U.S. Geological Survey (USGS) modular finite-difference flow model (McDonald and Harbaugh, 2003), which is considered to be the de facto standard code for simulating groundwater flow. The SWI2 package for MODFLOW may be used to represent in a simplified way variable-density flow associated with saltwater intrusion in coastal aquifers (Bakker et al., 2013).

Applications of the standard HYDRUS modules

The first paper of this first group of papers discusses the effects of temporal averaging of meteorological data on predictions of groundwater recharge. Batalha et al. (this issue) used HYDRUS-1D to show that temporal averaging of meteorological data can lead to significant bias in predictions of groundwater recharge. They found that an increase in the duration of the averaging interval of meteorological data (from hourly, daily, weekly, monthly to yearly time periods) will lead to lower estimates of groundwater recharge, especially at sites having coarse-textured soils. At one of the study sites in Brazil, daily averaged data produced recharge rates almost ten times greater than those obtained using yearly averaged data (Batalha et al., this issue). This same problem was also studied, with similar conclusions, by Szymkiewicz et al. (this issue) using the HYDRUS package for MODFLOW.

Berger (this issue) used the two-dimensional version of HYDRUS (2D/3D) to evaluate experimental data collected at a 10-m tipping trough representing capillary barriers. Capillary barriers are two-layered systems consisting of an upper layer made up of relatively fine-grained porous material (the capillary layer) underlain by a lower layer consisting of relatively coarse-grained porous material (the capillary block). Water percolating through the capillary layer under unsaturated conditions is then held above the interface between the two layers due to capillary forces and the large difference in their soil hydraulic conductivities. While HYDRUS described flow through the capillary layer and the capillary block relatively well, the software failed to reproduce an abrupt change in the flow pattern that was observed experimentally when increasing rainfall. Instead, the model produced a relatively smooth pattern without any distinct thresholds. Berger (this issue) discusses in detail possible causes for this mismatch, including experimental issues, the application of the model, or the model itself.

An application of HYDRUS-1D to the HYPROP evaporation method for estimating the unsaturated soil hydraulic properties is discussed by Bezerra Coelho et al. (this issue). While earlier applications of HYDRUS-1D using the evaporation method appeared many years ago (e.g., Schelle et al., 2010; Schindler et al., 2010; Šimůnek et al., 1998), Bezerra Coelho et al. (this issue) provide a much more complete analysis of the method. They used HYDRUS-1D to carry out an independent analysis of the HYPROP system, which standardized the evaporation method, for a broad range of soil textures. The authors conclude that overall, the HYPROP methodology performed extremely well for most soil textures and as such constitutes a much-needed addition to current soil hydraulic measurement techniques (Bezerra Coelho et al., this issue).

An important factor affecting the hydraulic behavior of many soils that is projected to increase in importance due to global climate change is soil water repellency. This feature is rarely modeled successfully using numerical models based on the standard Richards equation (e.g., Deurer and Bachmann, 2007; Diamantopoulos et al., 2013; Robinson et al., 2010). Filipović et al. (this issue) use HYDRUS (2D/3D) to estimate the hydraulic properties of soils exhibiting water repellency using experimental data collected with a disc infiltrometer, and with water and ethanol as the infiltration liquid. They then used the calibrated model to assess the water balance of a hillslope containing soils exhibiting different degrees of water repellency.

Another important factor that affects subsurface water flow, especially in mountainous areas, is the presence of stones that could dramatically constrain the soil volume through which water moves. While stony soils have been studied in the past using HYDRUS (2D/3D) (e.g., Hlaváčiková et al., 2016; Novák et al., 2011; Parajuli et al., 2017), those studies considered only hypothetical soil systems with simplified geometries and idealized distributions of stones. Hlaváčiková et al. (this issue) in this issue used HYDRUS-1D to assess the impact of stones in real soils of the High Tatras mountains in Slovakia on soil water storage and recharge. Their studies indicate that the presence of rock fragments in a moderate-to-high stony soil can significantly decrease the soil water storage (by some 25% or more) and affect the soil water dynamics.

Karimov et al. (this issue) used HYDRUS-1D to assess how changes in the large-scale cropping patterns of the Fergana Valley in Central Asia can produce water savings and social gains. They examined possible water savings by replacing alfalfa with winter wheat (with either a fallow period or the cultivation of green gram during the summer) for various irrigation scenarios such as high-deficit versus low-deficit irrigation. Karimov et al. (this issue) discussed not only various hydrological components (e.g., transpiration, evaporation, and recharge), but also the many economic and social gains that could be obtained with different cropping scenarios within a relatively broad developmental context.

Finally, Pontedeiro et al. (this issue) used HYDRUS-1D to reassess the Goiânia Radioactive Waste Repository in Brazil stemming from an accident in 1987 with an abandoned cesium chloride teletherapy source. They first obtained estimates of water infiltrating through the soil cover on top of the repository into and through the waste and its concrete liners and the underlying vadose zone towards groundwater. Interestingly, calculations accounted not only for hydrological fluxes resulting from local precipitation and evapotranspiration, including root water uptake by the grass cover, but also for the effects of concrete degradation on the hydraulic properties of the liners. Next, ^{137}Cs transport from the repository towards groundwater was considered while accounting for the effects of ^{137}Cs sorption and radioactive decay. Results indicated that very little if any radioactive material would reach the water table during the approximately 400-year lifespan of the repository, even when accounting for preferential flow through the waste using a dual-porosity (mobile-immobile water) contaminant transport model.

Development and applications of HYDRUS add-on modules

A large number of standard and non-standard add-on modules have been developed over the years to expand the applicability of the HYDRUS software packages. As summarized by Šimůnek et al. (2016) these modules include, but are not limited to, a) the UnsatChem module that simulates the transport and reactions of major ions, b) the HPx modules that consider various general biogeochemical reactions in soils, c) the C-Ride module that simulates the colloid-facilitated solute transport, d) the Wetland module that considers various biogeochemical reactions in constructed wetlands, e) the DualPerm module for simulations of nonequilibrium and/or preferential flow and transport, f) the Fumigant module that considers the fate and transport of fumigants, and g) the Isotope module to simulate the fate and transport of isotopes. The current thematic issue contains two manuscripts describing applications of two of these modules, notably the HPx module (Jacques et al. this issue) and the Wetland module (Pucher and Langergraber, this issue). Additionally, two manuscripts describe the coupling of HYDRUS-1D with DSSAT (Shelia et al., this issue) and MODFLOW (Szymkiewicz et al., this issue).

Jacques et al. (this issue) describe recent developments and applications of the HPx modules for multicomponent reactive transport during variably-saturated flow. The HPx modules are a result of coupling the HYDRUS computational codes with PHREEQC (Parkhurst and Appelo, 2013). They may be used to simulate one- and multi-dimensional water flow and solute transport, in conjunction with a large number of biogeochemical reactions, in variably-saturated soils and other porous systems. Jacques et al. (this issue) gave an overview of the most significant recent developments of HPx, such as the coupling of hydraulic properties with geochemical state variables (e.g., porosity and hydraulic conductivity), considering gaseous diffusion, and facilitating transport in two and three dimensions. They provide multiple examples demonstrating the use of HPx to simulate a range of processes relevant to soil organic matter dynamics in soils, the fate of dissolved organic matter and CO_2 transport in soils, as well as bioturbation processes.

Pucher and Langergraber (this issue) analyzed four vertical flow wetland systems using the Wetland module of HYDRUS (2D/3D). The Wetland module (Langergraber and Šimůnek, 2012) was developed in order to simulate governing biological and chemical transformation and degradation processes of wastewater constituents in subsurface flow treatment wetlands. Pucher and Langergraber (this issue) evaluated whether the default values of various biological and chemical parameters provided by the Wetland module can be used to represent collected experimental data. Their results indicate that for vertical flow wetlands with fine sand, no adjustments of the standard parameter set were needed, while for systems with coarser filter media as the main layer, the standard parameter set had to be adjusted to match simulated and measured effluent concentrations.

The HYDRUS codes previously have been coupled with several crop and/or root growth models as reviewed by Šimůnek et al. (this issue) and Hartmann et al. (2018). Shelia et al. (this issue) report another recent development, i.e., the implementation of HYDRUS flow routines into the DSSAT crop modeling system. DSSAT refers to a suite of field-scale, process-based crop models that simulate the phenological development of crops, including detailed information about various yield components, from emergence till maturity on the basis of crop genetic properties, environmental conditions (soil, weather) and management options (Jones et al., 2003). While the DSSAT system thus far relied on the "tipping bucket" water balance approach to represent soil hydrologic and water redistribution processes, implementation of the HYDRUS flow routines into DSSAT allows one to use now the more process-based Richards equation to represent these processes. The advantages and disadvantages of the two approaches are well known and have been discussed elsewhere (e.g., Scanlon et al., 2002). Shelia et al. (this issue) provide details about the coupling of the two models, as well as applications of the two approaches to multiple datasets involving not only measured water contents, but also multiple crop growth variables.

The last paper of this thematic issue (Szymkiewicz et al., this issue) discusses the simultaneous use of the HYDRUS and SWI2 packages for MODFLOW to simulate freshwater lens recharge and the position of the salt/freshwater interface. The study was applied to a sandy peninsula, a typical geomorphologic setting in many coastal areas such as along the Baltic and North Sea coasts. The MODFLOW groundwater flow model comes with a large number of "packages" to account for various processes, such as recharge from the vadose zone, and interactions with rivers and ponds. The HYDRUS package for MODFLOW is one such package that considers processes in the vadose zone (Beegum et al., 2018; Twarakavi et al., 2008). The SWI2 package is another package, which may be used to represent in a simplified way variable-density flow associated with saltwater intrusion in coastal aquifers (Bakker et al., 2013). Szymkiewicz et al. (this issue) used both packages simultaneously to highlight the sensitivity of calculated recharge rates to the temporal resolution of weather data (similarly as Batalha et al., this issue), leading to different trends in the evolution of freshwater-saltwater interfaces. They also found that root water uptake can significantly influence both the recharge rate and the position of the freshwater-saltwater interface.

CONCLUSIONS

The twelve papers in this thematic issue reflect the considerable depth and breadth of possible applications of the HYDRUS software packages and their specialized add-on modules. The thematic issue also indicates continuous improvement of the codes themselves and their GUI's, including the development of new features such as more flexible root growth options and a dynamic reservoir boundary condition, as well as coupling of the HYDRUS codes with separate crop growth models (e.g., DSSAT), biogeochemical models (e.g., PHREEQC), or larger-scale flow and transport models (e.g., MODFLOW). These improvements keep enhancing in minor and major ways the applicability of the HYDRUS family of codes to existing or new applications, and to new areas of research. They provide important additions to the many standard and non-standard add-on HYDRUS modules discussed in detail by Šimůnek et al. (2016).

REFERENCES

Bakker, M., Schaars, F., Hughes, J.D., Langevin, C.D., Dausman, A.M., 2013. Documentation of the Seawater Intrusion (SWI2) Package for MODFLOW. US Geological Survey Techniques and Methods, Book 6, Chap. A46, 47 p.

Beegum, S., Šimůnek, J., Szymkiewicz, A., Sudheer, K.P., Nambi, I.M., 2018. Implementation of solute transport in the vadose zone into the 'HYDRUS package for MODFLOW'. Groundwater, (under review).

Deurer, M., Bachmann, J., 2007. Modeling water movement in heterogeneous water-repellent soil: 2. A conceptual

numerical simulation. Vadose Zone Journal, 6, 446–457. DOI: 10.2136/vzj2006.0061.

Diamantopoulos, E., Durner, W., Reszkowska, A., Bachmann, J., 2013. Effect of soil water repellency on soil hydraulic properties estimated under dynamic conditions. Journal of Hydrology, 486, 175–186.

Hartmann, A., Šimůnek, J., Aidoo, M.K., Seidel, S.J., Lazarovitch, N., 2018. Modeling root growth as a function of different environmental stresses using HYDRUS. Vadose Zone Journal, 17, 16 p. DOI: 10.2136/vzj2017.02.0040.

Hlaváčiková, H., Novák, V., Šimůnek, J., 2016. The effects of rock fragment shapes and positions on modeled hydraulic conductivities of stony soils. Geoderma, 281, 39–48. DOI: 10.1016/j.geoderma.2016.06.034.

Jones, J.W., Hoogenboom, G., Porter, C.H., Boote, K.J., Batchelor, W.D., Hunt, L.A., Wilkens, P.W., Singh, U., Gijsman, A.J., Ritchie, J.T., 2003. DSSAT cropping system model. European Journal of Agronomy, 18, 235–265.

Langergraber, G., Šimůnek, J., 2012. Reactive transport modeling of subsurface flow constructed wetlands using the HYDRUS Wetland module. Vadose Zone Journal, 11, 2, 14 p. DOI: 10.2136/vzj2011.0104.

McDonald, M.G., Harbaugh, A.W., 2003. The history of MODFLOW. Ground Water, 41, 2, 280–283.

Novák, V., Kňava, K., Šimůnek, J., 2011. Determining the influence of stones on hydraulic conductivity of saturated soils using numerical method. Geoderma, 161, 3–4, 177–181. DOI: 10.1016/j.geoderma.2010.12.016.

Parajuli, K., Sadeghi, M., Jones, S.B., 2017. A binary mixing model for characterizing stony-soil water retention. Agricultural and Forest Meteorology, 244–245, 1–8.

Parkhurst, D.L., Appelo, C.A.J., 2013. Description of input and examples for PHREEQC Version 3 - A computer program for speciation, batch-reaction, one-dimensional transport, and inverse geochemical calculations. Chapter 43 of Section A, Ground Water, Book 6, Modeling Techniques. U.S. Department of the Interior, U.S. Geological Survey, Reston, Virginia, 497 p.

Robinson, D.A., Lebron, I., Ryel, R.J., Jones, S.B., 2010. Soil water repellency, a method of soil moisture sequestration in Pinyon-Juniper woodland. Soil Science Society of America Journal, 74, 2, 624–634.

Scanlon, B.R., Christman, M., Reedy, R.C., Porro, I., Šimůnek, J., Flerchinger, G.F., 2002. Intercode comparisons for simulating water balance of surficial sediments in semiarid regions. Water Resources Research, 38, 12, 1323, 59.1–59.16. DOI: 10.1029/2001WR001233.

Schelle, H., Iden, S.C., Peters, A., Durner, W., 2010. Analysis of the agreement of soil hydraulic properties obtained from multistep-outflow and evaporation methods. Vadose Zone Journal, 9, 4, 1080–1091.

Schindler, J., Durner, W., von Unold, G., Müller, L., 2010. Evaporation method for measuring unsaturated hydraulic properties of soils: Extending the measurement range. Soil Science Society of America Journal, 74, 4, 1071–1083.

Šimůnek, J., 2005. Models of water flow and solute transport in the unsaturated zone. In: Anderson, M.G., McDonnell, J.J. (Eds): Encyclopedia of Hydrological Sciences, Chapter 78. John Wiley & Sons, Ltd., Chichester, UK, pp. 1171–1180.

Šimůnek, J., Bradford, S.A., 2008. Vadose Zone Modeling: Introduction and importance. Vadose Zone Journal, 7, 2, 581–586. DOI: 10.2136/VZJ2008.0012.

Šimůnek, J., Wendroth, O., van Genuchten, M.T., 1998. Parameter estimation analysis of the evaporation method for determining soil hydraulic properties. Soil Science Society of America Journal, 62, 4, 894–905.

Šimůnek, J., van Genuchten, M.Th., Šejna, M., 2016. Recent developments and applications of the HYDRUS computer software packages. Vadose Zone Journal, 15, 7, 25 p. DOI: 10.2136/vzj2016.04.0033.

Steefel, C.I., Appelo, C.A.J., Arora, B., Jacques, D., Kalbacher, T., Kolditz, O., Lagneau, V., Lichtner, P.C., Mayer, K.U., Meeussen, J.C.L., Molins, S., Moulton, D., Shao, H., Šimůnek, J., Spycher, N., Yabusaki, S.B., Yeh, G.T., 2015. Reactive transport codes for subsurface environmental simulation. Computational Geosciences, 19, 3, 445–478. DOI: 10.1007/s10596-014-9443-x.

Twarakavi, N.K.C., Šimůnek, J., Seo, H.S., 2008. Evaluating interactions between groundwater and vadose zone using HYDRUS-based flow package for MODFLOW. Vadose Zone Journal, 7, 2, 757–768.

Vereecken, H., Schnepf, A., Hopmans, J.W., Javaux, M., Or, D., Roose, T., Vanderborght, J., Young, M.H., Amelung, W., Aitkenhead, M., Allisson, S.D., Assouline, S., Baveye, P., Berli, M., Brüggemann, N., Finke, P., Flury, M., Geiser, T., Govers, G., Ghezzehei, T., Hallett, P., Hendricks Franssen, H.J., Heppel, J., Horn, R., Huisman, J.A., Jacques, D., Jonard, F., Kollet, S., Lafolie, F., Lamorski, K., Leitner, D., McBratney, A., Minasny, B., Montzka, C., Nowak, W., Pachepsky, Y., Padarian, J., Romano, N., Roth, K., Rothfuss, Y., Rowe, E.C., Schwen, A., Šimůnek, J., Titak, A., van Dam, J., van der Zee, S.E.A.T.M., Vogel, H.J., Vrugt, J.A., Wöhling, T., Young, I.M., 2016. Modeling soil processes: Review, key challenges, and new perspectives. Vadose Zone Journal, 15, 5, 57 p. DOI: 10.2136/vzj2015.09.0131.

J. Hydrol. Hydromech., 66, 2018, 2, 133–142
DOI: 10.1515/johh-2017-0050

New features of version 3 of the HYDRUS (2D/3D) computer software package

Jiří Šimůnek[1*], Miroslav Šejna[2], Martinus Th. van Genuchten[3, 4]

[1] Department of Environmental Sciences, University of California, Riverside, CA 92521, USA.
[2] PC-Progress, Ltd., Prague, Czech Republic.
[3] Center for Environmental Studies, CEA, São Paulo State University, UNESP, Rio Claro, SP, Brazil.
[4] Department of Earth Sciences, Utrecht University, Utrecht, Netherlands.
[*] Corresponding author. E-mail: Jiri.Simunek@ucr.edu

Abstract: The capabilities of the HYDRUS-1D and HYDRUS (2D/3D) software packages continuously expanded during the last two decades. Various new capabilities were added recently to both software packages, mostly by developing new standard add-on modules such as HPx, C-Ride, UnsatChem, Wetland, Fumigant, DualPerm, and Slope Stability. The new modules may be used to simulate flow and transport processes in one- and two-dimensional transport domains and are fully supported by the HYDRUS graphical user interface (GUI). Several nonstandard add-on modules, such as Overland, Isotope, and Centrifuge, have also been developed, but are not fully supported by the HYDRUS GUI. The objective of this manuscript is to describe several additional features of the upcoming Version 3 of HYDRUS (2D/3D), which was unveiled at a recent (March 2017) HYDRUS conference and workshop in Prague. The new features include a flexible reservoir boundary condition, expanded root growth features, and new graphical capabilities of the GUI. Mathematical descriptions of the new features are provided, as well as two examples illustrating applications of the reservoir boundary condition.

Keywords: HYDRUS; Reservoir boundary condition; Pumping well; Root growth; Graphical user interface.

INTRODUCTION

The HYDRUS (2D/3D) software package and its various predecessors (e.g., UNSAT, SWMS-2D, CHAIN-2D, and HYDRUS-2D) have a long history that goes back to the early 1970s as documented in detail by Šimůnek et al. (2008, 2016a). The HYDRUS conferences often serve as a forum where new versions of HYDRUS (2D/3D) are unveiled. For example, Version 2 of HYDRUS (2D/3D) and several of its add-on modules (UnsatChem, DualPerm, C-Ride, HP2) were first introduced in 2013 at the Third International Conference on "HYDRUS Software Applications to Subsurface Flow and Contaminant Transport Problems," held in Prague, Czech Republic. Similarly, Version 3 of HYDRUS (2D/3D) was unveiled in 2017 at the Fifth HYDRUS conference in Prague. Similarly, as Version 2, Version 3 is supported by a number of standard and non-standard specialized HYDRUS modules that were summarized by Šimůnek et al. (2016a).

The objective of the present paper is to describe in detail two main computational modules that have been included in Version 3 of HYDRUS (2D/3D): a new "Reservoir" boundary condition" (BC) and a dynamic root system. We provide here not only mathematical descriptions of the new standard computational modules but also two examples illustrating the use of the reservoir BC: i.e., for evaluating the performance of a pumping well as well as of a falling head experiment. Additionally, selected new graphical capabilities of the software package are described.

THE RESERVOIR BOUNDARY CONDITION

Previous versions of HYDRUS (2D/3D) required that pressure heads at boundaries representing external water bodies be specified as external input. No feedback was possible to relate temporal changes of the water level in these external water bodies in response to interactions with the subsurface, such as infiltration or exfiltration. HYDRUS users typically assumed that the water level in an external water body (e.g., a furrow or borehole) was constant (e.g., Hinnell et al., 2009; Lazarovitch et al. 2009; Warrick et al., 2007), or they needed to prescribe the dynamics of the water level themselves.

Version 3 of the standard two-dimensional computational module of HYDRUS (2D/3D) offers a new system-dependent boundary condition, further referred to as the reservoir boundary condition. This option allows users to consider a reservoir that is external to the HYDRUS transport domain, while water can be added (injected) to or removed (pumped) from the reservoir. Flow into or out of the reservoir through its interface with the subsurface depends on the prevailing conditions in the flow domain (e.g., the position of the groundwater table) and external fluxes. Since mass balances of water and solute in the external reservoir are constantly being updated (based on all incoming and outgoing fluxes), the boundary conditions along the transport domain are dynamically adjusted depending upon the water level in the reservoir.

Reservoir boundary conditions potentially have a large number of applications such as estimating dynamically the water level in wells, in furrows during irrigation, and in wetlands. Another application concerns a relatively new approach to land development known as Low-Impact Development (LID), which is a "green" approach to storm-water management that seeks to mimic the natural hydrology of a site using decentralized microscale control measures (Coffman, 2002). Low-impact development practices range from the use of bioretention cells, infiltration (dry) wells or trenches, stormwater wetlands, wet ponds, level spreaders, permeable pavements, swales, green roofs, vegetated filter and buffer strips, sand filters, smaller culverts, to water harvesting systems (Brunetti et al., 2016, 2017). We provide later two applications where the reservoir BC is used to evaluate fluxes into or out of wells, as well as to

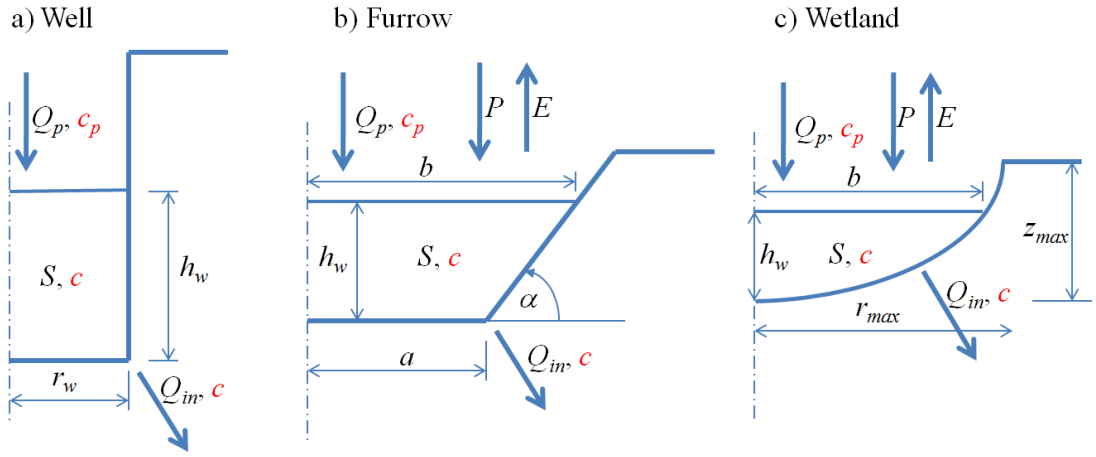

Fig. 1. Three different types of the reservoir boundary condition: a well, a furrow, and a wetland. In the figure h_w is the water level in the reservoir [L], S is the volume of water in the reservoir ([L^2] or [L^3] for two-dimensional and axisymmetric systems, respectively), Q_p is the pumping rate (positive for removal of water, negative for adding water) ([L^{2}T^{-1}] or [L^{3}T^{-1}] for two-dimensional and axisymmetric systems, respectively), c is the solute concentration in reservoir water [ML^{-3}], c_p is the solute concentration in injected water [ML^{-3}], P and E refer to the precipitation and evaporation rates [LT^{-1}], r_w is the radius of the well [L], a is a half-width of the furrow [L], α is the slope of the furrow side [–], r_{max} is the maximum width (radius) of the wetland [L], z_{max} is the maximum depth of the wetland [L], and b represents the width of the water surface ([L] or [L^2] for two-dimensional and axisymmetric systems, respectively).

simulate a falling head experiment.

The reservoir BC is implemented in HYDRUS (2D/3D) for three different geometries (Fig. 1): a well, a furrow, and a wetland. While the furrow BC is implemented only for two-dimensional transport domains, the well and wetland BCs are implemented for both two-dimensional planar and axisymmetric domains.

The Well Reservoir Boundary Condition

The position of the water level in the well is obtained by solving the following mass balance equation:

$$\frac{dV_w}{dt} = \pi r_w^2 \frac{dh_w}{dt} = Q_{in}(t) - Q_p(t) \tag{1}$$

which in HYDRUS is implemented in terms of the finite difference discretization:

$$\pi r_w^2 \frac{h_w^{j+1} - h_w^j}{\Delta t} = Q_{in} - Q_p$$
$$h_w^{j+1} = h_w^j + \frac{\Delta t}{\pi r_w^2}\left(Q_{in} - Q_p\right) \tag{2}$$

where V_w is the volume of water in the well [L^3], r_w is the well radius [L], h_w is the water level in the well [L], Q_{in} is the water flow rate into the well from the soil profile across the well wall (or its screened part) [L^{3}T^{-1}], Q_p is the pumping rate [L^{3}T^{-1}], Δt is the time step [T], and h_w^j and h_w^{j+1} are water levels in the well at the previous and current time levels [L], respectively (Fig. 1a). The fluxes Q_{in} and Q_p can have negative values, in which case they represent outflow from the well (infiltration into the soil profile) and the water flow rate entering the well, respectively.

Equation (1) can be solved providing that the initial position of the water level in the well, $h_{w,init}$, and the pumping rate are known. The parts of the boundary below and above the water level in the well are then assigned internally to be (time-variable) pressure head (Dirichlet) and seepage face boundary conditions, respectively. During execution, HYDRUS calculates which part of the seepage face boundary is active (with a prescribed zero pressure head) and which is inactive (with a prescribed zero flux). HYDRUS also calculates and reports fluxes separately across these two parts of the boundary along a well, and uses these fluxes in Eq. (1). Note that this option can also be used for 2D geometries. The surface area πr_w^2 is then replaced with the width, r_w, of the well bottom.

A similar mass balance equation as for water flow is used also for solute transport:

$$\frac{dV_w c}{dt} = V_w \frac{dc}{dt} + c\frac{dV_w}{dt} = Q_{in}c_{in} - Q_p c_p$$
$$V_w \frac{dc}{dt} = Q_{in}c_{in} - Q_p c_p - c\left(Q_{in} - Q_p\right) \tag{3}$$

where c is the solute concentration in the reservoir [ML^{-3}], c_{in} is solute concentration associated with mass transfer between the soil profile and water reservoir [ML^{-3}] (c_{in} is equal to c when water infiltrates into the soil profile and equal to the solute concentration in the soil profile when water exfiltrates into the reservoir), and c_p is the solute concentration associated with pumping or injection (equal to c for pumping or to the concentration of water being injected into the reservoir) [ML^{-3}]. An energy balance equation similarly as Eq. (3) was implemented also to account for heat transport and time-variable temperatures in the reservoir.

The Furrow Reservoir Boundary Condition

Similarly as for wells, the reservoir BC for furrows within HYDRUS is based on mass balance considerations to determine the position of the water level in the furrow, h_w [L]. The volume of water, S [L^2], in the furrow, and its change in time depending

upon the inflow and outflow rates, are described using the equations (Šimůnek et al., 2016b):

$$S = \frac{1}{2}h(a+b) = \frac{1}{2}h_w\left(a + a + \frac{h_w}{\tan\alpha}\right) = h_w a + \frac{h_w^2}{2\tan\alpha}$$
$$\frac{dS}{dt} = Q_{in}(t) - Q_p(t) + (P-E)b \qquad (4)$$
$$a\frac{dh_w}{dt} + \frac{h_w}{\tan\alpha}\frac{dh_w}{dt} = \left(a + \frac{h_w}{\tan\alpha}\right)\frac{dh_w}{dt} =$$
$$= Q_{in}(t) - Q_p(t) + (P-E)b$$

or in terms of their finite difference discretization:

$$\left(a + \frac{h_w^j}{\tan\alpha}\right)\frac{h_w^{j+1} - h_w^j}{\Delta t} = Q_{in} - Q_p + (P-E)b$$
$$h_w^{j+1} = h_w^j + \frac{\Delta t\tan\alpha}{h_w^j + a\tan\alpha}\left(Q_{in} - Q_p + Pb - Eb\right) \qquad (5)$$

where a is the half-width of the bottom of the furrow [L], b is the half-width of the water level [L], h_w is the water level in the furrow [L], Q_{in} the water infiltration rate from the furrow to the soil profile across the furrow walls [L^2T^{-1}], Q_p is the pumping rate (positive for removal of water, negative for adding water) [L^2T^{-1}], Δt is the time step [T], P and E are precipitation and evaporation rates [LT^{-1}], respectively, and h_w^j and h_w^{j+1} are water levels in the furrow at the previous and current time levels [L], respectively (Fig. 1b). Similarly, as for the well BC, parts of the boundary below and above the water level in the furrow are then assigned time-variable pressure head (Dirichlet) and seepage face boundary conditions, respectively.

A similar solute mass balance approach as for wells is used also for the furrow BC (Šimůnek et al., 2016b):

$$\frac{d(Sc)}{dt} = S\frac{dc}{dt} + c\frac{dS}{dt} = Q_p(t)c_p - Q_{in}(t)c$$
$$S\frac{dc}{dt} = Q_p(t)c_p - Q_{in}(t)c - c\left[Q_p(t) - Q_{in}(t) + (P-E)b\right] \qquad (6)$$
$$S\frac{dc}{dt} = Q_p(t)(c_p - c) - c\left[(P-E)b\right]$$

where c_p is the solute concentration of irrigation water (fertigation) [ML^{-3}; or dimensionless], and c is the average solute concentration of the furrow water and hence the concentration of the infiltrating water [ML^{-3}]. Note that we assume that precipitation and evaporation fluxes are devoid of solutes and that there is instantaneous and complete mixing of solute within the furrow. Precipitation will, therefore, lead to dilution of solute in the furrow water, while evaporation will lead to increasing concentrations. The furrow BC module requires as input the solute concentration in the irrigation water (c_p) and the timing of fertigation (i.e., the beginning and end time of fertigation). The module then calculates the solute concentration in the furrow water, c, which is subsequently used in a Cauchy (concentration flux) boundary condition together with the local infiltration flux calculated with HYDRUS. Similarly, as the standard computational module of HYDRUS, the Reservoir boundary condition cannot be used to account for precipitation/dissolution of mineral phases in the reservoir or its boundaries.

The Wetlands Reservoir Boundary Condition

Similarly, as for the well and furrow boundary conditions, users can specify a reservoir boundary condition along the boundary of the wetland (Fig. 1c). The bottom coordinates of a wetland are described using the following equations:

$$z = z_{\max}\left(\frac{r}{r_{\max}}\right)^p$$
$$r = r_{\max}\left(\frac{z}{z_{\max}}\right)^{1/p} \qquad (7)$$

where $z_{\max}$ is the depth of a wetland [L], $r_{\max}$ is the radius of a wetland [L], and p is a shape parameter (Fig. 1c). The volume of water in the wetland, V_w ([L^2] or [L^3] for two- and three-dimensional problems, respectively), and the water depth, h_w [L], for two-dimensional problems are calculated using:

$$dV = rdz = r_{\max}\left(\frac{z}{z_{\max}}\right)^{1/p}dz \qquad (8)$$
$$V = \frac{r_{\max}}{(z_{\max})^{1/p}}\int z^{1/p}dz = \frac{r_{\max}}{(z_{\max})^{1/p}}\left(\frac{p}{1+p}\right)z^{1/p+1}$$
$$h_w = \left[\left(\frac{1+p}{p}\right)\frac{(z_{\max})^{1/p}}{r_{\max}}V\right]^{\frac{p}{1+p}} \qquad (9)$$

and for axisymmetric problems using:

$$dV = \pi r^2 dz = \pi(r_{\max})^2\left(\frac{z}{z_{\max}}\right)^{2/p}dz \qquad (10)$$
$$V = \pi\frac{(r_{\max})^2}{(z_{\max})^{2/p}}\int z^{2/p}dz = \pi\left(\frac{r_{\max}}{z_{\max}^{1/p}}\right)^2\left(\frac{p}{2+p}\right)z^{2/p+1}$$
$$h_w = \left[\frac{1}{\pi}\left(\frac{2+p}{p}\right)\left(\frac{z_{\max}^{1/p}}{r_{\max}}\right)^2 V\right]^{\frac{p}{2+p}} \qquad (11)$$

A similar solute mass balance equation as for the well and furrow reservoir BCs is also used for the wetlands reservoir BC.

Before continuing with the two applications, we note that water flow and solute transport can occur in both directions between a reservoir and the transport domain depending upon the prescribed initial and boundary conditions. For example, a reservoir can be initially empty while groundwater table is present in the transport domain. Water will then flow from the transport domain into the reservoir, with HYDRUS dynamically adjusting the boundary conditions at the reservoir walls. The code will assign a time-variable pressure head boundary condition to the reservoir walls that are below the water level in the reservoir, and a seepage face boundary condition to the walls above the water level. At the same time, water may be pumped from or added to the reservoir using other boundary conditions. Alternatively, water could be initially present in or be added to the reservoir, while the transport domain is initially still dry. Water will then flow from the reservoir into the transport domain, in which case the water level in the reservoir and corresponding boundary conditions will be adjusted dynamically based on the fluxes into and out of the reservoir.

Additionally, the interface between the reservoir and the transport domain is also selected by the software users. For example, in the case of a well reservoir, users can assume that only the bottom or the walls of the well are permeable, or that some part of the well is lined (impermeable to water) or in contact only with certain soil horizons. Since the initial and boundary conditions for the reservoir and the transport domain are specified independently, many different combinations of these various scenarios can hence be accommodated with the new reservoir boundary condition module is HYDRUS. Two examples of these features are given in the next section.

RESERVOIR BOUNDARY CONDITION APPLICATIONS

We now provide two examples illustrating the use of the well reservoir boundary condition. The first example pertains to a pumping well, with water flowing from the transport domain into the well from which water is being pumped. The water level in the well depends on the balance between water inflow and pumping. The second example considers falling head infiltration, with water flowing from the reservoir into the transport domain, while the water level in the reservoir is correspondingly being adjusted. This example represents a classic falling head infiltration experiment. Additional examples involving furrow reservoir boundary conditions for both water flow and solute transport problems are given by Siyal et al. (2012) and Šimůnek et al. (2016b).

A pumping well

This example considers conditions typical of a pumping well. The transport domain in the example is assumed to be 5 m wide and 3 m deep. The well has a diameter of 0.25 m, is 2 m deep, and has an initial water level of 0.50 m above the well bottom. The soil profile is considered to be homogeneous and assumed to consist of loam, with the default van Genuchten (1980) parameters taken from the HYDRUS soil catalog based on textural class-averaged pedotransfer functions derived by Carsel and Parrish (1988). Initial conditions in the profile were assumed to be in static equilibrium with a groundwater table located 50 cm below the soil surface. Inflow into the well occurred through both the well bottom and its sides. Time-variable pressure head and seepage face boundary conditions were applied at the well boundary below and above the water level in the well, respectively. A constant pressure head boundary condition, corresponding to the initial pressure head conditions was specified along the right side of the domain, while no flow boundary conditions were imposed at all other boundaries. The pumping rate from the well was set equal to 0.03 m^3/h.

The transport domain was discretized into an unstructured triangular finite element mesh, with a targeted element size of 0.075 m. The size of finite elements was adjusted to 0.03 m at the well bottom and 0.3 m at the right side of the domain. The transport domain and its discretization are shown in Figure 2.

Figure 3 shows the water level and water volume in the well, as well cumulative water fluxes, as a function of time. Initially, the pumping rate was slightly smaller than the inflow rate of water from the soil into the well through the well walls below (Exfiltration) and above (Seepage) the water level in the well. As a result, the water level in the well and the well water volume slightly increase. However, the inflow of water into the well after about 10 hours was about equal to, and then became smaller than, the pumping rate, leading to a gradual but slow decrease in the water level in the well. Figure 4 shows calculated pressure head profiles and the position of the water table after 48 hours of pumping.

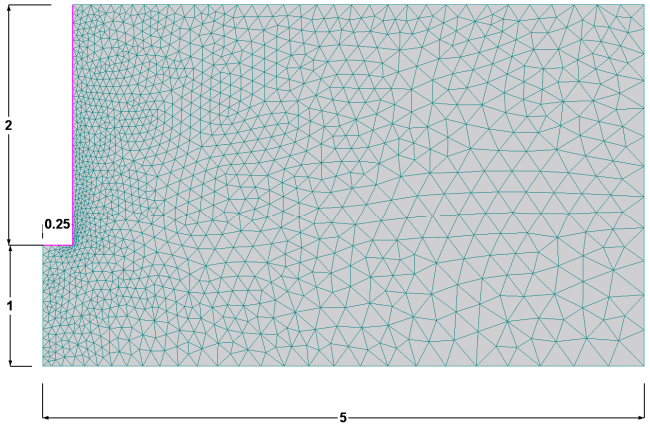

Fig. 2. The transport domain and its discretization for the pumping well example. Values in the figure are in meters.

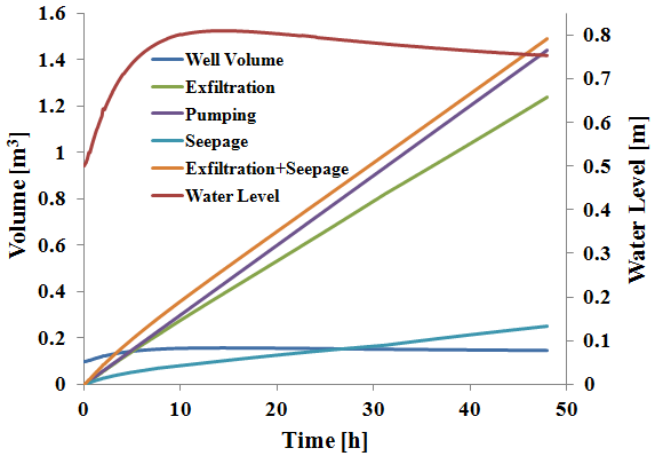

Fig. 3. Calculated water levels and water volumes in the well, and cumulative water fluxes as a function of time for the pumping well example. Note that the terms "Exfiltration" and "Seepage" represent cumulative flow from the transport domain into the well, while "Pumping" refers to the removal of water from the well.

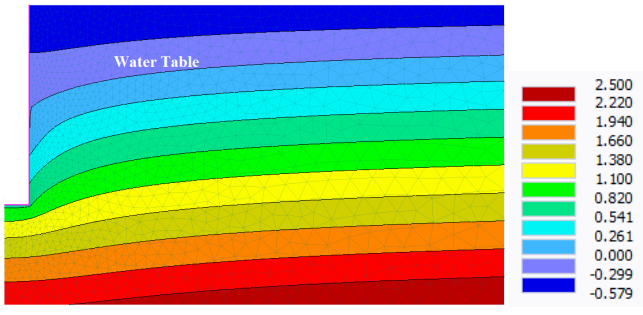

Fig. 4. Calculated pressure head (m) profile and position of the water table after 48 hours of pumping for the pumping well example.

While relatively simple, the example demonstrates the use of the new reservoir boundary condition. The problem in actuality can be made much more complex, for example by assuming a

heterogeneous soil profile, making the pumping rate time variable, assuming different parts of the well to be screened, and including contaminant transport among essentially all other features available in the standard HYDRUS (2D/3D) software package.

Falling head infiltration

In this example, the well reservoir boundary condition is used to simulate a falling head experiment when the water reservoir is placed on top of the soil. The transport domain in this example was 1.25 m wide and 1.30 m deep, and discretized into a structured finite element mesh consisting of 380 nodes and 684 elements. The soil profile was again considered to be homogeneous and to consist of loam, with the default van Genuchten (1980) parameters taken from the HYDRUS soil catalog. The radius of the reservoir placed on top of the soil surface was 0.20 m, and the initial water level in the reservoir 0.15 m above the soil surface.

Figure 5 shows that the water level and the water volume in the reservoir decreased as a result of water infiltrating into the soil profile. At the end of the experiment, all water initially in the reservoir infiltrated into the soil profile. Note that in Figure 5 the "Volume" at time zero is equal to cumulative "Infiltration" at the end of the experiment. Figure 6 shows the calculated pressure head profiles at 0.2 d when water is still infiltrating into the profile, and at 0.5 d during redistribution when the reservoir is empty. The plots hence represent situations during and after the falling head infiltration experiment.

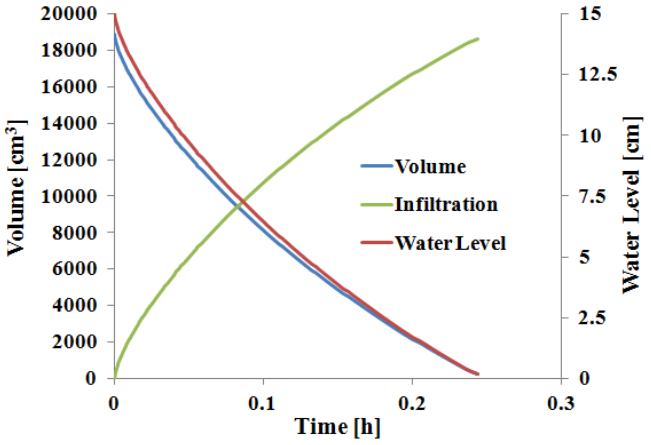

Fig. 5. Calculated water levels and water volumes in the reservoir on top of the soil, and cumulative infiltration volumes into the soil, as a function of time for the falling head experiment.

ROOT GROWTH

Previous Version 2 of HYDRUS(2D/3D) included a relatively comprehensive macroscopic root water and solute uptake model (Šimůnek and Hopmans, 2009) to account for the effects of both water and salinity stress on root water uptake, while additionally accounting for possible active and passive root contaminant or nutrient uptake. Root water and solute uptake both could furthermore be treated as being either non-compensated or compensated, while users could select the degree of compensation (Šimůnek and Hopmans, 2009).

HYDRUS-1D additionally allowed users to externally prescribe a time-variable rooting depth, either using the logistic growth function or a tabulated form. This feature was thus far not available in HYDRUS (2D/3D), which has been noted by several HYDRUS users (e.g., Karandish and Šimůnek, 2016; Ramos et al., 2012; Roberts et al., 2009; among others). The spatial distribution of roots in the root zone was assumed to remain constant during the simulations, and only the intensity of potential uptake (as a result of time-variable potential transpiration rates) could be specified as input. The HYDRUS models also did not allow the spatial extent of the rooting zone to change actively as a result of certain environmental stresses (e.g., Hartman et al., 2018).

To overcome these deficiencies, several studies either further modified the HYDRUS models (or their predecessors such as CHAIN-2D or SWMS-3D), or coupled the models with existing crop growth or root growth models. For example, Javaux et al. (2008, 2013) developed R-SWMS, a three-dimensional root growth model that couples the model of Somma et al. (1998) (based on SWMS-3D) with the root architecture model of Doussan et al. (1998). Zhou et al. (2012) coupled HYDRUS-1D with the WOFOST crop growth model (Boogaard et al., 1998), and used the resulting code to simulate the growth and yield of irrigated wheat and maize (Li et al., 2012, 2014). Han et al. (2015) similarly coupled HYDRUS-1D with a simplified crop growth version used in SWAT, based on the EPIC root growth model (Williams et al., 1989). They used the coupled model to simulate the contribution and impact of groundwater on cotton growth and root zone water balance.

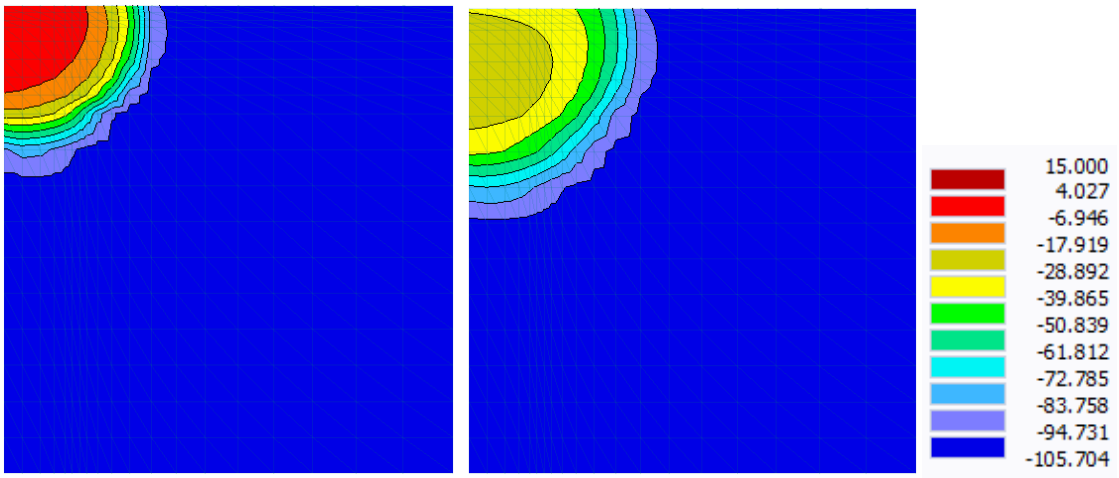

Fig. 6. Calculated pressure head (cm) profiles at 0.2 (left) and 0.5 d (right) for the falling head experiment.

Wang et al. (2014, 2015) further coupled EPIC with CHAIN-2D and HYDRUS-1D to assess the effects of furrow and sprinkler irrigation, respectively, on crop growth. Finally, Hartmann et al. (2018) implemented into both HYDRUS-1D and HYDRUS (2/3D) a root growth model developed by Jones et al. (1991). Their coupled model assumes that various environmental growth stress factors can influence root development under suboptimal conditions. Of the different software, only the models of Hartmann et al. (2018) are directly available from the HYDRUS website as a non-standard HYDRUS module (i.e., not fully supported by the HYDRUS GUI).

To extend the capabilities of the standard module of HYDRUS (2D/3D), a simple root growth model with similar capabilities as those in HYDRUS-1D was implemented into Version 3. The rooting depth, L_R, can now be either constant (the standard approach) or variable during the simulations. For annual vegetation, a growth model is required to simulate changes in rooting depth with time. Time-variable rooting depth values can be provided either using a table on input, or calculated with the program assuming that the actual rooting depth is the product of the maximum rooting depth, L_m [L], and a root growth coefficient, $f_r(t)$ [–], given by:

$$L_R(t) = L_m \; f_r(t) \tag{12}$$

For the root growth coefficient, $f_r(t)$, we use the classical Verhulst-Pearl logistic growth function

$$f_r(t) = \frac{L_0}{L_0 + (L_m - L_0)\, e^{-rt}} \tag{13}$$

where L_0 is the initial value of the rooting depth at the beginning of the growing season [L], and r the growth rate [T^{-1}]. The growth rate can be calculated either from the assumption that 50% of the rooting depth will be reached after 50% of the growing season has elapsed or from given data of the rooting depth at a specified time. The same approach is also used for the horizontal extent of the rooting zone, except that the maximum extent of the rooting zone in the horizontal direction is used instead of the maximum rooting depth.

When a variable rooting depth is considered, the spatial distribution of roots must be described using either the Vrugt (Vrugt et al., 2001a, 2001b) or Hoffman and van Genuchten (Hoffman and van Genuchten, 1983) functions. The Vrugt two-dimensional root distribution function is implemented in HYDRUS as follows (Vrugt et al., 2001a, 2001b):

$$b(x,z) = \left(1 - \frac{z}{Z_m}\right)\left(1 - \frac{x}{X_m}\right) e^{-\left(\frac{p_z}{Z_m}\left|z^* - z\right| + \frac{p_r}{X_m}\left|x^* - x\right|\right)} \tag{14}$$

where X_m and Z_m are the maximum rooting lengths in the x- and z- directions [L], respectively; x and z are distances from the origin of the plant (or tree) in the x- and z- directions [L], respectively; p_x [–], p_z [–], x^* [L], and z^* [L] are empirical parameters (Vrugt et al., 2001b), and $b(x,z)$ denotes the two-dimensional spatial distribution of the potential root water uptake rate [–]. The parameters x^* and z^* indicate the location in the profile having the maximum rooting density, while p_x and p_z are assumed to be zero for $x > x^*$ and $z > z^*$, respectively. We refer to Vrugt et al. (2001a, 2001b) for different configurations of the normalized spatial distribution of the potential root water uptake rate.

Alternatively, one can use the following function (Hoffman and van Genuchten, 1983):

$$b(z) = \begin{cases} \dfrac{1.667}{Z_m} & z > L - 0.2Z_m \\ \dfrac{2.0833}{Z_m}\left(1 - \dfrac{L - z}{Z_m}\right) & z \in \left(L - Z_m;\, L - 0.2Z_m\right) \\ 0 & z < L - Z_m \end{cases} \tag{15}$$

where L is the x-coordinate of the soil surface [L] and Z_m is the rooting depth [L].

Figure 7 shows an example of the two-dimensional spatial distribution of root water uptake at 10, 20, 30, and 40 d in a transport domain that is 100 cm wide and 150 cm deep. The plots are for the following root growth parameters: $L_{0x} = L_{0z} = 5$ cm at $t = 5$ d, $Z_m = L_{mz} = 100$ cm at $t = 45$ d, $X_m = L_{mx} = 75$ cm, $x^* = 0$, $z^* = 20$ cm, $p_x = p_z = 1$. The root growth rate r for these variables was equal to –0.0309 d^{-1}.

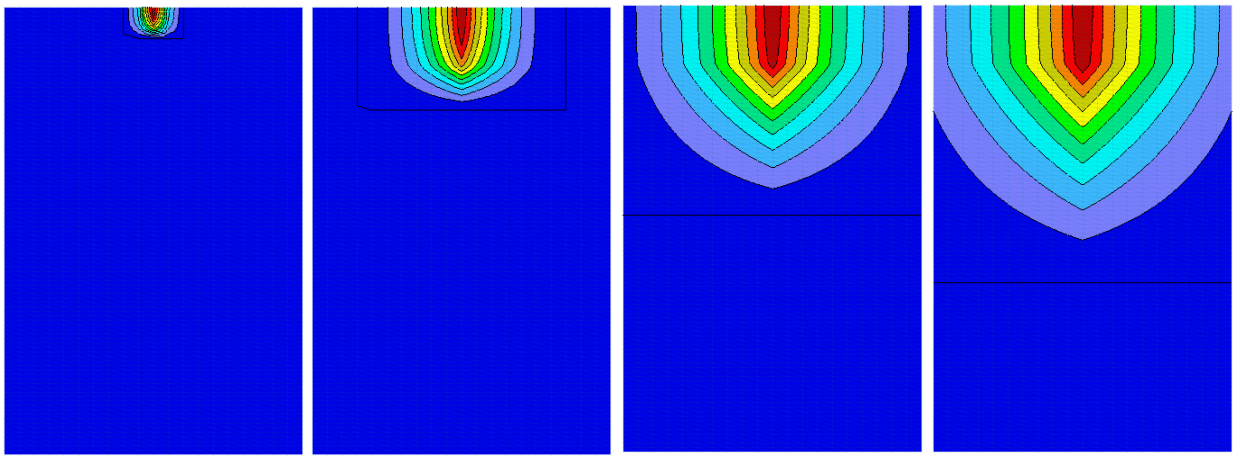

Fig. 7. Dynamic two-dimensional spatial distribution of root water uptake at 10, 20, 30, and 40 d for root growth parameters given in the text. The transport domain is 100 cm wide and 150 cm deep. The scale varies from zero (blue) to one (red) and is dimensionless.

THE HYDRUS (2D/3D) GRAPHICAL USER INTERFACE

The popularity of the HYDRUS software packages is in large part due to its inclusion of a large number of subsurface and near-surface water flow and solute transport processes (Šimůnek et al., 2016a). However, equally important has been the development of advanced graphical user interfaces (GUIs). The GUI of Version 3 of HYDRUS (2D/3D) now includes a significant number of major new features, as well as a large number of smaller corrections and improvements. Although the external look has been preserved and is similar to Version 2, Version 3 internally uses the latest software development tools and libraries, which is critical to ensure compatibility with new Windows operating systems and development of more efficient software in the future. This section provides a brief overview of the most important improvements and extensions.

One important objective with new version was to increase the performance and capacity of the GUI. The limit of Version 2 of HYDRUS (about 1 million finite elements) was extended by almost an order to 10 million finite elements. The extension was achieved by overall optimization of the code and developing a 64-bit version of HYDRUS, which can now use all physical memory available on modern PCs. This feature permitted a considerable increase in the size of HYDRUS simulations, with the main limiting factor now being the speed of the calculation module(s).

We further replaced many old HYDRUS (2D/3D) software components for charts and tables in Version 3 by new components, which also included fixing some known errors. Now all dialogs containing charts or tables are resizable, thus making entering and viewing data more comfortable. The GUI also supports the Unicode and can now correctly display special characters such as Greek symbols. Although manipulating graphical objects in HYDRUS, in general, was relatively easy thanks to drag-and-drop features, some operations (such as rotations) had to be defined numerically in a dialog box. Version 3 offers a new graphical tool called "Manipulator" for more user-friendly transformations of selected objects in two or three dimensions.

We also improved several features related to Mesh-sections, 3D mesh clipping and slicing. The optimization of a GUI for work with relatively large FE meshes required certain changes in using mesh-sections. While mesh-sections are still fully supported, the program by default does not generate as many mesh-sections as in Version 2. However, we created a new graphical tool called "Clipper" that can now be used to cut or slice a 3D mesh. Figures 8 and 9 show examples of these two applications. Another useful function related to mesh-sections is the possibility to select mesh nodes or elements by selecting geometric objects in a data-explorer tree.

The graphical display of velocity vectors for millions of mesh nodes is not only slow but usually also too complex for viewing. We improved the new GUI to allow displays of velocity vectors either at mesh nodes or raster points, while the raster parameters (such as the density of points) are fully adjustable. Figure 10 shows an example.

Previous Version 2 of HYDRUS (2D/3D) allowed one to show flowing particles, but only in two dimensions. Flowing particles are hypothetical objects that can be defined at any location of the transport domain by users, with the program then calculating trajectories and positions of these particles with time considering unretarded convective transport. The "flowing particles" feature is now available for both 2D and 3D projects.

Another new feature of Version 3 is the calculation and display of streamlines for a given steady-state flow velocity field. Streamlines are one of the most commonly used graphical representations of CFD (computational flow dynamics) results in that they can display very clearly the flow direction, such as shown in Figure 11. The software now also has an option to run flow animations, i.e., the movement of particles along streamlines (Fig. 12). Users can save this animation as a video file and use in presentations of HYDRUS results.

The ability of charts displaying the distribution of various quantities along boundary-lines and cross-section lines has also been extended in Version 3. The GUI now allows the display of results at multiple time-layers simultaneously in one chart. This feature allows one to compare very easily values of a given quantity at different times. Note that cross-section lines and charts now can be also applied to mesh slices created by the Clipper tool as described earlier and shown in Figure 8.

We further improved the 3D graphics of Version 3 of HYDRUS, including allowing the rendering to be smoother and faster. A transparent mode (object translucency) is now available also for the graphical display of results. An example of this is shown in Figure 13. We included at the same time new options for automatic numbering of isolines and displaying positions of minimum/maximum values of a current quantity.

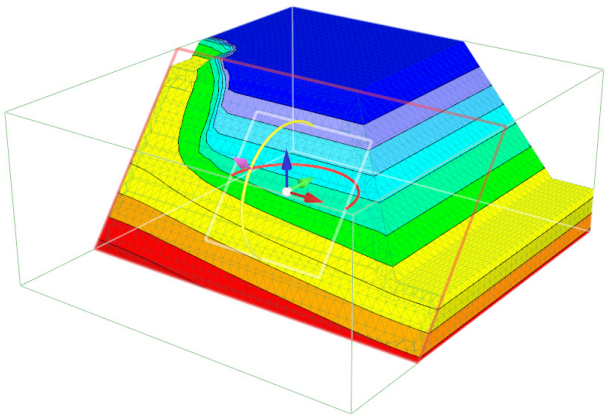

Fig. 8. Example showing **3D Clipping.** When working with 3D models, the visible mesh (or geometric objects) can be clipped to view values inside the domain. The clipper is controlled by a graphical tool (a manipulator).

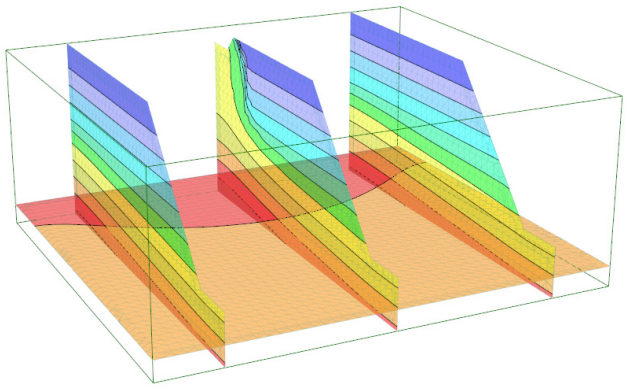

Fig. 9. Example showing **3D Slicing.** The slicer is another tool for better visualization of 3D objects. The number of slices, their position and rotation can be set either in a dialog or graphically.

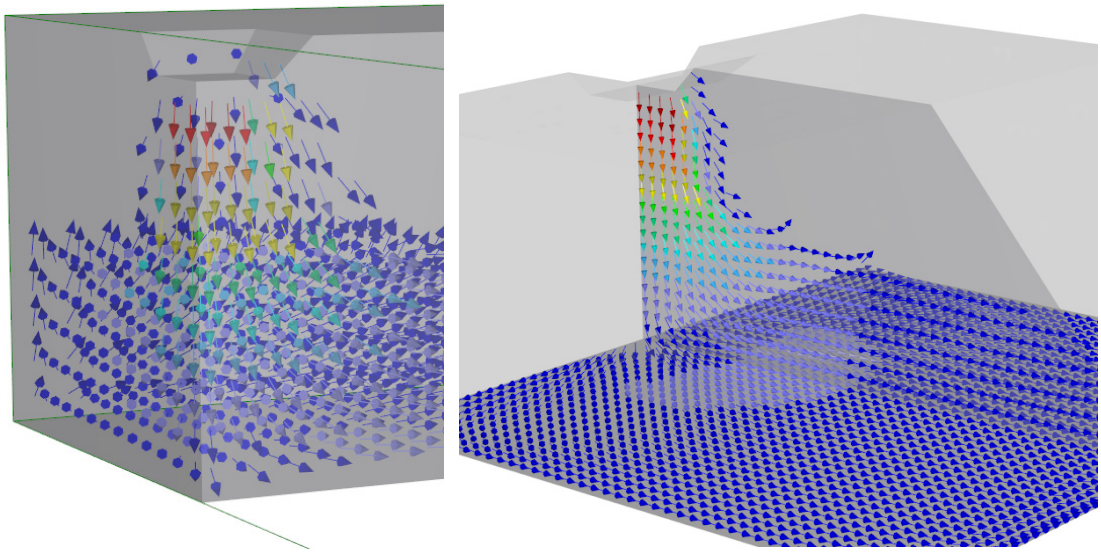

Fig. 10. Rasters for Vector Fields. Vector fields can be displayed in mesh-independent rasters, i.e., regular 2D/3D grids with an arbitrary density of points. Rasters can also be used with the Clipper and Slicer.

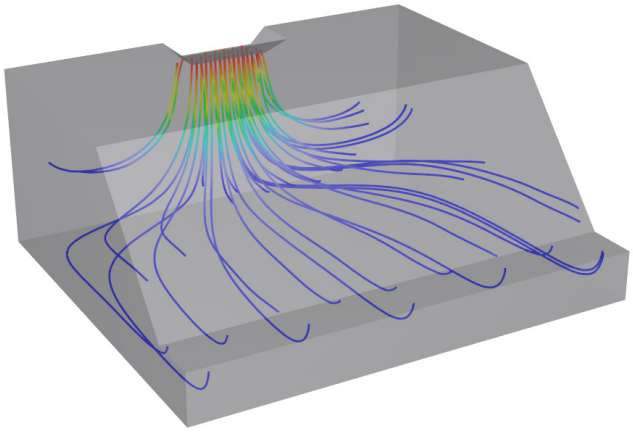

Fig. 11. Example showing **3D Streamlines.** Streamlines can be calculated for a given time layer (i.e., steady-state flow) from a set of seed points. Seed point sources of several types can be set graphically.

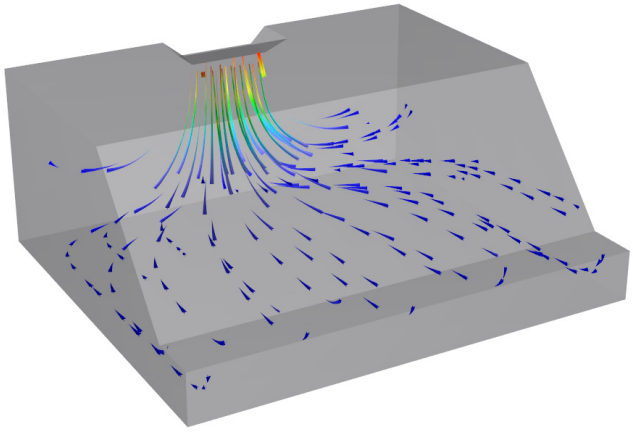

Fig. 12. Example of **Particle Animation**. The movement of particles can be animated as flowing-lines or flowing-particles.

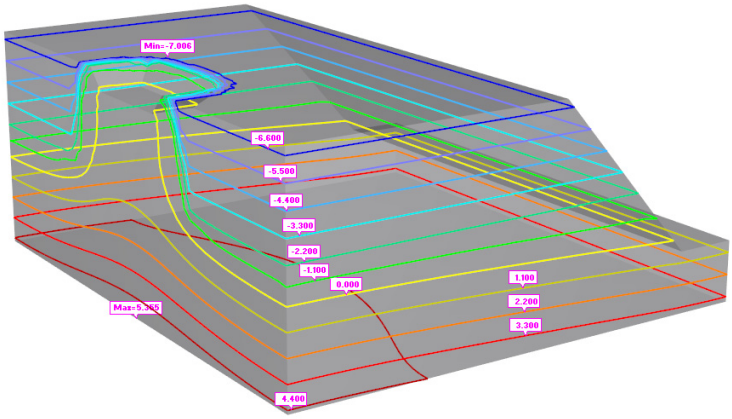

Fig. 13. Example of the **Transparent mode** of the HYDRUS GUI. The Transparent mode is available for all types of graphical displays of scalar and vector fields. Isolines are automatically numbered, and min/max values of a particular variable in the transport domain are automatically identified.

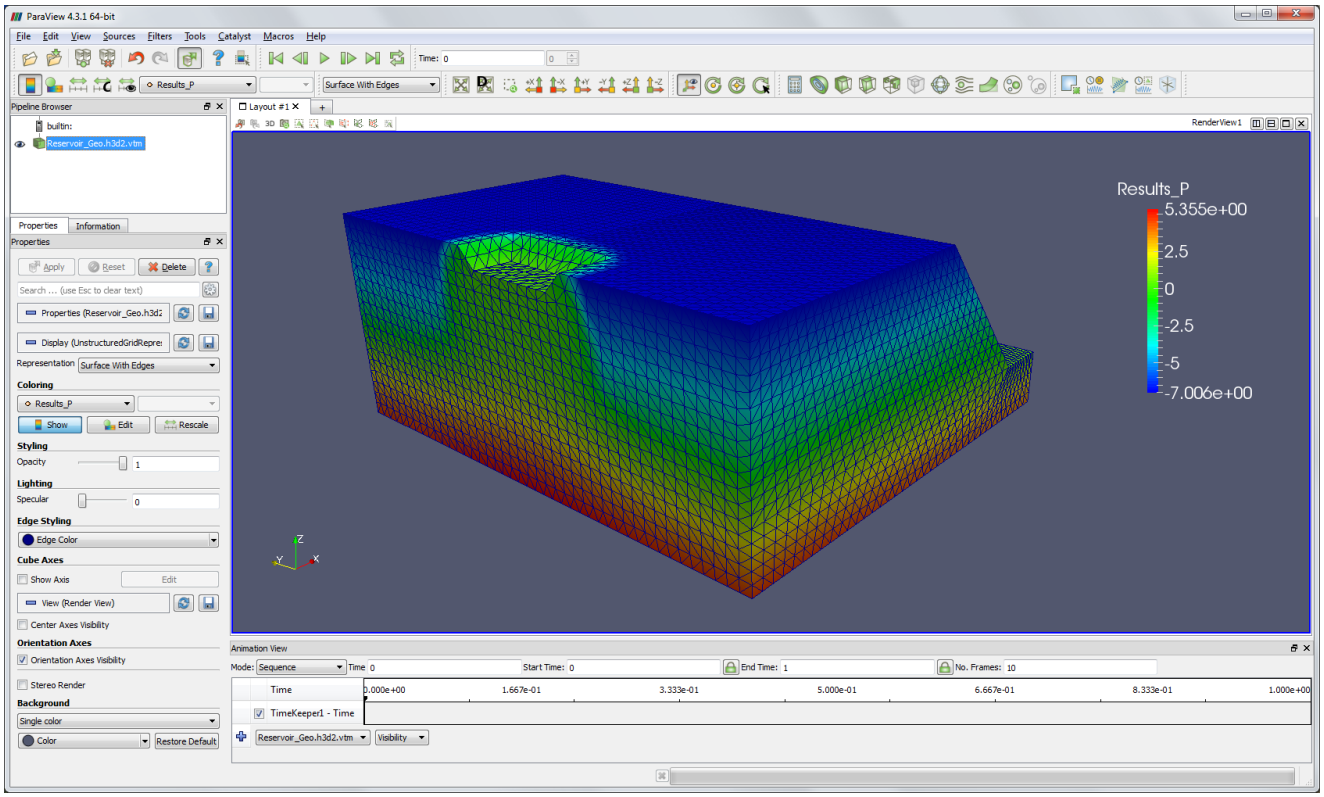

Fig. 14. Example showing **Export to ParaView.** ParaView is an open-source, multi-platform data analysis and visualization application. New visualization options include custom post-processing based on scripting or plugin modules. Details are at www.paraview.org.

Although we believe that HYDRUS post-processing has all of the most important features needed for project execution, some users may require additional functions specific to their own needs. The new version of HYDRUS offers a robust solution by exporting all results to VTK files. VTK is a well-known open source library intended for the visualization of scientific data. Exported HYDRUS results can then be opened in ParaView, such as illustrated in Figure 14, which is a free program based on VTK. Since both software products (VTK and ParaView) are open source, users have full control over the exported data and can implement any special post-processing as judged optimal for their application.

CONCLUSIONS

While HYDRUS (2D/3D) and its various predecessors, such as UNSAT, SWMS-2D, and CHAIN-2D, have been available to the public for over 20 years, the software package is under constant development, with new features being continuously added. This manuscript describes two main new capabilities (a general reservoir boundary condition and a dynamic root growth module) that recently were incorporated in the standard computational module. The capability to simulate the root growth in HYDRUS (2D/3D) has regularly been requested for quite some time by many users, and thus may well become a popular new feature. Similarly, the "Reservoir" boundary condition offers new capabilities for application to a large number of field problems, such as well pumping or the drying of wells, furrow irrigation design and analysis, falling head infiltration experiments, and a range of new approaches to land development known as Low-Impact Development (LID). We also summarized in this paper several new capabilities of the HYDRUS (2D/3D) graphical user interface. Continuous updating of the HYDRUS GUI not only guarantees that the software will be fully operational with new Window operating systems, but also will offer more convenient tools, options, and ease of use to its users.

REFERENCES

Boogaard, H., van Diepen, C., Rotter, R., Cabrera, J., van Laar, H., 1998. WOFOST 7.1: User's guide for the WOFOST 7.1 crop growth simulation model and WOFOST control center 1.5. Tech. Rep. DLO Winand Staring Ctr., Wageningen, the Netherlands.

Brunetti, G., Šimůnek, J., Piro, P., 2016. A comprehensive analysis of the variably-saturated hydraulic behavior of a green roof in Mediterranean climate. Vadose Zone Journal, 15, 9, 15 p. DOI: 10.2136/vzj2016.04.0032.

Brunetti, G., Šimůnek, J., Turco, M., Piro, P., 2017. On the use of surrogate-based modeling for the numerical analysis of Low Impact Development techniques. Journal of Hydrology, 548, 263–277. DOI: 10.1016/j.jhydrol.2017.03.013.

Carsel, R.F., Parrish, R.S., 1988. Developing joint probability distributions of soil water retention characteristics. Water Resources Research, 24, 755–769.

Coffman, L.S., 2002. Low-impact development: An alternative stormwater management technology. In: France, R.L. (Ed.): Handbook of Water Sensitive Planning and Design. Lewis Publ., Boca Raton, FL, pp. 97–123.

Doussan, C., Pages, L., Vercambre, G., 1998. Modelling of the hydraulic architecture of root systems: An integrated approach to water absorption - Model description. Ann. Bot., 81, 213–223.

Han, M., Zhao, C., Šimůnek, J., Feng, G., 2015. Evaluating the impact of groundwater on cotton growth and root zone water balance using Hydrus-1D coupled with a crop growth model. Agricultural Water Management, 160, 64–75. DOI: 10.1016/j.agwat.2015.06.028.

Hartmann, A., Šimůnek, J., Aidoo, M.K., Seidel, S.J., Lazarovitch, N., 2018. Modeling root growth as a function of different environmental stresses using HYDRUS. Vadose Zone Journal, 16 p. DOI: 10.2136/vzj2017.02.0040.

Hinnell, A.C., Lazarovitch, N., Warrick, A.W., 2009. Explicit infiltration function for boreholes under constant head conditions. Water Resour. Res., 45, W10429. DOI: 10.1029/2008WR007685.

Hoffman, G.J., van Genuchten, M.T., 1983. Soil properties and efficient water use: Water management for salinity control. In: Taylor, H.M., Jordan, W.R., Sinclair, T.R. (Eds.): Limitations and Efficient Water Use in Crop Production. Am. Soc. of Agron., Madison, WI, pp. 73–85.

Javaux, M., Schröder, T., Vanderborght, J., Vereecken, H., 2008. Use of a three-dimensional detailed modeling approach for predicting root water uptake. Vadose Zone Journal, 7, 1079–1088. DOI: 10.2136/vzj2007.0115.

Javaux, M., Couvreur, V., Vanderborght, J., Vereecken, H., 2013. Root water uptake: From three-dimensional biophysical processes to macroscopic modeling approaches. Vadose Zone Journal, 12, 4, 16 p. DOI: 10.2136/vzj2013.02.0042.

Jones, C., Bland, W., Ritchie, J., Williams, J.R., 1991. Simulation of root growth. Modeling Plant and Soil Systems-Agronomy Monograph, Segoe Rd., Madison, WI 53711, USA, ASA-CSSA-SSSA, 31, pp. 91–123.

Karandish, F., Šimůnek, J., 2016. A comparison of numerical and machine-learning modeling of soil water content with limited input data. Journal of Hydrology, 543, 892–909. DOI: 10.1016/j.jhydrol. 2016.11.007.

Lazarovitch, N., Warrick, A.W., Furman, A., Zerihun, D., 2009. Subsurface water distribution from furrows described by moment analyses. J. Irrig. Drain. Eng., 135, 1, 7–12.

Li, Y., Kinzelbach, W., Zhou, J., Cheng, G.D., Li, X., 2012. Modelling irrigated maize with a combination of coupled-model simulation and uncertainty analysis, in the northwest of China. Hydrol. Earth Syst. Sci., 16, 1465–1480.

Li, Y., Zou, Q., Zhou, J., Zhang, G., Chen, C., Wang, J., 2014. Assimilating remote sensing information into a coupled hydrology-crop growth model to estimate regional maize yield in arid regions. Ecological Modelling, 291, 15–27.

Ramos, T.B., Šimůnek, J., Gonçalves, M.C., Martins, J.C., Prazeres, A., Pereira, L.S., 2012. Two-dimensional modeling of water and nitrogen fate from sweet sorghum irrigated with fresh and blended saline waters. Agricultural Water Management, 111, 87–104. DOI: 10.1016/j.agwat.2012.05.007.

Roberts, T.L., Lazarovitch, N., Warrick, A.W, Thompson, T.L., 2009. Modeling salt accumulation with subsurface drip irrigation using HYDRUS-2D. Soil Sci. Soc. Am. J., 73, 1, 233–240. DOI: 10.2136/sssaj2008.0033.

Siyal, A.A., Bristow, K.L., Šimůnek, J., 2012. Minimizing nitrogen leaching from furrow irrigation through novel fertilizer placement and soil management strategies. Agricultural Water Management, 115, 242–251. DOI: 10.1016/j.jconhyd.2012.03.008.

Šimůnek, J., Hopmans, J.W., 2009. Modeling compensated root water and nutrient uptake. Ecological Modeling, 220, 4, 505–521. DOI: 10.1016/j.ecolmodel.2008.11.004.

Šimůnek, J., van Genuchten, M.T., Šejna, M., 2008. Development and applications of the HYDRUS and STANMOD software packages and related codes. Vadose Zone Journal, 7, 2, 587–600. DOI: 10.2136/VZJ2007.0077.

Šimůnek, J., van Genuchten, M. T., Šejna, M., 2016a. Recent developments and applications of the HYDRUS computer software packages. Vadose Zone Journal, 15, 7, 25 p. DOI: 10.2136/vzj2016.04.0033.

Šimůnek, J., Bristow, K.L., Helalia, S.A., Siyal, A.A., 2016b. The effect of different fertigation strategies and furrow surface treatments on plant water and nitrogen use. Irrigation Science, 34, 1, 53–69. DOI: 10.1007/s00271-015-0487-z.

Somma, F., Hopmans, J.W., Clausnitzer, V., 1998. Transient three-dimensional modeling of soil water and solute transport with simultaneous root growth, root water and nutrient uptake. Plant Soil, 202, 281–293.

van Genuchten, M.T., 1980. A closed-form equation for predicting the hydraulic conductivity of unsaturated soils. Soil Sci. Soc. Am. J., 44, 987–996.

Vrugt, J.A., Hopmans, J.W., Šimůnek, J., 2001a. Calibration of a two-dimensional root water uptake model. Soil Sci. Soc. Amer. J., 65, 4, 1027–1037.

Vrugt, J.A., van Wijk, M.T., Hopmans, J.W., Šimůnek, J., 2001b. One-, two-, and three-dimensional root water uptake functions for transient modeling. Water Resources Research, 37, 10, 2457–2470.

Wang, J., Huang, G., Zhan, H., Mohanty, B.P., Zheng, J., Huang, Q., Xu, X., 2014. Evaluation of soil water dynamics and crop yield under furrow irrigation with a two-dimensional flow and crop growth coupled model. Agricultural Water Management, 141, 10–22.

Wang, X., Huang, G., Yang, J., Huang, Q., Liu, H., Yu, L., 2015. An assessment of irrigation and fertilization practices: Sprinkler irrigation of winter wheat in the North China Plain. Agricultural Water Management, 159, 197–208.

Warrick, A.W., Lazarovitch, N., Furman, A., Zerihun, D., 2007. Explicit infiltration function for furrows. J. Irrig. Drain. Eng., 133, 4, 307–313.

Williams, J.R., Jones, C.A., Kiniry, J.R., Spanel, D.A., 1989. The EPIC crop growth model. Trans. ASAE, 32, 2, 497–511.

Zhou, J., Cheng, G., Li, X., Hu, B.X., Wang, G., 2012. Numerical modeling of wheat irrigation using coupled HYDRUS and WOFOST models. Soil Sci. Soc. Amer. J., 76, 2, 648–662. DOI: 10.2136/sssaj2010.0467.

Received 14 August 2017
Accepted 4 October 2017

J. Hydrol. Hydromech., 66, 2018, 2, 143–152
DOI: 10.1515/johh-2017-0051

Effect of temporal averaging of meteorological data on predictions of groundwater recharge

Marcia S. Batalha[1], Maria C. Barbosa[1], Boris Faybishenko[2], Martinus Th. van Genuchten[3, 4*]

[1] Department of Civil Engineering, Federal University of Rio de Janeiro, UFRJ, Rio de Janeiro, RJ, Brazil.
[2] Lawrence Berkeley National Laboratory, Berkeley, California, CA, USA.
[3] Center for Environmental Studies, CEA, São Paulo State University, UNESP, Rio Claro, SP, Brazil.
[4] Department of Earth Sciences, Utrecht University, Utrecht, Netherlands.
[*] Corresponding author. E-mail: rvangenuchten@hotmail.com

Abstract: Accurate estimates of infiltration and groundwater recharge are critical for many hydrologic, agricultural and environmental applications. Anticipated climate change in many regions of the world, especially in tropical areas, is expected to increase the frequency of high-intensity, short-duration precipitation events, which in turn will affect the groundwater recharge rate. Estimates of recharge are often obtained using monthly or even annually averaged meteorological time series data. In this study we employed the HYDRUS-1D software package to assess the sensitivity of groundwater recharge calculations to using meteorological time series of different temporal resolutions (i.e., hourly, daily, weekly, monthly and yearly averaged precipitation and potential evaporation rates). Calculations were applied to three sites in Brazil having different climatological conditions: a tropical savanna (the Cerrado), a humid subtropical area (the temperate southern part of Brazil), and a very wet tropical area (Amazonia). To simplify our current analysis, we did not consider any land use effects by ignoring root water uptake. Temporal averaging of meteorological data was found to lead to significant bias in predictions of groundwater recharge, with much greater estimated recharge rates in case of very uneven temporal rainfall distributions during the year involving distinct wet and dry seasons. For example, at the Cerrado site, using daily averaged data produced recharge rates of up to 9 times greater than using yearly averaged data. In all cases, an increase in the time of averaging of meteorological data led to lower estimates of groundwater recharge, especially at sites having coarse-textured soils. Our results show that temporal averaging limits the ability of simulations to predict deep penetration of moisture in response to precipitation, so that water remains in the upper part of the vadose zone subject to upward flow and evaporation.

Keywords: Groundwater recharge; Meteorological data; Temporal averaging; HYDRUS-1D; Infiltration; Evaporation.

INTRODUCTION

Having accurate estimates of water flow rates into and through the vadose zone, and related groundwater recharge rates, is critical in many hydrologic, environmental agricultural applications such as surface- and ground-water management, management and remediation of contaminated soils and groundwater, and irrigation and drainage operations in agriculture. As groundwater is increasingly being used, and available resources are slowly diminishing in many parts of the world, a critical need exists to develop sustainable groundwater use and management practices (Gleeson et al., 2015; Shah et al., 2000; Shiklomanov, 1997; Vörösmarty et al., 2000). This in turn requires an accurate quantitative understanding of the fundamental meteorological controls on groundwater recharge under conditions of climate change (Gorelick and Zheng, 2015; Maxwell and Kollet, 2008; Veldkamp et al., 2016). Groundwater depletion currently occurs in many arid and semi-arid areas due to excessive extraction, especially for irrigation (Aeschbach-Hertig and Gleeson, 2012), with global change exacerbating this problem in various parts of the world.

The expected intensification of precipitation due to global climate change, with a shift toward more heavy precipitation events of often short duration, may lead to an increase in groundwater recharge in tropical and other areas (Allan et al., 2010; Jasechko and Taylor, 2015; Owor et al., 2009). Failure to consider realistic changes in precipitation intensity can influence predictions of both climate change and groundwater recharge (Gee and Hillel, 1988; Mileham et al. 2009; Owor et al., 2009). Intense rainfall events may lead to episodic recharge events (Taylor et al., 2013), which are not accounted for in calculations of groundwater recharge when using monthly or especially annually averaged (aggregated) meteorological time series data, such as is the case with large-scale and long-time averaged water balance equations (Shiklomanov and Rodda, 2003) or using other methods (Kim and Jackson, 2012; Phillips, 1994; Scanlon et al., 2002).

Predictions of water flow into and through the vadose zone contributing to groundwater recharge are dependent upon the availability of meteorological data sets. Data of this type are often obtained from weather stations on daily, weekly, monthly or even yearly averaged time scales. Unfortunately, climate simulations using monthly or annually averaged (aggregated) simulations fail to consider high-intensity precipitation events of relatively short duration (Allan and Soden, 2008), and as such may severely underestimate groundwater recharge rates (Portmann et al., 2013; Wada et al., 2014).

While many methods exist for calculating recharge (e.g., Ngatcha et al., 2007; Scanlon et al., 2002), one common approach is to model variably saturated flow processes in the near-surface to partition precipitation into runoff, evaporation, root water uptake and deep drainage, and hence recharge (Assefa and Woodbury, 2013; Jiménez-Martinez et al., 2009; Leterme et al., 2012). Accurate modeling of vadose zone flow processes and recharge very much depends on having reliable weather data, including their temporal resolution such as daily versus monthly averaged data. Using high-resolution meteorological data is important for transient simulations, especially for

climates having high precipitation rates but also long periods without much rain. In an earlier study (Batalha et al., 2012) we showed that using monthly averaged daily precipitation and evapotranspiration data can produce very different results for recharge as compared to using data having a daily resolution. This occurs since net infiltration, and hence recharge, is very much dependent upon the intensity of short-term rainfall events, as well as the local soil hydraulic properties. On the other hand, the more regular availability of water near the soil surface when precipitation and evaporation or evapotranspiration rates are averaged over relatively long time periods, will lead to less deep penetration of moisture and higher calculated evaporation rates, as compared to transient simulations involving precipitation and evapotranspiration patterns recorded over time periods of days, hours, or even minutes.

Several previous studies have shown the effects of temporal averaging on near-surface flow water flow and contaminant transport processes. For example, Wang et al. (2009) conducted a series of flow and transport simulations with daily data of a typical semi-arid region subject to considerable temporal variability in precipitation. They concluded that reliance on annual meteorological data, as done routinely for contaminant transport simulations, can significantly underestimate the downward migration of contaminants. Predictive errors stemming from the use of annual data increased considerably with time and were more pronounced for very permeable soils that allow water to penetrate much deeper during single rainfall events. Saifadeen and Gladnyeva (2012) similarly inferred that averaging moisture input over larger time periods will lead to underestimates of the center of mass migration, especially for more permeable (coarse-textured) soils. Related contaminant transport examples for different water inflow conditions, with some including steady-state flow conditions, are provided by Marshall et al. (2000), Kuntz and Grathwohl (2009), Harman et al. (2011), Vero et al. (2014) and Yin et al. (2015). In another study relating precipitation and recharge based on monthly and annual averages for groundwater modeling, Jyrkama et al. (2002) concluded that on a monthly basis, precipitation and recharge rates exhibited little correlation due to the delay caused by water percolating through the unsaturated zone.

The various studies above indicate that calculations of water flow into and through the vadose zone may depend very much upon temporal averaging of available meteorological data. Unfortunately, hourly or even daily data are often unavailable from weather stations, while only monthly- or yearly-average data may be present. The overall goal of our study was to find out how different ways of temporally averaging meteorological data would affect infiltration and groundwater recharge processes. Specific objectives were to investigate differences in predicted recharge rates resulting from hourly, daily, weekly, monthly and yearly averaged meteorological data from three sites in Brazil having different climatological conditions: a tropical savanna (the Cerrado), a humid subtropical area (the temperate southern part of Brazil), and a very wet tropical area (Amazonia). In our current analysis we did not consider any land use effects by ignoring root water uptake. The analysis hence is limited to evaporation processes from bare soils.

SIMULATION METHODOLOGY

Various numerical approaches may be used to estimate groundwater recharge (Assefa and Woodbury, 2013; Jyrkama and Sykes, 2007). In this study we evaluated the different temporal scaling effects on groundwater recharge using the HYDRUS 1-D software package of Šimůnek et al. (2013, 2016), which has been previously used in several other recharge studies (e.g., Assefa and Woodbury, 2013; Jiménez-Martinez et al., 2009; Leterme et al., 2012; Neto et al., 2016). Simulations were carried out for a 2-m deep unsaturated soil profile subject to transient meteorological conditions involving precipitation, evaporation and possible runoff. Preliminary calculations, not further shown here, indicated that a soil profile of 2 m was sufficient to estimate deep drainage, and hence recharge. Simulations of mean annual recharge using a 4-m deep profile differed by at most 5% for the most extreme situation when a relatively fine-texture soil was considered.

One-dimensional water flow in the soil profile can be represented using the classical Richards equation as follows

$$\frac{\partial \theta(h)}{\partial t} = \frac{\partial}{\partial x}\left[K(h)\left(\frac{\partial h}{\partial x} - 1\right)\right] \tag{1}$$

where h is the soil water pressure head [L], θ is the volumetric water content [L^3L^{-3}], t is time [T], x is the spatial coordinate (positive downwards) [L], and K is the unsaturated hydraulic conductivity [LT^{-1}]. The soil hydraulic relationships $\theta(h)$ and $K(h)$ in Eq. (1) were described using the constitutive relationships of van Genuchten (1980):

$$S_e(h) = \frac{\theta(h) - \theta_r}{\theta_s - \theta_r} = \begin{cases} \left(1 + |\alpha h|^n\right)^{-m} & h < 0 \\ 1 & h \geq 0 \end{cases} \tag{2}$$

$$K(h) = K_s S_e^l \left[1 - \left(1 - S_e^{1/m}\right)^m\right]^2 \tag{3}$$

where S_e is effective saturation [–], θ_r and θ_s are the residual and saturated volumetric water contents, respectively [L^3L^{-3}], K_s is the saturated hydraulic conductivity [LT^{-1}], α [L^{-1}], n>1 [–] and l [–] are shape factors, and m = 1–1/n [–]. Following van Genuchten (1980), the pore-connectivity parameter l was fixed at a value of 0.5.

The 2-m deep soil profile was discretized into a 201-node finite element mesh with variably-sized elements (smaller values near the soil surface) to facilitate numerical convergence during the calculations. Atmospheric boundary conditions were considered at the soil surface to enable prescribed flux or pressure head conditions depending upon prevailing meteorological conditions (Šimůnek et al., 2013). The boundary fluxes and heads were limited by given precipitation and potential evaporation fluxes in combination with specific parameters to restrict boundary pressure heads to remain above prescribed minima (in our study –100,000 cm) during evaporation, and below certain maximum values (e.g., 0 cm) during precipitation events (surface runoff may then occur). Several simulations also considered the situation where ponding of up to 2.5 cm could occur. This situation may be more realistic for relative flat terrains with a low-permeability surface horizon. The lower boundary condition of the flow domain was set as free drainage ($\partial h/\partial x$ = 0). We note that HYDRUS-1D uses a self-adjusting time-stepping scheme for numerical solution of the Richards equation (Šimůnek et al., 2013). This is important since numerical time steps will be reduced automatically to sometimes seconds or less to correctly simulate high-intensity infiltration rates in relatively dry soils, while remaining consistent with the hourly or daily input data.

METEOROLOGICAL DATA

Data from three sites in Brazil (Fig. 1) representing different climatic regions were used for the groundwater recharge calculations. The sites represented the following regions (from driest to wettest site): a tropical savanna (the Cerrado region), a humid subtropical area (the temperate South of Brazil), and a tropical area (Amazonia). Average annual rainfall rates for the three sites were about 1500, 1600 and 2500 mm, respectively. Figure 2 shows daily rainfall data for the three weather stations. While annual rainfall in the Cerrado is still relatively high (about 1500 mm/yr), rainfall is not distributed evenly over the year. The Cerrado is characterized by summers (December–March) with intense rainfall, and very dry winters. The average monthly temperature variation is only about 4.4°C (even though daily temperatures vary about 12°C). Meteorological data from the Cerrado were taken from Paracatu Station located at 17.25S, 46.88W, and having an altitude of 625 m above mean sea level (a.s.l.).

The subtropical site in southern Brazil (further referred to as the Temperate site) has a warm but relatively temperate climate. As compared to the Cerrado, precipitation at this site is not much higher (about 1600 mm/y) but distributed far more evenly over the year. Even the driest month (July) shows considerable precipitation. Mean temperature varies by 8.8°C throughout the year, with daily variations being about 10°C. Meteorological data for this area were taken from the Urussanga weather station (28.51S, 49.17W) at an altitude of 48.2 m a.s.l. The third site, located in the Amazonia, is characterized by significant rainfall (about 2500 mm/y), and a very short "dry" period in August. Temperatures do not vary much along the year (only about 1.3°C), while daily variations are relatively small also (about 8°C).

Meteorological data for the three sites for a five-year period (2008 through 2012) were downloaded from the Brazilian National Meteorological Institute website (INMET, 2015). The data included daily precipitation (mm), maximum and minimum temperatures (°C), wind speed (km d^{-1}) at 200 cm above the land surface, air humidity (%) and daily sunshine hours. The data were used to calculate daily potential evaporation rates using the Penman-Monteith combination equation (Allen et al., 1998):

$$E_p = \frac{0.408\Delta(R_n - G) + \gamma \frac{900}{T+273} U_2 (e_a - e_d)}{\Delta + \gamma(1 + 0.34U_2)} \quad (4)$$

in which Δ is the slope of the saturation vapor pressure temperature curve (kPa $°C^{-1}$), and γ the psychrometric constant (kPa $°C^{-1}$) as follows:

$$\Delta = \frac{4098 e_a}{(T + 237.3)^2} \quad (5)$$

$$\gamma = \frac{P c_p}{\varepsilon \lambda} * 10^{-3} = 0.00163 \frac{P}{\lambda} \quad (6)$$

In the equations above, E_p is the potential evaporation rate [mm d^{-1}], R_n is net radiation at the soil surface [MJ $m^{-2} d^{-1}$], G is the soil heat flux density [MJ m^{-2} d^{-1}], T is the average daily air temperature [°C]; U_2 is the wind speed at 2 m height [m s^{-1}], e_a is the saturation vapor pressure at temperature T [kPa], e_d is actual vapor pressure [kPa], P is atmospheric pressure [kPa], c_p is the specific heat of moist air (assumed to be 1.013 kJ kg^{-1} $°C^{-1}$), ε is the ratio of the molecular weights of water vapor and dry air (0.622), and λ is the latent heat of vaporization [MJ kg^{-1}]. We emphasize that Eqs. (4)–(6) were used to calculate potential evaporation rates. Actual evaporation (and infiltration) rates are limited by the soil to produce (or accept) the potential surface fluxes as modeled using the atmospheric boundary conditions of HYDRUS-1D (Šimůnek et al., 2013).

Fig. 1. Location of the three meteorological sites in Brazil (adapted from an image mask from the IBGE site (ftp://geoftp.ibge.gov.br/mapas_interativos/) using Google Earth Software).

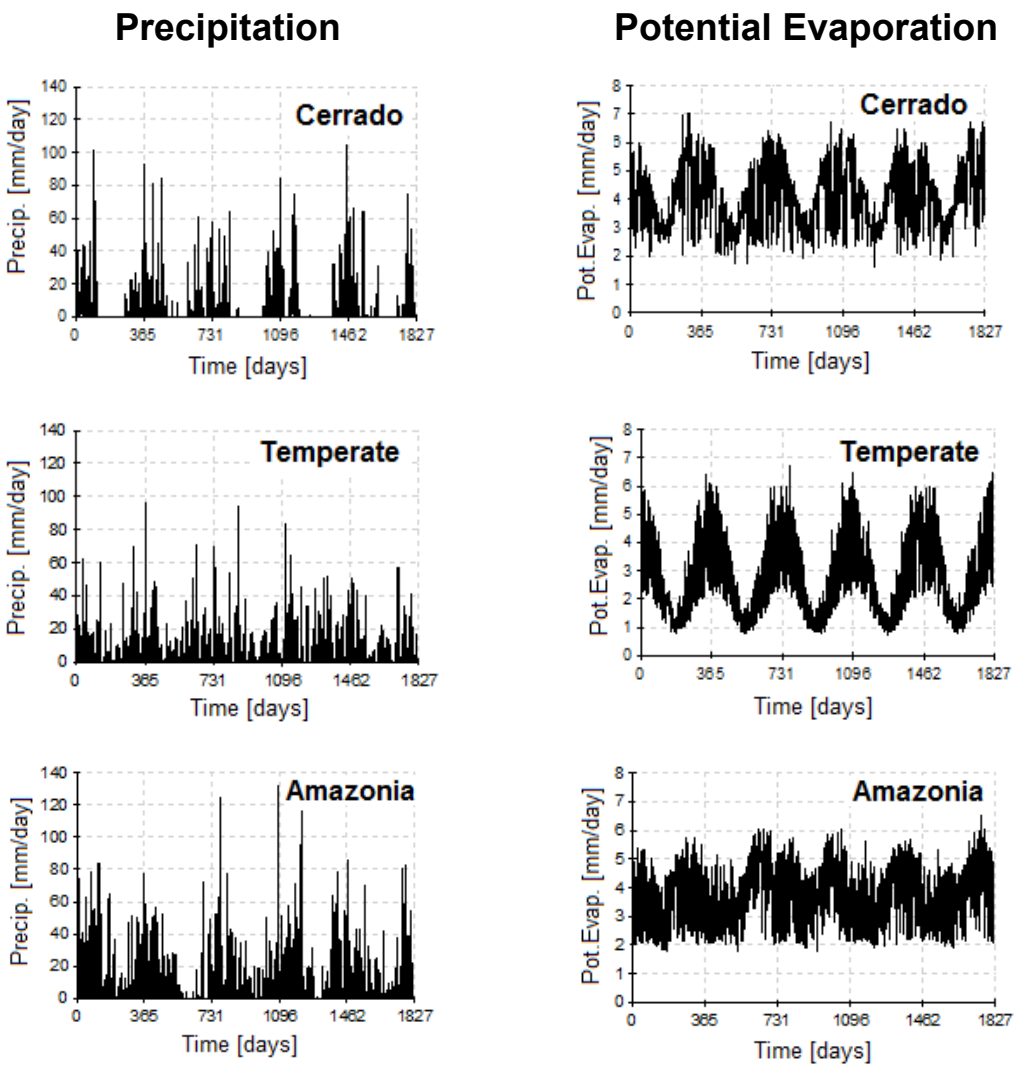

Fig. 2. Observed daily precipitation and calculated daily potential evaporation rates for the Cerrado, Temperate and Amazonia sites.

Figure 2 shows daily precipitation and calculated potential evaporation rates for the Cerrado, Temperate and Amazonia sites. The plots show that the Cerrado has well-defined seasons with precipitation concentrated mostly in the Brazilian summer months, while precipitation at the Amazonia site and especially the Temperate site are distributed much more evenly over the year. By comparison, potential evaporation is least variable during the year at the Amazonia site, ranging from 2 to about 6 mm/day, and most variable in the Temperate region (ranging between 2.5 and 6 mm/d in the summer and between 1 and 1.5 mm/d in the winter months). The precipitation data in Figure 2 represent daily rates (daily totals) during the 5-year study period. We also carried out recharge calculations using hourly input values of precipitation and evaporation. Unfortunately, hourly data are generally not collected at meteorological stations. For our hourly recharge calculations we used precipitation data from Criciuma, which is located about 30 km from the Temperate (South) weather station in Urussanga and has very similar climatological conditions as those in Criciuma. The hourly data were obtained in 2008 by Soares et al. (2012) for an acid mine drainage project in the area. Since only one year of hourly precipitation data were available, the 2008 data were scaled up or down in such a way that the daily values for the years 2009–2012 were respected. For the 5-year study we obtained in this way close to 44,000 hourly precipitation data entries.

We also generated hourly potential evaporation data corresponding to the hourly precipitation data. One possible approach to generate these is to use hourly time steps in a Penman-Monteith type procedure as advocated by ASCE (2005). Since our study already used daily potential evaporation rates, we downscaled the daily rates to hourly values in a manner consistent with the daily total values. The conversion was done in accordance with previous experimental studies of hourly evaporation and evapotranspiration rates by van Bavel (1966), van Bavel and Hillel (1976), and Katul and Parlange (1992), as well as with similar studies of diurnal patterns of other meteorological variables such as temperature (Ephrath et al., 1996; Kimball and Bellamy, 1986; Wann et al., 1985). The approach, as also programmed in the HYDRUS-1D code, assumes that the daily evaporation rate (the daily total) can be distributed sinusoidally over the day into hourly rates such that they represent about 12% of the daily total between 0–6 am and between 18–24 pm, and 88% during the remainder of the day (Šimůnek et al., 2013). Mathematically, the distribution over the day (24 h) for the potential evaporation rate is then described by

$$E_p(t) = \begin{cases} 0.24\overline{E_p} & (t < 0.264d \ \text{ or } \ t > 0.736d) \\ 2.75\overline{E_p}\sin\left(\dfrac{2\pi t}{24} - \dfrac{\pi}{2}\right) & 0.264d \le t \le 0.736d) \end{cases} \quad (7)$$

where $\overline{E_p}$ is the daily value of the potential evaporation rate.

The procedures above allowed us to define daily and hourly meteorological data for the 5-year recharge calculations. Our temporal averaging procedure considered at first daily precipitation and temperatures as well as later also all parameters needed for the Penman-Monteith equation yielding daily evaporation rates. Once daily evaporation and precipitation data were available for the different sites, the data were averaged over time using the expression:

$$MP = \frac{1}{n}\sum_{i=1}^{n} mp_i \qquad \begin{cases} n = 7 & \text{for weekly approach} \\ n = 30 & (28, 29 \text{ or } 31) \text{ for monthly} \\ n = 365 & (366) \text{ for yearly} \end{cases} \qquad (8)$$

where mp_i represents the available daily meteorological data (i.e., precipitation or evaporation), n is the period of temporal averaging, and MP is the average daily rate of the meteorological parameter over the time period being considered.

To assess the effect of soil texture on recharge as calculated using the temporally average data, we decided to carry out the simulations for three different soil types covering relatively coarse- to fine-textured soils: a loamy sand, a loam and a clay loam. Soil hydraulic parameters for these soils were defined using pedotransfer functions derived by Carsel and Parrish (1988). The parameters used are presented in Table 1. We used these parameters to define initial pressure head conditions for each simulation that were consistent with the long-term average recharge rates obtained for the particular meteorological conditions.

Table 1. Soil hydraulic parameters in Eqs. (1) and (2) for the three soils used in the simulations.

Soil Texture	θ_r (–)	θ_s (–)	α (cm^{-1})	n (–)	K_s ($cm\ d^{-1}$)
Loamy sand	0.057	0.410	0.124	2.28	350.
Loam	0.078	0.430	0.036	1.56	25.0
Clay loam	0.095	0.410	0.019	1.31	6.24

RESULTS AND DISCUSSION

In this section we compare results of the recharge calculations for the temporal averaging schemes involving daily, weekly, monthly and yearly averaged meteorological data. Figure 3 shows that rapid temporal changes in the recharge rate at the Cerrado site occur when daily averaged meteorological data are used as compared to monthly averaged values, while the overall patterns are generally identical (values of the daily and monthly recharge rates are shown on the left-hand side y-axis). However, the pattern of daily recharge rates when using yearly averaged data (values shown on the right-hand side axis) is significantly different from those for the daily and monthly averaged meteorological data.

Figure 4 shows box-and-whisker diagrams (Chambers et al., 1983) of the daily recharge rates obtained for the Cerrado site using daily, monthly, and yearly averaged meteorological data. The plots include the minimum, first quartile (25th percentile), median, third quartile (75th percentile), and maximum quartiles, as well as the upper and lower whiskers representing the +/– 1.5 interquartile ranges between the first and third quartiles of the corresponding upper and lower quartiles. The statistical parameters are also summarized in Table 2. The data show that, notwithstanding the differences between the minimum and maximum recharge values obtained with the daily and monthly

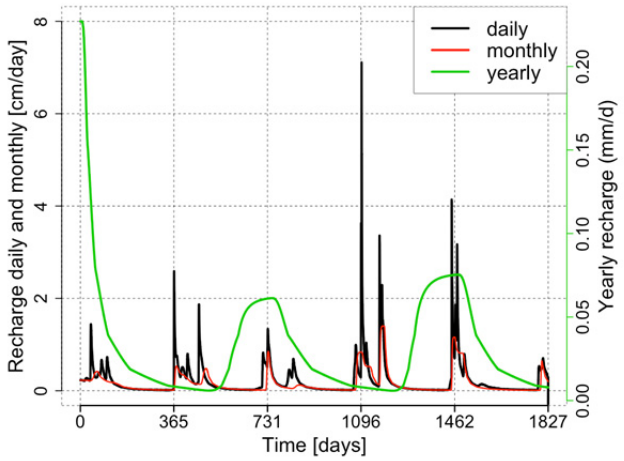

Fig. 3. Time series of groundwater recharge rates obtained using daily, monthly, and yearly averaged meteorological data from the Cerrado site. Please note the different scales for the daily and monthly data (left side) and the yearly data (right side).

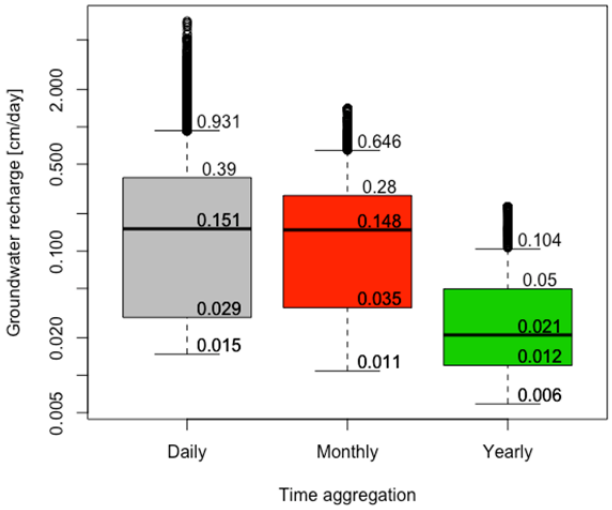

Fig. 4. Box-and-whisker plots and statistical parameters of groundwater recharge rates obtained using daily, monthly, and yearly averaged meteorological data from the Cerrado site, as calculated using the time series shown in Figure 3.

Table 2. Statistical parameters of recharge rates at the Cerrado site as obtained with daily, monthly, and yearly averaged meteorological data.

	Daily	Monthly	Yearly
Lower hinge	–0.288	0.0108	0.00588
25%	0.0268	0.0350	0.0120
Median	0.148	0.148	0.0211
75%	0.414	0.280	0.0496
Upper hinge	0.994	0.646	0.104

averaged input data, the median values are the same (0.148 cm/d) and much larger than the median of the recharge rate obtained with yearly averaged data (0.021 cm/d). Note that the vertical axis in Figure 4 is given on a log scale to demonstrate to more clearly visualize the range of variations in recharge for the three types of input data.

To quantitatively assess differences in the calculated recharge rates using daily, monthly, and yearly averaging of the weather data, we also applied a Kolmogorov-Smirnov (KS) goodness-of-fit test. The nonparametric KS test is used to

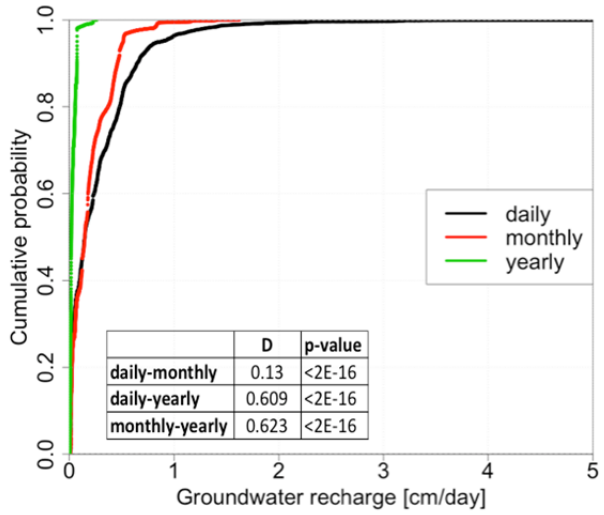

Fig. 5. Cumulative distributions of groundwater recharge rates obtained using daily, monthly, and yearly averaged meteorological data from the Cerrado site (the table shows results of the Kolmogorov-Smirnov test).

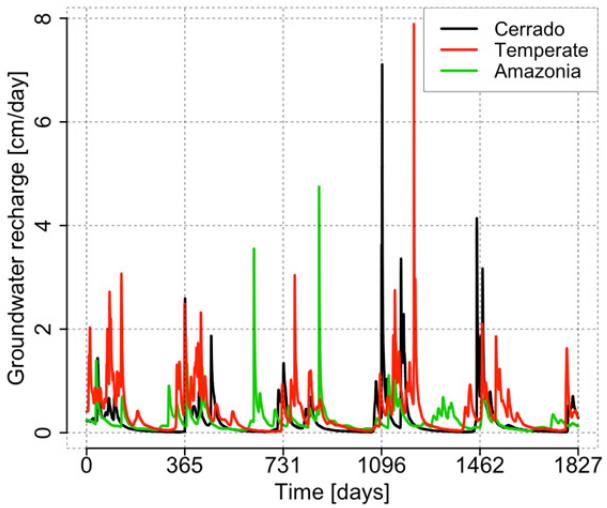

Fig. 6. Comparison of daily groundwater recharge for three sites, demonstrating different temporal seasonal patterns, depending on meteorological conditions at the sites.

determine the probability that a given dataset is drawn from the same parent population as a second dataset (called the two-sample KS test; Marsaglia et al., 2003). The KS statistics are measures of the supremum, being the greatest distance between the empirical cumulative distribution functions (CDFs) of the datasets. The CDFs, along with results of calculations, are shown in Figure 5. Based on the *D* statistical measure of the discrepancy between the CDFs, we reject the hypothesis that the distributions are similar. This can be seen from the table entries in Figure 4, which show that the difference between the daily and monthly recharge rates is far less than the difference between daily and yearly values, as well as between the monthly and yearly recharge estimates.

Calculated daily recharge rates for the three ways of temporal averaging are shown in Figures 6 and 7. Figure 6 demonstrates differences in the temporal distributions of groundwater recharge caused by different patterns of precipitation, while Figure 7 depicts the corresponding box-and-whiskers plots along with the statistical parameters for recharge at the three sites. As expected from the climatic conditions at the three sites (Fig. 2), the lowest values of recharge are at the Cerrado site (the negative lower value indicates that evaporation actually slightly exceeded infiltration), and the highest values are at the Amazonia site.

Figure 8 compares results for the three soil types at each site. Each plot shows for the same period of averaging the calculated annual recharge rates. In all cases, the highest recharge rates occurred when using daily averaged data, while the yearly averaged data always produced the lowest values. The plots show that differences between the higher and lower values can be very significant. The most extreme situation occurred for the Cerrado, where daily averaged data generated up to 9 times higher annual average recharge rates than when yearly averaged data were used. The main reason relates to the irregular distribution of the meteorological data, especially precipitation, over the year (Fig. 2). The more uneven the precipitation distribution, the higher the difference in calculated recharge rates. When precipitation is confined to only a short period of the year, more water penetrates below layers near the soil surface from which upward flow and evaporation is still possible. This effect is clearly shown when comparing results for the Cerrado with those for the Temperate and Amazonia sites. Even though

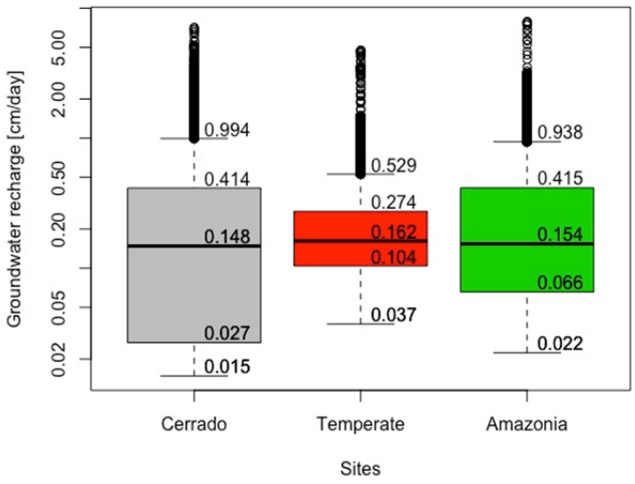

Fig. 7. Box-and-whisker plots and statistical parameters of groundwater recharge rates obtained using daily, monthly, and yearly averaged meteorological data from the Cerrado, Temperate and Amazonia sites, as calculated using the time series shown in Figure 6.

the annual precipitation rate at the Temperate site (1600 mm) was only slightly larger than at the Cerrado site (1500 mm), the differences in calculated recharge rates between the daily and annually averaged data were much smaller for the Temperate site. The same occurs for the Amazonia site, even with its much larger annual precipitation rates. Using daily averaging, the recharge rates can still be 25 to 82% higher than for yearly averaging, depending upon soil type.

Figure 8 further shows that the effect of soil texture on the calculations can be quite important when the temporal averaging period is relatively short (daily or weekly). Coarser soils tend to produce 30 to 40% more recharge as long as the hydraulic conductivity is relatively high to allow most of the infiltrated water to move rapidly below the zone of influence for upward flow. On the other hand, fine-textured soils may act as buffers by keeping moisture closer to the surface to enable subsequently upward flow and evaporation. This occurs especially when the hydraulic conductivity of the surface layer is lower than the precipitation rate, in which case fine-textured soils facilitate runoff and thus further diminish infiltration and recharge.

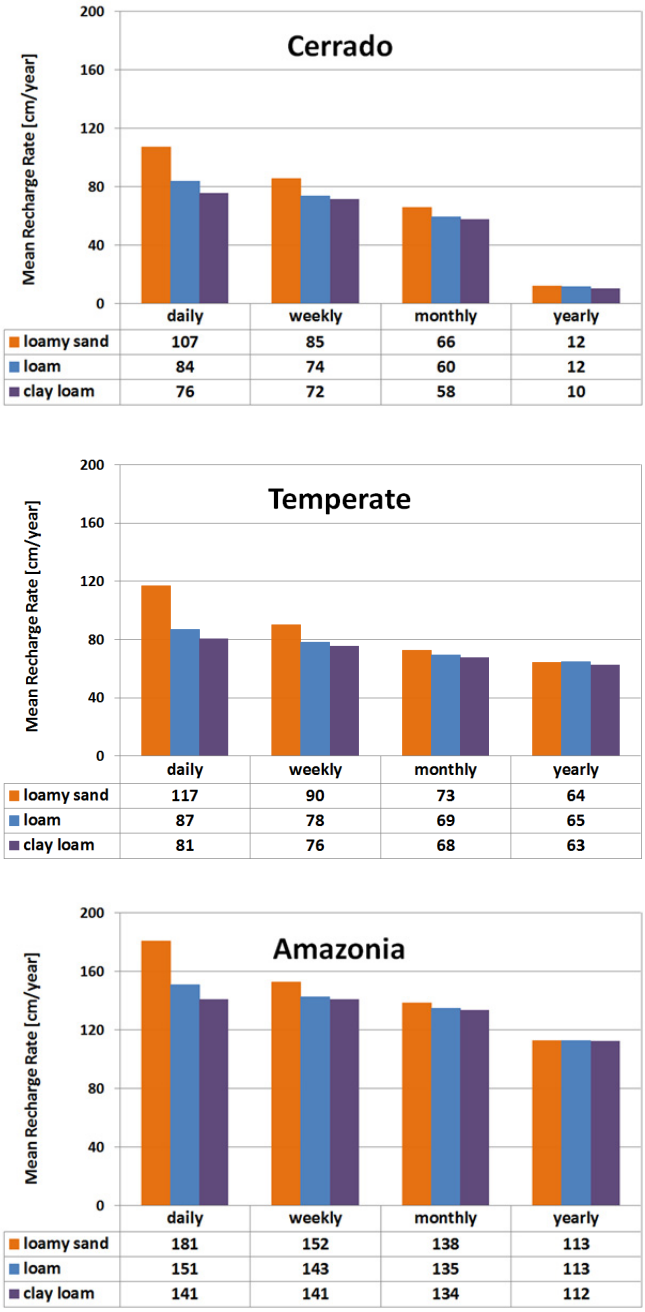

Fig. 8. Calculated average annual recharge rates at the Cerrado (top), Temperate (middle) and Amazonia (bottom) sites as obtained using daily, monthly, and yearly averaged meteorological data.

Calculated groundwater recharge rates as a percentage of rainfall for the same period (2008 through 2012) at the different sites are presented in Table 3. Estimated recharge rates calculated in this study using the daily averaged weather data were surprisingly independent of location, ranging mostly between 50% for the fine-textured clay loam soil, to about 75% for the more coarse-textured loamy sand. Values for the weekly, monthly and yearly averaged data on average were always lower, especially when using the yearly data of the Cerrado, where recharge became less than 8% of annual precipitation, irrespective of soil type. The Cerrado situation is quite similar to what was observed in (semi-) arid sites for contaminant transport by Wang et al. (2009) and Harman et al. (2011).

Table 3. Calculated recharge rates as a percentage of rainfall at the Brazilian Cerrado, Temperate and Amazonia sites.

Averaging	Loamy sand	Loam	Clay loam
	--------- Cerrado ---------		
Daily	72	56	51
Weekly	58	50	48
Monthly	44	40	39
Yearly	8	8	7
	--------- Temperate ----------		
Hourly	76	47 / 51*	22 / 46*
Daily	72	54	50
Weekly	56	48	47
Monthly	45	43	42
Yearly	39	40	39
	--------- Amazonia ----------		
Daily	73	61	57
Weekly	62	58	57
Monthly	56	55	54
Yearly	46	46	45

*The first value refers to a runoff and the second to a ponding boundary condition

Those studies showed that daily averaged calculations predicted significant contaminant transport, while little transport occurred when annually averaged precipitation data were considered.

The data in Table 3 indicate recharge always will be underestimated when monthly and, especially, yearly averaged meteorological data are used. The hourly values for the Temperate site generated much more variation among soil type when runoff was considered. The values in Table 3 (between 40 and 75%, except for the Cerrado) are well within the range of literature values documented by Kim and Jackson (2012) for unvegetated surfaces. They also correspond to or exceed the upper limits of annual values for vegetated surfaces inventories by Kim and Jackson (2012) and determined by Santoni et al. (2010) and Assefa and Woodbury (2013), among others. As noted by Assefa and Woodbury (2013) and confirmed by our results, recharge rates can be very variable in time (see also Fig. 6) depending upon transient weather conditions and soil type. Still, we acknowledge that our values should be higher, in part since we did not consider any root water uptake in this study.

The plots and data in Figure 8 indicate that cumulative recharge is always lower when considering yearly averaged data. Similar calculations that include also results for the hourly averaged precipitation and evaporation data are presented in Figure 9 for the Temperate site. The simulations show that runoff is now becoming also an important term, especially for the fine-textured (clay loam) soils. In that case the hourly precipitation rates can become larger than the saturated hydraulic conductivity (K_s), leading to runoff when an atmospheric boundary condition with possible runoff is considered (Figure 8, top plots). It is also possible to allow water to pond on the surface by assuming the presence of a relatively flat soil surface, in which case little or no runoff may occur. The simulations shown in Figure 8 (bottom) were obtained for the intermediate situation where runoff would occur only when reaching a ponding depth of more than 2.5 cm on the soil surface. Results for the hourly data in that case are now very close to those for the daily meteorological data. The results in Figure 10 indicate that the runoff component can be important and with standard numerical calculations will show up mostly when hourly averaged data are used, and then only for medium- and especially fine-textured soils. No difference between the hourly

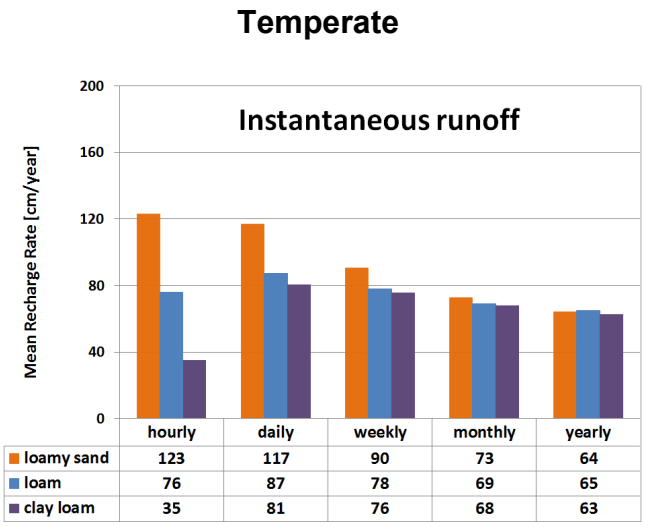

	hourly	daily	weekly	monthly	yearly
loamy sand	123	117	90	73	64
loam	76	87	78	69	65
clay loam	35	81	76	68	63

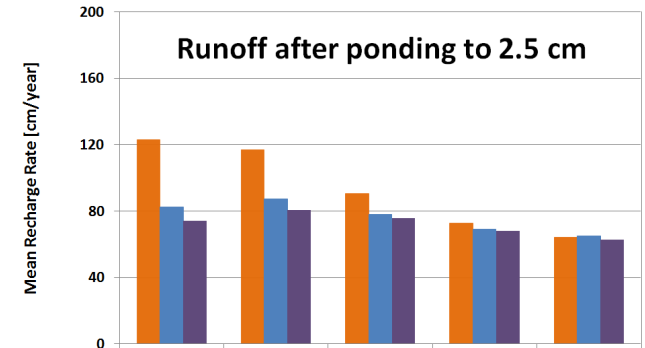

	hourly	daily	weekly	monthly	yearly
loamy sand	123	117	90	73	64
loam	83	87	78	69	65
clay loam	74	81	76	68	63

Fig. 9. Calculated average annual recharge rates for the Temperate site as obtained using hourly, daily, weekly and monthly averaged weather data assuming atmospheric boundary conditions with instantaneous runoff (top plot) and with runoff occurring only after reaching a ponding level of 2.5 cm.

and daily calculations occurred for loamy sand since the hourly averaged precipitation rates never exceeded the saturated hydraulic conductivity of 350 cm/day. On the other hand, when ponding is considered, the results for the hourly averaged data tend to closely approximate results for the daily averaged data also for the fine-textured soil.

The important effect of possible runoff is further demonstrated in Figure 10, which shows cumulative recharge during 5 years for both the hourly averaged data (dotted lines) and the daily averaged data (continuous lines) for both the loam and clay loam soils. Results are for the cases with instantaneous runoff (dotted line) and runoff after ponding to 2.5 cm (dashed line). Calculations show that hourly averaged data lead to far less infiltration, and hence lower recharge rates, for the clay loam soil.

CONCLUDING REMARKS

In this study we evaluated the effects of temporal averaging of meteorological data on calculated groundwater recharge rates for three sites in Brazil having very different climatological conditions. Calculations showed that the use of temporally averaged meteorological data can lead to very different results in the recharge calculations, decreasing from daily, weekly,

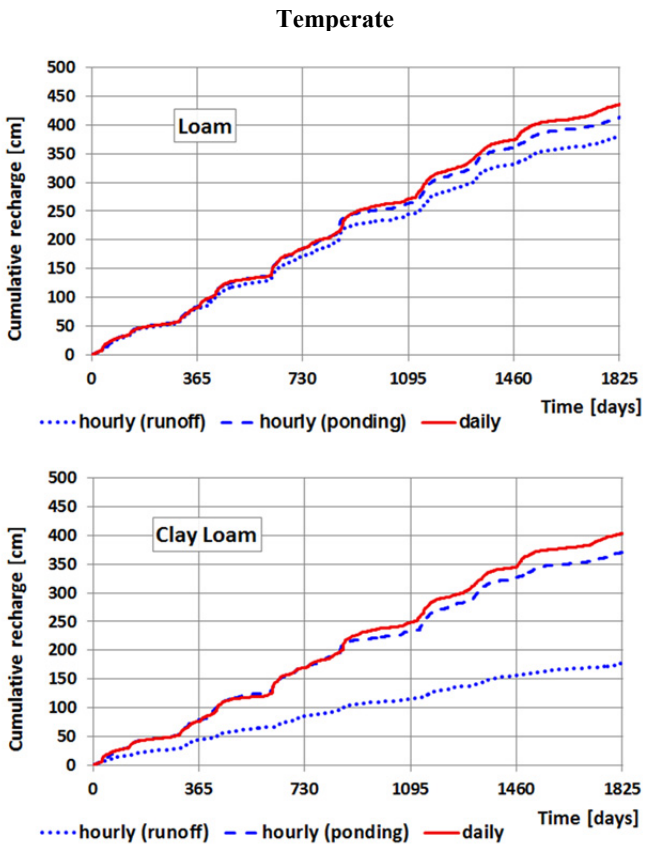

Fig. 10. HYDRUS-1D calculated cumulative recharge rates obtained with hourly and daily data for the loam (top) and clay loam (bottom) soils with and without ponding.

monthly, to yearly averaged data, with the yearly average data always producing the lowest recharge rates. Results were especially sensitive to averaging when applied to the Cerrado Region in Brazil where recharge rates using daily averaged data were up to 9 times the recharge rate for yearly averaged meteorological data. But the effects were also apparent for the Temperate and Amazonia sites where the differences ranged from 25 to 82%. The important effects of averaging at the Cerrado site were related to the highly uneven rainfall distribution over the year involving distinct wet and dry seasons. Yearly averaging may then even lead to near-zero recharge rates in certain time periods, with concomitant significant underestimates of the actual recharge rates.

While rainfall and its temporal distribution in time are important determinants for recharge, another factor is soil type. When averaging weather data (and hence infiltration) over longer periods of time, infiltrated water will fail to reach soil depths below the influence of evaporation, even in coarse-textured soils. The soils then do not dry out very much, thus causing evaporation rates to be overestimated, and recharge underestimated, in some cases by up to 50%. By comparison, fine-textured soils can better regulate near-surface soil moisture conditions during high precipitation events, leading to recharge rates that are less dependent upon time averaging (daily to monthly values), except for the yearly averaged data.

Another important effect of temporal averaging of weather data is its effect on runoff, which relates to the amount of water not infiltrated into a soil during a rainfall event. Infiltration rates during a particular precipitation event ultimately depend on the saturated hydraulic conductivity, K_s. Runoff will occur when the precipitation rate is higher than K_s for an appreciable

time period depending on the initial soil moisture conditions. Long-term averaging will smooth available precipitation data to rates that will always be less than K_s, especially for weekly, monthly and yearly averaged data. Even daily averaged data seldom produce runoff, unless very fine-textured soils are present. Lack of runoff will then actually increase local recharge rates. This is why in actuality hourly calculations should be used for fine-textured soils, subject of course to data availability. Differences, however, will become less significant if ponding will occur in relatively flat areas, thus minimizing runoff. Overall results of this study indicate that daily averaged meteorological data should be used as much as possible, while yearly averaged data should be avoided as much as possible.

We emphasize that the current study is limited to simulations of vadose zone flow and evaporation, without directly modeling of root water uptake, which would lead to reduced recharge rates. We plan to document the additional effects of land use in a separate document. We further acknowledge that other processes such as especially preferential flow in a heterogeneous soil profile may also modify recharge rates, especially during high-precipitation events in conjunction with surface ponding.

Acknowledgements. BF's part of this study was supported by NGEE-Tropics, funded by the U.S. Department of Energy, Office of Science, Office of Biological and Environmental Research, and Office of Advanced Scientific Computing, under the DOE Contract No. DE-AC02-05CH11231.

REFERENCES

Aeschbach-Hertig, W., Gleeson, T., 2012. Regional strategies for the accelerating global problem of groundwater depletion. Nature Geosci., 5, 853–861.

Allan, R.P., Soden. B.J., 2008. Atmospheric warming and the amplification of precipitation extremes. Science, 321, 1481–1481.

Allan, P., Soden, B.J., John, V.O., Ingram, W., Good, P., 2010. Current changes in tropical precipitation. Environ. Res. Lett., 5, 025205, 7 p.

Allen R.G., Pereira, L.S., Raes, D., Smith, M., 1998. Crop Evapotranspiration; Guidelines for Computing Crop Water Requirements. FAO Irrigation and Drainage Paper 56. Food and Agriculture Organization of the United Nations, Rome, Italy.

ASCE, 2005. The ASCE Standardized Reference Evapotranspiration Equation. Environmental and Water Resources Institute of ASCE, Final Report. American Society of Civil Engineers, Reston, VA, USA.

Assefa, K.A., Woodbury, A.D., 2013. Transient, spatially varied groundwater recharge modeling. Water Resour. Res., 49, 4593–4606.

Batalha, M.S., Bezerra, C.R., Jacques, D., Barbosa, M.C., Pontedeiro, E.M., van Genuchten, M.Th., 2012. Multicomponent transport predictions of ^{226}Ra in soil following the use of phosphogypsum. In: Proc. 4th Int. Conf. on Engineering for Waste and Biomass Valorization, WASTENG, Porto, Portugal, 6 p.

Carsel R.F., Parrish. R.S., 1988. Developing joint probability distributions of soil water retention characteristics. Water Resour. Res., 4, 755–769.

Chambers, J.M., Cleveland, W.S., Kleiner, B., Tukey, P.A., 1983. Graphical Methods for Data Analysis. Wadsworth & Brooks/Cole.

Ephrath, J.E., Goudriaan, J., Marani, A., 1996. Evaluation and calibration of three models for daily cycle of air temperature, radiation, wind speed and relative humidity by equations from daily characteristics. Agric. Syst., 51, 4, 377–393.

Gee, G.W., Hillel, D., 1988. Groundwater recharge in arid regions: Review and critique of estimation methods. Hydrol. Process., 2, 255–266. DOI: 10.1002/hyp.3360020306.

Gleeson, T., Befus, K.M., Jasechko, S., Luijendijk, E., Cardenas, M.B., 2015. The global volume and distribution of modern groundwater. Nature Geosci., 9, 161–167.

Gorelick, S.M., Zheng, C., 2015. Global change and the groundwater management challenge. Water Resour. Res., 51, 3031–3051, DOI: 10.1002/ 2014WR016825.

Harman, C.J., Rao, P.S.C., Basu, N.B., McGrath, G.S., Kumar, P., Sivapalan, M., 2011. Climate, soil, and vegetation controls on the temporal variability of vadose zone transport. Water Resour. Res., 47, W00J13

INMET, 2015. Instituto Nacional de Meteorologia, Ministério da Agricultura, Pecuária e Abastecimento <http://www.inmet.gov.br/portal/index.php?r=bdmep/bdmep>, Brazil.

Jasechko, S., Taylor, R.G., 2015. Intensive rainfall recharges tropical groundwaters Environ. Res. Lett., 10, 124015.

Jimenez-Martinez, J., Skaggs, T.H., van Genuchten, M.Th., Candela, L., 2009. A root zone modelling approach to estimating groundwater recharge from irrigated areas. J. Hydrol., 367, 138–149.

Jyrkama, M.I., Sykes, J.F., 2007. The impact of climate change on spatially varying groundwater recharge in the grand river watershed (Ontario). J. Hydrol., 338, 237–250.

Jyrkama, M.I., Sykes, J.F., Normani, S.D., 2002. Recharge estimation for transient ground water modeling. Ground Water, 40, 638–648.

Katul, G.G., Parlange, M.B., 1992. A Penman-Brutsaert model for wet surface evaporation. Water Resour. Res., 28, 121–126.

Kim, J.H., Jackson, R.B., 2012. A global analysis of groundwater recharge for vegetation, climate, and soils. Vadose Zone J., 11, 1.

Kimball, B.A., Bellamy, L.A., 1986. Generation of diurnal solar radiation, temperature, and humidity patterns. Energy Agric., 5, 185–197.

Kuntz, D., Grathwohl, P., 2009. Comparison of steady-state and transient flow conditions on reactive transport of contaminants in the vadose zone. J. Hydrol., 369, 225–233.

Leterme, B., Mallants, D., Jacques, D., 2012. Sensitivity of groundwater recharge using climatic analogues and HYDRUS-1D. Hydrol. Earth Syst. Sci., 16, 2485–2497.

Marsaglia, G.W., Tsang, W., Wang, J., 2003. Evaluating Kolmogorov's distribution. J. Stat. Softw., 8, 18.

Marshall, J.D., Shimada, B.W., Jaffe, P.R., 2000. Effect of temporal variability in infiltration on contaminant transport in the unsaturated zone. J. Contam. Hydrol., 46, 151–161.

Maxwell, R.M., Kollet, S.J., 2008. Interdependence of groundwater dynamics and land-energy feedbacks under climate change. Nature Geosci., 1, 665–669.

Mileham, L., Taylor, R.G., Todd, M., Tindimugaya, C., Thompson, J., 2009. Climate change impacts on the terrestrial hydrology of a humid, equatorial catchment: sensitivity of projections to rainfall intensity. Hydrol. Sci. J., 54, 727–738.

Neto, D.C., Chang, H.K., van Genuchten, M.Th., 2016. A mathematical view of water table fluctuations in a shallow aquifer in Brazil. Ground Water, 54, 82–91.

Ngatcha, B.N., Mudry, J., Sarrot, R.J., 2007. Groundwater recharge from rainfall in the southern border of Lake Chad in Cameroon. World Appl. Sci. J., 2, 125–131.

Owor, M., Taylor, R.G., Tindimugaya, C., Mwesigwa, D., 2009. Rainfall intensity and groundwater recharge: Empirical evidence from the Upper Nile Basin. Environ. Res. Lett., 4, 035009.

Phillips, F.M., 1994. Environmental tracers for water movement in desert soils of the American Southwest. Soil Sci. Soc. Am. J., 58, 15–24.

Portmann, F.T., Döll, P., Eisner, S., Flörke, M., 2013. Impact of climate change on renewable groundwater resources: assessing the benefits of avoided greenhouse gas emissions using selected CMIP5 climate projections. Environ. Res. Lett. 8, 024023.

Saifadeen, A., Gladnyeva, R., 2012. Modeling of solute transport in the unsaturated zone using HYDRUS-1D. TVVR 12/5020, Water Resources Engineering, Lund University, Sweden.

Santoni, C.S., Jobbágy, E.G., Contreras, S., 2010. Vadose zone transport in dry forests of central Argentina: Role of land use. Water Resour. Res., 46, W10541.

Scanlon, B.R., Healy, R.W., Cook, P.G., 2002. Choosing appropriate techniques for quantifying groundwater recharge. Hydrogeol. J., 10, 18–39.

Shah, T., Molden, D., Sakthivadivel, R., Seckler, D., 2000. The global groundwater situation: Overview of opportunities and challenges. IWMI Books, Rep. H025885. Int. Water Manage. Ins., Colombo, Sri Lanka.

Shiklomanov, I.A., 1997. Comprehensive assessment of the freshwater resources of the world. World Meteor. Org., Stockholm, Sweden.

Shiklomanov, I.A., Rodda, J.C., 2003. World Water Resources at the Beginning of the Twenty-First Century. Cambridge University Press, Cambridge, UK.

Šimůnek, J., Šejna, M., Saito, H., Sakai, M., van Genuchten, M.Th., 2013. The HYDRUS-1D Software Package for Simulating the One-Dimensional Movement of Water, Heat, and Multiple Solutes in Variably-Saturated Media, Version 4.17. Dep. of Environmental Sciences, University of California, Riverside, California, USA.

Šimůnek, J., van Genuchten, M.Th., Šejna, M., 2016. Recent developments and applications of the HYDRUS computer software packages. Vadose Zone J., 15, DOI: 10.2136/vzj2016.04.0033.

Soares, P.S.M., Souza, V.P., Possa, M.V., Soares. A.B., 2012. Projeto Cooperativo para Realização de Experimento de Avaliação de Desempenho de Cobertura Seca para Mitigação de Drenagem Ácida de Mina em Escala Piloto Centro de Tecnologia Mineral (CETEM). Relatório Final de Projeto Elaborado Para a Carbonífera Criciúma S.A., Rio de Janeiro, Brazil.

Taylor, R.G., Todd, M.C., Kongola, L., Maurice, L., Nahozya, E., Sanga, H., MacDonald, A.M., 2013. Evidence of the dependence of groundwater resources on extreme rainfall in East Africa. Nature Climate Change, 3, 374–378.

van Bavel, C.H.M., 1966. Potential evaporation: The combination concept and its experimental verification. Water Resour. Res., 2, 3, 455–467.

van Bavel, C.H.M., Hillel, D.I., 1976. Calculating potential and actual evaporation from a bare soil surface by simulation of concurrent flow of water and heat. Agric. Meteorol., 17, 453–476.

van Genuchten, M.Th., 1980. A closed-form equation for predicting the hydraulic conductivity of unsaturated soils. Soil Sci. Soc. Am. J., 44 892–898.

Veldkamp, T.I.E., Wada, Y., Aerts, J.C.J.H., Ward, P.J., 2016. Towards a global water scarcity risk assessment framework: Incorporation of probability distributions and hydro-climatic variability. Environ. Res. Lett., 11, 024006.

Vero, S.E., Ibrahim, T.G., Creamer, R.E., Grandt, J., Healy, M.G., Henry, T., Kramers, G., Richards, K.G., Fenton, O., 2014. Consequences of varied soil hydraulic and meteorological complexity on unsaturated zone time lag estimates. J. Contam. Hydrol., 170, 53–67.

Vörösmarty, C.J., Green, P., Salisbury, J., Lammers, R.B., 2000. Global water resources: Vulnerability from climate change and population growth. Science, 289, 284–288.

Wada, Y., Wisser, D., Bierkens, M.F.P., 2014. Global modeling of withdrawal, allocation and consumptive use of surface water and groundwater resources. Earth Syst. Dyn., 5, 15–40.

Wang, P., Quinlan, P., Tartakovsky, D.M., 2009. Effects of spatio-temporal variability of precipitation on contaminant migration in the vadose zone. Geophys. Res. Lett., 36, L12404.

Wann, M., Yan, D., Gold, H.J., 1985. Evaluation and calibration of three models for daily cycle of air temperature. Agric. Forest Meteorol., 34, 121–128.

Yin, Y., Sykes, J.F., Normani, S.D., 2015. Impacts of spatial and temporal recharge on field-scale contaminant transport model calibration. J. Hydrol., 527, 77–87.

Received 16 August 2017
Accepted 20 November 2017

J. Hydrol. Hydromech., 66, 2018, 2, 153–160
DOI: 10.1515/johh-2017-0059

Operational validation of HYDRUS (2D/3D) for capillary barriers using data of a 10-m tipping trough

Klaus Berger

University of Hamburg, Institute of Soil Science, Allende-Platz 2, 20146 Hamburg, Germany.
Tel.: +49 40 42838 2006. Fax: +49 40 42838 2024. E-mail: klaus.berger@uni-hamburg.de

Abstract: Capillary barriers are an interesting alternative component for cover systems of landfills and contaminated sites. Provided they are sufficiently validated, soil hydrological models could be fast and powerful tools for the dimensioning of capillary barriers. Outflow rates measured in a 10 m long tipping trough for one material combination and two slopes from stationary periods were compared to simulation results of HYDRUS (2D/3D), Version 2.05. The measured outflow rates show a typical pattern with slope-dependent threshold values indicating the efficiency of the capillary barrier. This flow pattern could not be reproduced with HYDRUS (2D/3D) that for different input setups produced smooth patterns without thresholds. The input setup was varied for different soil hydraulic models (van Genuchten-Mualem vs. Brooks-Corey), homogeneous and heterogeneous transport domains (no scaling vs. stochastically distributed scaling factors considering the Miller-Miller similitude), different HYDRUS versions (standard vs. alternative; i.e., with material properties assigned either to finite element nodes or finite elements, respectively), and different lower boundary conditions (seepage face vs. free drainage). Differences between measured and simulated outflow patterns could be caused by the measurements, the application of the model, or by the model itself. The van Genuchten-Mualem model may not be suitable to describe the soil hydrological relationships of these particular materials. The reason for the mismatch, however, could not be identified yet.

Keywords: Capillary barriers; Funneled flow; Landfills; Cover systems; Operational validation; HYDRUS (2D/3D).

INTRODUCTION

Capillary barriers are two-layer systems consisting of an upper layer made of a relatively fine-grained and fine-porous material (e.g., sand), the so-called ‘capillary layer’, underlain by a lower layer made of a relatively coarse-grained and coarse-porous material (e.g., gravel), the so-called ‘capillary block’. There is a sharp interface between the two layers that is sloped. Water percolating through a capillary layer under unsaturated conditions is held at the interface due to capillary forces (a capillary barrier effect). When inflow into the capillary layer is relatively small, nearly no water breaks through the interface into the capillary block. Instead, water moves laterally in the capillary layer along the interface (a wick[ing] effect or a capillary diversion) (see, e.g., Oldenburg and Pruess, 1993; Yeh et al., 1994). This type of flow is called ‘funneled flow’ (Kung 1990; illustrated using the dye tracer experiment depicted in Figure 1). However, when inflow into the capillary layer becomes higher, water begins to break through the interface. As inflow decreases, breakthrough decreases as well and the capillary barrier ‘recovers’.

Capillary barriers are not only a curious soil hydrological phenomenon, but they also represent an interesting component in cover systems for landfills and contaminated sites. Cover systems are multi-layer systems consisting of layers that perform specific tasks. Especially on steep slopes, capillary barriers can be used as a stand-alone barrier or as a component of a liner that is overlain by a compacted cohesive layer or a geomembrane for limiting inflow into the capillary layer.

For the use in cover systems, capillary barriers have to be dimensioned. This means that suitable material combinations of the capillary layer and capillary block, and a suitable maximum distance to a drain that removes water from the system have to be determined depending on site-specific conditions. The following parameters are relevant:

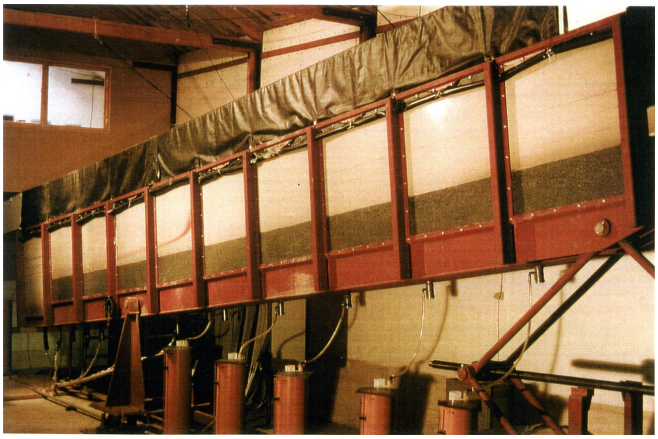

Fig. 1. A front view of the filled 10-m tipping trough (dark brown material = capillary block, light-colored material = capillary layer, and collection sump in the left-most segment). A dye tracer experiment with a red tracer is depicted on the left side. The irrigation system is inside the black box on the top of the tipping trough. Photo: Institute of Soil Science, University of Hamburg.

1. Soil hydrological properties of the materials of the capillary layer and the capillary block;
2. Slope;
3. Slope length / maximum distance to the drain;
4. Shape of the slope (convex - concave; convergent - divergent);
5. Infiltration rate into the capillary layer. This depends on the climate of the site and the layers above the capillary barrier.

There are several principal methods available to dimension capillary barriers with specific advantages and disadvantages. Table 1 gives an overview of the most important methods. Several empirical investigations with large test fields (lysimeters)

Table 1. Important principle methods for dimensioning capillary barriers and their advantages and disadvantages.

I.	Empirical investigations with large test fields (lysimeters)
Advantages:	Close to reality due to field size
Disadvantages:	Limited to very few parameter values and material combinations Requires experience and accuracy to avoid systematic errors Time-consuming (many years) Very expensive Measurement results depend on the weather as a boundary condition and are therefore not reproducible
II.	Empirical investigations with tipping troughs (tilt gutters) in pilot plant scale
Advantages:	Relatively close to the reality in the field Measurement results are (approximately) reproducible
Disadvantages:	Limited to some parameter values and material combinations Relatively time-consuming (many months) Expensive
III.	Simulations with 2D or 3D models
Advantages:	Allows analyzing many parameter values and material combinations Fast Low costs Simulation results are reproducible
Disadvantages:	Requires sufficient validation of the model for a particular type of application

were performed in Germany, for example, on the landfill Georgswerder in Hamburg, which had six test fields, each 50 m long and 10 m wide, one having a capillary barrier below a compacted cohesive layer (Melchior, 1993; Melchior et al., 2010). Other test fields in Germany with capillary barrier were operated on the landfills 'Am Stempel' near Marburg and 'Monte Scherbelino' near Frankfurt am Main (Jelinek, 1997), and in Karlsruhe (Zischak, 1997). Further test fields were operated but are mostly only documented in German (overviews of these test fields can be found in Steinert (1999) and Pfeiffer (2006)).

Tipping troughs on a pilot plant scale of capillary barriers existed in Germany at the University of Hamburg (length x depth x height of 10.0 m x 0.5 m x 1.0 m; Steinert, 1999; Steinert et al., 1997a,b), the Technical University of Darmstadt (2 troughs with L x D x H of 8.0 m x 0.2 m x 1.5 m; Holfelder, 2002; Kämpf, 2000; Kämpf et al., 2003; von der Hude, 1999), the Technical University of Munich (L x D x H of 6.0 m x 0.6 m x 1.0 m; Barth 2003), and the University of Giessen (L x D x H of 6.0 m x 0.6 m x 1.0 m; Pfeiffer, 2006). However, objectives of the research and materials of the capillary barriers were different in these studies, and thus the results are difficult to compare. Furthermore, several tipping troughs on a laboratory scale (approximately 1 m length) were operated in Germany, e.g., at the University of Hamburg. The results of these small troughs could, however, hardly be transferred to a field scale (Steinert, 1999).

Comparisons of measured and simulated data for tipping troughs were performed in Germany for SWMS_2D (Berger, 2017; Steinert, 1997a,b), for HYDRUS-2D (Kämpf, 2000; Kämpf et al., 2003; Pfeiffer, 2006), and for Feflow 5.0 (Barth, 2003). The authors assessed the success of output comparisons very differently, from 'failure' to 'in principle possible,' 'satisfactory' to 'good'. However, Barth (2003) and Kämpf et al. (2003) especially emphasized the importance of the soil hydraulic properties for the simulation results.

Simulations with two- or three-dimensional models such as HYDRUS (2D/3D) (Radcliffe and Šimůnek, 2010; Šejna et al., 2016; Šimůnek et al., 2016) have major advantages compared to empirical investigations (see Table 1), but require prior validation. This is required for any particular type of application to assure that the simulation results are close to reality and can be transferred into the field. Validation is a complex methodology (Knepell and Arangno, 1993; Konikow and Bredehoft, 1992; Oreskes et al., 1994; see also Berger, 1999). An important aspect of it is operational validation, i.e., comparisons of simulations and measurement results. One such output comparison was performed for HYDRUS (2D/3D), version 2.05 (2.05.0230) (Šejna et al., 2016; Šimůnek et al., 2016), using outflow data of a capillary barrier constructed in a 10 m long tipping trough (Steinert, 1999). The aim of the simulation was to reproduce measured outflow patterns that describe the efficiency of the capillary barrier.

MATERIAL AND METHODS

Experiments with a 10 m long tipping trough

Design, experiments, and measurement results with the tipping trough (a tilt gutter) are described in detail in German in Steinert et al. (1997a) and Steinert (1999), and with the first results and more concisely in Steinert et al. (1997b). The following description is focused on information relevant to the simulations discussed below.

The tipping trough (see Figs. 1, 2, and 3) was 10 m long and 0.5 m deep. The capillary barrier constructed inside had a height of 1 m (0.3 m capillary block, 0.7 m capillary layer). The bottom of the trough was divided into 10 segments by steel panels of 0.15 m height (for an exception, see below). Each segment was 1 m long with a separate outflow at the bottom. The capillary barrier was constructed in the upper 9 segments with a central measurement area of 0.3 m depth and two margins at the front and on the back, each with a depth of 0.1 m, separated by steel panels of 0.15 m height. The final segment was separated by a 0.3 m high steel panel and filled with the material of the capillary layer. It served as a collection sump for the capillary layer and had a bottom 0.13 m below the bottom of the other 9 segments.

The slope of the trough was continuously adjustable up to 1:3 (33%) by a scissors jack operated by a crank handle. The entire trough stood on weighing cells with a resolution of 1 kg. The empty trough weighed about 4 t; the trough filled with materials weighed around 13 t, depending on the mass of water in the trough. Outflows were measured with a maximum resolution of 0.1 l. An irrigation system on the top of the trough allowed for a uniform irrigation of the entire surface of the capillary layer with a continuously adjustable irrigation rate between 0.1 and 30 mm/d. A second independent irrigation system was at the end wall.

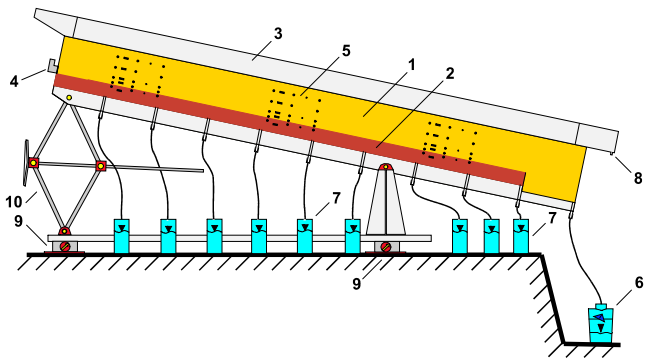

Fig. 2. A schematic side view of the tipping trough at an inclination of 1:5 (1: capillary layer; 2: capillary block; 3: cover of the top irrigation system; 4: end wall irrigation system; 5: soil hydrological measurement field; 6: collection bin of the capillary layer; 7: collection bins of the capillary block; 8: overflow of the top irrigation system; 9: weighing cells; 10: scissors jack with crank handle) (from Steinert (1999), translated into English).
(Note: This Figure is side-inverted to Figs. 1 and 3.)

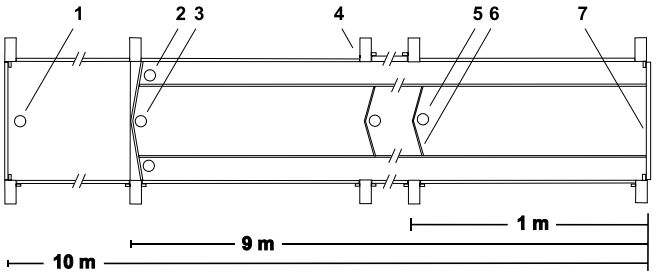

Fig. 3. A schematic top view of the bottom of the tipping trough (1: outflow of the capillary layer/collection sump; 2: outflow of the back margin; 3: central outflow of the 9th capillary block segment; 4: steel bar; 5: central outflow of the 1st capillary block segment; 6: steel panel; 7: end wall) (from Steinert (1999), translated into English).

The capillary layer was constructed from medium sand. This material originates from the dredged material from the river Elbe that has been treated in a mechanical treatment plant for harbor sediments (called 'METHA'), which is operated by the Hamburg Port Authority. The capillary block consisted of gravel with grain diameters ranging mainly from 1 to 3 mm. Both materials have a narrow particle size distribution.

Experiments with a material combination of the capillary layer and capillary block took several months without interruption. The evaluation was focused on outflow rates from the capillary layer and the capillary block at different inflow rates.

Simulations with HYDRUS (2D/3D)

Simulations were performed for one material combination, two slopes, and for periods of steady state flow. Two slopes were investigated: a steep slope with 1:5 (20%) and a flat slope with 1:25 (4%). Only periods with a constant irrigation rate from the top, no end wall irrigation, and a maximum weighing difference of the entire tipping trough of 5 kg were simulated. Each period was evaluated in a separate simulation run. The simulation period was set to 34,560 minutes (24 days) to assure steady state at the end of each simulation run. The outflow patterns were characterized by outflow rates from the capillary layer and the capillary block at the end of each simulation run. In the simulations, only outflow from the bottom capillary block segment was simulated, and measured outflows from all 9 capillary block segments of a stationary period were added for comparison. Measured and simulated outflow rates (in dimensions of L^2/T) from the capillary layer were reduced, assuming that direct flow is perpendicular from the upper boundary into the final capillary layer segment and thus bypasses the capillary block (11.4% of the inflow rate for the slope 1:5, and 10.3% for 1:25, respectively). The purpose of this is to reflect only the efficiency of the capillary barrier.

Simulations were performed using a "2D general" HYDRUS geometry in the vertical plane and the units of cm for length and minutes for time. The finite element (FE) mesh parameters and resulting FE mesh statistics are summarized in Table 2. Mesh refinements were used at the upper and lower boundaries (inflow and outflow) and especially along the interface of the capillary layer and the capillary block, which is a critical zone for the efficiency of the capillary barrier. The upper boundary was assigned a constant flux. The initial condition was set to a constant pressure head of –50 cm at each node.

To reproduce the measured outflow patterns of the capillary barrier, the model input setup was varied as summarized in Table 3. In particular:

Table 2. FE mesh parameters (above) and FE mesh statistics (below) used in the numerical simulations. The number of FE nodes and elements generated by HYDRUS with the same FE mesh parameters differ slightly for the two slopes.

Targeted FE-size: 5 cm	Stretching in x-direction: factor 2
Refinements: 1. Upper boundary (irrigation) 2. Lower boundaries (outflows) 3. Interface of the capillary layer and capillary block	 FE-size 2.5 cm + 2 points per outflow FE-size 0.6 cm

Slope	FE nodes	1D-elements	2D-elements
1:5	42513	2010	84597
1:25	42443	1917	84470

Table 3. Input setup for the numerical simulations.

	Scenario 1	Scenario 2
Soil hydraulic model	van Genuchten-Mualem	Brooks and Corey
Homogeneous/Scaling	No scaling	Stochastically distributed scaling factors using the Miller- Miller similitude
HYDRUS version	Standard	Alternative
Lower boundary condition (Outflow)	Seepage face (with zero pressure head)	Free drainage

Soil hydraulic models: Water content-pressure head relationships were measured with a pressure plate apparatus using samples taken in the tipping trough (Steinert et al., 1997a) and evaluated with RETC (van Genuchten et al., 1991) (see Table 4, which also includes the measured saturated hydraulic conductivities, and Fig. 4). The parameters of the van Genuchten-Mualem model were already used in earlier simulations with SWMS_2D (Steinert et al., 1997a). Sometimes, coarse materials can be better described using the Brooks and Corey model.

Table 4. Soil hydrological parameters of METHA-sand and 1/3 gravel in the van Genuchten-Mualem model (above) and the Brooks and Corey model (below).

METHA-sand $r^2 = 0.996$	Mean	95% confidence interval	
α (cm^{-1}) n (–)	0.0302 5.11	0.0283 4.28	0.0321 5.95
θ_s (–) θ_r (–)	0.3056 0.0400	– –	– –
k_s (m s^{-1}) k_s (cm min^{-1})	1.3 e–4 0.78	–	–
1/3 gravel $r^2 = 0.998$			
α (cm^{-1}) n (–)	0.206 3.75	0.197 3.42	0.214 4.08
θ_s (–) θ_r (–)	0.375 0.033	– –	– –
k_s (m s^{-1}) k_s (cm min^{-1})	1.2 e–2 72	–	–

Material	θ_r (–)	θ_s (–)	α (cm^{-1})	n (–)
METHA-sand	0.0339	0.296	0.0418	2.12
1/3 gravel	0.036	0.255	0.210	2.36

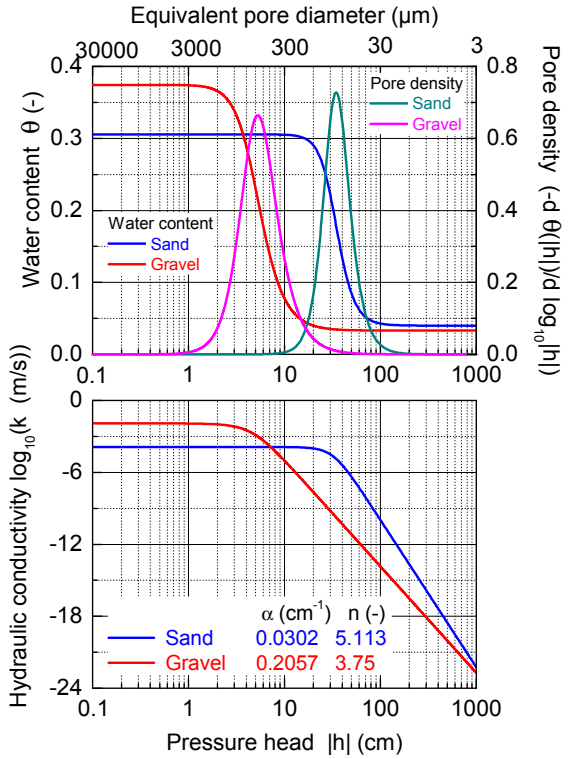

Fig. 4. Water content–pressure head functions, pore density distributions, and hydraulic conductivity–pressure head functions for the METHA-sand and 1/3 gravel using the van Genuchten-Mualem model.

Therefore, the Brooks-Corey parameters, including the residual and the saturated water contents, were also fitted to the water content-pressure head data using RETC (see Table 4). The values of the residual and the saturated water content differed from those determined for the van Genuchten-Mualem model. In the simulations with the Brooks-Corey model, the lower limit of the tension interval of the internal interpolation tables was set to 24 cm, i.e., slightly higher than the bubbling pressure.

Scaling: The first set of simulations assumed homogeneous and isotropic materials. However, homogeneity is a concept that cannot be found in pure form in nature. Due to spatial heterogeneity, the breakthrough of the capillary barrier may occur in fingers that are self-reinforcing with increasing inflow rates. Therefore, stochastically distributed scaling factors were used to model spatial heterogeneity. The Miller-Miller similitude with default values as given in the HYDRUS user interface was selected, except for the standard deviation of log10(y) of the hydraulic conductivity scaling factor, which, after some tests, was set to 0.125.

HYDRUS version: The standard HYDRUS version assigns material properties to the nodes of the FE mesh. According to Heiberger (1996, p. 52), this approach does not allow for a sharp interface between two layers, but leads to an interface layer with alternating intermediate material properties. In the alternative HYDRUS version (Šimůnek, 2017), material properties are assigned directly to the FE elements, thus allowing abrupt textural changes and sharp interfaces between two layers.

Of the 16 possible combinations of the input setup (2 soil hydraulic property models, homogeneous vs heterogeneous, 2 HYDRUS versions, and 2 lower boundary conditions), 9 combinations were simulated. Seven combinations, among them six with a free drainage boundary condition, were not simulated because further insights were not expected from their results.

RESULTS AND DISCUSSION

Comparison of measured and simulated outflow rates

The results are depicted in Figs. 5 to 8. The dependence of measured and simulated outflow rates on the inflow rates is shown in Figs. 5 and 8 in the same manner. The slope 1:25 is in the left column, the slope 1:5 is in the right column, flow from the capillary layer is in the upper row and flow from the capillary block is in the lower row. Symbols mark simulated stationary periods. Every pair of simulated outflow rates from the capillary layer and the capillary block for the same inflow rate should sum up to the inflow rate (steady state). Actually, in most cases the simulated outflow rates summed up to 99.8 to 100.0% of the inflow rates. Sometimes, the percentage was a

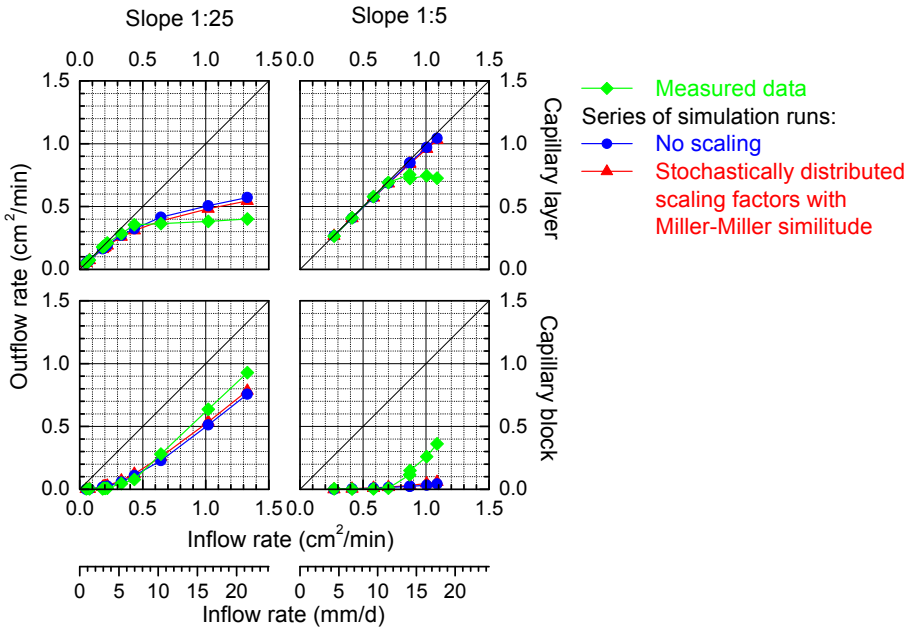

Fig. 5. Comparisons of measured and simulated outflow rates from a capillary layer and a capillary block dependent on the inflow rates for the model setup with the van Genuchten-Mualem model, a standard HYDRUS version, and a seepage face.

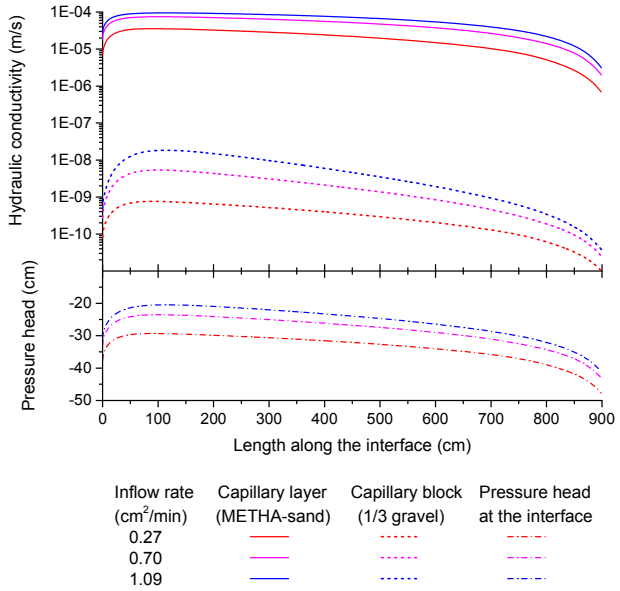

Fig. 6. The pressure heads along the interface between the capillary layer and the capillary block, as well as the corresponding hydraulic conductivities in the two materials calculated using the van Genuchten-Mualem model. The results are for the model setup with the van Genuchten-Mualem model, no scaling, the standard HYDRUS version, a seepage face boundary condition, the 1:5 slope, and three inflow rates (the smallest, a medium, and the largest inflow rate). The length along the interface is directed from the bottom (0 cm) to the top (900 cm) of the capillary barrier.

bit smaller, namely for the flat slope 1:25 and the smallest inflow rate, or if a simulation run was aborted. In the latter case, the latest available stored result was evaluated. To simplify the interpretation of the results, the inflow rates in Figs. 5 and 8 are shown in the abstract simulation unit of cm^2/min as well as in mm/d, which is commonly used for precipitation, evapotranspiration, and discharge.

The measured data show typical flow patterns (Fig. 5). At small inflow rates, almost all infiltration water moves laterally downward in the capillary layer along the interface and almost no outflow is measured from the capillary block. For the flat slope 1:25 and the first threshold of the inflow rate of approximately 4 mm/d, water starts breaking through the interface into the capillary block, leading to an increase in capillary block outflow. For the second threshold of the inflow rate of 7.0 mm/d, most of the additional water infiltrating into the capillary layer breaks through into the capillary block and the outflow rate from the capillary layer increases only slightly. For the steep slope 1:5, only one threshold can be identified. At this threshold of 11.4 mm/d, all additional water infiltrating into the capillary layer breaks through into the capillary block and the outflow rate from the capillary layer remains approximately constant. With respect to the efficiency of the capillary barrier in cover systems, the capillary layer outflow at the (second) threshold can be denoted as the 'lateral drainage capacity' of the capillary barrier (Steinert et al., 1997a). This characteristic is different from the 'diversion capacity' of Ross (1990) (see also Lacroix Vachon et al., 2015). The objective of the numerical simulations was to reproduce this flow pattern and to identify the threshold(s).

However, the simulated outflow rates show a different flow pattern with a smooth increase in the outflow rates from the capillary layer and the capillary block, without any visible thresholds. In the model setup with the van Genuchten-Mualem model, the standard HYDRUS version, and a seepage face (Fig. 5), HYDRUS reproduced the outflow rates at small to medium inflow rates well. However, especially for the steep slope 1:5 and high inflow rates, HYDRUS overestimated the outflow rates from the capillary layer and underestimated those from the capillary block. Thus, the model overestimated the efficiency of the capillary barrier just for those conditions (steep slopes) for which capillary barriers are to be used. Simulations performed in 1995 with the predecessor model SWMS_2D (Šimůnek et al., 1992) and modified values of the van Genuchten-Mualem parameters and the saturated hydraulic conductivities of Table 4 (among others α and n of the 95% confidence intervals) yielded smooth outflow patterns as well (Berger, 2017; Steinert et al., 1997a).

Fig. 6 illustrates the reason for the simulated smooth outflow pattern without visible thresholds for the 1:5 slope and the model setup with the van Genuchten-Mualem model, no scaling, the standard HYDRUS version, and a seepage face boundary condition. The hydraulic conductivities along the interface of the capillary barrier in the capillary layer and the capillary block differ by about 4 to 5 orders of magnitude. The ratio of the hydraulic conductivities of the capillary layer and the capillary block decreases with increasing inflow rates. However, for the largest inflow rate the hydraulic conductivity of the capillary layer material is still about 4 orders of magnitude larger than that of the capillary block material.

Fig. 5 also shows that the corresponding outflow rates simulated without scaling and with stochastically distributed scaling factors for the Miller-Miller similitude are close together. This result also holds for the model setup with the Brooks and Corey model, the standard HYDRUS version, and a seepage face. This means that if fingering occurs in the simulation (due to heterogeneity), it does not play as important a role as expected.

The simulation results with the alternative HYDRUS version indicate a more efficient capillary barrier, i.e., the outflow rates from the capillary layer were larger and those from the capillary block were smaller compared to those simulated using the

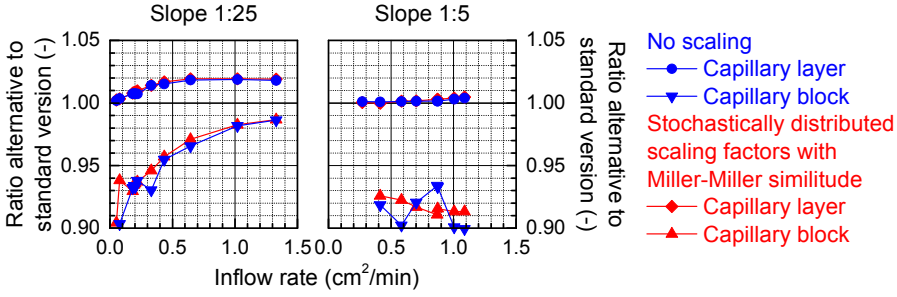

Fig. 7. A ratio of corresponding outflow rates from a capillary layer and a capillary block dependent on the inflow rates simulated by alternative and standard HYDRUS (2D/3D) versions for the model setup with the van Genuchten-Mualem model and a seepage face.

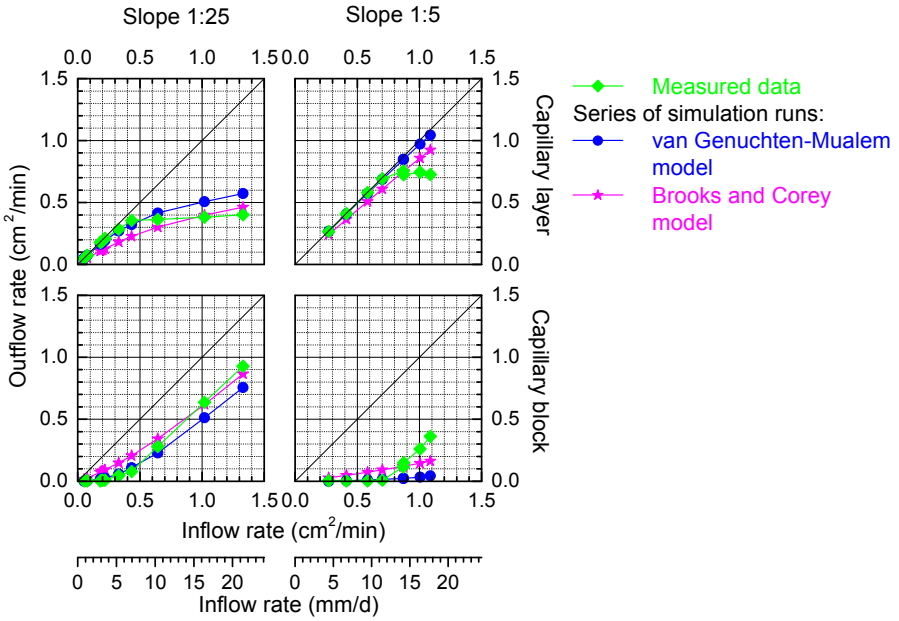

Fig. 8. Comparisons of measured and simulated outflow rates from a capillary layer and a capillary block for different inflow rates and slopes, and for a model setup with no scaling, a standard HYDRUS version, and a seepage face.

standard HYDRUS version (see Fig. 7 for the model setup with the van Genuchten-Mualem model and a seepage face). However, for the fine FE mesh used in these simulations, the impact of the alternative HYDRUS version is relatively small. While for the slope 1:25, the outflow rates from the capillary layer increased up to 2% compared to the standard HYDRUS version, for the steep slope 1:5, the differences were less than 1%. The outflow rates from the capillary block simulating with the alternative HYDRUS version were between 90 and 99% of those simulated with the standard version. However, the base of these percentages is very small compared to the outflow rates from the capillary layer (the very small values may be one reason for the irregular, counter-intuitive 'up and down' of the ratios for the 1:5 slope in Fig. 7). Unpublished results of similar simulations with a much coarser FE mesh (i.e., 367 nodes and 785 elements) showed a much larger impact of the HYDRUS version. The alternative HYDRUS version produced outflow rates from the capillary layer up to 41% higher than the standard HYDRUS version. Obviously, the impact of how soil hydraulic properties are assigned, either to FE nodes (as in the standard HYDRUS version) or to FE elements (as in the alternative HYDRUS version) becomes smaller for a smaller FE-size. The outflow rates obtained with the alternative HYDRUS version matched the measured outflow rates worse than those obtained with the standard version. However, when using fine FE meshes the impact of the HYDRUS version can be neglected in this application because the differences to the results of the standard version are small.

For the model setup with no scaling, the standard HYDRUS version, and a seepage face, the HYDRUS model with the Brooks and Corey model predicted a less efficient capillary barrier with a larger breakthrough into the capillary block and smaller outflow rates from the capillary layer compared to the van Genuchten-Mualem model (Fig. 8). However, the model setup with the Brooks and Corey model also produced smooth outflow patterns without visible thresholds. Although the match between the simulated and measured data is not bad for the slope 1:25, the efficiency of the capillary barrier is significantly overestimated for the slope 1:5 and large inflow rates.

Replacing the seepage face lower boundary condition with the free drainage boundary condition had almost no impact on the outflow rates for the model setup with the van Genuchten-Mualem model and no scaling. This remained true for both the standard and alternative HYDRUS versions. However, 22 out of the 38 simulation runs with free drainage aborted, which led to slightly irregular outflow patterns.

Possible reasons for the mismatch between measured and simulated outflow rates

Due to the systematic measurement and simulation results, the mismatch between measured and simulated outflow rates is very likely caused by systematic rather than random errors. There are three groups of possible reasons explaining the mismatch between measured and simulated outflow rates.

1) Errors in the empirical investigation

Although the 10-m tipping trough is a well-defined device, it is relatively large and thus there may be many sources of errors and uncertainties in the experiments. For example, the materials filling the tipping trough may be spatially heterogeneous because of the method of filling the device, or water flow may be impacted by variable temperatures in the lab. Furthermore, there may have been no stationary flow in the assumed stationary periods because of water redistribution inside of the tipping trough. Even so, the typical measured flow pattern with distinct threshold values of the inflow rates that indicates the efficiency of the capillary barrier and depends on the material combination and the slope is well confirmed (Steinert, 1999).

2) Errors in the application of the model

The simulation task, such as the shape of the tipping trough and the capillary barrier, is quite well defined. However, some material properties were not considered in the simulations due to missing measurement data. For example, hysteresis of the soil hydrological functions and the anisotropy of the hydraulic conductivity of used materials was not evaluated. Both materials (METHA-sand and 1/3 gravel) were technically pre-treated and therefore had a specific grain-size and pore-size distribution. This may be one reason why the parameterization of the van Genuchten-Mualem model for the soil hydrological functions was not unique (see point 3 below).

The spatial heterogeneity of material properties was modeled using scaling of soil hydraulic properties. If fingering plays an

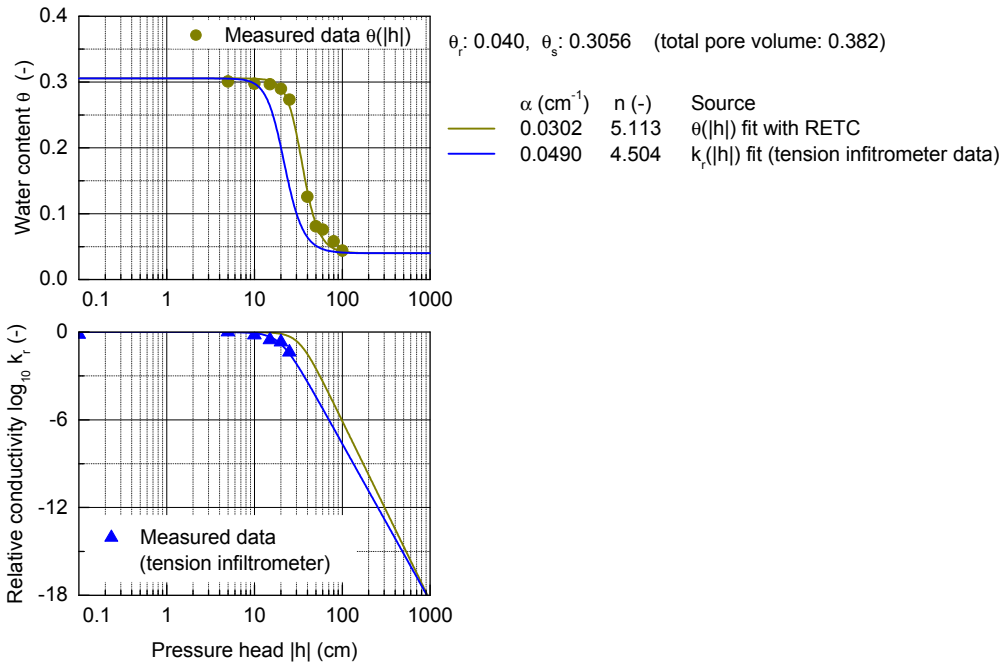

Fig. 9. Two fits of the van Genuchten-Mualem model to different measured data sets of the METHA-sand.

important role in flow across the interface of the capillary layer and capillary block, two-dimensional simulations are not sufficient to capture such phenomenon because they assume constant conditions in the third dimension. Fingers as separate three-dimensional entities require three-dimensional explicit representation.

3) Errors or unsuitable approaches in the model

This is a complex problem, which is in large part beyond the scope of this paper. For example, the van Genuchten-Mualem model (van Genuchten, 1980) may not be suitable to describe the soil hydraulic relationships of the technical pre-treated materials used in the capillary barrier. The fitting of the van Genuchten-Mualem model to two data sets for the METHA-sand measured with different methods resulted in significantly different parameter values for α and n (see Fig. 9). These data sets include water content-pressure head data from a pressure plate apparatus and unsaturated hydraulic conductivity data from tension infiltrometer measurements. Furthermore, to achieve a good fit for the water content-pressure head data, θ_s had to be set equal to only 80% of the total pore volume. The importance of the hydraulic parameters for the simulation results has already been emphasized by other authors (Barth, 2003; Kämpf et al., 2003).

None of the reasons mentioned in this brief discussion seem to be essential for explaining the mismatch between measured and simulated flow patterns of the capillary barrier. Thus, this problem unfortunately remains unsolved.

CONCLUSIONS

The model application described in this paper is quite simple. The shape of the tipping trough and of the capillary barrier inside is well defined, the two materials are quite well defined, and only stationary periods are simulated. The flow processes along and across the interface of the capillary layer and capillary block are critical for successful modeling of capillary barriers. The HYDRUS (2D/3D) model could not reproduce the measured outflow patterns and could not identify the threshold values indicating the efficiency of the capillary barrier. Possible sources of errors explaining the mismatch between measured and simulated outflow patterns were discussed. Errors could exist in the empirical investigation, the application of the model, or in the model itself. However, it is the author's opinion that the essential reason(s) for the mismatch between simulated and measured outflow rates could not yet be identified. To improve the results, further simulations could be performed to determine the soil hydraulic properties by inverse modeling for particular stationary periods.

According to the simulation results described in this paper and those of other authors (e.g., Barth, 2003; Kämpf et al., 2003), the two-dimensional models as HYDRUS (2D/3D) should currently not replace empirical investigations of tipping troughs or test fields for the dimensioning of capillary barriers.

Acknowledgments. The empirical investigation in the tipping trough and the simulations with SWMS_2D were funded by the German Federal Ministry for Education, Science, Research and Technology (BMBF) within the integrated research project 'Advanced Landfill Liner Systems' under the project number 1440 569A-39. The author thanks Dr. habil. Stefan Melchior and Prof. Dr. Günter Miehlich, who led the empirical investigation, and Dr. Bernd Steinert, Matthias Türk, Karin Burger and all involved staff members for their work. The author also thanks Prof. Jirka Šimůnek for providing the alternative HYDRUS (2D/3D) version.

REFERENCES

Barth, C., 2003. Die Wirksamkeit der Kapillarsperre als Deponieoberflächenabdichtung. Feldversuche auf der Deponie Bayreuth. [The efficiency of the capillary barrier as landfill sealing. Field experiments on the landfill Bayreuth.] PhD Thesis. University of Munich, Germany. (In German.)

Berger, K., 1999. Validation of the Hydrologic Evaluation of Landfill Performance (HELP) model for simulating the water balance of cover systems. Environmental Geology, 39, 11, 1261–1274.

Berger, K., 2017. Comparison and validation of SWMS_2D and

HYDRUS (2D/3D) for capillary barriers using data of a 10-m tipping trough. In: Proceedings Sixteenth International Waste Management and Landfill Symposium, 2–6 October 2017, S. Margherita di Pula, Cagliari, Italy. CISA Publisher, 10 p.

Heiberger, T.S., 1996. Simulating the effects of a capillary barrier using the two-dimensional variably saturated flow model SWMS_2D / HYDRUS-2D. Master thesis. Oregon State University, 124 p.

Holfelder, T., 2002. Temperaturbeeinflusste Transportprozesse in Kapillarsperren zur Oberflächenabdichtung von Deponien und Altlasten. [Temperature-affected transport processes in capillary barriers for the surface sealing of landfills and contaminated sites.] PhD Thesis. Technical University of Darmstadt, Germany. (In German.)

Jelinek, D., 1997. Die Kapillarsperre als Oberflächenbarriere für Deponien und Altlasten - Langzeitstudien und praktische Erfahrungen in Feldversuchen. [The capillary barrier as surface barrier for landfills and contaminated sites. – Long-term studies and practical experiences in field studies.] PhD Thesis. Technical University of Darmstadt, Germany. (In German.)

Kämpf, M., 2000. Fließprozesse in Kapillarsperren zur Oberflächenabdichtung von Deponien und Altlasten - Grundlagen zur hydraulischen Bemessung. [Flow processes in capillary barriers for surface sealing of landfills and contaminated sites – Fundamentals for dimensioning.] PhD Thesis. Technical University of Darmstadt, Germany. (In German.)

Kämpf, M., Holfelder, T., Montenegro, H., 2003. Identification and parameterization of flow processes in artificial capillary barriers. Water Resources Research, 39, 10, 9 p.

Knepell, P.L., Arangno, D.C., 1993. Simulation Validation. A Confidence Assessment Methodology. IEEE Computer Society Press, Los Alamitos, CA.

Konikow, L.F., Bredehoeft, J.D., 1992. Ground-water models cannot be validated. Adv. Water Resour., 15, 75–83. – Comment by de Marsily, G., Combes, P., Goblet, P., 1992. Adv. Water Resour., 15, 367–369. – Reply to Comment by J.D. Bredehoeft, Konikow, L.F., 1992. Adv. Water Resour., 15, 371–372.

Kung, K.-J.S., 1990. Preferential flow in a sandy vadose zone: 2. Mechanism and implications. Geoderma, 46, 1–3, 59–71.

Lacroix Vachon, B., Abdolahzadeh, A.M., Cabral, A.R., 2015. Predicting the diversion length of capillary barriers using steady state and transient state numerical modeling: case study of the Saint-Tite-des-Caps landfill final cover. Canadian Geotechnical Journal, 52, 2141–2148.

Melchior, S., 1993. Wasserhaushalt und Wirksamkeit mehrschichtiger Abdecksysteme für Deponien und Altlasten. [Water balance and efficiency of multi-layered cover systems for landfills and contaminated sites.] PhD Thesis. University of Hamburg, Germany, 330 p. (In German.)

Melchior, S., Sokollek, V., Berger, K., Vielhaber, B., Steinert, B., 2010. Results from 18 years of in situ performance testing of Landfill Cover Systems in Germany. Journal of Environmental Engineering, ASCE, 136, 8, 518–523.

Oldenburg, C.M., Pruess, K., 1993. On numerical modeling of capillary barriers. Water Resour. Res., 29, 4, 1045–1056.

Oreskes, N., Shrader-Frechette, K., Belitz, K., 1994. Verification, validation, and confirmation of numerical models in the Earth sciences. Science, 263, 641–646.

Pfeiffer, B., 2006. Vergleichende Untersuchungen von Kapillarsperren aus Natur- und Recyclingbaustoffmaterialien als Beitrag zur Deponieoberflächenabdichtung und Ressourcenschonung. [Comparative studies of capillary barriers from natural and recycling materials as a contribution for landfill sealing and preservation of resources.] PhD Thesis. University of Giessen, Germany. (In German.)

Radcliffe, D.E., Šimůnek, J., 2010. Soil Physics with HYDRUS. Modeling and Applications. CRC Press, Boca Raton, FL, 372 p.

Ross, B., 1990. The diversion capacity of capillary barriers. Water Resources Research, 26, 10, 2625–2629. (See also WRR, 27, 8, 2155–2157).

Šejna, M., Šimůnek, J., van Genuchten, M.Th., 2016. The HYDRUS Software Package for Simulating the Two- and Three-Dimensional Movement of Water, Heat, and Multiple Solutes in Variably-Saturated Porous Media. User Manual, Version 2.05. PC Progress, Prague, Czech Republic, 306 p.

Šimůnek, J., 2017. Alternative HYDRUS-2D code to allow definition of abrupt textural changes. Personal communication.

Šimůnek, J., Vogel, T., van Genuchten, M.T., 1992. The SWMS_2D code for simulating water flow and solute transport in two-dimensional variably saturated media. Vs. 1.1. Research Report 126. U.S. Salinity Lab., Riverside, CA, 169 p.

Šimůnek, J., van Genuchten, M.Th., Šejna, M., 2016. Recent developments and applications of the HYDRUS computer software packages. Vadose Zone Journal, 15, 7, 25 p. DOI: 10.2136/vzj2016.04.0033.

Steinert, B., 1999. Kapillarsperren für die Oberflächenabdichtung von Deponien und Altlasten - Bodenphysikalische Grundlagen und Kipprinnenuntersuchungen. [Capillary barriers for the surface lining of landfills and contaminated sites. Soil physical fundamentals and tipping trough experiments.] PhD Thesis. University of Hamburg, Germany, 250 p. (In German.)

Steinert, B., Melchior, S., Burger, K., Berger, K., Türk, M., Miehlich, G., 1997a. Dimensionierung von Kapillarsperren zur Oberflächenabdichtung von Deponien und Altlasten. [Dimensioning of capillary barriers for the surface lining of landfills and contaminated sites.] Hamburger Bodenkundliche Arbeiten 32, 420 p. (In German.)

Steinert, B., Melchior, S., Burger, K., Berger, K., Türk, M., Miehlich, G., 1997b. Design of capillary barriers for capping of landfills and contaminated sites. In: August, H., Holzlöhner, U., Meggyes, T. (Eds.): Advanced Landfill Liner Systems. Th. Telford, London, pp. 286–301.

van Genuchten, M.Th., 1980. A closed-form equation for predicting the hydraulic conductivity of unsaturated soils. Soil Sci. Soc. Am. J., 44, 892–898.

van Genuchten, M.Th., Leij, F.J., Yates, S.R., 1991. The RETC Code for Quantifying the Hydraulic Functions of Unsaturated Soils. EPA Report No. 600/2-91/065. U.S. Salinity Laboratory, Riverside, California, 83 p.

von der Hude, K. N., 1999. Kapillarsperren als Oberflächenabdichtungen auf Deponien und Altlasten. Laborversuche und Bemessungsregeln. [Capillary barriers as surface sealing on landfills and contaminated sites. Laboratory experiments and dimensioning rules.] PhD Thesis. Technical University of Darmstadt, Germany. (In German.)

Yeh, T.-C.J., Guzman, A., Srivastava, R., Gagnard, P.E., 1994. Numerical simulation of the wicking effect in liner systems. Ground Water, 32, 1, 2–11.

Zischak, R., 1997. Alternatives Oberflächenabdichtungssystem "Verstärkte mineralische Abdichtung mit untenliegender Kapillarsperre". [Alternative cover system "Strengthened cohesive liner with capillary barrier below".] PhD Thesis. University of Karlsruhe, Germany. (In German.)

Received 28 June 2017
Accepted 22 December 2017

J. Hydrol. Hydromech., 66, 2018, 2, 161–169
DOI: 10.1515/johh-2017-0046

Further tests of the HYPROP evaporation method for estimating the unsaturated soil hydraulic properties

Camila R. Bezerra-Coelho[1], Luwen Zhuang[2], Maria C. Barbosa[1], Miguel Alfaro Soto[3], Martinus Th. van Genuchten[2, 4*]

[1] Department of Civil Engineering, Federal University of Rio de Janeiro, UFRJ, Rio de Janeiro, RJ, Brazil.
[2] Department of Earth Sciences, Utrecht University, Utrecht, Netherlands.
[3] Department of Applied Geology, São Paulo State University, UNESP, Rio Claro, SP, Brazil.
[4] Department of Nuclear Engineering, Federal University of Rio de Janeiro, UFRJ, Rio de Janeiro, RJ, Brazil.
[*] Corresponding author. E-mail: rvangenuchten@hotmail.com

Abstract: Many soil, hydrologic and environmental applications require information about the unsaturated soil hydraulic properties. The evaporation method has long been used for estimating the drying branches of the soil hydraulic functions. An increasingly popular version of the evaporation method is the semi-automated HYPROP© measurement system (HMS) commercialized by Decagon Devices (Pullman, WA) and UMS AG (München, Germany). Several studies were previously carried out to test the HMS methodology by using the Richards equation and the van-Genuchten-Mualem (VG) or Kosugi-Mualem soil hydraulic functions to obtain synthetic data for use in the HMS analysis, and then to compare results against the original hydraulic properties. Using HYDRUS-1D, we carried out independent tests of the HYPROP system as applied to the VG functions for a broad range of soil textures. Our results closely agreed with previous findings. Accurate estimates were especially obtained for the soil water retention curve and its parameters, at least over the range of available retention measurements. We also successfully tested a dual-porosity soil, as well as an extremely coarse medium with a very high van Genuchten n value. The latter case gave excellent results for water retention, but failed for the hydraulic conductivity. In many cases, especially for soils with intermediate and high n values, an independent estimate of the saturated hydraulic conductivity should be obtained. Overall, the HMS methodology performed extremely well and as such constitutes a much-needed addition to current soil hydraulic measurement techniques.

Keywords: Soil hydraulic properties; Evaporation method; HYPROP; HYDRUS-1D; van Genuchten-Mualem equations.

INTRODUCTION

Reliable data about the unsaturated soil hydraulic properties are crucial for many hydrologic, agricultural and environmental applications. A large number of experimental methodologies have been developed and tested over the years to estimate the soil water retention and unsaturated soil hydraulic conductivity (Dane and Hopmans, 2002; Klute (Ed.), 1986). A direct approach for the soil water retention function is to measure a series of water content (θ) and pressure head (h) pairs, and then to fit a particular function to the data. Direct measurement techniques include methods using a hanging water column or sand box, pressure cells, pressure plate extractors, suction tables, soil freezing, and many other approaches as reviewed by Looney and Falta (Eds.) (2000), Dane and Hopmans (2002), and Bittelli and Flury (2009), among others. Once the pairs of θ and h data are obtained, the results may be analyzed in terms of specific analytical functions such as those by Brooks and Corey (1964), van Genuchten (1980), Fredlund and Xing (1994), Kosugi (1996), or Assouline et al. (1998). Several convenient software packages are available for this purpose (van Genuchten et al., 1991; Wraith and Or, 1998). Alternatively, the data could be analyzed without assuming specific analytical functions, for example by using linear, cubic spline or other interpolation techniques (Bitterlich et al., 2004; Kastanek and Nielsen, 2001).

Similar direct approaches involving pairs of conductivity and pressure head or water content data are in principle also possible for the $K(h)$ or $K(\theta)$ functions (Dane and Hopmans, 2002; Klute and Dirksen, 1986), including for the saturated hydraulic conductivity, K_s. The latter parameter can be measured in the laboratory using a variety of constant or falling head methods, and in the field using single or double ring infiltrometers, constant head permeameters, and various auger-hole and piezometer methods (Dane and Topp (Eds.), 2002). Unfortunately, pairs of $K(h)$ or $K(\theta)$ data are not easily obtained in the very dry range unless more specialized approaches are used such as hot-air, centrifugation or dew-point techniques (Arya, 2002; Nimmo et al., 2002; Scanlon et al., 2002). Consequently, unsaturated hydraulic conductivity properties often are still estimated using inverse or parameter estimation procedures.

Parameter estimation methods generally involve measurements of several capacity and flow attributes (e.g., water contents, pressure heads, boundary fluxes), which are then used in combination with a numerical solution of the Richards equation to obtain estimates of the hydraulic parameters in the adopted soil hydraulic functions. Popular methods include one-step and multi-step outflow methods (Hopmans et al., 2002; Kool et al., 1987; van Dam et al., 1994), tension infiltrometer methods (Šimůnek et al., 1998a) and evaporation methods (Šimůnek et al., 1998b), although many other laboratory and field methods also exist or can be similarly employed (Hopmans et al., 2002).

One frequently used approach is the evaporation method, stemming from the early work by Gardner and Miklich (1962) using horizontal columns, and subsequent modifications by Wind (1968) and others. Measurements of the evaporation rate and tension at multiple depths in the sample permitted the simultaneous direct estimation of the water retention and hydraulic conductivity. Key contributions have been by Halbertsma (1996), Klute and Dirksen (1986), Becher (1970), Plagge (1991),

Wendroth et al. (1993), Bertuzzi and Voltz (1997), and many others, including analyses of the data using parameters estimation approaches (Šimůnek et al., 1998b, Iden and Durner, 2008). An increasingly popular version of the evaporation method is the HYPROP© measurement system (further referred to here as HMS), which allows semi-automated direct measurements of water retention and conductivity pairs over a relatively wide range of pressure head values (Peters and Durner, 2008; Peters et al., 2015; Schindler et al., 2010a, b, and others). The HMS approach has been commercialized jointly by Decagon Devices (Pullman, WA, USA) and UMS AG (Munich, Germany), now known as the METER group. The commercial system involves pressure head measurements versus time at two depths within a short 5-cm soil sample as water evaporates from its surface, with the evaporation rate determined by weighing the column.

Several studies have been carried out to test the HYPROP evaporation approach against multistep outflow and other methods (e.g., Schelle et al., 2010; Zhuang et al., 2017). Peters and Durner (2008) and Peters et al. (2015) tested the HMS approach assuming synthetic (virtual) data for the two pressure heads within the sample, as well as for the evaporation rate (and hence the sample weight), as a function of time as generated with numerical solutions of the Richards equation. Peters and Durner (2008) used for this purpose the hydraulic functions of van Genuchten-Mualem (1980), while Peters et al. (2015) used the equations of Kosugi (1996) as well as the PDI model of Peters and colleagues (Iden and Durner, 2014; Peters, 2013, 2014) to account for the effects of film, corner and isothermal vapor flow in very dry soils.

In this study we follow a very similar approach using the standard van Genuchten-Mualem approach to provide an independent test of the HYPROP evaporation method. HMS performance is studied in particular for a broad range of soils having different van Genuchten α and n parameters, as well as for a dual-porosity medium as described with the composite hydraulic functions of Durner (1994). We first give a very brief description of the HYPROP evaporation method. The HYDRUS-1D software package (Šimůnek et al., 2016) is used next to generate virtual (synthetic) pressure heads in the column, as well as the evaporation rate (and hence the weight of the soil sample), as a function of time. The data are subsequently used in the HYPROP-Fit software (Pertassek et al., 2015) to estimate the hydraulic properties of the assumed porous media, thus providing a means for testing HMS performance. We also investigated the use of different potential evaporation rates, thus providing tests of the robustness of the HYPROP method for different soil types and environmental conditions.

THE HYPROP MEASUREMENT SYSTEM (HMS)

The HMS setup involves pressure head measurements at two depths within a standard 5-cm short soil column as water evaporates from the sample surface. Water contents and fluxes are determined by weighing the sample. Measured pressure heads, water contents, and evaporation fluxes are subsequently used to derive the water retention and unsaturated hydraulic conductivity functions (Pertassek et al., 2015; Peters and Durner, 2008; Schindler et al., 2010a). The measurement range at the wet side is restricted by limitations of pressure transducers to accurately register very small pressure head differences, reason why it is often recommended to measure the saturated hydraulic conductivity independently. At the dry side limitations are due to water cavitation in the tensiometers, usually at about –800 cm. Improved tensiometers are now being used that resist cavitation to pressure heads as low as –3000 cm or more (Schindler et al., 2010a, b). Major advantages of the HYPROP method are its automation once the system is installed, and the fact that pairs of $\theta(h)$ and $K(h)$ are being generated. The latter means that no preselected functional forms of the water retention and/or conductivity curve (such as those the Brooks and Corey or van Genuchten-Mualem equations) need to be used. Once the data are obtained, any set of hydraulic functions could potentially be applied to the data.

Figure 1 shows the setup of the standard HMS system (Schindler et al., 2010a), sometimes referred to also as the simplified evaporation method, SEM. Pressure heads versus time are recorded at two locations (1.25 cm and 3.75 cm from the evaporating surface), while the evaporation rate is measured

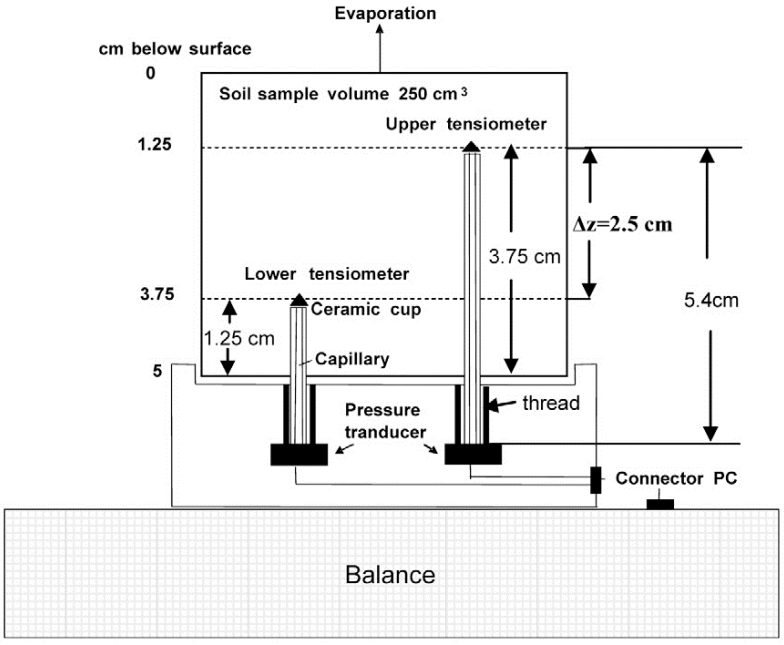

Fig. 1. Schematic of the HYPROP measurement system, HMS (after Schindler et al., 2010a).

Table 1. Values of the soil hydraulic parameters assumed in this study for relatively fine-textured (F), medium-textured (M), coarse-textured (C), and very coarse-textured (VC) soils, and for three medium-textured media (M1, M2, M3) having different pore- or particle-size distributions (psd) as reflected by the VG parameter *n*.

Case	Soil texture	θ_r (cm^3/cm^3)	θ_s (cm^3/cm^3)	α (cm^{-1})	n (–)	K_s (cm/day)	L (–)
	Effect of soil texture (fine to very coarse)						
F	Fine	0.0	0.500	0.0080	1.30	10.0	0.50
M	Medium	0.0	0.450	0.0160	1.80	50.0	0.50
C	Coarse	0.0	0.400	0.0320	2.50	250.0	0.50
VC	Very coarse	0.1	0.400	0.0219	10.0	1000.0	0.50
	Effect of the pore-size distribution, psd (broad to narrow)						
M1	Broad psd	0.0	0.450	0.016	1.30	50.0	0.50
M2	Medium psd	0.0	0.450	0.016	1.80	50.0	0.50
M3	Narrow psd	0.0	0.450	0.016	2.50	50.0	0.50

by repeated weighting. Measurements continue until the upper tensiometer reaches some limiting value (Schindler et al., 2010a). The data are subsequently analyzed from the average water content, the pressure head readings of the two tensiometers, and the mean total head gradients between the two tensiometers. We refer to Schindler et al (2010a, b) and Peters et al. (2015) for detailed descriptions of the setup and the data analysis.

The data in our study were generated by running HYDRUS-1D simulations, very similar as done by Peters and Durner (2008) and Peters et al. (2015). For most of the simulations we used a spatial discretization involving 61 nodes, with mesh refinement near the sample upper surface to accommodate higher local pressure head gradients during the simulations. More elements were used for soils having a narrow pore-size distribution (i.e., large van Genuchten *n* values). In most cases we imposed a relatively high potential evaporation rate of 1 cm/day, thus assuming that evaporation may have been enhanced by ventilation (e.g., Wendroth et al., 1993). Imposing lower potential evaporation rates (e.g., 0.4 or 0.2 cm/day) were not found to have significant effects on the results, except for slowing the experiments. The potential evaporation rate was implemented as a system-dependent boundary conditions until a critical pressure head, h_{crit}, was reached, after which a constant pressure head is imposed. We used for most cases the HYDRUS-1D default value of -10^5 cm for h_{crit}, except for very coarse-textured samples for which we used less extreme values to limit numerical problems. The bottom boundary was a zero fluid flux condition, while as initial condition we used an equilibrium profile with a pressure head of 4 cm at the bottom of the 5 cm sample. We assumed that all of the virtual experiments were carried out at a constant temperature of 20°C. Average water contents of the sample as needed for the HMS analysis were estimated from the initial water content and the calculated evaporation rates.

Soil hydraulic properties for most scenarios were described using the standard van Genuchten-Mualem formulation given by (van Genuchten, 1980)

$$S_e(h) = \frac{\theta(h) - \theta_r}{\theta_s - \theta_r} = \frac{1}{\left[1 + |\alpha h|^n\right]^m} \tag{1}$$

$$K(S_e) = K_s S_e^{\,L}\left[1 - \left(1 - S_e^{\,1/m}\right)^m\right]^2 \tag{2}$$

where S_e is effective saturation [–], θ_s and θ_r are the saturated and residual water contents, respectively [L^3L^{-3}], K_s is the saturated hydraulic conductivity [LT^{-1}], α [L^{-1}] and n [–] are semi-empirical shape parameters, m = 1–1/n, and L is a pore-connectivity parameter [–], which we fixed in the HYDRUS-1D simulations at 0.5 following the original study by Mualem (1976).

We explored the effects of a wide range of hydraulic parameters values on the HMS results, notably by varying values of the hydraulic parameters α and n. Table 1 lists only those examples that are specifically discussed in this paper. The examples in Table 1 are separated into two sets covering (1) a range of values typical of fine-, medium-, coarse-, and very coarse-textured soils, and (2) several medium-textured samples having increasingly narrow pore-size distributions as reflected by increasingly larger n values. Our study assumed the residual water content, θ_r, to be zero, except for the very coarse (VC) example. The analyses would be essentially the same if fixed non-zero θ_r values were used. We fixed θ_r in our study by reasoning that additional independent water retention measurements often are needed (especially for fine-textured media) to define the very dry side of the hydraulic functions, such as conventional pressure plate extractor and/or WP4 dew-point potentiometer measurements (e.g., Gubiani et al., 2012). We note that Peters et al. (2015) were also concerned about possible vapor flow and other complications in the very dry side of the hydraulic properties. We decided not to address these issues within the context of the HMS studies, but to focus instead only on the hydraulic properties at relatively wet and intermediate water contents.

We additionally explored the performance of a dual-porosity soil whose hydraulic properties are described using the composite hydraulic functions of Durner (1994) and Priesack and Durner (2006) for $S_e(h)$ and $K(S_e)$ given by

$$S_e(h) = \frac{\theta(h) - \theta_r}{\theta_s - \theta_r} = \frac{w_1}{[1 + |\alpha_1 h|^{n_1}]^{m_1}} + \frac{w_2}{[1 + |\alpha_2 h|^{n_2}]^{m_2}} \tag{3}$$

$$K(S_e) = K_s \frac{\left(w_1 S_1 + w_2 S_2\right)^L \left\{ w_1 \alpha_1 [1 - (1 - S_1^{\,1/m_1})^{m_1}] + w_2 \alpha_2 [1 - (1 - S_2^{\,1/m_2})^{m_2}] \right\}^2}{\left(w_1 \alpha_1 + w_2 \alpha_2\right)^2} \tag{4}$$

respectively, where S_i, α_i, n_i, and m_i (i = 1,2) are the same as in (1) and (2) for the macropore and micropore regions, respectively (or of the fracture and matrix regions if interpreted for unsaturated fractured rock), while w defines the division of the porous medium in macropore and micropore regions. Values of the various parameters used in Eqs. (3) and (4) were θ_r = 0.10, θ_s = 0.50, L = 0.50, K_s = 50 cm d^{-1}, $w_1 = w_2$ = 0.5, α_1 = 0.2 cm^{-1}, n_1 = 2.5, α_2 = 0.002 cm^{-1}, and n_2 = 2.0.

Once the pressure heads and actual evaporation rates (and hence sample weights) were generated using HYDRUS-1D, the HYPROP-Fit analysis was applied to the synthetic numerical data, leading to estimates of the original soil hydraulic parameters. HYPROP-Fit used the root mean square error (RMSE) to quantify differences between the synthetic (y_i) water retention or unsaturated hydraulic conductivity data, and calculated values (y_i^c) based on the fitted VG curves. RMSE values were calculated using

$$RMSE = \sqrt{\sum_{i=1}^{n_p} \frac{1}{n_p} (y_i^c - y_i)^2} \qquad (5)$$

where n_p is the number of data points, and y_i refers to either water content, θ_i, or the logarithm of the unsaturated hydraulic conductivity, log(K_i).

RESULTS AND DISCUSSION

Figure 2, 3 and 4 show results for, respectively, the fine-textured (F), medium-textured (M) and coarse-textured (C) soils as identified in Table 1. The top left plot in each figure shows calculated pressure heads, $h_1(t)$ and $h_2(t)$, of the top and lower tensiometers, respectively, of the HMS setup, while the top right plot shows the cumulative actual evaporation rate (or cumulative weight loss per cm^2 sample area), $W(t)$, as obtained with HYDRUS-1D. Calculated pressure heads and evaporation rates were obtained at regular time intervals (e.g., every 10 seconds during the first hour, every 10 minutes during the next 9 hours, and every two hours after 10 hours). Using values at regular time intervals, as compared to irregular HYDRUS-1D output times resulting from the self-adjusting numerical time stepping scheme, was found to produce smoother values of the pressure heads and evaporation rates versus time, leading to more accurate HMS results. Calculated values of the pressure heads (as equivalent suctions) and sample weights were subsequently inserted in the HYPROP-Fit software (Pertassek et al., 2015) to generate the water retention and hydraulic conductivity data as shown in the bottom plots of Figures 2, 3 and 4. Those plots also include the HMS fitted complete VG hydraulic functions.

Figure 2 shows the HMS estimated soil hydraulic properties values and fitted VG hydraulic functions for the fine-textured soil. As to be expected, the HMS estimated retention data cover a limited range of water contents because of limitations imposed on possible tensiometer data. Still the HMS estimated VG retention parameter values (Table 2) show very good agreement with the original values (Table 2). Estimated values for the saturated conductivity (K_s) and the pore connectivity parameter (L) were reasonably close to the true values. Fixing K_s to the assumed synthetic value of 10 cm/day produced a much-improved value of L.

HMS water retention results for the medium-textured soil (M) in Figure 3 show a very nice coverage of the water contents, while the fitted water retention parameters were again essentially identical to the originally assumed values (Table 2). The HMS hydraulic conductivity values and fitted curve function were also in excellent agreement with the original values. In this case there was little reason to fix K_s to the true value since both K_s and L were estimated very well. This shows that the HMS approach worked well for the medium-textured soil, without an obvious need to obtain independent estimates of K_s.

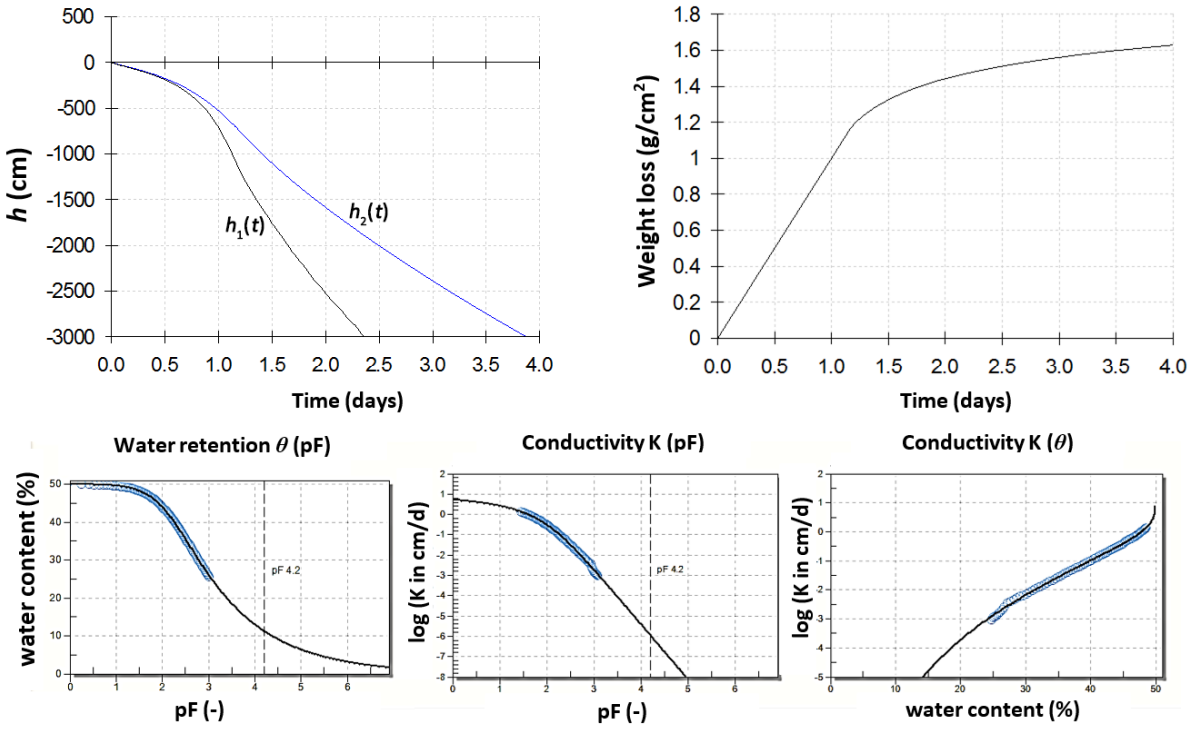

Fig. 2. HYDRUS-1D predictions of the pressure heads $h_1(t)$ and $h_2(t)$ and the cumulative weight loss $W(t)$ (top plots) for the fine-textured soil (F) obtained using the VG parameter values listed in Table 1, and plots of the HMS generated water retention and hydraulic conductivity data, together with the HYPROP-Fit estimated VG hydraulic functions using the parameters for case FH-1 (Table 2).

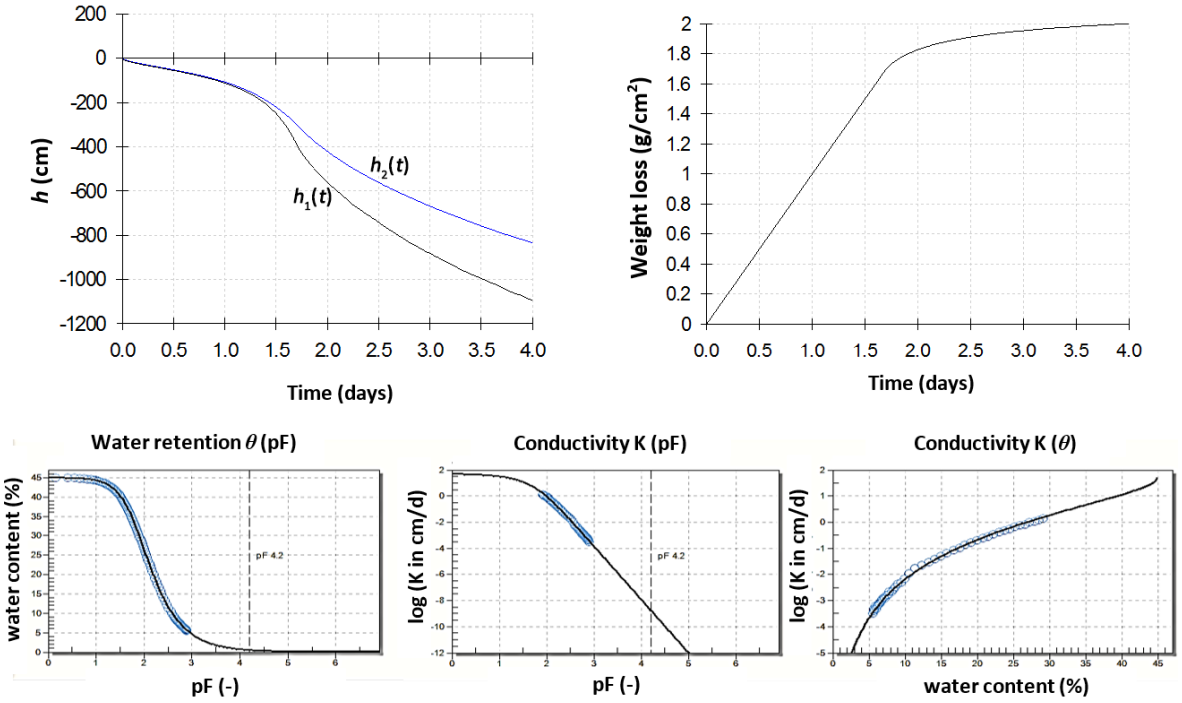

Fig. 3. HYDRUS-1D predictions of the pressure heads $h_1(t)$ and $h_2(t)$ and the weight loss $W(t)$ (top plots) for the medium-textured soil (M) obtained using the VG parameter values listed in Table 1, and plots of the HMS generated water retention and hydraulic conductivity data, together with the HYPROP-Fit estimated VG hydraulic functions using the parameters for case MH-1 (Table 2).

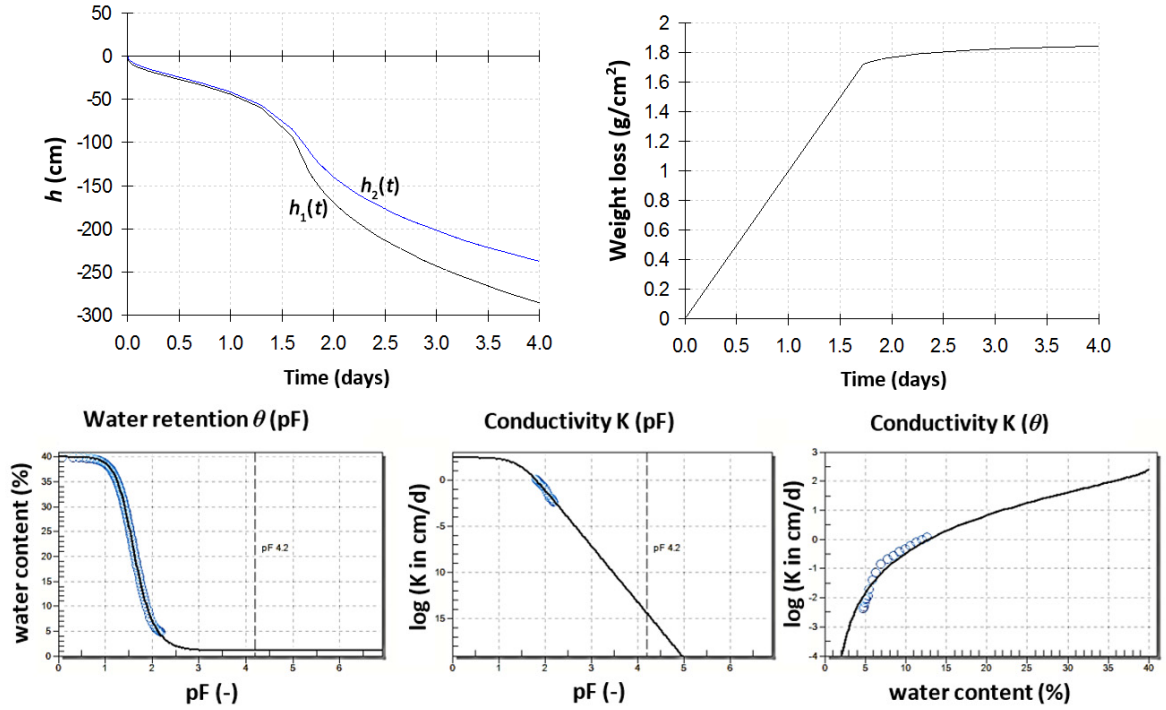

Fig. 4. HYDRUS-1D predictions of the pressure heads $h_1(t)$ and $h_2(t)$ and the weight loss $W(t)$ (top plots) for the coarse-textured soil (C) obtained using the VG parameter values listed in Table 1, and plots of the HMS generated water retention and hydraulic conductivity data, together with the HYPROP-Fit estimated VG hydraulic functions using the parameters for case CH-1 (Table 2).

The coarse-textured soil similarly provided excellent results for soil water retention as shown by the lower left plot in Figure 4 and the HMS estimated retention parameters in Table 2. However, estimation of the hydraulic conductivity parameters K_s and L was relatively poor, with the correct values being overestimated by more than 100%. However, fixing the value of K_s to its correct values was found to produce very reasonable values of L. This shows the importance of obtaining independent estimates of the hydraulic conductivity at or near saturation for coarse-texture media. Our result for the very coarse medium (VC), to be presented later, further supported this conclusion.

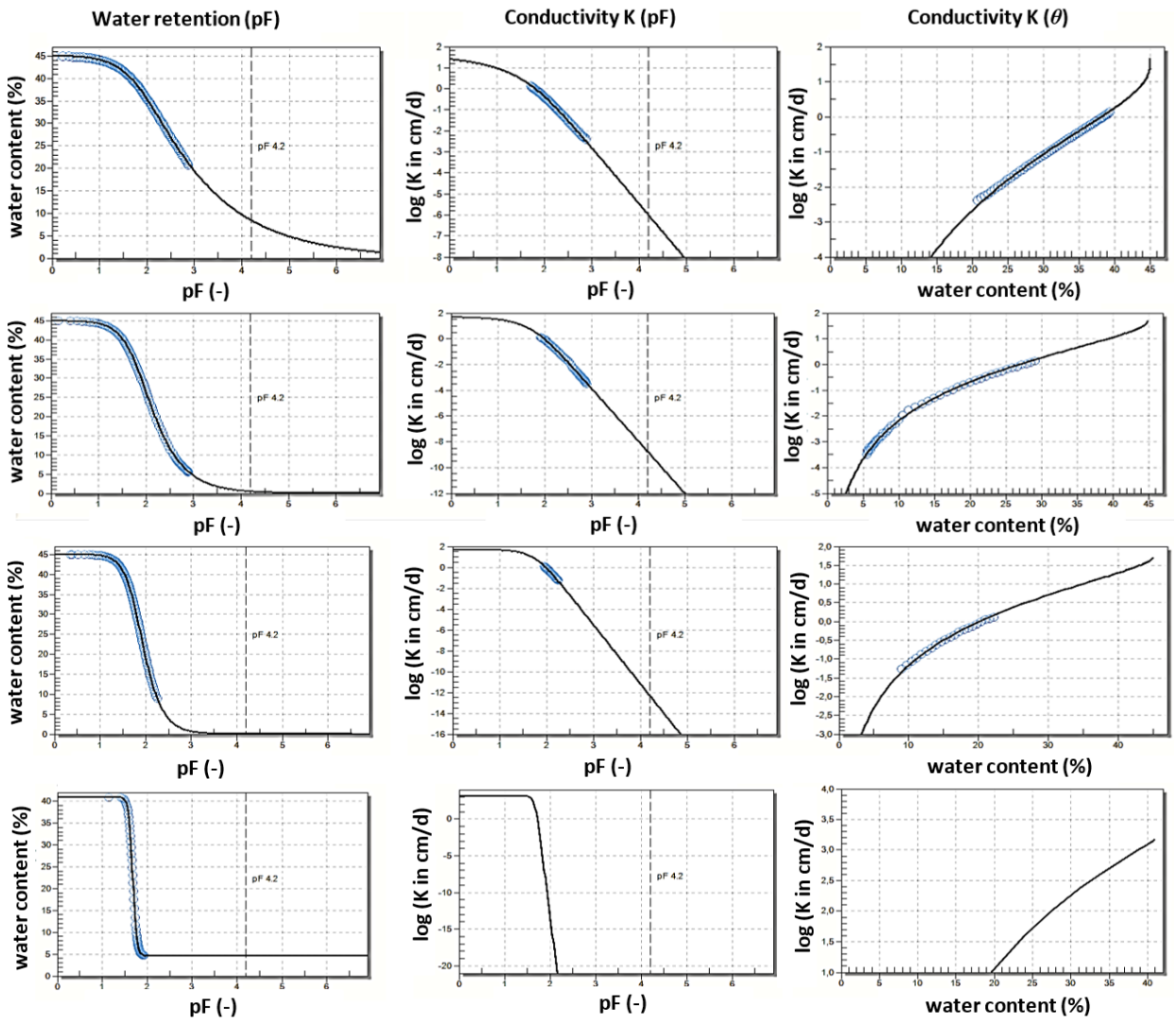

Fig. 5. HMS generated results for the hydraulic properties of the medium-textured soils assuming increasingly higher *n* values indicative of more narrow pore-size distributions. The plots from top to bottom are for *n* values of 1.3, 1.8, 2.5, and 10.0 representing cases B, M, N and VC in Table 2, respectively.

Figures 2, 3 and 4 showed results for typical fine-, medium- and coarse-textured soils, with each case having different values of the van Genuchten α and n parameters. We wanted to investigate more specifically the effects of varying n values on the HMS results, while keeping α constant. When n varies from small to large, the slope of the retention curve becomes increasingly steeper as the pore-size distribution becomes narrower. Figure 5 shows results when the value of n value for the medium-textured soil varies from 1.3 (case B) to 1.8 (M) to 2.5 (N). Not further included in this figure are the HYDRUS-1D predicted values of heads $h_1(t)$, $h_2(t)$ and $W(t)$. However, the figure does contain results also for the very coarse medium (VC) having an extremely large n value of 10.0. We note that n values of above 10.0 or even higher are not uncommon for some soils (not necessarily coarse soils) such as golf course sands or other media such as quartz, carbonate sands and certain limestones (e.g., Sakaki et al., 2012; Wang et al., 2016).

The results in Figure 5 show excellent descriptions of the soil water retention curves of all four soils, but especially when n increases to the VC case. Again, this was to be expected since the water retention data cover an increasingly narrower range of water contents. HMS estimated water retention data in all cases essentially duplicated the originally assumed synthetic values (Table 2). However, as n increased, the descriptions of the hydraulic conductivity curves deteriorated, with the range of estimated conductivity values becoming increasingly smaller up to the VC case where HMS failed to produce any conductivity data. This indicates that the HMS procedure does not work well for the hydraulic conductivity when applied to soils having very narrow pore- or particle-size distributions.

We further tested HMS performance for several dual-porosity soils whose hydraulic properties were described with Eqs. (3) and (4). Results more or less followed the conclusions obtained for the other soils in that they were most accurate when a wide range of water retention and pressure head data was covered by the tensiometers. Best results were again obtained for relatively small and intermediate values of n. Results for a typical case are shown in Figure 6, with the fitted dual-porosity parameters listed in Table 3. For some of the trials we again fixed the very dry end of the retention curve by assuming that other methods (e.g., WP4 dew point measurements) were used to define that part of the curve. The water retention parameters were estimated well, even when the value of the residual water content was also estimated using the HMS approach. The value of K_s was also estimated well (Table 3). However, the tortuosity parameter L was poorly estimated, even when K_s was fixed at the original (synthetic) value of 50 cm/day.

Table 2. Values of the HYPROP-Fit estimated soil hydraulic parameters for the various cases considered in this study. F, M, C and VC represent relatively fine, medium, coarse- and very coarse-textured soils, respectively, as referred to in Table 1, while B, M and N are medium-textured soils representing relatively broad to more narrow pore-size distributions. Assumed hydraulic parameters used in the HYDRUS simulations are in bold (see also Table 1), while the HYPROP-Fit generated parameters are identified with extra letters and numbers (e.g., FH-1 and FH-2).

Case	Soil texture	θ_s (cm^3/cm^3)	α (cm^{-1})	n (–)	K_s (cm/day)	L (–)	*RMSE* (θ)	*RMSE* (log K)
	Effect of soil texture (fine to very coarse)							
F	**Fine**	**0.500**	**0.008**	**1.30**	**10.0**	**0.50**	–	–
FH-1	Fine	0.499	0.0074	1.32	8.37	0.27	0.0006	0.033
FH-2	Fine	0.500	0.0078	1.31	10.0*	0.42	0.0009	0.041
M	**Medium**	**0.450**	**0.016**	**1.80**	**50.**	**0.50**	–	–
MH-1	Medium	0.449	0.0154	1.83	47.8	0.48	0.0009	0.042
MH-2	Medium	0.449	0.0154	1.80	50.0*	0.51	0.0009	0.043
C	**Coarse**	**0.400**	**0.032**	**2.50**	**250.**	**0.50**	–	–
CH-1	Coarse	0.399	0.0318	2.59	812.	1.16	0.0015	0.079
CH-2	Coarse	0.398	0.0317	2.61	250*	0.56	0.0015	0.138
CH-3	Coarse	0.400*	0.0319	2.57	250*	0.58	0.0016	0.144
VC	**Very coarse**	**0.410**	**0.0219**	**10.0**	**1000.**	**0.50**	–	–
VCH-1	Very coarse	0.410	0.0215	10.0	1000*	5.94	0.0001	–
	Effect of pore-size distribution (broad to narrow)							
B	**Broad**	**0.450**	**0.016**	**1.30**	**50.0**	**0.50**	–	–
BH-1	Broad	0.450	0.0153	1.31	39,6	–0.04	0.0005	0.013
BH-2	Broad	0.450*	0.0157	1.30	50.0*	0.31	0.0007	0.033
M	**Medium**	**0.450**	**0.016**	**1.80**	**50.0**	**0.50**	–	–
MH-1	Medium	0.449	0.0154	1.83	47.8	0.48	0.0009	0.042
MH-2	Medium	0.449	0.0154	1.80	50.0*	0.51	0.0009	0.043
N	**Narrow**	**0.450**	**0.016**	**2.50**	**50.0**	**0.50**	–	–
NH-1	Narrow	0.450	0.0157	2.52	38.4	0.19	0.0004	0.011
NH-2	Narrow	0.450	0.0157	2.52	50.0*	0.42	0.0004	0.029

*Fixed parameter value in the HYPROP-Fit optimization

Table 3. Values of the assumed (DP) and HYPROP-Fit (DPH) estimated soil hydraulic parameters for the dual-porosity soil, and RMSE values of the optimizations.

Case	θ_r (cm^3/cm^3)	θ_s (cm^3/cm^3)	w_1	α_1 (cm^{-1})	n_1 (–)	α_2 (cm^{-1})	n_2 (–)	K_s (cm/day)	L (–)	*RMSE* (θ)	*RMSE* (log K)
DP	**0.100**	**0.500**	**0.500**	**0.200**	**2.50**	**0.002**	**2.00**	**50.0**	**0.50**	–	–
DPH-1	0.119	0.504	0.553	0.214	2.15	0.002	2.15	43.6	–0.083	0.0015	0.0334
DPH-2	0.111	0.504	0.448	0.216	2.15	0.002	2.09	50.0*	0.071	0.0015	0.0361
DPH-3	0.094	0.500*	0.484	0.203	2.25	0.002	1.95	50.0*	0.37	0.0015	0.0398
DPH-4	0.081	0.500*	0.503	0.202	2.28	0.002	1.88	50.0*	0.50*	0.0015	0.0422

*Fixed parameter value in the HYPROP-Fit optimization

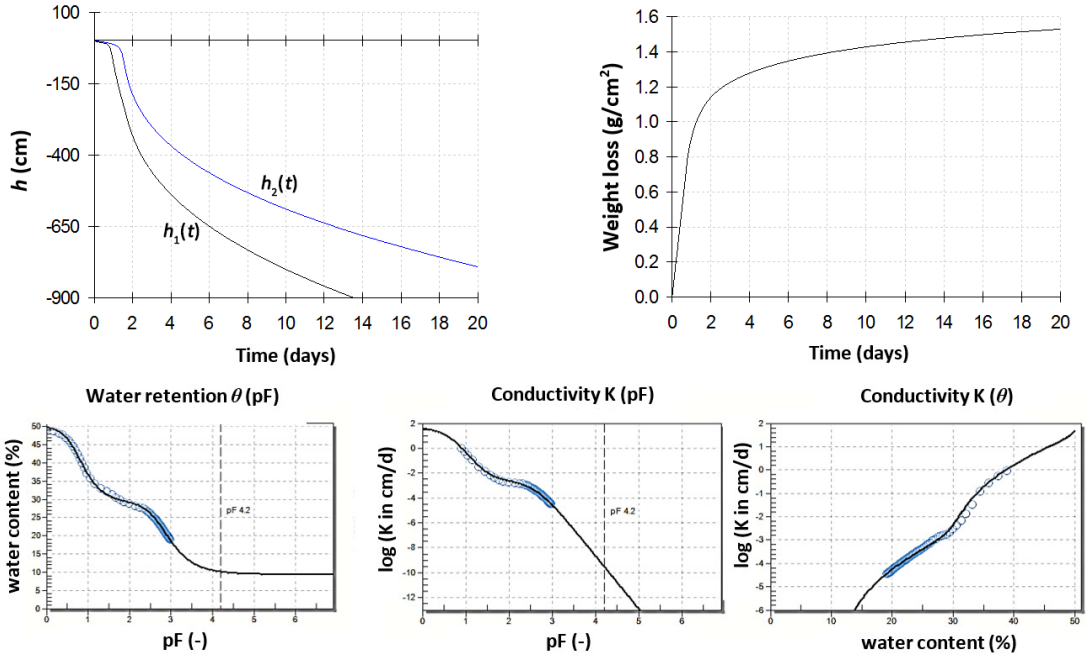

Fig. 6. HYDRUS-1D predictions of the pressure heads $h_1(t)$ and $h_2(t)$ and the cumulative weight loss $W(t)$ (top plots) for the dual-porosity soil (DP) obtained using the hydraulic parameter values listed in Table 3, and plots of the HMS generated water retention and hydraulic conductivity data, together with the HYPROP-Fit estimated dual-porosity functions using the parameters for case DPH-1 in Table 3.

Overall, the dual-porosity examples indicate that reliable estimates will be obtained when the tensiometers and supporting equipment (possibly WP4) cover a complete range of retention data. Additional measurements of the saturated conductivity will help, especially for determining the pore connectivity parameter *L*. Still, we were very pleased with the results given the many DP parameters involved and their possible correlations.

We conclude that the HMS approach is a very attractive addition of the current suite of measurement approaches for the soil water retention and unsaturated hydraulic conductivity properties. We were especially impressed by the accuracy and completeness of the retention measurements, including for soils having narrow pore size distributions. The hydraulic conductivity measurements were in most cases very much acceptable also, especially for relatively fine- and medium-textured soils characterized by intermediate α and n values.

CONCLUDING REMARKS

The evaporation method has long been used for estimating the drying branches of the soil hydraulic functions. The HYPROP measurement system (HMS) is rapidly becoming an increasingly popular alternative method for measurements of the soil water retention and unsaturated hydraulic conductivity properties. Our tests of the HMS approach parallel results obtained in two earlier studies (Peters and Durner, 2008; Peters et al., 2015) carried out to assess the accuracy of the HMS methodology by using the Richards equation to obtain synthetic date for use in the HMS analysis, and then to compare results against the original properties. Our analysis covered a very broad range of soils, including a soil with a very narrow pore-size distribution as reflected by an n value of 10.0. Accurate estimates were in most or all cases obtained for the soil water retention curve and its parameters, at least over the range of retention data used in the HMS analysis. The extremely coarse medium (VC) with $n = 10$ gave excellent results for water retention, but failed for the hydraulic conductivity. Except for relatively fine and intermediate soil textures, most cases do still benefit from independent estimate of the hydraulic conductivity at and/or near saturation. Overall, the HMS methodology performed very well and as such constitutes a much-needed addition to current soil hydraulic measurement techniques.

REFERENCES

Arya, L.M. 2002. Wind and hot-air methods. In: Dane, J.H., Topp, G.C. (Eds.): Methods of Soil Analysis. Part 4. Physical Methods. Soil Sci. Soc. Am., Madison, WI, pp. 916–920.

Assouline, S., Tessier D., Bruand, A., 1998. A conceptual model of the soil water retention curve. Water Resour. Res., 34, 2, 223–231.

Becher, H.H., 1970. Ein Verfahren zur Messung der ungesattigten Wasserleitfahigkeit. Z. Pflanzenernaehrung u. Bodenkd., 128, 1–12. (In German.)

Bertuzzi, P., Voltz, M., 1997. The Wind method: A standard laboratory method adopted by the French INRA laboratories. In: Proc. Workshop The use of pedotransfer in soil hydrology research, Orleans, France, pp. 51–53.

Bittelli, M., Flury, M., 2009. Errors in water retention curves determined with pressure plates. Soil Sci. Soc. Am. J., 73, 1453–1460. DOI: 10.2136/sssaj2008.0082.

Bitterlich, S., Durner, W., Iden, S.C., Knabner, P., 2004. Inverse estimation of the unsaturated soil hydraulic properties from column outflow experiments using free-form parameterizations. Vadose Zone J., 3, 971–981.

Brooks, R.H., Corey, A.T., 1964. Hydraulic properties of porous media. Hydrology paper 3. Colorado State Univ., Fort Collins, CO.

Dane, J.H., Hopmans, J.W., 2002. Soil water retention and storage. In: Dane, J.H., Topp, G.C. (Eds.): Methods of Soil Analysis. Part 4. Physical Methods. Soil Sci. Soc. Am., Madison, WI, pp. 675–720.

Dane, J.H., Topp, G.C. (Eds.), 2002. Methods of Soil Analysis. Part 4. Physical Methods. Soil Sci. Soc. Am., Madison, WI.

Durner, W., 1994. Hydraulic conductivity estimation for soils with heterogeneous pore structure. Water Resour. Res., 32, 9, 211–223.

Fredlund, D.G., Xing, A., 1994. Equations for the soil water characteristic curve. Can. Geotechn. J., 31, 521–532.

Gardner, W.R., Miklich, F.J., 1962. Unsaturated conductivity and diffusivity measurements by a constant flux method. Soil Sci., 93, 271–274.

Gubiani, P.I., Reichert, J.M., Campbell, C., Reinert, D.J., Gelain, N.S., 2012. Assessing errors and accuracy in dew-point potentiometer and pressure plate extractor measurements. Soil Sci. Soc. Am. J., 77, 1, 19–24. DOI: 10.2136/sssaj2012.0024.

Halbertsma, J., 1996. Wind's evaporation method; determination of the water retention characteristics and unsaturated hydraulic conductivity of soil samples. Possibilities, advantages and disadvantages. In: European Workshop on Advanced Methods to Determine Hydraulic Properties of Soils, Thurnau, Germany, 10–12 June 1996. Department of Hydrology, University of Bayreuth, 107 p.

Hopmans, J.W., Šimůnek, J., Romano, N., Durner, W., 2002. Inverse modeling of transient water flow. In: Dane, J.H., Topp, G.C. (Eds.): Methods of Soil Analysis. Part 4. Physical Methods. SSSA, Madison, WI, pp. 963–1008,

Iden, S.C., Durner, W., 2008. Free-form estimation of soil hydraulic properties using Wind's method. Europ. J. Soil Sci., 59, 6, 1228–1240. DOI:10.1111/j.1365-2389.2008.01068.x.

Iden, S.C., Durner, W., 2014. Comment to "Simple consistent models for water retention and hydraulic conductivity in the complete moisture range" by A. Peters. Water Resour. Res., 50, 7530–7534.

Kastanek, F.J., Nielsen, D.R., 2001. Description of soil water characteristics using cubic spline interpolation. Soil Sci. Soc. Am. J., 65, 279–283.

Klute, A. (Ed.), 1986. Methods of Soil Analysis. Part 1. Physical and Mineralogical Methods. 2nd ed. Am. Soc. Agron., Madison, WI, pp. 1025–1054.

Klute, A., Dirksen, C., 1986. Hydraulic conductivity and diffusivity: laboratory methods. In: Klute, A. (Ed.), Methods of Soil Analysis. Part 1. Physical and Mineralogical Methods. 2nd ed. Agron. Monogr. 9. ASA, Madison, WI, pp. 687–734.

Kool, J.B., Parker J.C., Genuchten, M.Th., 1987. Parameter estimation for unsaturated flow and transport models, a review. J. Hydrol., 91, 255–293.

Kosugi, K., 1996. Lognormal distribution model for unsaturated soil hydraulic properties. Water Resour. Res., 32, 2697–2703.

Looney, B.B., Falta, R.W. (Eds.), 2000. Vadose Zone Science and Technology Solutions. Battelle Press, Columbus, OH, 1540 p.

Mualem, Y., 1976. A new model for predicting the hydraulic conductivity of unsaturated porous media. Water Resour. Res., 12, 513–522.

Nimmo, J.R., Perkins, K.S., Lewis, A.M., 2002. Steady-state centrifuge. In: Dane, J.H., Topp, G.C. (Eds.): Methods of Soil Analysis. Part 4. Physical Methods. SSSA Book Ser. 5, SSSA, Madison, WI, pp. 903–916.

Pertassek, T., Peters, A., Durner, W., 2015. HYPROP-FIT Software User's Manual, V.3.0. UMS GmbH, Munich, Germany, 66 p.

Peters, A., 2013. Simple consistent models for water retention and hydraulic conductivity in the complete moisture range. Water Resour. Res., 49, 6765– 6780.

Peters, A., 2014. Reply to comment by S. Iden and W. Durner on Simple consistent models for water retention and hydraulic conductivity in the complete moisture range. Water Resour. Res., 50, 7535–7539.

Peters, A., Durner, W., 2008. Simplified evaporation method for determining soil hydraulic properties. J. Hydrol., 356, 147–162.

Peters, A., Iden, S.C., Durner, W., 2015. Revisiting the simplified evaporation method: Identification of hydraulic functions considering vapor, film and corner flow. Journal of Hydrology, 527, 531–542.

Plagge, R., 1991. Bestimmung der ungesättigten Wasserleitfähigkeit im Boden. Ph.D. diss. Dep. Landschaftsentwicklung, Techn. Univ. Berlin, Berlin. (In German.)

Priesack, E., Durner, W., 2006. Closed-form expression for the multimodal unsaturated conductivity function. Vadose Zone J., 5, 121–124. DOI:10.2136/vzj2005.0066.

Sakaki, T., Limsuwat, A., Cihan, A., Frippiat, C., Illangasekare, T.H., 2012. Water retention in a coarse soil pocket under wetting and drainage cycles. Vadose Zone J., 11, 1. DOI: 10.2136/vzj2011.0028.

Scanlon, B.R., Andraski, B.J., Bilskie, J., 2002. Miscellaneous methods for measuring matric or water potential. In: Dane, J.H., Topp, G.C. (Eds.): Methods of Soil Analysis. Part 4. Physical Methods, Chapter 3.3. Soil Sci. Soc. Am., Madison, WI, pp. 642–670.

Schelle, H., Iden, S.C., Peters, A., Durner, W., 2010. Analysis of the agreement of soil hydraulic properties obtained from multistep-outflow and evaporation methods. Vadose Zone J., 9, 1080–1091. DOI: 10.2136/vzj2010.0050.

Schindler, U., von Unold, G., Durner, W., Müller, L., 2010a. Evaporation method for measuring unsaturated hydraulic properties of soils: extending the range. Soil Sci. Soc. Am. J., 74, 1071–1083. DOI: 10.2136/sssaj2008.0358.

Schindler, U., Durner, W., von Unold, G., Müller, L., Wieland, R., 2010b. The evaporation method: extending the measurement range of soil hydraulic properties using the air-entry pressure of the ceramic cup. J. Plant Nutr. & Soil Sci., 173, 563–572. DOI: 10.1002/jpln.200900201.

Šimůnek, J., Wang, D., Shouse, P.J., van Genuchten, M.Th., 1998a. Analysis of field tension disc infiltrometer data by parameter estimation. Int. Agrophysics, 12,167–180.

Šimůnek, J., Wendroth, O., van Genuchten, M.Th., 1998b. A parameter estimation analysis of the evaporation method for determining soil hydraulic properties. Soil Sci. Soc. Am. J., 62, 4, 894–905.

Šimůnek, J., van Genuchten, M.Th., Šejna, M., 2016. Recent developments and applications of the HYDRUS computer software packages. Vadose Zone J., 15, DOI: 10.2136/vzj2016.04.0033.

van Dam, J.C., Stricker, J.N.M., Droogers, P., 1994. Inverse method to determine soil hydraulic functions from multistep outflow experiments. Soil Sci. Soc. Am. J., 58, 3, 647–652.

van Genuchten, M.Th., 1980. A closed-form equation for predicting the hydraulic conductivity of unsaturated soils. Soil Sci. Soc. Am. J., 44, 892–898.

van Genuchten, M.Th., Leij, F.J., Yates, S.R., 1991. The RETC code for quantifying the hydraulic functions of unsaturated soils. Report EPA/600/2–91/065. U.S. Environmental Protection Agency, Ada, OK.

Wang, S., Tokunaga, T.K., Wan, J., Dong, W., Kim, Y., 2016. Capillary pressure-saturation relations in quartz and carbonate sands: Limitations for correlating capillary and wettability influences on air, oil, and supercritical CO2 trapping, Water Resour. Res., 52, DOI: 10.1002/2016WR018816.

Wendroth, O., Ehlers, W., Hopmans, J.W., Klage, H., Halbertsma, J., Wösten, J.H.M., 1993. Reevaluation of the evaporation method for determining hydraulic functions in unsaturated soils. Soil Sci. Soc. Am. J., 57, 1436–1443.

Wind, G.P., 1968. Capillary conductivity data estimated by a simple simple method for determining soil hydraulic properties in the method. In: Rijtema, P.E., Wassink, H. (Eds.): Proc. Wageningen Symp. Water in the Unsaturated Zone. Vol. 1. June 1966. Int. Assoc. Scientific Hydrol., Gentbrugge, Belgium, pp. 181–191.

Wraith, J.M., Or, D., 1998. Nonlinear parameter estimation using spreadsheet software. J. Nat. Resour. Life Sci. Educ., 27, 13–19.

Zhuang, L., Bezerra Coelho, C.R., Hassanizadeh, S.M., van Genuchten, M.Th., 2017. Analysis of the hysteretic hydraulic properties of unsaturated soil. Vadose Zone J., 16, 5. DOI: 10.2136/vzj2016.11.0115.

Received 21 July 2017
Accepted 11 August 2017

Note: Colour version of Figures can be found in the web version of this article.

J. Hydrol. Hydromech., 66, 2018, 2, 170–180
DOI: 10.2478/johh-2018-0002

Inverse estimation of soil hydraulic properties and water repellency following artificially induced drought stress

Vilim Filipović[1*], Thomas Weninger[2], Lana Filipović[1], Andreas Schwen[3], Keith L. Bristow[4], Sophie Zechmeister-Boltenstern[5], Sonja Leitner[5]

[1] University of Zagreb, Faculty of Agriculture, Department of Soil Amelioration, Svetošimunska 25, 10000 Zagreb, Croatia.
[2] University of Natural Resources and Life Sciences Vienna (BOKU), Institute of Hydraulics and Rural Water Management, Muthgasse 18, 1190 Vienna, Austria.
[3] Austrian Agency for Health and Food Safety (AGES), Institute for Plant Protection Products, Spargelfeldstraße 191, 1220 Vienna, Austria.
[4] CSIRO Agriculture & Food, PMB Aitkenvale, Townsville, QLD 4814, Australia.
[5] University of Natural Resources and Life Sciences Vienna (BOKU), Institute of Soil Research, Peter-Jordan-Straße 82, 1190 Vienna, Austria.
[*] Corresponding author. Tel.: 00385 1 2393711. E-mail: vfilipovic@agr.hr

Abstract: Global climate change is projected to continue and result in prolonged and more intense droughts, which can increase soil water repellency (SWR). To be able to estimate the consequences of SWR on vadose zone hydrology, it is important to determine soil hydraulic properties (SHP). Sequential modeling using HYDRUS (2D/3D) was performed on an experimental field site with artificially imposed drought scenarios (moderately M and severely S stressed) and a control plot. First, inverse modeling was performed for SHP estimation based on water and ethanol infiltration experimental data, followed by model validation on one selected irrigation event. Finally, hillslope modeling was performed to assess water balance for 2014. Results suggest that prolonged dry periods can increase soil water repellency. Inverse modeling was successfully performed for infiltrating liquids, water and ethanol, with R^2 and model efficiency (E) values both > 0.9. SHP derived from the ethanol measurements showed large differences in van Genuchten-Mualem (VGM) parameters for the M and S plots compared to water infiltration experiments. SWR resulted in large saturated hydraulic conductivity (K_s) decrease on the M and S scenarios. After validation of SHP on water content measurements during a selected irrigation event, one year simulations (2014) showed that water repellency increases surface runoff in non-structured soils at hillslopes.

Keywords: Inverse modeling; Water and ethanol infiltration; SHP estimation; Water dynamics; HYDRUS (2D/3D).

INTRODUCTION

Soil water repellency (SWR) is a reduction in the rate of wetting and retention of water in soil caused by drying and the presence of various hydrophobic coatings on soil particles. The physical background is not yet fully understood, but it is widely accepted that this phenomenon is most likely caused by water-repellent compounds that can coat soil mineral particles or be present as interstitial matter in soil pores (Doerr et al., 2000). SWR can increase substantially due to seasonal events, e.g. drought periods and/or wildfires (Jordan et al., 2013; Schwen et al., 2015). With the projected continuation of climate change, frequency and severity of drought events will intensify in most regions of the globe and the relevance of SWR effect on soil water dynamics is expected to increase in the future (Fischer and Knutt, 2014; Stocker et al., 2013).

SWR is not a stationary soil property but highly variable over time, depending on soil water content. Generally, SWR increases with decreasing water content (Jordan et al., 2013). Furthermore, although dry soils may be very water repellent initially, the repellency effect can disappear after prolonged contact with water. The duration of this process is described as repellency persistence. Besides persistence, SWR is also defined by severity of repellency, both of which can be expressed quantitatively (Chau et al., 2014). The intensity of SWR is characterized by the contact angle between soil surface and infiltrating water (Subedi et al., 2013). Hydrophobic conditions are present if contact angle above 90° is present, however even the contact angle in between 0° and 90° can affect water infiltration (Hallett et al., 2001). The SWR cannot be measured directly as physical value in the field, but has to be obtained indirectly, e.g. by observing the difference in flow behavior between water and fully-wetting fluid. Due to specific physico-chemical properties of ethanol (i.e. lower surface tension), ethanol is considered to be complete wetting fluid which is commonly used in SWR estimation (i.e. zero repellency; Lamparter et al., 2010; Watson and Letey, 1970). Further established methods (laboratory) are based on the influence which SWR has on other soil physical parameters, e.g. contact angle between water and soil surface, water drop penetration time, or capillary effect (Letey et al., 2000; Shang et al., 2008).

In comparison to non-repellent soils, water repellent soils have different infiltration patterns (initially postponed infiltration which increases after contact angle between water and soil particles decreases e.g. Bughici and Wallach, 2016; Debano, 1975) and increased fractions of preferential flow (e.g. Ritsema et al., 1993; 2000) or surface runoff (Lemmnitz et al., 2008). Soil infiltration experiments with a KBr tracer performed by Clothier et al. (2000) demonstrated (i) transient behavior of fingered preferential flow during the breakdown of hydrophobicity as a result of increasing soil water content, and (ii) solute penetration of the whole soil pore space after complete wetting. Hence, SWR appears to be reversible and very dynamic in time and space, thus making it difficult to predict. In a review by Jordan et al. (2013) the authors show that the majority of previous SWR studies are focused on the relationship between SWR and different soil properties (texture, organic matter content, soil chemical characteristics) or microbiological activity as a

response to soil management. However, SWR dynamics under different climatic scenarios and how it can affect soil moisture in the long term remains unclear.

To assess the water dynamics under various field conditions as well as for predictions of future scenarios, modeling has proven to be an appropriate tool (Šimůnek et al., 2016; Vereecken et al., 2016). However, in available modeling software applications for plot or profile scale SWR is not accounted for as a separate parameter, but may be preferably expressed during the procedure of soil hydraulic properties (SHP) estimation. Several studies highlight that the influence of SWR on SHP is evident in the hysteresis effect (Bauters et al., 1998; Czachor et al., 2010). Generally, the hysteresis is highly related to SWR, and the SWR effect is primarily detectable on the wetting curve (Hardie et al., 2013; Stoffregen and Wessolek, 2014). In a laboratory study focusing on SWR-influenced SHP, Diamantopoulos et al. (2013) performed multistep inflow/outflow experiments with water and ethanol on four substrates, where they gradually induced water repellency by adding water repellent material (hydrophobic sand) in different ratios to soil. The experiments were performed with initially dry or initially saturated conditions to account for hysteresis, and inverse parameter estimation was performed to obtain SHP. Their results showed that SWR affects SHP on the wetting curve, contributing to the hysteresis effect, and that the artificial mixtures with a higher fraction of water repellent substances had a larger effect of SWR on SHP compared to naturally repellent soils. Therefore, during SHP estimation in water repellent soils, it is important to account for the most severe SWR effects expected during the initial soil wetting process (infiltration).

Hysteretic forms of SHP are sometimes implemented in modeling applications to account for SWR, e.g. Nieber et al. (2000) simulated infiltration in wettable and water repellent sand with a 2D finite-element model where SWR was taken into account by including hysteresis in the water retention curve and two slightly different equations for the unsaturated hydraulic conductivity function. Ganz et al. (2014) modeled water infiltration patterns in water repellent soils as well, but using a 3D-simulation in HYDRUS (2D/3D). They emphasized a strong need for the inclusion of hysteresis (model implemented in HYDRUS by Lenhard and Parker, 1992) and a scaling procedure based on independently measured contact angle data (method by Bachmann et al., 2007).

To investigate the impact of different rainfall distribution patterns on soil water dynamics, modeling using data from an artificially induced drought stress field experiment was performed in order to investigate the full effect of SWR on the hysteretic wetting curve. The objective of this study was (i) to estimate SHP from disc infiltrometer experiments with water and ethanol using inverse modeling approach and (ii) to further assess the impact of different artificially induced drought scenarios on SWR and consequently on local vadose zone hydrology using HYDRUS (2D/3D).

MATERIALS AND METHODS

Field site description

The experimental field was set up at the iLTER-site (International Long Term Ecological Research) in the Rosalian Mountains, Austria (47°42′26.33″ N, 16°17′54.5″ E, 600 m a.s.l.; Leitner et al., 2017). The mean annual temperature is 6.5°C and the mean annual precipitation is 796 mm at this location. The experimental site was situated in a forested hillslope with mature beech trees (*Fagus silvatica* L.) and no understory on a plateau with a sloping angle of 16°. The soil type was classified as Podsolic Cambisol according to the WRB (World reference base for soil resources, IUSS, 2014) covering impermeable granitic bedrock at 75–80 cm below the soil surface following the hillslope curvature. The soil profile was covered with an organic matter O horizon (0–7 cm), followed by an eluvial humus Aeh-horizon (7–25 cm), a cambic, slightly humusoses-quioxidic Bhs-horizon (25–50 cm) over weathered granitic rock debris (C-horizon 50–75 cm) (Schwen et al., 2014). To assess the impact of changed rainfall distribution patterns on various soil properties, this experimental trial was established in 2013 (Leitner et al., 2017). Briefly, two artificially induced drought stress scenarios were applied during the vegetation period (May-October): a moderately (M) stressed scenario which had six consecutive cycles of four weeks drying followed by an intensive 75 mm irrigation, and a severely (S) stressed scenario which had three cycles of eight weeks drying followed by a larger irrigation event with 150 mm of irrigation. Stressed plots were protected from natural rainfall during vegetation periods by a plastic roof 1.20 m above the soil surface (each treatment having 4 plots, 2 m × 2 m, Fig. 1). Plots were irrigated with sprinkler irrigation systems with axial-flow full cone nozzles (Series 460, Lechler GmbH) installed under the roofs using descaled tap water from a nearby field station. The duration of the irrigation events were 2h each. To be able to compare the results with natural conditions, four control plots (C) received only natural rainfall. Drought plots had additional trenches (20 cm deep) at the upper end of the plot to avoid any lateral flow and/or surface runoff from elevated ground to enter the plots. In each plot, soil volumetric water content was measured at 10 cm depth in the Aeh horizon (VWC, TDR theta ML2x probes, UMS, Germany), with measurement intervals of 30 minutes. Climatic data were collected from a meteorological station located 500 m from the field site and used to calculate evapotranspiration according to Penman-Monteith (Monteith, 1981).

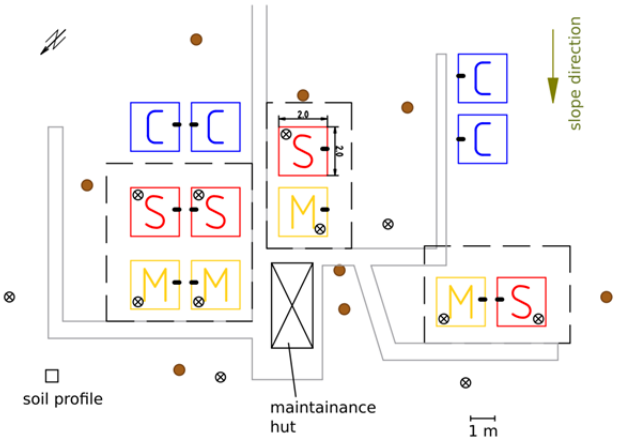

Fig. 1. iLTER experimental site scheme with bold lines as bridge pathways, dashed lines as plot roofs, colored squares as experimental units (2 × 2 m), black bold dashes as TDR-probes, X-ed circles as locations of performed infiltration experiments and brown points as trees. C stands for control, M for moderate, and S for severe stress. Infiltration experiments for control areas in Schwen et al. (2015) were conducted outside of the equipped squares to minimize influences to the soil system, especially to soil biology by ethanol.

Measurements of soil hydraulic parameters

Infiltration experiments were performed during September 2014 in all three scenarios (M, S, and C) in four repetitions as described elsewhere (Schwen et al., 2014, 2015) using a self-

Table 1. Basic soil physical properties at the iLTER experimental site (Austria) for Podsolic Cambisol soil profile: clay, silt and sand fraction, total porosity φ, bulk density ρb, and soil organic carbon (OC) content, Values were derived from a soil profile where samples were taken from incremental 5-cm-layers (uppermost sample from depth = 0–5cm), averaged for soil horizons (standard deviation in brackets). More detailed in Schwen et al., 2014, Fig. 1(b).

Horizon	Depth	Clay	Silt	Sand	OC	Porosity, φ	Bulk density, ρ_b
	cm	g g^{-1}	g g^{-1}	g g^{-1}	g g^{-1}	cm^3 cm^{-3}	g cm^{-3}
O	0–7	0.120 (–)	0.520 (–)	0.360 (–)	0.051 (–)	0.630 (–)	0.980 (–)
Aeh	7–25	0.090 (0.0125)	0.252 (0.0343)	0.659 (0.0438)	0.016 (0.0095)	0.510 (0.0326)	1.300 (0.0941)
Bhs	25–50	0.088 (0.0092)	0.240 (0.0524)	0.673 (0.0611)	0.002 (0.0027)	0.428 (0.0268)	1.516 (0.0712)
C	50–75	0.083 (0.0382)	0.191 (0.0204)	0.726 (0.0565)	0.000 (–)	0.378 (0.0164)	1.644 (0.0391)

constructed tension disc glass infiltrometer which allowed using both water and ethanol as infiltrating liquids (Schwen et al., 2015). These data served as an input for SHP estimation using inverse modeling (the procedure is explained in the next section). Before the infiltration measurements were made, the organic litter was removed to ensure that the measurements were performed at the top of the mineral Aeh horizon. Additionally, a thin layer of uniform glass beads was used at the soil surface to ensure good contact between soil and the porous disc (Dragonite, Jaygo Inc.; diameter: 0.45 mm). Infiltration measurements (water and ethanol) were conducted using different pressure heads (e.g., –10, –5, –3, –1 cm), in four replicates (one per plot) with each liquid. At the end of the water infiltration, the soil was covered to prevent any physical disturbance. Two days later, infiltration experiments were performed at the same specific spots using ethanol as the infiltration liquid with the glass beads layer replaced where necessary. Differences in the dynamic viscosity (η) of water (η = 1.0 mPa) and ethanol (η = 1.2 mPa) results in different liquid infiltration rates, even at identical liquid contents. To be able to compare the two infiltration experiments, the infiltration rates of ethanol were corrected for the difference in viscosity between water and ethanol using a factor of 1.2 (Jarvis et al., 2008). Considering different physicochemical properties of water and ethanol, the ethanol pressure head values were scaled based on the capillary rise equation which takes into account the difference between surface tension and density of particular liquids:

$$h_i = \frac{2\sigma_i cos\gamma}{r\rho_i g} \quad (1)$$

where σ is the surface tension (mN m^{-1}), γ is the contact angle (°), r is the equivalent capillary radius (m), ρ is the density of the liquid (g cm^{-3}), and g is the acceleration due to gravity (m s^{-2}). The subscript i refers to water (w) or ethanol (e). With the water and ethanol surface tension at 20°C of 72.7 mN m^{-1} and 22.4 mN m^{-1}, and a density of 0.998 g cm^{-3} and 0.789 g cm^{-3}, respectively, a correction factor between h_e and h_w of 2.5 was assumed (Diamantopoulos et al., 2013; Lamparter et al., 2010). Multiplying h_e with 2.5 results in the effective supply pressure ($h_{e,\,eff}$) giving the applied ethanol pressure heads of –25, –12.5, –7.5, and –2.5 cm. The correction factor assumes that the contact angles of water/ethanol and soil surface are identical ($\gamma_e = \gamma_w$), despite the fact that water contact angle in the field was oscillating in time. However, the differences in the contact angle reflect SWR through the different infiltration volumes for each liquid and consequently inversely estimated SHP. Initial water content was determined using the gravimetric method on undisturbed soil cores of 250 cm^3 volume (n = 4 per treatment). Average initial water content values were 0.17, 0.19, and 0.31 cm^3 cm^{-3} for M, S and C treatments prior to the water infiltration experiments. The same water contents were assumed to be present prior to ethanol infiltration experiments (no additional sampling/measurements were done in order to prevent disruption of the infiltration spots). Using the same soil core samples, SHP were estimated using the evaporation method (Schindler et al., 2010; device: HYPROP, UMS GmbH, Munich, Germany). Although SHP was measured by the evaporation method, only part of the measured data was used to obtain certain hydraulic parameters (porosity, θ_s) while the rest of the curve fitting was performed using inverse modeling based on the data from the infiltration experiments. SWR tend to be more expressed in drier soils and decreases with increased soil moisture (Dekker and Ritsema, 1994; Diamantopoloulos et al., 2013; Liu et al., 2012), thus starting with initially dried soil and performing infiltration experiments to investigate SWR in different treatments seemed appropriate. Particle size distribution was determined by a combination of sieving and sedimentation experiments according to Gee and Or (2002). Basic soil physical properties for the iLTER experimental site are given in Table 1.

Numerical modeling

Numerical modeling was performed with the HYDRUS (2D/3D) model (Šimůnek et al., 2016) using a three-step simulation process:

1. Inverse modeling based on water and ethanol field infiltration data – to obtain SHP;
2. Simulation of a particular irrigation event using obtained SHP – to validate the model using field TDR measurements;
3. Seasonal simulation (2014) – to assess the effect of SWR on water dynamics in hillslope areas.

This approach is explained in more detail in the following sections.

Inverse modeling to estimate soil hydraulic properties

Tension disc infiltration measurement data (average of four repetitions) with water and ethanol for the S, M, and C plots (Schwen et al., 2015) were used to obtain SHP using inverse modeling (Hopmans et al., 2002). A numerical solution of the Richards' equation coupled with the Levenberg-Marquardt nonlinear minimization method implemented in the HYDRUS (2D/3D) model was used. The program solves the equation numerically using a quasi-three-dimensional axisymmetric finite element code. The Richards' equation, which describes isothermal Darcian flow in a variably saturated rigid porous

medium, is used in the model in its modified form (Šimůnek et al., 1998):

$$\frac{\partial \theta}{\partial t} = \frac{1}{r}\frac{\partial}{\partial r}\left(rK\frac{\partial h}{\partial r}\right) + \frac{\partial}{\partial z}\left(K\frac{\partial h}{\partial z}\right) + \frac{\partial K}{\partial z} \quad (2)$$

where θ is the volumetric water content [L^3 L^{-3}], h is the pressure head [L], K is the unsaturated hydraulic conductivity [L T^{-1}], r is a radial coordinate [L], z is vertical coordinate [L], positive upwards, and t is time [L]. Equation (2) was solved numerically for the following initial and boundary conditions which reflect the initial and boundary conditions of the tension disc infiltrometer experiment:

$$\theta(r,z,t) = \theta_i \quad t = 0 \quad (3)$$

$$h(r,z,t) = h_0 \quad 0 < r < r_0,\ z = 0 \quad (4)$$

$$\frac{\partial h(r,z,t)}{\partial z} = -1 \quad r > r_0,\ z = 0 \quad (5)$$

$$h(r,z,t) = h_i \quad r^2 + z^2 \to \infty \quad (6)$$

where θ_i is the initial soil water content [L^3 L^{-3}], h_0 is the time-variable supply pressure head imposed by the tension disc infiltrometer for water (–10, –5, –3, –1 cm) and ethanol (–25, –12.5, –7.5, –2.5 cm) [L], and r_0 is the disc radius (porous disc radius of 2.9 cm) [L]. The SHP, estimated from ethanol infiltration volumes (scaled to match water physicochemical properties), were assumed to reflect the water infiltration in hydrophilic soil.

Soil hydraulic functions $\theta(h)$ and $K(h)$ used in the inverse and direct simulations (next section) were described using the van Genuchten-Mualem model (VGM, van Genuchten, 1980) defined as follows:

$$\theta(h) = \theta_r + \frac{\theta_s - \theta_r}{\left(1 + |\alpha h|^n\right)^m} \quad \text{for } h < 0 \quad (7)$$

$$\theta(h) = \theta_s \text{ for } h \geq 0$$

$$K(h) = K_s S_e^l \left(1 - \left(1 - S_e^{\frac{1}{m}}\right)^m\right)^2 \quad (8)$$

$$S_e = \frac{\theta - \theta_r}{\theta_s - \theta_r} \quad (9)$$

$$m = 1 - \frac{1}{n};\quad n > 1 \quad (10)$$

where θ_r and θ_s denote residual and saturated volumetric water content [L^3 L^{-3}], respectively, K_s is the saturated hydraulic conductivity [L T^{-1}], S_e is the effective saturation [–], α [L^{-1}] and n [–] are shape parameters, and l [–] is a pore connectivity parameter. Pore connectivity parameter (l) was fixed to 0.5 as recommended by Mualem et al., (1976) to avoid optimization of large number of parameters. Please note that the initial condition was given in terms of the soil water content (values presented in field site description chapter). Šimůnek and van Genuchten (1997) showed that, compared to the use of pressure head, providing initial condition in this form ensures a more stable and unique solution of the inverse problem. Soil surface boundary conditions below the disc infiltrometer and the remaining soil surface are represented by Eqs. 4 and 5, respectively. Eq. 6 assumes that all subsurface boundaries are distant from the supply source and do not influence the results in any way. The inverse solution was obtained using a combination of cumulative infiltration data and observed initial/final water content after minimization of the objective function. The simulated axisymmetrical domain was 15 cm wide and 20 cm long soil block with 2501 nodes and increased density along the upper boundary due to the tension disc infiltrometer placement. The soil hydraulic parameters (θ_r, α, n, and K_s) were initially derived from particle size distribution and bulk density data using the ROSETTA pedotransfer functions (Schaap et al., 2001) (See Table 2). The θ_r parameter was not modified, as Šimůnek et al. (1998) and González et al. (2015) found that this parameter had little effect on the simulated θ and h time series. The inverse modeling approach proposed by Šimůnek and van Genuchten (1996) was then used to calibrate α, n, and K_s in the top soil layer of each treatment starting with the initial Aeh horizon properties (Table 2).

Modeling water dynamics in the M, S and C scenarios

After performing inverse VGM parameters estimation, direct modeling was performed. Simulations included selected irrigation event (on June 24th 2014, starting 60 hours before and after irrigation was performed) in the M and S treatments during one year period (2014, on a daily time frame) in all three scenarios (M, S, and C). Simulations were performed for two-dimensional variably saturated porous media using Richards' equation:

$$\frac{\partial \theta}{\partial t} = \frac{\partial}{\partial x_i}\left[K\left(K_{ij}^A \frac{\partial h}{\partial x_j} + K_{iz}^A \right)\right] - S \quad (11)$$

where θ represents the soil volumetric water content [L^3 L^{-3}], h pressure head [L], x_i (i = 1, 2) the spatial coordinates [L], t time [T], K_{ij}^A is the components of the dimensionless hydraulic conductivity anisotropy tensor (K^A) in the two main spatial directions x_i, K is the unsaturated hydraulic conductivity [L T^{-1}], and S accounts for root water uptake [L^3 L^{-3} T^{-1}]. The root water uptake was calculated using the Feddes et al. (1978) equation. The potential root water uptake was calculated taking into account seasonal dynamics of LAI and interception of the canopy at the forest sites (beech trees). A constant rooting depth (75 cm) with a root distribution adapted from Huang et al. (2011) was assumed. Effective precipitation was further calculated by subtracting losses due to interception from gross precipitation. Seasonal variations in beech canopy were estimated using dynamic LAI with a maximum value of 5.8 and interception capacity of 2.0 mm (Armbruster et al., 2004; Breuer et al., 2003). Based on the assumptions stated above, potential root water uptake was calculated in the study of Schwen et al. (2014), performed on the same site.

The simulated domain in 2D vertical space (for specific irrigation event simulation and one year modeling) was 0.75 m deep and 2 m long (corresponding to one plot; see Figure 6 in the results section). Atmospheric boundary conditions were selected at the top and seepage conditions at the right side (down slope) to mimic the possible lateral subsurface movement as the soil profile was located on an impermeable sloped

Table 2. Van Genuchten-Mualem (VGM) soil hydraulic parameters derived from pedotranfer soil functions (PTFs, Rosetta) based on soil texture and bulk density (Table 1) with the measured saturated water content value θ_s based on evaporation experiments (Schwen et al., 2014).

Horizon	θ_r	θ_s	α	n	K_s	l
	$cm^3\ cm^{-3}$	$cm^3\ cm^{-3}$	cm^{-1}	–	$cm\ day^{-1}$	–
Aeh	0.0433	0.47	0.026	1.4554	88.37	0.5
Bhs	0.0404	0.35	0.0335	1.4563	44.22	0.5
C	0.0391	0.32	0.0427	1.4735	36.8	0.5

bedrock. The simulation domain had 14882 nodes with the increased density at the top boundary (with 29350 2D elements). The soil layering and hydraulic properties were selected according to the Table 2, with the Aeh horizon extended to the soil surface.

Although Richards' equation is not considered applicable for hydrophobic medium (e.g., Diamantopoulos and Durner, 2013), because SWR is a reversible process and not a constant state, some of the classical physical approaches are still suitable when critical water content is exceeded.

Numerical simulations (i.e., infiltration volumes and TDR measurements) were evaluated using the coefficient of determination (R^2), root mean square error ($RMSE$) and model efficiency coefficient (E) (Nash and Sutcliffe, 1970):

$$R^2 = \left(\frac{\sum_{i=1}^{n}(O_i - \bar{O})(S_i - \bar{S})}{\sqrt{\sum_{i=1}^{n}(O_i - \bar{O})}\sqrt{\sum_{i=1}^{n}(S_i - \bar{S})} } \right) \tag{12}$$

$$RMSE = \left[\frac{\sum_{i=1}^{n}(S_i - O_i)^2}{n} \right]^{0.5}$$

$$E = 1 - \frac{\sum_{i=1}^{n}(O_i - S_i)^2}{\sum_{i=1}^{n}(O_i - \bar{O})^2} \tag{13}$$

where O_i and S_i are observed and simulated values, respectively, $\bar{O}$ and $\bar{S}$ represent the averages of observed and simulated values, respectively, and n is the number of observed/simulated points.

RESULTS AND DISCUSSION

Inverse simulations of tension disc infiltrometer data

Tension disc infiltration data were used to estimate SHP by performing inverse modeling with HYDRUS (2D/3D). Modeled data is compared with field data in Fig. 2. Water infiltration for the M and S scenarios had a very steady slow inflow rate

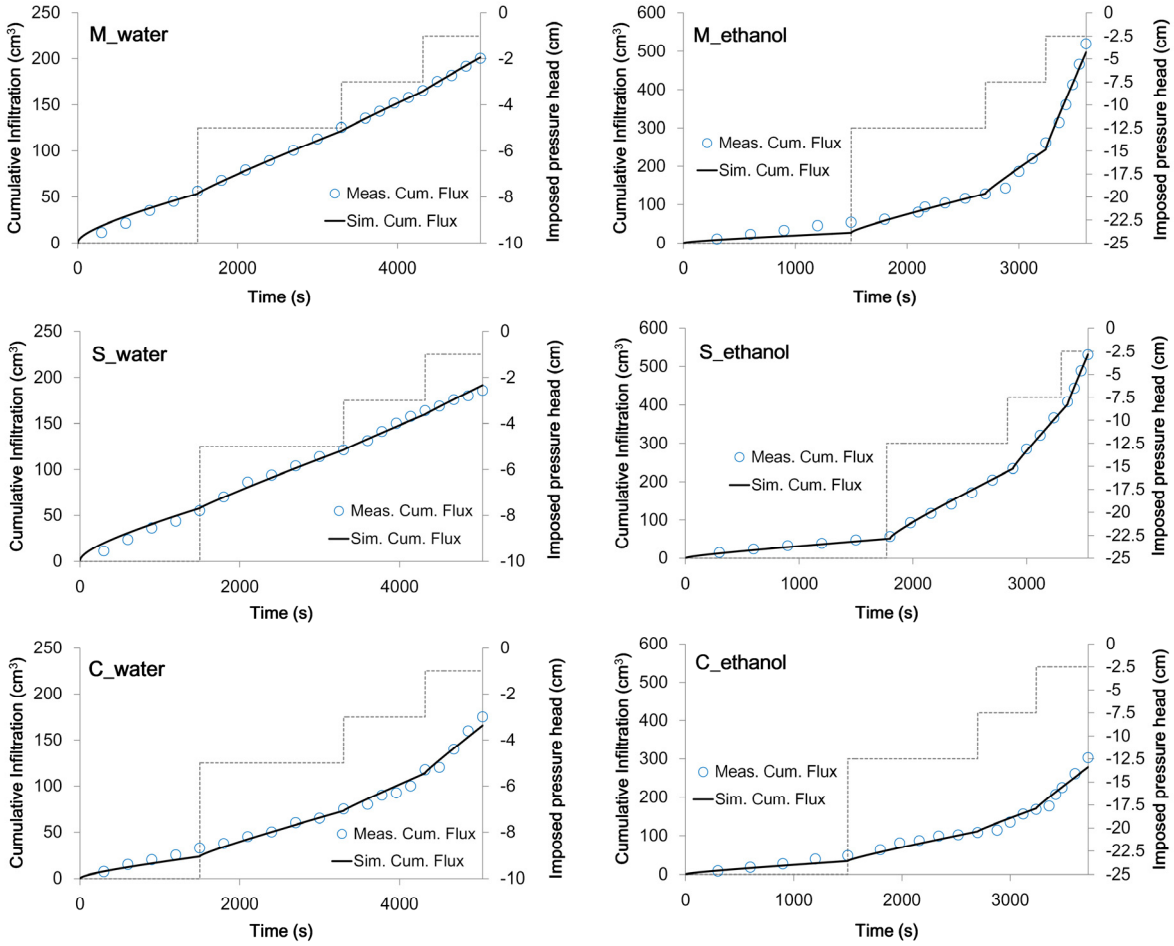

Fig. 2. Measured (circle) and simulated (solid line) infiltration cumulative fluxes for the M (moderately stressed), S (severe stressed) and C (control) scenarios with fitting performed using inverse optimization for water and ethanol liquids in HYDRUS (2D/3D) with an indication of the imposed pressure head and its duration (dotted line). Ethanol curves (_ethanol) are scaled in order to take account the different physicochemical properties and are directly comparable to water curves (_water).

Table 3. VGM parameters derived with inversion procedure using HYDRUS(2D/3D) from field infiltrometer data performed with water (_w) and ethanol (_e) liquids and statistical parameters (R^2, E, $RMSE$) describing goodness of model fitting for Aeh horizon.

Scenario	α	n	K_s	R^2	E	$RMSE$
	(cm^{-1})	(–)	cm day^{-1}			(cm^3)
M_w	0.036	1.717	23.45	0.998	0.998	2.77
M_e	0.100	1.713	1454.26	0.981	0.985	21.6
S_w	0.025	1.389	27	0.995	0.995	4.14
S_e	0.055	2.178	440	0.999	0.999	4.25
C_w	0.101	1.318	257.02	0.989	0.9910	5.11
C_e	0.056	1.393	460.8	0.982	0.981	11.03

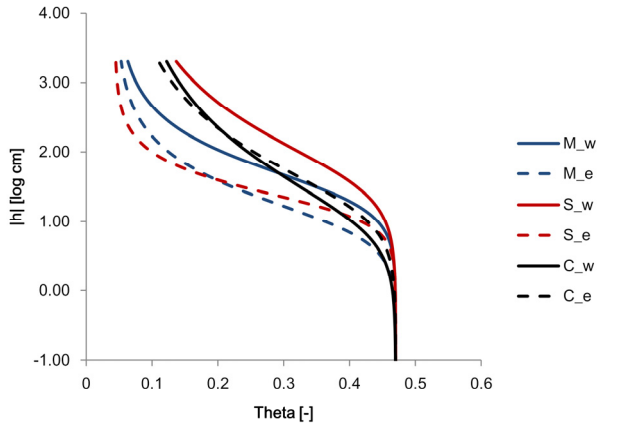

Fig. 3. Plotted retention curves for different VGM soil hydraulic parameter sets for various precipitation manipulation scenarios and different liquids (w, water vs. e, ethanol). Ethanol curves (_e) are scaled in order to take account the different physicochemical properties and are directly comparable to water curves (_w). M, moderately stressed scenario; S, severely stressed scenario; C, control scenario.

during the entire infiltration experiment and did not respond to the change in supply pressure. By contrast, a typical water infiltration curve found for non-repellent soils was observed in scenario C (although with reduced effect e.g. Šimůnek and van Genuchten, 1997), showing increased infiltration volumes at lower pressure heads (close to saturation). On the contrary, for M and S scenarios data showed reduced infiltration at lower pressure heads (h = –3 cm and –1 cm) and indicated that the larger pores were more hydrophobic than the smaller pores (Leue et al., 2015; Schwen et al., 2015). The final infiltration volumes were similar with 200.4, 185.7 and 175 ml for M, S and C scenarios, respectively. However, if these results are compared to the ethanol experimental data, it can be seen that the ethanol infiltration volumes are larger, with the final volumes of 519, 531 and 303 ml for M, S and C scenarios, respectively, indicating increased water repellency in the M and S scenarios. These data also show that the C scenario showed the smallest difference in total volume and infiltration curve behavior between water and ethanol. Similar results were observed by Jarvis et al. (2008) where they compared grassland to arable land with water and ethanol measurements and found that water repellency is smaller when water and ethanol infiltration volumes are similar (and *vice versa*).

The inverse optimization modeling worked well in both cases, showing a good fit for both infiltrating liquids, which can be observed visually and through statistical indicators (Fig. 2; Table 3). This shows that the VGM model describes soil hydraulic parameters well at this site. Observations through the profile indicate the presence of few macropores with a rather uniform structure (Schwen et al., 2014), suggesting that a single porosity model would be sufficient to describe the soil water dynamics (e.g. van Genuchten, 1980). Table 3 shows a large difference between soil hydraulic properties with water and ethanol for all optimized parameters. A large increase in K_s values in the M and S scenarios was found when ethanol as a complete wetting liquid was used (Table 3) compared to water infiltration where K_s was lower. Decreases of 98.3% and 93.8% in K_s values were noticed when comparing ethanol and water infiltration for M and S scenarios. In contrast, the control scenario shows a lower increase of 44.2% compared to the water infiltration measurements. This difference also indicates that

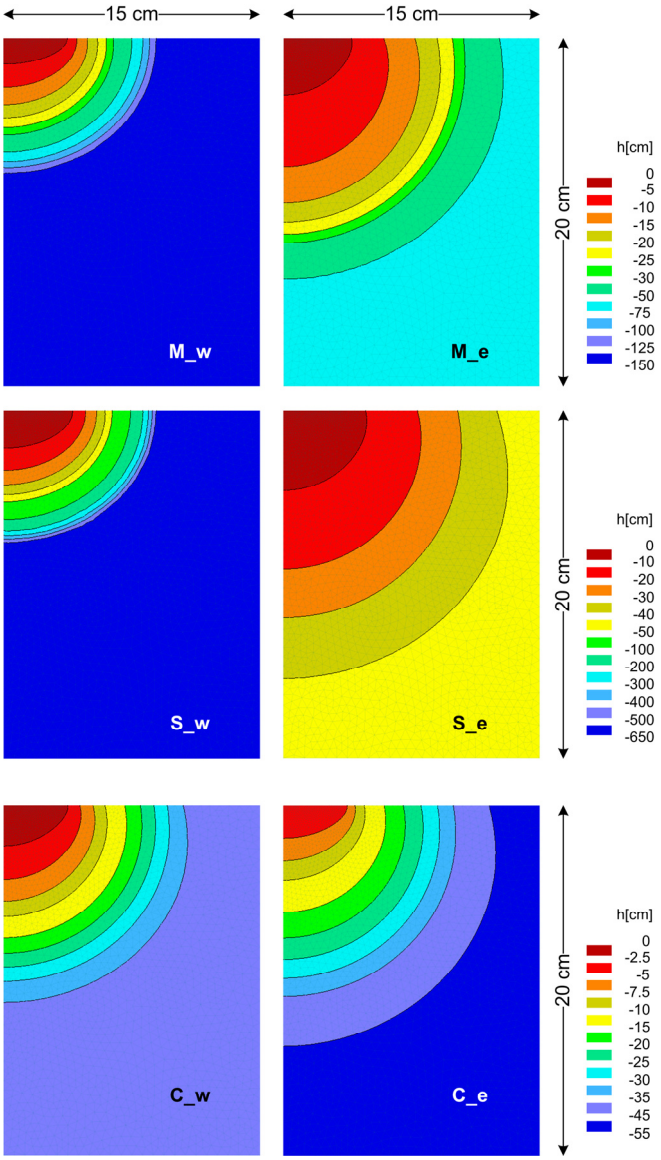

Fig. 4. Pressure head distribution for M (moderately stressed) S (severely stressed) and C (control) scenarios at the end of the tension infiltration field experiment using water (_w) and ethanol (_e).

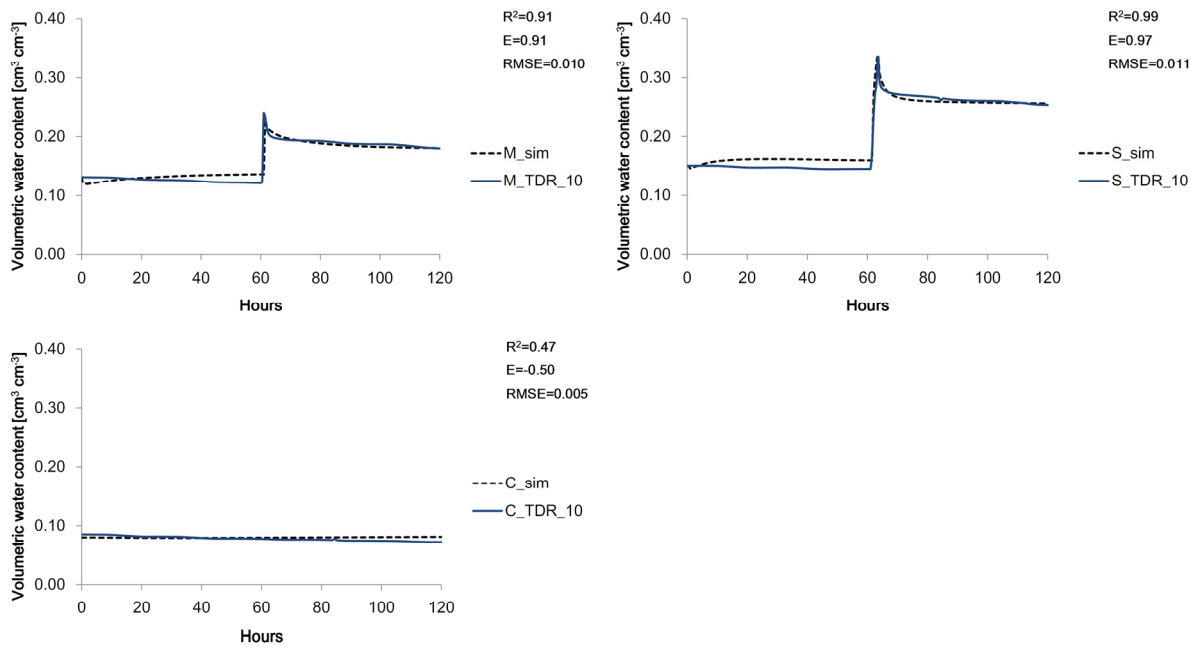

Fig. 5. Measured and simulated soil volumetric water content at 10 cm depth (Aeh horizon, TDR) using optimized parameters from water infiltration experiments from M (moderately stressed) S (severely stressed) and C (control) scenarios for the irrigation event at 24th of June 2014 (60 h before and after the event) with a 75 mm after 4 weeks of drought (M plots) and 150 mm irrigation after 8 weeks of drought (S plots) of irrigation for the event duration of 120 h.

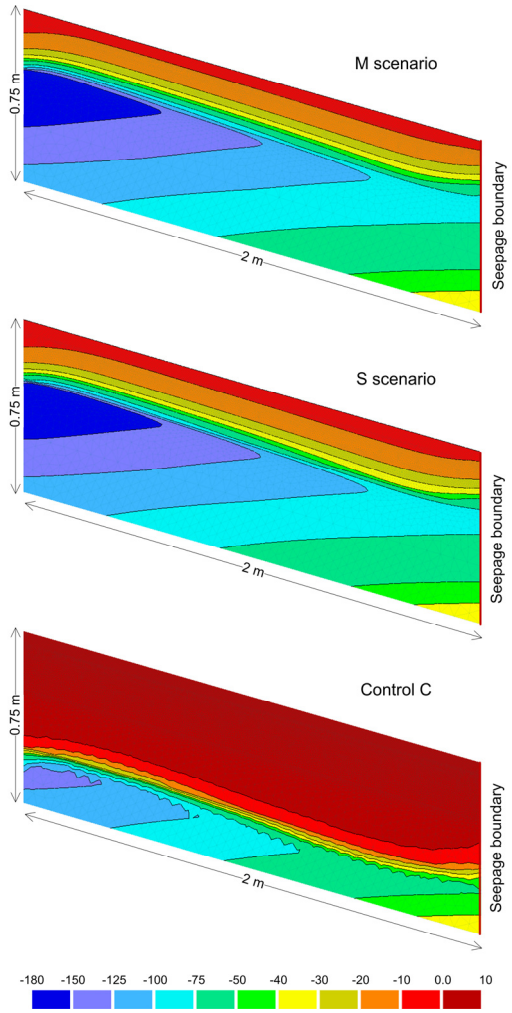

Fig. 6. Pressure head distribution for M (moderately stressed) S (severely stressed) and C (control) scenarios on the August 20th 2014 after 150 mm of the irrigation event on the previous day.

the control scenario had a certain degree of soil water repellency, which was most likely linked to the natural rainfall distribution e.g. critically low soil water content during longer periods with no rain (Schwen et al., 2015).

Fig. 3 shows fitted water retention curves based on the Table 2 parameter set for measurements derived from water (full lines) and ethanol infiltration (dotted lines). Again greater differences in the shape of the retention curve at the larger tension (dryer soil condition) were recorded between the artificially induced drought stress scenarios, while the control plot had a similar shape of the retention curve for both, water and ethanol obtained SHP. It should be noted that the small differences in water retention curves of control plot might be also connected to the fitting procedure in HYDRUS since more than one set of SHP can be realistic. In addition to changes in K_s values, α and n values were increased significantly during the optimization process for ethanol data (M and S plots), resulting in a different curve shape.

Pressure head snapshots were taken at the final time of the simulated disc tension infiltration field experiment performed in HYDRUS (2D/3D) (Fig. 4). These data show that the water infiltration plume in M and S scenarios is significantly reduced compared with the ethanol infiltration plume, resulting in a very dry bottom part of the soil block (20 cm depth) even after 1.5 hours of infiltration. This part of the soil block had a pressure head of approximately –150 and –650 cm for M and S scenarios, respectively, while the ethanol treated soil had a pressure head around –75 cm. The control plot also showed differences in final pressure head values, but the lowest pressure heads were –41.58 cm for water and –54.21 cm for ethanol infiltration, respectively. The differences in duration and infiltration volumes between the two applied liquids should also be taken into consideration. Occurrence of such extensive infiltration reduction increases the risk of preferential flow in structured soils (Jarvis et al., 2008) and the potential of surface runoff as well (Cerdà and Doerr, 2007), which is further evaluated through simulations of artificially induced drought stress scenarios in the next section.

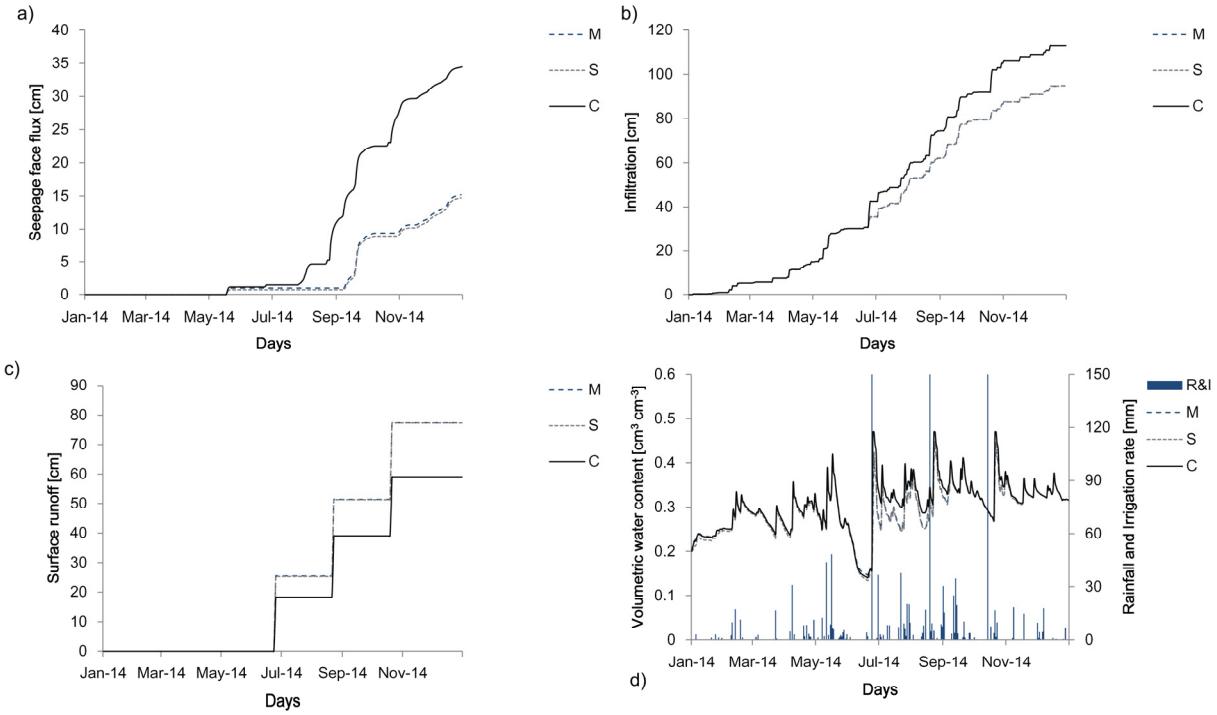

Fig. 7. Simulated cumulative seepage face flux (at the right side boundary, a), cumulative infiltration (b), cumulative runoff (c) and volumetric water content (d) at the M (moderately stressed) S (severely stressed) and C (control) scenarios during 2014 using natural rainfall and irrigation events.

Simulations of artificially induced drought stress scenarios

After the SHP were obtained by inverse modeling, a direct simulation of a particular irrigation event (on June 24th 2014) was performed for the M and S scenarios and also for the control scenario without any irrigation (Fig. 5). The selected event was simulated with a temporal resolution of 1h to provide detailed information regarding the model performance using the obtained SHP. The simulation was set to start and finish 60 hours before and after the irrigation event. Because the plots were covered during the rest of the season, simulating such shorter periods before and after the irrigation event in order to validate the model was assumed sufficient. The simulations were performed using the properties of the Aeh horizon derived from the water infiltration inverse modeling and compared to water contents measured by TDR probes at 10 cm depth (Aeh horizon) while the rest of the horizons had the same values for each layer as presented in the Table 2. Simulation of water content reproduced the field observation well with R^2 values above 0.9 and confident model efficiency values, while the model efficiency was low (–0.50) in the control scenario due to the absence of any variation during this limited period. Still, the RMSE of 0.005 indicated a good fit of the data of the control scenario. These model performance results for water content simulations are in line with previous studies using the HYDRUS model (e.g., Ajdary et al., 2007; Kandelous et al., 2011; Nakhaei and Šimůnek, 2014).

Fig. 5 clearly shows a dependence between soil water content and the amount of applied irrigation water for the M and S scenarios, e.g. an instant increase of soil water content in the M scenario from 0.12 to 0.29 cm^3 cm^{-3} at the time 60.5 hours is observed, and in S scenario from 0.15 to 0.34 cm^3 cm^{-3}, both corresponding to the 75 and 150 mm of irrigation, respectively. The control scenario did not show any increase in soil water content due to the absence of natural rainfall and irrigation.

After obtaining hydraulic properties from the infiltration experiment and validating the model by comparing it to field water content measurements, one year simulations were performed for 2014 using a daily time step. The simulation included plant uptake and natural rainfall and irrigation events, in order to maximize the difference between the scenarios (in terms of water balance) and to reveal potential downsides of the water repellency (e.g., surface runoff, low water content). Fig. 6 shows the pressure head distribution on August 20th, 2014 (one day after irrigation events on both irrigated plots) in the three scenarios. The differences between the scenarios are seemingly negligible for the M and S scenarios. The low conductivity of the Aeh layer (23.45 cm day^{-1} and 27 cm day^{-1} for the M and S scenario, respectively) delayed the infiltration of the irrigation plume and induced surface runoff. On the contrary, due to its non-repellent state which was expressed in larger K_s values (257.02 cm day^{-1}), the irrigation plume saturated simulated profile till approximately 50 cm depth.

Our simulations suggest that in this particular case, the effect of hydrophobicity on large scale hydrology can have a substantial impact on water balance and its distribution between the infiltration and surface runoff. Fig. 7 shows differences in water balance (e.g., seepage face flux, infiltration rate and surface runoff) between artificially induced drought stress scenarios and the control plot. Due to similar SHP for the two imposed scenarios, the water balance and its distribution is almost identical. However, large seepage face flux (which in this case mimics subsurface lateral flow because of the impermeable bedrock at 75 cm) can be observed in the control plot (34.7 cm vs. 15 cm in the drought scenarios). Small K_s values in the M and S scenarios resulted in decreased infiltration and subsurface flow but increased surface runoff (77 cm in drought stress scenarios vs. 59 cm in control). The simulated water content (Fig. 7d) followed the rainfall and irrigation inputs very well and reflected the increased water levels at the top as well. The

extent of the oscillations was linked directly to the estimated SHP, e.g. a quicker response of volumetric water content changes can be seen in a control plot with the applied irrigation (simulated). Our results are in accordance with previous studies (e.g. Lemmnitz et al., 2008) which indicate that the occurrence of soil water repellency on hillslopes is important when addressing larger scale soil hydrology on a seasonal basis.

CONCLUSIONS

The HYDRUS (2D/3D) model was used to estimate soil hydraulic properties from field tension disc infiltration experiments and to quantify soil water repellency effects using data from water and ethanol infiltration measurements. Additionally, simulations to fit the TDR field moisture measurements and to perform 2D water balance modeling on an artificially induced drought stress field experiment were conducted. The water and ethanol infiltration experiments showed a large variation among the treatments and control scenario, revealing the importance of prolonged soil drying on soil water repellency. The inverse modeling was performed successfully with R^2 and model efficiency (E) values above 0.9, indicating good fit with the field measured infiltration data for both liquids (water and ethanol). Soil hydraulic properties derived from the ethanol measurements showed significantly greater K_s values for the M and S scenarios, thus suggesting linkage between water repellency and reduced infiltration. Direct simulation of irrigation events showed good reliability of the model to fit water contents measured at 10 cm depth using TDR probes. One year simulations (2014) showed that the non-structured water repellent soils have a potential to produce increased surface runoff, as well as reduced subsurface lateral flow (if impermeable or low conductivity layer is present) or vertical drainage. Climatic change scenarios are predicting more intense and prolonged droughts, as well as more extreme rainfall events, which can lead to increased soil water repellency and result in changed water flow patterns at the plot scale. Further studies are needed to clarify the occurrence, non-linear nature and impact of SWR.

Acknowledgements. This project was partly funded by the Austrian Climate and Energy Fund (ACRP 6–DRAIN–KR13AC6K11008). Sonja Leitner received a PhD fellowship of the AXA Research Fund. We also acknowledge travel funding from the bilateral agreement project HR20/2016 funded by the Austrian Agency for International Cooperation in Education (OeAD) and the Ministry of the Science and Education of the Republic of Croatia.

REFERENCES

Ajdary, K., Singh, D.K., Singh, A.K., Khanna, M., 2007. Modelling of nitrogen leaching from experimental onion field under drip irrigation. Agr. Water Manage., 89, 15–28.

Armbruster, M., Seegert, J., Feger, K.H., 2004. Effects of changes in tree species composition on water flow dynamics – model applications and their limitations. Plant Soil, 264, 13–24.

Bachmann, J., Deurer, M., Arye, G., 2007. Modeling water movement in heterogeneous water-repellent soil: 1. Development of a contact angle–dependent water-retention model. Vadose Zone J., 6, 436–445.

Bauters, T.W.J., DiCarlo, D.A., Steenhuis, T.S., Parlange, J.-Y., 2000. Soil water content dependent wetting front characteristics in sands. J. Hydrology, 231–232, 244–254.

Breuer, L., Eckhardt, K., Frede, H.G., 2003. Plant parameter values for models in temperate climates. Ecol. Model., 169, 237–293.

Bughici, T., Wallach, R., 2016. Formation of soil-water repellency in olive orchards and its influence on infiltration pattern. Geoderma, 262, 1–11.

Cerdà, A., Doerr, S.H., 2007. Soil wettability, runoff and erodibility of major dry-Mediterranean land use types on calcareous soils. Hydrol. Process., 21, 17, 2325–2336.

Chau, H.W., Biswas, A., Vujanovic, V., Si, B.C., 2014. Relationship between the severity, persistence of soil water repellency and the critical soil water content in water repellent soils. Geoderma, 221–222, 113–120.

Clothier, B.E., Vogeler, I., Magesan, G.N., 2000. The breakdown of water repellency and solute transport through a hydrophobic soil. J. Hydrol., 231–232, 255–264.

Czachor, H., Doerr, S.H., Lichner, L., 2010.Water retention of repellent and subcritical repellent soils: new insights from model and experimental investigations. J. Hydrol., 380, 104–111.

Debano, L.F., 1975. Infiltration, evaporation, and water movement as related to water repellency 1. In: Gardner, W.R., Moldenhauer, W.C. (Eds.): Soil Conditioners. SSSA Spec. Publ. 7. SSSA, Madison, WI., pp. 155–164.

Dekker, L.W., Ritsema, C.J., 1994. How water moves in a water repellent sandy soil, 1. Potential and actual water repellency. Water Resour. Res., 30, 2507–2517.

Diamantopoulos, E., Durner, W., 2013. Physically-based model of soil hydraulic properties accounting for variable contact angle and its effect on hysteresis. Adv. Water Resour., 59, 169–180.

Diamantopoulos, E., Durner, W., Reszkowska, A., Bachmann, J., 2013. Effect of soil water repellency on soil hydraulic properties estimated under dynamic conditions J. Hydrol., 486, 175–186.

Doerr, S.H., Shakesby, R.A., Walsh, R.P.D., 2000. Soil water repellency: its causes, characteristics and hydro-geomorphological significance. Earth Sci. Rev., 51, 33–65.

Feddes, R.A., Kowalik, P.J., Zaradny, H., 1978. Simulation of Field Water Use and Crop Yield. John Wiley & Sons, New York.

Fischer, E.M., Knutti, R., 2014. Detection of spatially aggregated changes in temperature and precipitation extremes. Geophys. Res. Lett., 41, 2, 547–554.

Ganz, C., Bachmann, J., Noell, U., Diujnisveld, W.H.M., Lamparter, A., 2014. Hydraulic modeling and in situ electrical resistivity tomography to analyze ponded infiltration into a water repellent sand. Vadose Zone J., 13, 1, 1–14.

Gee, G.W., Or, D., 2002. Particle-size analysis. In: Dane, J.H., Topp, G.C. (Eds.): Methods of Soil Analysis. Part 4 – Physical Methods. SSSA Book Series, No. 5. SSSA, Madison, WI, USA, pp. 1381–1402.

González, M.G., Ramos, T.B., Carlesso, R., Paredes, P., Petry, M.T., Martins, J.D., Aires, N.P., Pereira, L.S., 2015. Modelling soil water dynamics of full and deficit drip irrigated maize cultivated under a rain shelter. Biosyst. Eng., 132, 1–18. DOI: 10.1016/j.biosystemseng.2015.02.001.

Hallett, P.D., Baumgartl, T., Young, I.M., 2001. Subcritical water repellency of aggregates from a range of soil management practices. Soil Sci. Soc. Am. J., 65, 184–190.

Hardie, A.H., Lisson, S., Doyle, R.B., Cothing, W.E., 2013. Evaluation of rapid approaches for determining the soil water retention function and saturated hydraulic conductivity in a hydrologically complex soil. Soil Till. Res., 130, 99–108.

Hopmans, J.W., Šimůnek, J., Romano, N., Durner, W., 2002. Inverse methods. In: Dane, J.H., Topp, G.C. (Eds.): Methods of Soil Analysis. Part 4. SSSA Book Series, No. 5. SSSA, Madison, WI, pp. 963–1008.

Huang, M., Barbour, S.L., Elshorbagy, A., Zettl, J.D., Si, B.C., 2011. Water availability and forest growth in coarse-textures soils. Canad. J. Soil Sci., 91, 199–210.

IUSS, 2014. World reference base for soil resources. FAO, Rome.

Jarvis, N., Etana, A., Stagnitti, F., 2008. Water repellency, near-saturated infiltration and preferential solute transport in a macroporous clay soil. Geoderma, 143, 223–230.

Jordán, A., Zavala, L.M., Mataix-Solera, J., Doerr, S.H., 2013. Soil water repellency: origin, assessment and geomorphological consequences. Catena, 108, 1–5.

Kandelous, M.M., Šimůnek, J., van Genuchten, M.Th, Malek, K., 2011. Soil water content distributions between two emitters of a subsurface drip irrigation system. Soil Soil Sci. Soc. Am. J., 75, 488–497.

Lamparter, A., Bachmann, J., Deurer, M., Woche, S.K., 2010. Applicability of ethanol for measuring intrinsic hydraulic properties of sand with various water repellency levels. Vadose Zone J., 9, 445–450.

Leitner, S., Minixhofer, P., Inselsbacher, E., Keiblinger, K.M., Zimmermann, M., Zechmeister-Boltenstern, S., 2017. Short-term soil mineral and organic nitrogen fluxes during moderate and severe drying-rewetting events. Appl. Soil Ecol., 114, 28–33.

Lemmnitz, C., Kuhnert, M., Bens, O., Güntner, A., Merz, B., Hüttl, R.F., 2008. Spatial and temporal variations of actual soil water repellency and their influence on surface runoff. Hydrol. Process., 22, 1976–1984.

Lenhard, R.J., Parker, J.C. 1992. Modeling multiphase fluid hysteresis and comparing results to laboratory investigations. In: Genuchten, M.Th., Leij, F.J., Lund, L.J. (Eds.); Proc. Intl. Workshop on Indirect Methods for Estimating the Hydraulic Properties of Unsaturated Soils. University of California, Riverside, CA.

Letey, J., Carrillo, M.L.K., Pang, X.P., 2000. Approaches to characterize the degree of water repellency. J. Hydrol., 231–232, 61–65.

Leue, M., H.H. Gerke, Godow, S.C., 2015. Droplet infiltration and organic matter composition of intact crack and biopore surfaces from clay-illuvial horizons. J. Plant Nutr. Soil Sci., 178, 250–260.

Liu, H., Ju, Z., Bachmann, J., Horton, R., Ren, T., 2012. Moisture-dependent wettability of artificial hydrophobic soils and its relevance for soil water desorption curves. Soil Sci. Soc. Am. J., 76, 342–349.

Monteith, J.L., 1981. Evaporation and surface temperature. Q. J. R. Meteorol. Soc., 107, 1–27.

Mualem, Y., 1976. A new model for predicting the hydraulic conductivity of unsaturated porous media. Water Resour. Res., 12, 3, 513–521.

Nakhaei, M., Šimůnek, J., 2014. Parameter estimation of soil hydraulic and thermal property functions for unsaturated porous media using the HYDRUS-2D code. J. Hydrol. Hydromech., 62, 7–15.

Nash, J.E., Sutcliffe, J.V., 1970. River flow forecasting through conceptual models. Part I. A discussion of principles. J. Hydrol., 10, 282–90.

Nieber, J., Bauters, T.W.J., Steenhuis, T.S., Parlange, J.Y., 2000. Numerical simulation of experimental gravity-driven unstable flow in water repellent sand. J. Hydrol., 231–232, 295–307.

Ritsema, C.J., Dekker, L.W., 2000. Preferential flow in water repellent sandy soils: principles and modeling implications. J. Hydrol., 231–232, 308–319.

Ritsema, C., Dekker, L.W., Hendrickx, J.M.H., Hamminga, W., 1993. Preferential flow mechanism in a water repellent sandy soil. Water Resour. Res., 29, 2183–2193.

Schaap, M.G., Leij, F.J., van Genuchten, M.T., 2001. ROSETTA: a computer program for estimating soil hydraulic parameters with hierarchical pedotransfer functions. J. Hydrol., 251, 163–176.

Schindler, U., Durner, W., von Unold, Georg., Müller, L., 2010. Evaporation method for measuring unsaturated hydraulic properties of soils: extending the measurement range. Soil Sci. Soc. Am. J., 74, 1071–1083.

Schwen, A., Zimmermann, M., Bodner, G., 2014. Vertical variations of soil hydraulic properties within two soil profiles and its relevance for soil water simulations. J. Hydrol., 516, 169–181.

Schwen, A., Zimmermann, M., Leitner, S., Woche, S.K., 2015. Soil Water Repellency and its Impact on Hydraulic Characteristics in a Beech Forest under Simulated Climate Change. Vadose Zone J., 14, 12, 1–11.

Shang, J., Flury, M., Harsh, J.B., Zollars, R.L., 2008. Comparison of different methods to measure contact angles of soil colloids. J. Colloid Interface Sci., 328, 299–307.

Šimůnek, J., van Genuchten, M.Th., 1996. Estimating unsaturated soil hydraulic properties from tension disc infiltrometer data by numerical inversion. Water Resour. Res., 32, 2683–2696.

Šimůnek, J., van Genuchten, M.Th., 1997. Parameter estimation of soil hydraulic properties from multiple tension disc infiltrometer data. Soil Sci., 162, 383–398.

Šimůnek, J., Angulo-Jaramillo, R., Schaap, M.G., Vandervaere, J.P., van Genuchten, M.T., 1998. Using an inverse method to estimate the hydraulic properties of crusted soils from tension disc infiltrometer data. Geoderma, 86, 61–81.

Šimůnek, J., van Genuchten, M.Th., Šejna, M., 2016. Recent developments and applications of the HYDRUS computer software packages. Vadose Zone J., 15, 7. DOI: 10.2136/vzj2016.04.0033

Stocker, T.F., Qin, D., Plattner, G.-K. Tignor, M.M.B., Allen, S.K., Boschung, J., Nauels, A., Xia, Y., Bex, V., Midgley, P.M. (Eds.), 2013. Climate Change. The Physical Science Basis. Summary for Policymakers. Working Group I Contribution to the Fifth Assessment Report of the Intergovernmental Panel on Climate Change. Cambridge Univ. Press, Cambridge and New York, pp. 1–30.

Stoffregen, H., Wessolek, G., 2014. Scaling the hydraulic functions of a water repellent sandy soil. Int. Agrophys., 28, 349–358.

Subedi, S., Kawamoto, K., Komatsu, T., Moldrup, P., Wollesen de Jonge, L., Müller, K., Clothier, B., 2013. Contact angles of water-repellent porous media inferred by tensiometer-TDR probe measurement under controlled wetting and drying cycles. Soil Sci. Soc. Am. J., 77, 1944–1954.

van Genuchten, M.Th., 1980. A closed-form equation for predicting the hydraulic conductivity of unsaturated soils. Soil Sci. Soc. Am. J., 44, 892–898.

Vereecken, H., Schnepf, A., Hopmans, J.W., Javaux, M., Or, D., Roose, T., Vanderborght, J., Young, M.H., Amelung, W., Aitkenhead, M., Allison, S.D., Assouline, S., Baveye, P., Berli, M., Brüggemann, N., Finke, P., Flury, M., Gaiser, T., Govers, G., Ghezzehei, T., Hallett, P., Hendricks Franssen, H.J., Heppell, J., Horn, R., Huisman, J.A., Jacques, D., Jonard, F., Kollet, S., Lafolie, F., Lamorski, K., Leitner,

D., McBratney, A., Minasny, B., Montzka, C., Nowak, W., Pachepsky, Y., Padarian, J., Romano, N., Roth, K., Rothfuss, Y., Rowe, E.C., Schwen, A., Šimůnek, J., Tiktak, A., Van Dam, J., van der Zee, S.E.A.T.M., Vogel, H.J., Vrugt, J.A., Wöhling, T., Young, I.M., 2016. Modeling soil processes: Review, key challenges, and new perspectives. Vadose Zone J., 15, 5. DOI: 10.2136/vzj2015.09.0131.

Watson, C.L., Letey, J., 1970. Indices for characterizing soil-water repellency based upon contact angle-surface tension relationships. Soil Sci. Soc. Am. Proc., 34, 841–844.

Received 17 July 2017
Accepted 29 December 2017

Note: Colour version of Figures can be found in the web version of this article.

J. Hydrol. Hydromech., 66, 2018, 2, 181–188
DOI: 10.1515/johh-2017-0052

The influence of stony soil properties on water dynamics modeled by the HYDRUS model

Hana Hlaváčiková*, Viliam Novák, Zdeněk Kostka, Michal Danko, Jozef Hlavčo

Institute of Hydrology, Slovak Academy of Sciences, Dúbravská cesta 9, 841 04 Bratislava, Slovak republic.
* Corresponding author. E-mail: hlavacikova@uh.savba.sk

Abstract: Stony soils are composed of two fractions (rock fragments and fine soil) with different hydrophysical characteristics. Although stony soils are abundant in many catchments, their properties are still not well understood. This manuscript presents an application of the simple methodology for deriving water retention properties of stony soils, taking into account a correction for the soil stoniness. Variations in the water retention of the fine soil fraction and its impact on both the soil water storage and the bottom boundary fluxes are studied as well. The deterministic water flow model HYDRUS-1D is used in the study. The results indicate that the presence of rock fragments in a moderate-to-high stony soil can decrease the soil water storage by 23% or more and affect the soil water dynamics. Simulated bottom fluxes increased or decreased faster, and their maxima during the wet period were larger in the stony soil compared to the non-stony one.

Keywords: Rock fragments; Soil water retention; Water storage; Outflow; Numerical modeling; HYDRUS-1D.

INTRODUCTION

Stony soils are composed of the fine soil fraction, i.e., small mineral particles with a diameter of less than 2 mm, and larger rock fragments, e.g., gravel, cobbles, stones, and boulders. The size, shape, degree of weathering, geological origin, position, and a spatial distribution of rock fragments (RF) in a soil profile can strongly influence the stony soil's properties, mainly the soil´s water retention and hydraulic conductivity. They can also affect soil water movement, infiltration, and the runoff formation. Although stony soils occur in many forested, mountainous, and even agricultural areas, the influence of RF on hydrological processes, water balance, and water storage are often neglected. The standardized methodology for incorporating the effects of RF on hydraulic properties and hydraulic modeling of stony soils is not available.

The research on the hydrological role of stony soils in the High Tatra Mountains began at the Institute of Hydrology of the Slovak Academy of Sciences during the international research project, which was initiated after an extraordinary windthrow in 2004. The windthrow uprooted forest in an approximately 120 km^2 area and was one of ten most devastating storms in Europe over the last several decades (Gardiner et al., 2010). The international research community tried to assess the effects of such a disaster on hydrological, biogeochemical, and other processes in the affected area. Mountain soils in the High Tatra Mountains contain a lot of rock fragments. To quantify hydrological processes, it was necessary to consider the impact of RF on water flow dynamics in the soil (Novák and Kňava, 2012).

There are only a few studies that try to quantify the influence of stoniness on hydrological processes, water contents (Coppola et al., 2013), and water balance modeling (Wegehenkel et al., 2017). One of several reasons for this oversight is the sample size. Rock fragments present in stony soils are often several times larger than small mineral soil particles. Therefore, characteristics of the bulk stony soil have to be measured on an adequate representative elementary volume (REV), the size of which may be 1 m^3 or larger, which is often impossible to do. According to the REV theory, a heterogeneous porous medium can be characterized by average properties of a specific volume (REV). This volume has to be large enough to average out the discontinuities of the soil structural elements (a spatial arrangement of pores and particles) but at the same time small enough compared to the entire volume of the porous medium in which the transport processes occur (Buchter et al., 1994). The appropriate REV is obtained when the porous medium property is invariant to the REV dimensions. A heterogeneous porous medium (soil) is replaced by a "hypothetically homogeneous" one, which is characterized by the effective characteristics. The effective characteristics of a stony soil characterize it as a whole and are denoted as bulk characteristics, later indicated by the subscript „b". A standardized methodology of the estimation of REV does not yet exist. The REV of 100 cm^3 (a standard sampling cylinder) has proved to be large enough for relatively homogeneous soils. Baker and Bouma (1976), Kutílek and Nielsen (1994), and Lichner (1994) recommended defining the REV of a soil as the soil sample volume, which contains no less than 20 basic elements of the soil structure (in the case of stony soils rock fragments) in the soil sample cross section. Buchter et al. (1994) recommended that the dry weight of the stony soil REV should be at least 100-times the weight of the biggest solid rock fragment. If the maximum diameter of rock fragments is about 10 cm and their weight about 1.5 kg, then the minimum REV weight should be about 150 kg.

Another difficulty in quantifying hydrological processes in stony soils arises when attempting to measure these processes. The presence of RF causes many practical problems, such as the complications that come up when inserting probes in stony soils or installing lysimeters. Moreover, field measurements encounter a large variability of stony soil characteristics even on small plots, which further complicates soil sampling and infiltration measurements. The use of tracers is difficult in stony soils as well.

An alternative way of quantifying characteristics of stony soils is to separately measure characteristics of both components (a fine soil fraction and rock fragments) and then combine them. This approach was adopted by Bouwer and Rice (1984), Brakensiek et al. (1986), Peck and Watson (1979), and Ravina and Magier (1984). Another approach is to estimate

hydrophysical characteristics of stony soils by numerical modeling. Novák et al. (2011) were the first who used the HYDRUS-2D model in the numerical Darcy experiment. The same approach was later applied by Hlaváčiková et al. (2016) and Beckers et al. (2016). These studies examined the role of stoniness, the size of RF (Novák et al., 2011), and the shape, distribution, and position of RF in the stony soil on saturated (Hlaváčiková et al., 2016) and unsaturated hydraulic conductivities (Beckers et al., 2016).

Stony soils are usually classified according to the relative fraction of rock fragments in soil (soil stoniness) expressed as a relative volume or a relative mass. There are different systems of stony soil classifications. In this study, we applied the *Morphogenetic Classification System of Slovak Soils* (Societas Pedologica Slovaca, 2014). This system classifies stony soils according to a relative volume of RF as follows: slightly stony soils (with the rock fragments relative volume of 5–10 volumetric %), moderately stony soils (with 10–25% of rock fragments), and highly stony soils (with 25–50% of rock fragments). Soils with more than 50% of rock fragments and less than 30% of organic material are classified as psefitic soils. The USDA classification allows classifying soils according to the volume of RF as: 1) nongravelly, noncobbly, nonstony soils and with less than 15% of RF, 2) gravelly, cobbly, or stony soils with 15–35% of RF, and 3) extremely gravelly, extremely cobbly, or extremely stony soils with 35–60% of RF (USDA, 2017). Rock fragments are described by their size (diameter) as gravels (2–75 mm), cobbles (75–250 mm), stones (250–600 mm), and boulders (> 600 mm) (Soil Survey Division Staff, 1993, cit. acc. to Garcia-Gaines and Frankenstein, 2015).

Stony soils represent 30% of soils in Western Europe, 60% in the Mediterranean region (Poesen and Lavee, 1994), and 43% of forest soils in Sweden (Stendahl et al., 2009). In Slovakia, Šály (1978) estimated that up to 80% of Slovak forest soils contain rock fragments. The systematic analysis of agricultural soils across the Slovak territory has shown that 47.2% of Slovak arable soils are classified as stony soils (VÚPOP, 2017).

The main objective of this study was to analyze the extent to which the presence of rock fragments in a stony soil can influence a) the soil water content, b) the water storage in the soil profile, and c) the bottom flux from the soil profile. The second objective was to evaluate the influence of the retention variability of the fine soil fraction on the soil water content, the water storage, and the potential bottom boundary flux. The objectives were achieved using the HYDRUS-1D model (Šimůnek et al., 2013, 2016). The soil hydraulic characteristics and the stoniness were obtained from the Červenec site, located in the Western Tatra Mts., Slovakia (Fig. 1).

MATERIAL AND METHODS

Study site

The study site is located in the Jalovecký creek catchment of the Western Tatra Mountains in Slovakia. Natural conditions in the catchment are typical of the highest part of the Carpathians. The catchment covers an area of 22.2 km^2. Topography is characterized by a mean slope of 30° and the elevation ranges from 800 to 2178 m a.s.l. (the mean elevation of 1500 m a.s.l.). The bedrock is mostly formed by crystalline rocks and

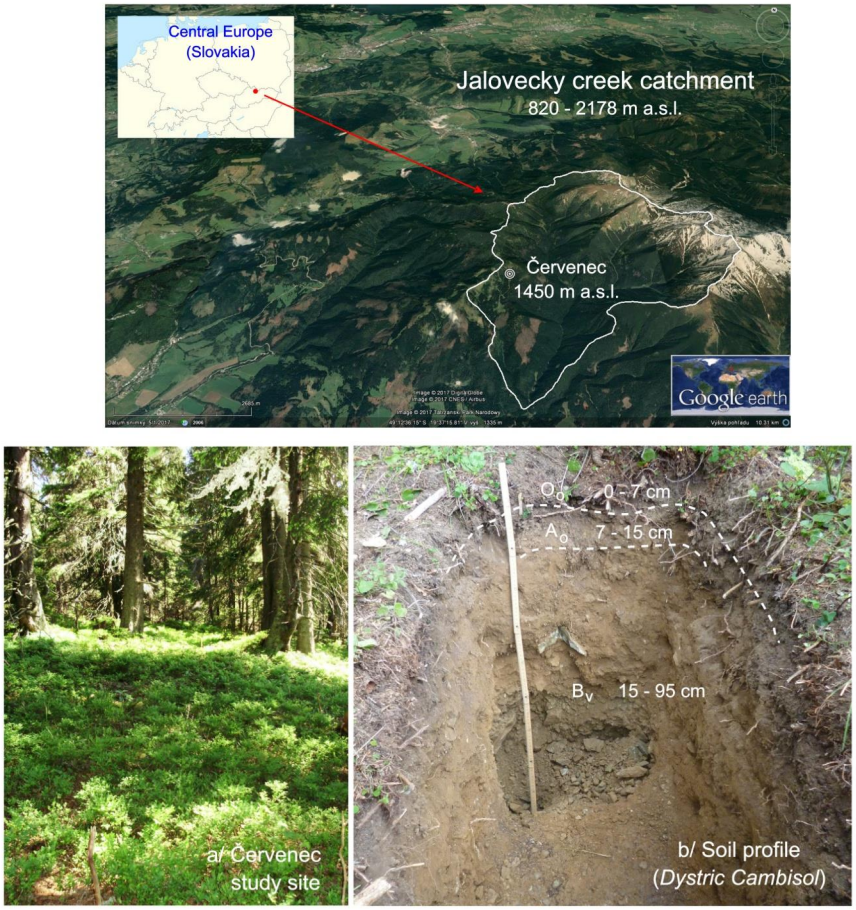

Fig. 1. Location of the study site Červenec and a typical soil profile.

granitoides. Mesozoic rocks dominated by limestone and dolomite occur at some places. Soils are represented by Cambisol, Pozdol, Lithosol, and Leptosol. Their depth is 70–100 cm. The stoniness of the soils is large and varies from 10–65% or more. The topsoil has a high hydraulic conductivity that surpasses the infiltration capacity several times. The Institute of Hydrology systematically has continuously monitored basic water balance components in the catchment, which is supplemented by additional experimental hydrological measurements, since the late 1980s (Holko et al., 2011; Krajčí et al., 2016).

In this study, the soil hydraulic characteristics from the site called Červenec were used for illustrative purposes (Fig. 1). This site is located at an altitude of 1450 m a.s.l. and has a moderately steep terrain (the slope angle is 14°). A moderate-to-high stony shallow soil is typical for the site. The soil type is classified as Cambisol and has a sandy loam texture. Mean air temperature is 3.1°C and mean annual precipitation is 1562 mm. A 130-year old Norway spruce forest (*Picea abies*) and a low crop of *Vaccinium myrtillus* L. grow in the area.

Hydrophysical properties

To model water flow in a stony soil, retention characteristics of the fine soil fraction, the maximum retention capacity of rock fragments, and the stoniness are needed. The stoniness was measured in the soil pit with a 1 m^2 area that was 95 cm deep, extending down to the soil and weathered bedrock interface. Detailed information and results can be found in Hlaváčiková et al. (2015). The soil profile was divided into five layers. The uppermost layer is formed by the organic O_o horizon (0–10 cm). The parameters of this layer remained constant during modeling. The retention parameters of the other four layers (10–40 cm, 40–60 cm, 60–85 cm, and 85–95 cm) were changed according to the stoniness of a particular soil layer. The stoniness, as it was measured in the soil pit, is presented in Table 1.

Since the measurement of the retention capacity of the stony soil would require an excessively large representative elementary volume (REV) of the sample, it was necessary to estimate the effective (bulk) retention properties of the stony soil from the separate retention characteristics of the fine soil fraction and rock fragments. The soil water retention curves (SWRC) for layers containing rock fragments were approximated from the SWRC of the fine soil fraction and measured stoniness R_v using the modified equation of Bouwer and Rice (1984)

$$\theta^b = (1 - R_v)\,\theta^f + R_v \theta^{rf} \tag{1}$$

where θ^b is the effective (bulk) volumetric water content of a stony soil ($cm^3\ cm^{-3}$), θ^f is the volumetric water content of the fine soil fraction ($cm^3\ cm^{-3}$), R_v is the stoniness expressed as the relative volume of RF ($cm^3\ cm^{-3}$), and θ^{rf} is the volumetric water content in the rock fragments. The modification of the Bouwer and Rice equation consisted of adding a term to Eq. (1) representing the retention of rock fragments. Since the rock fragments in the study site were characterized by the low maximum water capacity, a constant value of θ^{rf} (with its maximum of 5 vol. %) was used in the model. The maximum water capacity of RF was determined by the gravimetric method using 20 samples with the size of rock fragments 2–10 cm. The samples were dried at 105°C, weighted, and gradually saturated for up to 7 days until their weight stabilized (Hlaváčiková et al., 2015).

Figure 2a shows measured water retention curves of the fine soil fraction and their approximation using the van Genuchten (1980) formula. The soil water retention curves were measured on undisturbed soil samples with a volume of 100 cm^3. The samples were taken in three replicates from the soil depth of 0–10 cm, representing the forest floor horizon, and in ten replicates from the soil depth of 30–60 cm, representing the fine mineral soil of the remaining part of the soil profile. It was not possible to take undisturbed soil samples from deeper soil depths because of the stoniness. Sampling in the depth of 10–40 was complicated by the large density of tree roots.

Undisturbed samples taken from the soil depths of 30–60 cm did not indicate any relationship between the depth of the soil profile and the shape of the SWRC. The content of rock fragments in the samples was determined after the measurement of soil water retention curves. The average value of the soil

Table 1. The van Genuchten SWRC parameters (θ_r, θ_s, α, n), the saturated hydraulic conductivity K_s, and the soil stoniness R_v. The reference SWRC is the mean SWRC, min and max SWRCs are obtained from the mean SWRC by adding the confidence intervals for particular soil layers.

		Reference SWRC			
Soil depth (cm)	0–10 cm	10–40 cm	40–60 cm	60–85 cm	85–95 cm
θ_r ($cm^3\ cm^{-3}$)	0.05	0.05	0.05	0.05	0.05
θ_s ($cm^3\ cm^{-3}$)	0.600	0.597	0.487	0.323	0.241
α (cm^{-1})	0.043	0.260	0.260	0.260	0.259
n (–)	1.504	1.139	1.139	1.139	1.139
		Min SWRC			
Soil depth (cm)	0–10 cm	10–40 cm	40–60 cm	60–85 cm	85–95 cm
θ_r ($cm^3\ cm^{-3}$)	0.05	0.05	0.05	0.05	0.05
θ_s ($cm^3\ cm^{-3}$)	0.600	0.507	0.416	0.279	0.210
α (cm^{-1})	0.043	0.211	0.211	0.211	0.211
n (–)	1.504	1.149	1.150	1.150	1.150
		Max SWRC			
Soil depth (cm)	0–10 cm	10–40 cm	40–60 cm	60–85 cm	85–95 cm
θ_r ($cm^3\ cm^{-3}$)	0.05	0.05	0.05	0.05	0.05
θ_s ($cm^3\ cm^{-3}$)	0.600	0.687	0.560	0.368	0.273
α (cm^{-1})	0.043	0.299	0.299	0.299	0.299
n (–)	1.504	1.131	1.131	1.131	1.131
R_v ($cm^3\ cm^{-3}$)	0.00	0.00	0.20	0.50	0.65
K_s ($cm\ h^{-1}$)	210	45	45	45	45

Values θ_r, θ_s, K_s correspond to effective parameters ("bulk") in layers with RF.

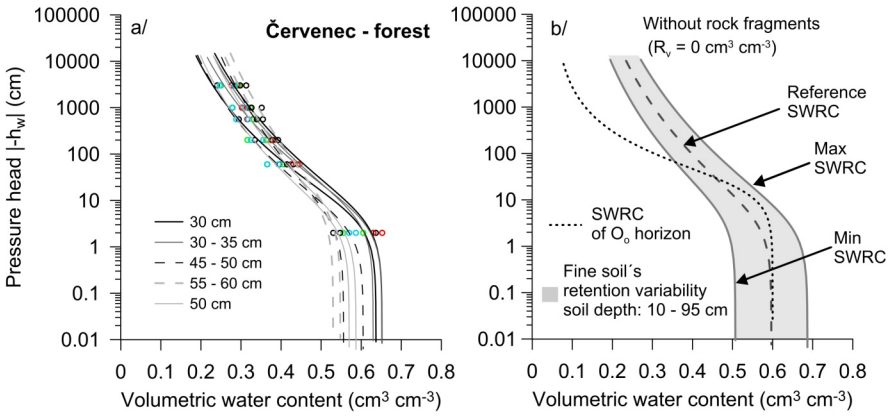

Fig. 2. a/ Measured (circles) and approximated (lines) soil water retention curves (SWRC) from the Červenec site, and b/ the SWRCs with a probability of 95% representing the soil depth of 10–95 cm. A dashed line represents the mean (reference) SWRC of the fine soil fraction; a dotted line corresponds to the SWRC of the organic soil horizon.

sample stoniness was about 12%. According to EN ISO 11274:2014, it is not necessary to modify retention curves of stony soils unless the stoniness exceeds 20%. Therefore, undisturbed samples from the soil depth of 30–60 cm were used to describe water retention of the fine soil fraction. It was also assumed that the retention properties of the fine soil fraction are valid for the soil depths of 10–95 cm and can represent the variability of the soil for given soil depths. The variability of fine soil retention was expressed using the confidence intervals (Fig. 2b), which correspond to the mean values of the volumetric water content ± 2 standard deviations (assuming a Gaussian probability distribution function). The mean SWRC is referred to in the remainder of this paper as the reference SWRC for $R_v = 0$ cm^3 cm^{-3}. The confidence intervals are denoted as min or max SWRC for $R_v = 0$ cm^3 cm^{-3}.

The process of preparation and estimation of retention properties of the fine soil fraction of stony soils can alternatively include the possibility of preparing disturbed soil samples (a fine soil fraction only, i.e., sieved particles with a diameter smaller than 2 mm). This methodology is appropriate when it is not possible to take undisturbed soil samples. However, the structure, and consequently retention properties of these samples, will differ from undisturbed samples and they will closely depend on the method of their preparation.

Figure 3 shows all SWRC used in modeling. The SWRC (the reference function and its confidence intervals) for soil layers containing rock fragments (below a depth of 40 cm) were derived using Eq. (1). They were expressed as the reference SWRC (derived from the mean reference SWRC for $R_v = 0$ cm^3 cm^{-3}) and the confidence intervals (min, max) were derived from the SWRC confidence intervals (min, max SWRC for $R_v = 0$ cm^3 cm^{-3}). Parameters of all soil water retention curves (either reference or confidence intervals) for particular soil depths are in Table 1. Figure 3 shows how the retention of the soil profile decreases with increasing stoniness. The stoniness at soil depths of 40–60 cm was 0.2 cm^3 cm^{-3}, while at depths of 60–85 cm it was 0.5 cm^3 cm^{-3}. The presence of stones in deeper soil layers caused a reduction of the retention capacity of particular soil layers by almost one half.

Two scenarios were considered in the modeling study. Scenario 1 represented a non-stony soil, while scenario 2 represented a stony soil. Hydraulic conductivities for the two scenarios were the same. The saturated hydraulic conductivities of the 0–10 cm and 10–95 cm soil layers were set to mean measured values of 210 cm h^{-1}, and 45 cm h^{-1}, respectively.

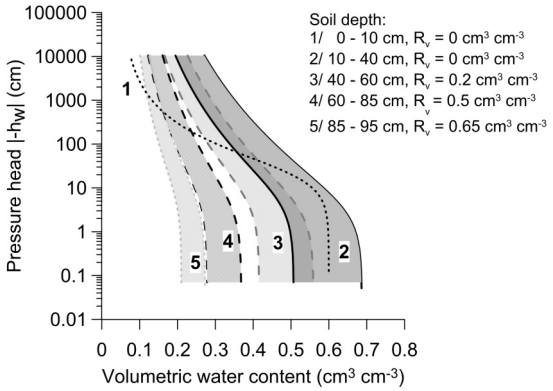

Fig. 3. The soil water retention curve for the organic soil horizon (0–10 cm) (1) and for deeper soil horizons (2–5) corrected according to the soil stoniness R_v (cm^3 cm^{-3}). Shaded areas represent the fine soil water retention variability of a particular soil depth interval.

The saturated hydraulic conductivities were estimated using single ring infiltration measurements and laboratory measurements (Hlaváčiková et al., 2014). The forest floor soil horizon typically has a large infiltration capacity which decreases with the soil depth and the increase in the rock fragments content. This trend has been confirmed using infiltration measurements in several soil profiles at different sites in the catchment (not shown here). As this study focuses primarily on the reduced retention capacity of the stony soil caused by stoniness and its influence on the soil water content and the bottom boundary outflow, hydraulic conductivities remained constant across different stoninesses.

The first set of modeling runs was performed for the 2013 vegetation season (June to September). The model was run using daily values of meteorological data collected at the nearby meteorological station. Throughfall was measured directly at the experimental site. Phenological parameters of the crop present at the site, representing *Vaccinium myrtillus* L., were set as follows: LAI (leaf area index) was 1.07 cm^2 cm^{-2}, the crop height was 30 cm, the root depth was 30 cm, and albedo was 0.2 (–). LAI was set according to the direct measurement of one-sided leaf area of Vaccinium myrtillus for a unit soil surface area (1 m^2). The second set of modeling runs was carried out using 1-minute time steps for the short, extreme rainfall event, which occurred on 14–16 May 2014. Transpiration and evaporation fluxes were neglected in this second scenario.

The bottom boundary condition specified at a depth of 95 cm was a free drainage. This condition was chosen because the rate of water flow on the soil-weathered bedrock interface was not known. It was assumed that all water, which flows through the bottom boundary of the soil, contributes to the formation of subsurface outflow. Simulated soil water contents were compared with measured values to verify that simulated results did not contradict the reality. Soil water contents were measured using the Delta-T devices. A limited set of manual measurements using the Wet-2 sensor was available for a soil depth of 0–10 cm. Continuous measurements by the SM300 sensor were carried out at the soil depth of 40 cm. Finally, the water balance error was checked for both types of modeling runs.

Several assumptions and simplifications were considered for water flow modeling. It was assumed that water flow could be described by the Richards equation in the unsaturated zone of the soil profile and that water flowed only through the soil matrix and preferential flow could be neglected. The single porosity HYDRUS-1D model (ver. 4.17) was used (Šimůnek et al., 2013).

Modeled soil water contents, water storage, and bottom boundary outflows for the stony soil were compared with modeled values for the non-stony soil using the root mean square error (RMSE) and the mean relative error (MRE in %).

RESULTS AND DISCUSSION

The stoniness of the soil profile at the study site Červenec increased with the soil depth. It varied according to soil layers from 0.2 $cm^3 cm^{-3}$ in the soil depth of 40–60 cm to 0.65 $cm^3 cm^{-3}$ in 85–95 cm. The overall average stoniness of the soil profile was 0.28 $cm^3 cm^{-3}$. According to *Morphogenetic Classification System of Slovak Soils* (Societas Pedologica Slovaca, 2014), the soil can be classified as a highly stony soil. The modeling results indicated that the presence of rock fragments caused a substantial reduction in the retention capacity of the soil profile, especially below the soil depth of 60 cm. The simulated and measured volumetric water contents as a function of time in different depths are shown in Figure 4.

The presence of rock fragments in the studied soil profile caused the volumetric water content to decrease on average by 0.06, 0.16, and 0.2 $cm^3 cm^{-3}$ in the soil depths of 55, 75, and 90 cm, respectively (Fig. 4, thicker dashed lines). These values corresponded to a relative decrease by 18–56%. Consequently, the total soil water storage (for the entire stony soil profile) decreased by 7.6 cm (23%). It is worth mentioning that the vegetation growing at the site, namely Norway spruce *Picea abies*, which was not considered in the modeling, is generally characterized as a primary "surface rooter". While this fact was not confirmed in some studies (e.g., Puhe, 2003), most of the root mass is usually not deeper than 40 cm, which can be partially explained by the stoniness of the soil.

The flux at the bottom soil boundary increased or decreased faster in the stony soil than in the non-stony soil, especially during wet periods (Fig. 5). Maximum bottom flux values were larger in the stony soil as well. On the other hand, the simulated bottom flux during the dry period was smaller in the stony soil than in the non-stony soil. This was caused mainly by the smaller water retention of the stony soil. However, cumulative fluxes for the entire vegetative period were not very different for the two soils. Simulated outflows were 161 and 148 mm for the stony and non-stony soils, respectively, which correspond to 38% and 41% of infiltration. It can be expected that these differences throughout the hydrological year will be minimal.

The difference between water dynamics in the stony and non-stony soils was significant, particularly in the short time periods. Water flow was therefore simulated for one real rainfall event (Fig. 6). The outflow from the stony soil was 18% larger than from the non-stony soil during this rainfall event. The outflow coefficients were 69% and 58% for the stony and the non-stony soil, respectively.

With respect to the retention variability of the fine soil fraction, its effect decreased with an increase in the stoniness as expected (Fig. 4, shaded area). The retention variability of the fine soil fraction produced a change in the volumetric water content in the entire soil profile (soil depths of 10–90 cm, not shown here). The largest variability in the range of ±0.06 $cm^3 cm^{-3}$ compared to the reference volumetric water content was in the soil depths with minimum stoniness (10–40 cm). For example, at a depth of 90 cm, this variability was only about ± 0.02 $cm^3 cm^{-3}$ (Fig. 4).

As discussed earlier, it is not easy to estimate effective (bulk) hydrophysical properties of stony soils. The methods used to prepare the samples with the fine soil fraction of stony soils and how their retention characteristics are consequently estimated will affect modeling results. The retention properties of the fine soil fraction can be derived either from undisturbed soil samples (in a case of a small stoniness) or from disturbed samples (in a case of a highly stony soil). It is not known how much the retention properties of the fine soil fraction derived using these two approaches affect modeling results. However, according to our experience, it can be expected that the influence of different methods of estimating retention properties of the soil fine fraction on modeled water contents will decrease with increasing soil stoniness.

The retention variability of the fine soil fraction changed the total soil water storage of the entire soil profile in the range of ±5.2 cm (±15%) in the non-stony soil. The corresponding change in the stony soil was ±3.8 cm, a decrease of 11.5–34%. The effect of the retention variability of the fine soil fraction on cumulative outflow in the non-stony and stony soils varied in the range of 13.9–15.8 cm (±6.7%) and 15.3–17 cm (an increase by 3.3–14.8%), respectively.

Tables 2 and 3 show components of the water balance equation for the vegetative period and for an extreme rainfall event, respectively. The water storage at the beginning and the end of the simulated period are shown as well.

Properties of stony soils are a result of mutual interaction among factors in a complex soil system. Modeling of water flow in stony soils requires several simplifications and approximations, such as the assumption of laminar water flow expressed by the Richards equation or in the case of this study, neglecting of preferential flow (PF). The presence of PF is certainly a very important phenomenon, especially in forest and mountain soils. In the case of stony soils, a special type of macropores, called lacunar pores, can occur at the interface of rock fragments and the fine soil fraction. However, the parameters describing these processes, such as the fraction of water flow transported by preferential pathways in the stony soil or the rate of the water flow exchange between slower and faster flow areas in the stony soil, were not available. This is a great challenge for further research. However, it should be emphasized that the goal of this study was to estimate the influence of the reduced retention capacity of stony soils by the presence of RF on the soil water dynamics. Preferential pathways are not only caused by the presence of rock fragments, but also by different biological, geochemical, and hydrological processes taking place in soils. PF together with the presence of rock fragments in stony soils affects the water storage and, consequently, soil water dynamics.

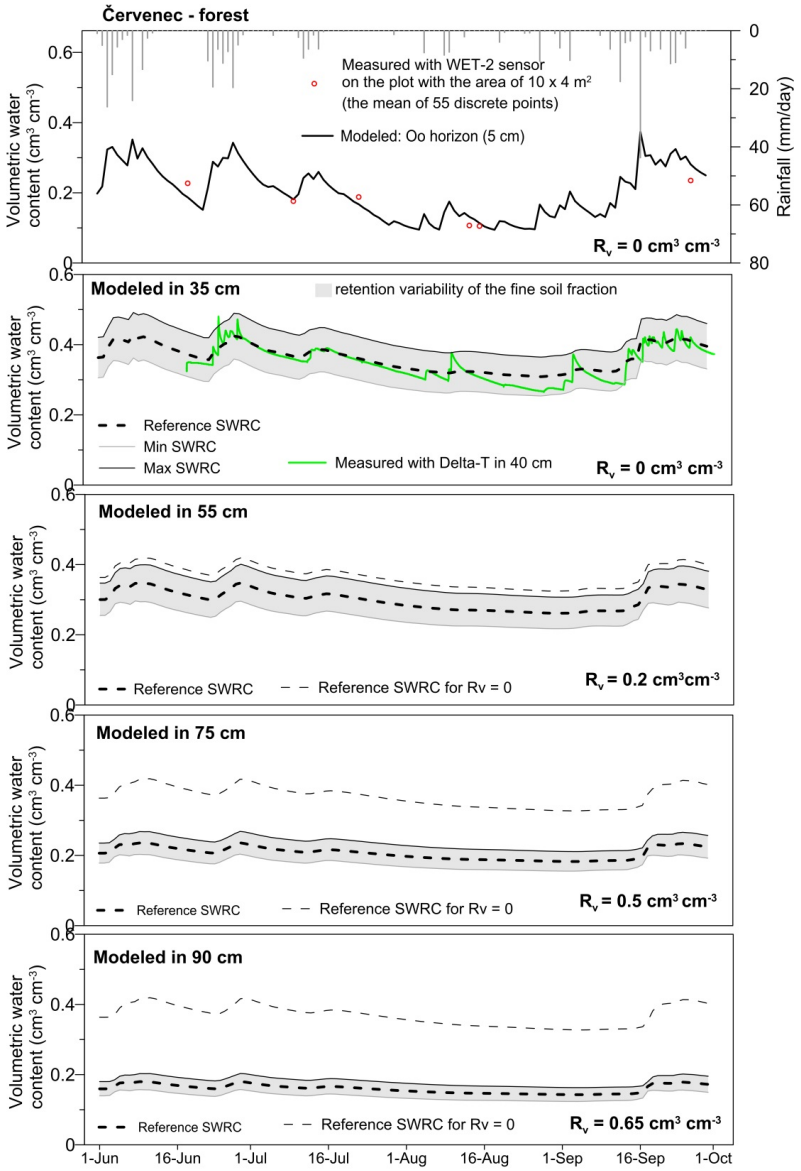

Fig. 4. Precipitation (top), and measured and simulated volumetric water contents in the stony soil profile. Simulations considered the variability of the fine soil water retention (shaded area). The reference SWRC for $R_v = 0$ denotes to the mean SWRC used in the scenario of a non-stony soil (without rock fragments). The reference SWRC for the stony soil ($R_v > 0$) denotes the mean SWRC modified by the stoniness. It indicates the differences in modeled water contents caused by the stoniness (increasing with the soil depth).

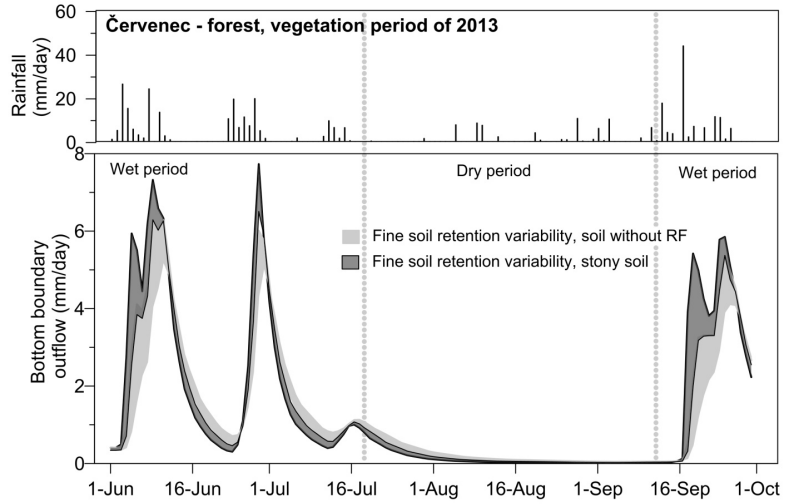

Fig. 5. Precipitation (top) and bottom boundary outflow (at a depth of 95 cm) from the non-stony and stony soil profile. Simulations considered the variability of the fine soil water retention.

Table 2. Components of the soil profile water balance and water storage at the beginning and the end of the simulated vegetative period. Surface runoff did not occur.

01.06. – 30.9.2013	Cumulative infiltration (mm)	Cumulative evaporation (mm)	Cumulative transpiration (mm)	Cumulative bottom boundary outflow (mm)	Outflow as a percentage of infiltration (%)	Initial water storage (01.06) (mm)	Final water storage (30.09.) (mm)	Absolute water balance error (mm)
Non-stony soil, Reference SWRC	380	127	74	148	37.9	328.4	363.6	4
Non-stony soil, Min SWRC	380	124	74	158	40.5	279.5	308.0	3
Non-stony soil, Max SWRC	380	129	75	139	35.7	377.6	418.6	4
Stony soil, Reference SWRC	380	123	74	161	41.2	256.2	281.8	3
Stony soil, Min SWRC	380	120	73	170	43.6	220.8	241.2	3
Stony soil, Max SWRC	380	126	74	153	39.3	292.3	322.7	4

Table 3. Components of the soil profile water balance and water storage at the beginning and the end of the rainfall period, and 7 days after the rainfall onset. Cumulative surface runoff with a value of 0.3 mm was neglected.

May 14 – 16, 2015	Cumulative infiltration (mm)	Cumulative bottom boundary outflow (mm)	Initial water storage (at the rainfall onset) (mm)	Final water storage* (mm)	Absolute water balance error (mm)
Non-stony soil, Reference SWRC					
*/ at the end of rainfall (16 May)	234	74	282	441	1
*/ 7 days after rainfall onset (21 May)	234	138	282	377	1
Stony soil, Reference SWRC					
*/ at the end of rainfall (16 May)	234	111	221	344	0
*/ 7 days after rainfall onset (21 May)	234	163	221	291	1

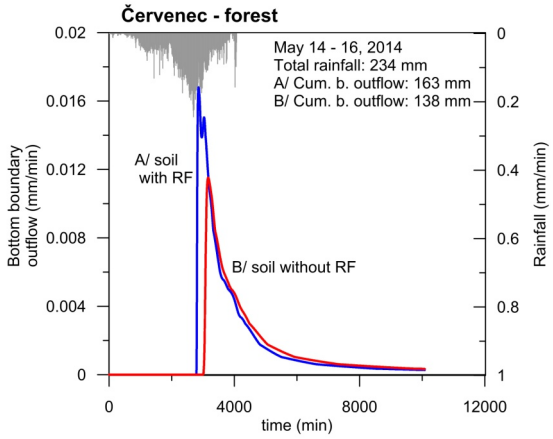

Fig. 6. Extreme rainfall and the bottom boundary flux (at a depth of 95 cm) of the non-stony and stony soil profile.

CONCLUSIONS

The presence of rock fragments in stony soils complicates the measurement of the hydrophysical characteristics of stony soils, which are needed for water flow modeling. The direct measurement of the soil moisture dynamics in stony soils is problematic as well. It may even be impossible in the case of a large stoniness considering the problems with the installation of measurement devices on one hand and the interpretation of measured values on the other. Therefore, using a suitable model as a tool for estimating water dynamics in a stony soil seems to be a promising approach to overcoming these problems.

A simple methodology was used in this study to estimate the effects of rock fragments on the water dynamics in the stony soils and the corresponding soil water storage by water flow modeling. The results of modeling showed that:

1, Neglecting the presence of stones in modeling of water flow in the moderately or highly stony soils can result in a substantial overestimation of the soil water storage.

2, Rock fragments reduce the volume of the soil that is available for water flow and thus speed-up the water dynamics in the stony soils, especially during the short wet periods. Numerical modeling showed that outflow from the stony soils following rainfall is characterized by higher maxima and lower minima compared to the non-stony soils. The stoniness can contribute to the extreme outflows from the catchment.

The response of the stony soils to the rainfall events compared with the response of non-stony soils depends on a number of mutually influencing factors such as the rainfall intensity and duration, the initial soil water content, and the soil profile depth. The stony soil properties, such as the amount, size, and distribution of rock fragments in the soil profile, the retention of rock fragments, the fine soil fraction properties (retention and hydraulic conductivity), the presence of active preferential flow paths, and the bedrock properties can strongly influence outflow formation. The terrain and the bedrock slope will contribute to the soil's response to rainfall events by lateral outflow, especially in the case of less permeable bedrock.

Further research of structured stony soils and the verification of the proposed methodology are highly recommended, as the effects of rock fragments on the hydrological cycle of forested or agricultural stony soils is still often neglected.

Acknowledgement. This contribution was supported by the grant agency of the Slovak Academy of Sciences VEGA, project No. 2/0055/15 and is the result of the project implementation ITMS 26240120004 Centre of excellence for integrated flood protection of land supported by the Research & Development Operational Program funded by the ERDF. Some equipment that provided data for this study was obtained within the framework of European Regional Development Fund Project 26220120062 ‘Centre of excellence for the integrated river basin management in changing environmental conditions’.

REFERENCES

Baker, F.G., Bouma, J., 1976. Variability of hydraulic conductivity in two subsurface horizons of two silt loam soils. Soil Sci. Soc. Am. J., 40, 219–222.

Beckers, E., Pichault, M., Pansak, W., Degré, A., Garré, S., 2016. Characterization of stony soil´hydraulic conductivity using laboratory and numerical experiments. Soil, 2, 421–431.

Bouwer, H., Rice, R.C., 1984. Hydraulic Properties of Stony Vadose Zones. Ground Water, 22, 696–705.

Brakensiek, D.L., Rawls, W.J., Stephenson, G.R., 1986. Determining the saturated hydraulic conductivity of a soil containing rock fragments. Soil Sci. Soc. Am. J., 50, 834–835.

Buchter, B., Hinz, C., Flühler, H., 1994. Sample size for determination of coarse fragment content in a stony soil. Geoderma, 63, 265–275.

Coppola, A., Dragonetti, G., Comegna, A., Lamaddalena, N., Caushi, B., Haikal, M.A., Basile, A., 2013. Measuring and modeling water content in stony soils. Soil & Tillage Research, 128, 9–22.

EN ISO 11274:2014. Soil quality – Determination of the water-retention characteristic – Laboratory methods (ISO 11274:1998+Cor. 1:2009). European Committee for Standardization, CEN-CENELEC Management Centre, Brussels.

Garcia-Gaines, R.A., Frankenstein, S., 2015. USCS and the USDA Soil Classification System: Development of a Mapping Scheme. U.S. Army Engineer Research and Development Center, Vicksburg, 46 p.

Gardiner, B., Blennow, K., Carnus, J., Fleischer, P., Ingemarson, F., Landmann, G., Lindner, M., Marzano, M., Nicoll, B., Orazio, C., Peyron, J.L., Reviron, M.P., Schelhaas, M., Schuck, A., Spielmann, M., Usbeck, T., 2010. Destructive Storms in European Forests: Past and Forthcoming Impacts. Final Report to European Commission. – DG Environment. European Forest Institute, Joensuu, Finland, 138 p.

Hlaváčiková, H., Novák, V., Orfánus, T., Danko, M., Hlavčo, J., 2014. Stony soil hydrophysical characteristics. I. Hydraulic conductivities. Acta Hydrologica Slovaca, 15, 24–34. (In Slovak with English abstract and summary.)

Hlaváčiková, H., Novák, V., Holko, L., 2015. On the role of rock fragments and initial soil water content in the potential subsurface runoff formation. J. Hydrol. Hydromech., 63, 71–91.

Hlaváčiková, H., Novák, V., Šimůnek, J., 2016. The effects of rock fragment shapes and positions on modeled hydraulic conductivities of stony soils. Geoderma, 281, 39–48.

Holko, L., Kostka, Z., Šanda, M., 2011. Assessment of frequency and areal extent of overland flow generation in a forested mountain catchment. Soil & Water Res., 6, 43–53.

Krajčí, P., Danko, M., Hlavčo, J., Kostka, Z., Holko, L., 2016. Experimental measurements for improved understanding and simulation of snowmelt events in the Western Tatra Mountains. J. Hydrol. Hydromech., 64, 316–328.

Kutílek, M., Nielsen, D.R., 1994. Soil Hydrology. Cremlingen – Destedt, Catena Verlag, 370 p.

Lichner, L., 1994. Contribution to the saturated hydraulic conductivity of soils with macropores measurement. J. Hydrol. Hydromech., 42, 421–430. (In Slovak with English abstract.)

Novák, V., Kňava, K., 2012. The influence of stoniness and canopy properties on soil water content distribution: simulation of water movement in forest stony soil. Eur. J. Forest Res., 131, 1727–1735.

Novák, V., Kňava, K., Šimůnek, J., 2011. Determining the influence of stones on hydraulic conductivity of saturated soils using numerical method. Geoderma, 161, 177–181.

Peck, A.J., Watson, J.D., 1979. Hydraulic conductivity and flow in non-uniform soil. In: Proc. Workshop on soil physics and soil heterogeneity, CSIRO Division of Environmental Mechanics, Canberra, Australia.

Poesen, J., Lavee, H., 1994. Rock fragments in top soils: significance and processes. Catena, 23, 1–28.

Puhe, J., 2003. Growth and development of the root system of Norway spruce (*Picea abies*) in forest stands – a review. Forest Ecology and Management, 175, 253–273.

Ravina, I., Magier, J., 1984. Hydraulic conductivity and water retention of clay soils containing coarse fragments. Soil Sci. Soc. Am. J., 48, 736–740.

Šály, R., 1978. Soil – Basic Component of Forest Production. Príroda Publ. House, Bratislava. (In Slovak.)

Šimůnek, J., Šejna, M., Saito, H., Sakai, M., van Genuchten, M.T., 2013. The HYDRUS-1D Software Package for Simulating the One-Dimensional Movement of Water, Heat, and Multiple Solutes in Variably-Saturated Media, Version 4.17. Department of Environmental Sciences, University of California Riverside, Riverside, CA, USA, 308 p.

Šimůnek, J., van Genuchten, M.T., Šejna, M., 2016. Recent developments and applications of the HYDRUS computer software packages. Vadose Zone J., 15, 7. DOI: 10.2136/vzj2016.04.0033.

Societas Pedologica Slovaca, 2014. Morphogenetic Classification System of Slovak Soils. Basal Reference Taxonomy. 2nd revised edition Bratislava: NPPC–VÚPOP Bratislava, 96 p. (In Slovak with English abstract.)

Stendahl, J., Lundin, L., Nilsson, T., 2009. The stone and boulder content of Swedish forest soils. Catena, 77, 285–291.

USDA, 2017. Determination of grain size distribution. http://www.nrcs.usda.gov/wps/portal/nrcs/detail/soils/survey/office/ssr10/tr/?cid=nrcs144p2_074845#item1b. Accessed 20 June 2017.

van Genuchten, M.T., 1980. A closed-form equation for predicting the hydraulic conductivity of unsaturated soils. Soil Sci. Soc. Am. J., 44, 987–996.

VÚPOP, 2017. Representation of stoniness categories in Slovak agricultural soils. http:// www. podnemapy. sk/portal/ reg_pod_infoservis/skelet/skelet.aspx. (In Slovak.)

Wegehenkel, M., Wagner, A., Amoriello, T., Fleck, S., Messenburg, H., 2017. Impact of stoniness correction of soil hydraulic parameters on water balance simulations of forest plots. J. Plant Nutr. Soil Sci., 180, 71–86.

Received 11 May 2017
Accepted 17 August 2017

Note: Colour version of Figures can be found in the web version of this article.

J. Hydrol. Hydromech., 66, 2018, 2, 189–201
DOI: 10.1515/johh-2017-0054

Can a change in cropping patterns produce water savings and social gains: A case study from the Fergana Valley, Central Asia

Akmal Kh. Karimov[1*], Munir A. Hanjra[2], Jiří Šimůnek[3], Botir Abdurakhmannov[4]

[1] International Water Management Institute (IWMI), Central Asia Regional Office, Tashkent, Uzbekistan.
[2] International Water Management Institute (IWMI), Southern Africa Regional Office, Pretoria, South Africa.
[3] Department of Environmental Sciences, University of California Riverside, Riverside, CA, USA.
[4] Tashkent Institute of Irrigation and Melioration, Tashkent, Uzbekistan.
[*] Corresponding author. E-mail: akmalkarimov040@gmail.com

Abstract: The study examines possible water savings by replacing alfalfa with winter wheat in the Fergana Valley, located upstream of the Syrdarya River in Central Asia. Agricultural reforms since the 1990s have promoted this change in cropping patterns in the Central Asian states to enhance food security and social benefits. The water use of alfalfa, winter wheat/fallow, and winter wheat/green gram (double cropping) systems is compared for high-deficit, low-deficit, and full irrigation scenarios using hydrological modeling with the HYDRUS-1D software package. Modeling results indicate that replacing alfalfa with winter wheat in the Fergana Valley released significant water resources, mainly by reducing productive crop transpiration when abandoning alfalfa in favor of alternative cropping systems. However, the winter wheat/fallow cropping system caused high evaporation losses from fallow land after harvesting of winter wheat. Double cropping (i.e., the cultivation of green gram as a short duration summer crop after winter wheat harvesting) reduced evaporation losses, enhanced crop output and hence food security, while generating water savings that make more water available for other productive uses. Beyond water savings, this paper also discusses the economic and social gains that double cropping produces for the public within a broader developmental context.

Keywords: HYDRUS-1D; Food security; Crop evapotranspiration; Water budget; Syrdarya River.

INTRODUCTION

The population of Central Asia doubled during the last 30 years (from 1980 to 2010), thereby increasing the demand for food crops with corresponding implications for water, land, and ecosystem resources. Since the independence of the Central Asian States in 1991, there have been various agricultural policy reforms that included the abolishment of state-planned crop production as well as the implementation of various policies, such as certain cropping patterns, to increase the operational autonomy of farmers and to achieve a range of economic and national political goals. For instance, as they moved from centrally-planned to market economies after the 1990s, the newly independent states reoriented their national agricultural policies toward "grain independency." Ensuing changes in cropping patterns were also thought to promote rural growth, increase farmers' incomes and national food security, as well as to build community resilience against water scarcity and the rising demand for water to grow more food crops. This was prioritized by the end of the 1990s by shifting from a cotton (6-year)/alfalfa (3-year) crop rotation to a cotton (2-year)/winter wheat (2-year) sequence. Various studies showed that such interventions impacted food production and consumption, as well as public welfare (Anderson, 2007) and ecosystem services (Spoor, 1998). The changes in cropping patterns from alfalfa to wheat reduced the irrigation water demand. Reducing water diversions for irrigation in the Fergana Valley also resulted in reduced return flow to the river system. In addition, the competition for water between upstream hydropower and irrigation caused an unpredictable inter-seasonal and long-term variability of Syrdarya River flow rates. The many factors involved made it difficult to precisely evaluate the impact of changes in the cropping pattern on water resources available for downstream users.

Two aspects of the cropping changes require clarification: the magnitude of water savings, and likely socioeconomic gains of the changes to the public. In this paper, water savings are defined as the reallocation of water from a current use that produces low, negligible, or negative benefits, to those that generate higher benefits (Molden, 1997; Seckler 1996). Managing the irrigation demand by reducing the beneficial use in agriculture may not always bring real water savings (Ward and Pulido-Velazquez, 2008). It may result in lowering the productivity of the use of thermal and land resources, affecting instream use values (Ward and Booker, 2003), increasing salinity (Khan and Hanjra, 2008), and negatively impacting ecosystem health (Karimov et al., 2014), but it may also deliver other socioeconomic benefits including incomes, employment, revenue, and gains in food security (Molden et al., 2010) for both rural and urban consumers. This highlights the necessity to quantitatively assess the impact of cropping changes beyond land and water savings and to consider also other social gains to the wider public. This paper thus analyzes the effect of water savings and socioeconomic gains due to the replacement of alfalfa by winter wheat within the context of agricultural policy changes that were implemented since 1992 in the Fergana Valley, upstream of the Syrdarya River basin in Uzbekistan.

Irrigated agriculture (0.9 million ha) in the Fergana Valley represents an example of large-scale irrigation in Asia. The valley has enormous potential for food crop production. For instance, the valley receives thermal resources with a capacity to evaporate about 10,000 Mm^3 yr^{-1} of water (Karimov et al., 2012). Irrigated crops grown in the valley have the potential to utilize 70–80% of received solar energy if crop growth is not constrained by water deficits or other agronomic and economic factors. However, actual evapotranspiration is much less and ranges from 5,500–6,500 Mm^3yr^{-1}, of which only 70% is transpired by crops (Karimov et al., 2012). While utilizing only 38–

45% of available energy, farmers of the Fergana Valley produce over 0.85 million tons (Mt) of cotton, 1.3 Mt of wheat, and 1 Mt of vegetables and other agricultural commodities. Current production could be increased twofold if thermal, land, and water resources are used in the most productive way. In order to achieve this, it is important to reallocate water from uses that produce low or no benefits to those that generate higher benefits (Molden, 1997; Molden and Sakthivadivel, 1999), and thus improve water productivity, achieve more welfare per drop of water (Giordano et al., 2017; Molden et al., 2010), and contribute towards building community resilience and enhancing water, food, and energy security (Hanjra and Qureshi, 2010; Jalilov et al., 2013; Karimov et al., 2017).

A centerpiece of the applied agricultural policies was the replacement of cotton/alfalfa crop rotation, which dominated in the Fergana Valley in the past, with a cotton/wheat sequence that should increase grain production and reduce cotton-grown areas by allocating these lands to vegetables. Unfortunately, additional opportunities for crop intensification through double cropping, such as growing green gram or other food legume crops on the fallow land after harvesting winter wheat, did not receive state policy support.

Green gram (*Vigna radiata* L.) is an important food legume in some parts of Central Asia, including the densely populated Fergana Valley and the Tashkent region. Adoption of green gram may offer important welfare benefits to rural areas (Mavlyanova and Sharma, 2015; Verkaart et al., 2017). The green gram cropping season is short and ranges from 90-120 days, depending on the variety (Mavlyanova and Sharma, 2015). Since the harvesting season of winter wheat in the study area ends by June 20 and the next sowing season starts on October 1, short-duration varieties of green gram can be grown between these dates during the summer season. However, due to shortage of water for irrigation of cotton from June to August, policy makers restricted double cropping during the summer season to "save" water for irrigation of cotton. As a consequence, green gram prices in local markets have risen, in some years reaching $1–2 per kg (U.S. Dollars). Gram is also a very nutritious source of protein for human consumption and a key ingredient of animal feed. It is a leguminous crop that can improve soil carbon and nitrogen fixation, enhance soil fertility (Gan et al., 2010), and reduce costs of nitrogen fertilizers and their negative impacts on waterways and the ecosystem (Evans et al., 2012; Huang et al., 2017). These multitudes of benefits thus motivated our choice of modeling green gram (or other pulse crops/legumes) as a second crop in order to contribute to the discussion on sustainable crop intensification as well as related policy and institutional support measures in the region.

The shift in cultivation from alfalfa to winter wheat was attractive to policy makers for several reasons, particularly as a measure to achieve grain independency and as a low investment strategy to bring rapid results by decreasing irrigation water demands. However, real water savings due to a decrease in the irrigation water demand were often only assumed rather than empirically demonstrated (Awan et al., 2017; Cai et al., 2002; Nandalal and Hipel, 2007) in a post-policy implementation context and with associated socioeconomic benefits such as gains in national revenue, farmers income, employment, food security, and livelihood. Although further increases in crop output via intensification through double cropping and corresponding social gains are possible through supportive policy changes, they have not been examined in the literature. Therefore, the objectives of this paper were twofold: 1) to estimate water savings and socioeconomic gains from the replacement of alfalfa with winter wheat, and 2) to test double cropping as a strategy for increasing water savings and socioeconomic gains due to changes in the cropping pattern through further agricultural reforms.

This study uses the HYDRUS-1D (Šimůnek et al., 2008) software to simulate crop transpiration and evaporation from the alfalfa, winter wheat/fallow and winter wheat/green gram double cropping fields. The central thrust of our analysis is to examine double cropping by using the winter wheat/green gram cropping system as an example, thus contributing to the discussion on further reforms and liberalization of the agricultural policies. We analyzed three alternative irrigation regimes: full irrigation (FI), high-deficit irrigation (HDI), and low-deficit irrigation (LDI), all under deep and shallow water table conditions in the Fergana Valley. Silt loam soils, which dominate in the central part of the valley, were selected for this analysis. The results of this modeling exercise could contribute to the discussion on policy options available for enhancing the food security and social gains in other large irrigation systems and river basins that are prone to water scarcity and are facing resilience and sustainability challenges similar to the Fergana Valley.

METHODS AND DATA

Study area

The Fergana Valley is located upstream of the Syrdarya River and is a part of three countries of Central Asia: Kyrgyzstan, Tajikistan, and Uzbekistan. The climate is semi-arid with a low quantity of precipitation and high summer temperatures. Annual precipitation varies from 100 to 250 mm in the central part of the valley and increases to 300 mm in the piedmont areas. The mean average temperature is 14°C, the average minimum temperature –18°C, and the average maximum temperature +45°C. The altitude increases from west to east from 330 m above sea level (a.s.l.) to 600 m a.s.l. The valley is filled with alluvial deposits washed out by multiple rivers in the mountain zone. Rivers in the Fergana Valley are divided into four types according to the source of water: glacier-snow, snow-glacier, snow, and snow-rain (Shultsc, 1949). The glacier and snow-fed river systems have maximum high flows from July through August, the snow and glacier-fed river systems from May through June, the snow-fed river systems from April through May, and the snow and rain-fed river systems in April. Three zones representing hydrogeological conditions of the Fergana Valley are a groundwater natural-recharge zone (Zone A), a groundwater springs zone dominated by upward fluxes (Zone B), and a groundwater discharge zone (Zone C), as shown in Fig. 1 (Borisov, 2007; Mirzaev, 1974). These hydrogeological conditions favor the use of fresh groundwater. However, groundwater is used in a few areas only to supplement canal irrigation. As a consequence of underutilization of groundwater, about 200,000 ha of the irrigated land have a relatively shallow water table (less than 2 m below the soil surface), which causes at times secondary salinization. As a result, over 55% of irrigated soils are prone to salinity, including 71,922 ha of highly saline lands in the hydrogeological Zone C. A detailed description of soils of the study area is given by Shreder et al., (1977) and Talipov (1992).

Two main time periods can be identified in the recent history of crop cultivation in the Fergana Valley. Until the early 1990s, cotton/alfalfa crop rotation dominated the irrigated lands. Fig. 2 shows that in 1992, the areas under cotton and alfalfa were 39% and 20% of the total irrigated area, respectively, while winter wheat was grown only on 8% of the irrigated area. The irrigation demand of the Fergana Valley at the time was about

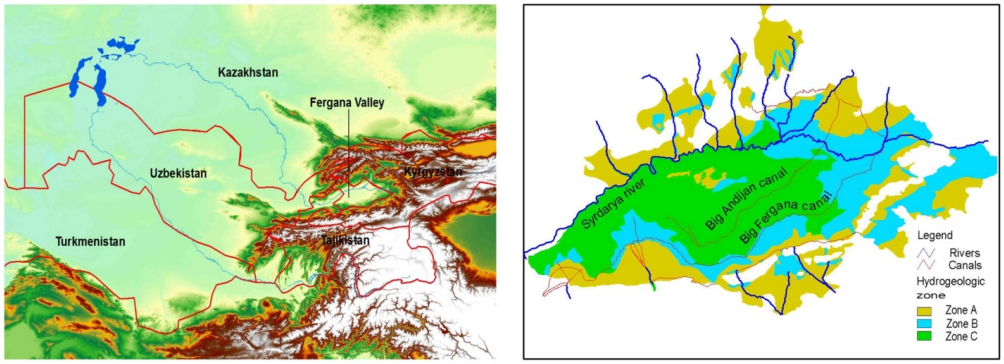

Fig. 1. (a) The Aral Sea basin and (b) hydrogeological zones of the Fergana Valley.

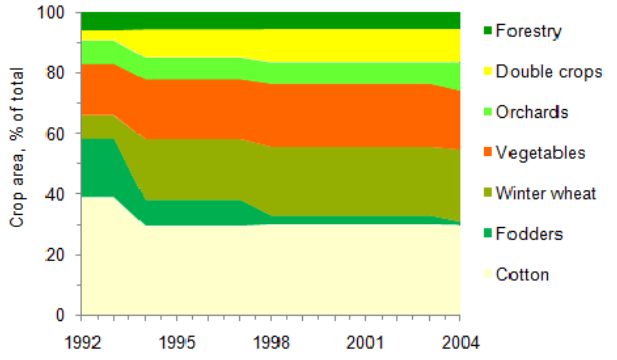

Fig. 2. Changes in the cropping patterns in the Fergana Valley.

12,000 Mm^3 yr^{-1}, with plentiful water available for crop production. As the Central Asian States moved from centrally planned to market economies, various agricultural reforms, including changes in cropping patterns, were implemented. After 1995, the dominant cotton/alfalfa crop rotation in the region was replaced by a cotton/wheat sequence due to the national policy of increasing grain production and enhancing food security. The area under irrigated winter wheat was increased to 27%, while the area under alfalfa was reduced to just 1% of the total irrigated area. Also, the cotton-grown area was reduced by another 47,348 ha, mostly replaced by the cultivation of vegetables. Currently, two main crops, cotton and winter wheat, occupy about 54% of the irrigated lands of 900,000 ha. Farmers sow winter wheat in early October and harvest it in June, and sow cotton in April and harvest it in September-October. As a result of the cropping changes, the irrigation demand in the Fergana Valley was reduced by about 800 Mm^3yr^{-1}.

The changes in the cropping pattern had two main national policy goals: (1) to increase the production of grain crops and therefore to gain independency and national food security, and (2) to reduce the consumption of water per unit of crop production (i.e., to increase water productivity and address water scarcity). The first objective was easily achieved thanks to the expansion of the area allocated to winter wheat, coupled with an increase in average wheat yield from 2 to 5 t/ha. The achievement of the second objective (i.e., increasing water productivity) was not straightforward due to the wide extent of shallow groundwater, which resulted in upward fluxes into the crop root zone, and consequently non-consumptive evapotranspiration and water losses from fallow land after winter wheat harvesting. Sustainable management of the shallow water table and cropping changes are thus key to improving water productivity and food security.

HYDRUS-1D simulations

The HYDRUS-1D software package (Šimůnek et al., 2008; 2016) was used to estimate crop transpiration and soil evaporation, as well as to examine the effects of policy/crop changes on potential water savings. HYDRUS-1D is a finite-element numerical model that simulates the one-dimensional movement of water, heat and multiple solutes in variably-saturated porous media. The model has been previously used and verified in a number of studies modeling the contribution of shallow groundwater to root water uptake and crop evapotranspiration (e.g., Forkutsa et al., 2009; He et al., 2017; Hernandez, 2001; Li et al., 2015; Sanchez et al., 2003; Shouse et al., 2011; Soylu et al., 2011). For instance, Forkutsa et al. (2009) simulated soil water dynamics and transport of salts in plots with irrigated cotton influenced by a shallow groundwater, while Shouse et al. (2011) analyzed root water uptake from a shallow saline groundwater. Li et al. (2015) similarly studied the dynamics of soil water, soil salinity, and depths to the groundwater table as affected by root water uptake of Chinese tamarisk. He et al. (2017) further used HYDRUS-1D to simulate the irrigated winter wheat/summer maize rotation system in the North China Plain for a total of 15 years. One of the advantages of the model for our study is that it provides estimates of upward fluxes from a shallow groundwater table during deficit irrigation (e.g., Karimov et al., 2014).

The HYDRUS-1D model simulates variably-saturated water flow by solving the Richards equation written as:

$$\frac{\partial \theta}{\partial t} = \frac{\partial}{\partial z} K \left(\frac{\partial h}{\partial z} + 1 \right) - S \qquad (1)$$

where θ is the volumetric water content (cm^3/cm^3), t represents time (day), z is the vertical coordinate (positive upward) (cm), h denotes the pressure head (cm), K is the unsaturated hydraulic conductivity (cm/day), and S is the soil water extraction rate by plant roots (cm^3/cm^3/day).

HYDRUS-1D used the Penman-Monteith equation (Allen et al., 1998) to estimate evapotranspiration rates. We used the model to first estimate evapotranspiration, soil evaporation, and crop transpiration for alternative cropping systems for different irrigation scenarios. Then, based on the results of these simulations, we compared water savings, crop yield, and water productivity of alternative cropping systems. The following indicators were evaluated for each cropping pattern: water resources available for reallocation (WR), water savings (WS), and changes in productive water use (PW), all given in mm over the cropping season. Water resources available for reallocation, WR_a, were estimated as follows:

$$WR_a = ET_{a.a} - ET_{a.w} \quad (2)$$

where $ET_{a.a}$ is the estimated actual evapotranspiration from the alfalfa field, and $ET_{a.w}$ the estimated actual evapotranspiration for the alternative cropping system.

Water savings, *WS*, were estimated as follows:

$$\begin{aligned} WS_{a.wf} &= E_a - E_{wf} \\ WS_{a.wg} &= E_a - E_{wg} \end{aligned}, \quad (3)$$

where $WS_{a.wf}$ are water savings obtained by replacing alfalfa with the winter wheat/fallow system, $WS_{a.wg}$ are water savings obtained by replacing alfalfa with winter wheat/green gram double cropping, E_a is soil evaporation from the alfalfa field, E_{wf} is soil evaporation from the winter wheat/fallow field, and E_{wg} is soil evaporation from the winter wheat/green gram double cropping field.

Water resources, gained by shifting from alfalfa to alternative cropping systems, represent a sum of changes in non-productive evaporation and productive crop transpiration. Water savings account for only a fraction of released water resources (i.e., non-productive evaporation) and ignore the reduction in productive water use. Changes in productive water use were estimated as the difference in transpiration between alfalfa and the alternative crop fields:

$$\begin{aligned} PW_{a.wf} &= T_a - T_{wf} \\ PW_{a.wg} &= T_a - T_{wg} \end{aligned}, \quad (4)$$

where $PW_{a.wf}$ and $PW_{a.wg}$ are the productive water reductions as a result of replacing alfalfa with the winter wheat/fallow and winter wheat/green gram double cropping systems, respectively, while T_a, T_{wf} and T_{wg} represent crop transpiration from the alfalfa, winter wheat/fallow and winter wheat/green gram cropping systems, respectively.

The yield of alternative cropping systems was estimated using FAO's expression for the yield response to *ET* (Doorenbos and Kassam, 1979):

$$\left(1 - \frac{Y_a}{Y_x}\right) = k_y \left(1 - \frac{ET_a}{ET_x}\right) \quad (5)$$

where Y_x and Y_a are the maximum and actual yields (kg/ha), respectively, ET_x and ET_a are crop evapotranspiration for no water stress conditions and actual evapotranspiration (mm), respectively, and k_y is a yield response factor representing the effect of a reduction in evapotranspiration on yield losses. For winter wheat/green gram double cropping, the wheat equivalent yield of green gram was calculated on the basis of average prices of green gram and wheat grain. The yield response factor was adopted as follows: 1.1 for alfalfa, 1.0 for winter wheat, and 1.15 for green gram (Doorenbos and Kassam, 1979). The water productivity (*WP*) was then calculated using the following relationship:

$$WP = \frac{Y_a}{ET_a} \quad (6)$$

The revenue from the cultivation of alfalfa was computed by multiplying the average local price with the yield of alfalfa hay, while the same was done for wheat/green gram. The economic water productivity of alfalfa was calculated by multiplying the water productivity with the average local price of alfalfa hay, with again the same procedure applied to wheat/green gram.

HYDRUS-1D input parameters

The soil profile was assumed to be 300 cm deep. Soil textures and soil bulk densities were determined on soil samples collected in 2006 from a field in the Kuva district at soil depths of 0–30, 30–60, 60–90, 90–120, 120–180, and 180–300 cm. Soil water contents were determined before sowing of winter wheat in the same soil profile. The soil texture throughout the entire soil profile was found to be silt loam according to the USDA classification. For the purpose of numerical modeling, the soil profile was divided into six soil horizons that were characterized by four soil materials, determined based on the soil description.

The van Genuchten-Mualem model (van Genuchten, 1980) was selected for the soil water retention curves and unsaturated hydraulic conductivity functions. Simulations were run without considering hysteresis. Initial values of the van Genuchten–Mualem parameters of each soil layer were taken from the HYDRUS-1D database for silt loam. These parameters were then calibrated using an inverse analysis of data from the lysimeter study carried out earlier in the same area by Ganiev (1979). The lysimeters, having a 1.44 m^2 surface area, were packed with a monolithic silt loam soil, and sown with cotton. The groundwater table in the lysimeters was kept at constant depths of 1.5, 2, 2.5, and 3 m below the soil surface. Soil water contents before the growing season, along with the climate and cotton phenology parameters, were used as input to the model. Daily estimates of upward fluxes from the groundwater table and soil water contents during the growing season, found in the lysimeter study, were used to define the objective function for the inverse analysis. The inverse simulation period spanned 365 days and the model calibration consisted of several steps. First, the van Genuchten-Mualem parameters of the two upper soil layers were optimized while they were kept constant for the two lower soil layers. Then, parameters of the upper two soil layers were updated and kept constant, while they were optimized for the lower two soil layers. This procedure was repeated several times until differences between measured and simulated values stopped decreasing. The final root mean square errors (RMSE) and the relative mean absolute errors (RMAE) between measured and simulated values were relatively low and equal to 0.0199 cm and 1.48%, respectively. The correlation coefficient between simulated and measured values (r) was 0.927. The final inversely estimated van Genuchten-Mualem parameter values of each soil layer are presented in Table 1, in which θ_{res} is the residual water content, θ_{sat} is the saturated soil water content, a and n are shape parameters, K_s is the saturated hydraulic conductivity, and l is the pore-connectivity parameter.

The upper boundary condition was defined using the atmospheric boundary condition at the soil surface in terms of observed daily precipitation (Fig. 3) and calculated potential evapotranspiration rates, the later depending upon the selected cropping system. The lower boundary condition consisted of time-variable daily pressure head values representing the position of the groundwater table. Root water uptake was simulated using the approach of Feddes et al. (1978), with water stress parameters for the crops (Table 2) taken from the HYDRUS-1D database (Taylor and Ashcroft, 1972; Wesseling et al., 1991). Our analysis did not consider the effects of solute stress on root water uptake. While dissolved solids in groundwater within the irrigated zone were about 3000 mg/l, and some salt accumulation

Table 1. van Genuchten-Mualem parameters for soil hydraulic properties.

Soil layer, cm	0–60	60–120	120–180	180–300
Soil type/Parameters	Silt loam	Silt loam	Silt loam	Silt loam
θ_{res} [cm^3/cm^3]	0.038	0.0010	0.0012	0.0010
θ_{sat} [cm^3/cm^3]	0.407	0.250	0.301	0.336
α [1/cm]	0.024	0.014	0.0016	0.0157
n [–]	1.43	5.16	1.65	1.73
K_s [cm/d]	11.4	1.08	27.6	4.48
l [–]	0.00055	0.054	0.0098	0.0065

Table 2. Root water uptake: water stress response parameters (Feddes et al., 1978; Šejna et al., 2012) used in the HYDRUS model.

Root water uptake parameters	Unit	Alfalfa	Winter wheat	Green gram
PO	[cm]	0	0	–15
POpt	[cm]	–1	–1	–30
P2H	[cm]	–1500	–500	–750
P2L	[cm]	–1500	–900	–2000
P3	[cm]	–16000	–16000	–8000
r2H	[cm/day]	0.5	0.5	0.5
r2L	[cm/day]	0.1	0.1	0.1

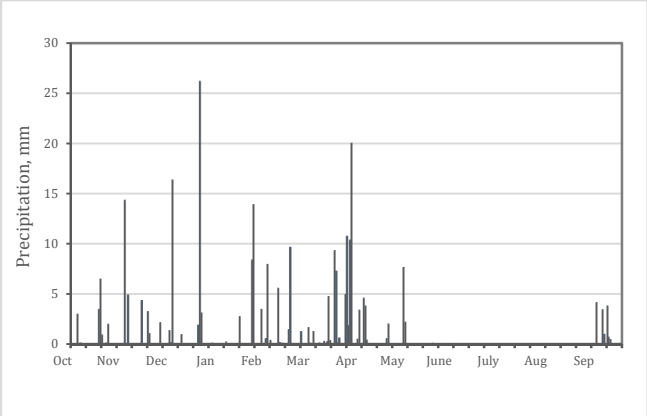

Fig. 3. Precipitation in the Fergana Valley from 1 October, 1994 to 1 October, 1995.

must have occurred in the soil as a result of upward flow from the water table, we decided to focus in our current study only on water stress effects. The effects of salinity stress likely would not change the main conclusions of this study, at least qualitatively, while we recognize that follow-up studies could benefit from a more precise analysis that considers the combined effects of water and salinity stress on root water uptake.

Crop development was accounted for in the model using a daily crop height, a rooting depth, and a soil cover fraction. (Table 3). These parameters, especially the maximum rooting depth, may vary for different scenarios with different irrigation regimes and groundwater depths (Foxx et al., 1982; Grismer, 2015). Unfortunately, little data are available about root development in the presence of shallow groundwater. Considering these limitations, the parameters were selected to be conservative and assumed applicable for the range of conditions simulated by the model.

Climate data, including daily maximum and minimum temperatures, relative humidity, sunshine hours, rainfall, and wind speed, were measured at the Fergana weather station located at a longitude of 71.75^o, a latitude of 40.38^o, and an elevation of 547 m a.s.l. Climate data were used from March 1994 to October 1995 with crop growing seasonal totals, representing long-term average. Using these parameters, simulations were carried out for periods of 365 days consistent with the cropping seasons.

Simulated scenarios

Three following scenarios were analyzed:

Scenario A: Cultivation of alfalfa. Four irrigation regimes were considered: full irrigation (FI) with pre-irrigation soil moisture contents at 70% of soil field capacity (Shreder et al., 1977); low deficit irrigation (LDI) by reducing irrigations by 25%; high deficit irrigation (HDI) by reducing irrigations by 50%; and rainfed conditions without supplemental irrigation. Four groundwater table depths (of 3, 2.5, 2, and 1.5 m) were considered further for each irrigation regime to examine the effects of water table depth on water use of alfalfa. Irrigation applications (including precipitation) were 722–929 mm under full irrigation, 600–757 mm under LDI, 477–582 mm under HDI, and 232 mm under rainfed conditions. The selected irrigation rates for shallow groundwater conditions took into consideration upward fluxes as determined in the lysimeter study of Ganiev (1979). Higher irrigation rates were chosen for the deep groundwater conditions having small upward fluxes and lower rates for shallow groundwater conditions with their large upward fluxes. The simulated period for alfalfa was from March 1 to February 28 of the following year.

Scenario B: Winter wheat and land fallowing. After harvesting winter wheat in mid-June, the field was kept fallow until October. The same four irrigation regimes and groundwater table depths as for alfalfa were considered also for winter wheat. Irrigation applications were again reduced for the higher water tables. Irrigation applications were 419–609 mm under FI, 349–524 mm under LDI, 265–434 mm under HDI, and 185 mm rainfall for rainfed conditions. Simulations for winter wheat covered the period from October 1 to September 30 of the following year. Daily precipitation and potential evaporation rates (the latter when precipitation was zero) were used as an atmospheric boundary condition for land fallowing from June 15 to September 30.

Scenario C: Winter wheat followed by green gram (double cropping). The irrigation regime for winter wheat was the same as for the previous scenario, while for green gram we implemented the irrigation scheme considered by Webber (2008).

Table 3. Main crop parameters for alfalfa, winter wheat, and green gram cultivated in the Fergana Valley*.

Crop parameters	Unit	Alfalfa	Winter wheat	Green gram
Crop height, max	cm	68	100	40
Root depth, max	cm	120	100	60
LAI/Crop cover, max		–/1.0	–/0.98	4.2/–
Crop vegetation season		6/03–1/11	4/10–10/06	14/06–1/10
Crop harvesting		17/05; 28/06; 19/08; 1/10	10/06	24/09–1/10
Yield, max	t/ha	33	5.5	2

*Data compiled from Edgorov et al. (2006), Sumochkina et al. (1977), Webber (2008), Allen et al. (1998, 2005), Smeal et al. (1991), and Sommer et al. (2013).

Total irrigation applications for the winter wheat/green gram system were 652–847 mm under FI, 587–762 mm under LDI, 503–672 mm under HDI, and 423 mm for rainfed winter wheat followed by the irrigated green gram. Higher irrigation rates were used again for deep groundwater conditions with low values of upward fluxes and lower rates for shallow groundwater conditions with their higher upward fluxes. The calculated period for the winter wheat/green gram system was from October 1 to September 30 of the following calendar year.

The FAO Excel sheet (Allen et al., 1998) was used for specifying irrigation schedules, dates, and application rates for each crop and simulated groundwater depth using values of the upward fluxes obtained from the lysimeter study discussed above (Ganiev, 1979). Upward fluxes in the lysimeter studies were available only for rainfed conditions. HYDRUS-1D hence used daily irrigation rates from the FAO Excel sheet as input, and then estimated upward fluxes, crop transpiration and evaporation for each irrigation regime and groundwater depth. This is a more accurate approach than the FAO approach since the HYDRUS-1D simulations consider soil texture and soil moisture changes with depth.

The simulation period was the same for all scenarios, i.e., 365 days. However, wheat is sown in the region at the beginning of October and harvested in mid-June, while alfalfa is sown at the beginning of March. We thus followed local farming practices in the region. Values of total irrigation, taken for conditions with a deep groundwater level, were reduced for shallower groundwater tables following locally adopted recommendations. Farmers often irrigate crops based on water availability, which may deviate from crop irrigation requirements (Reddy et al., 2012) and indicate the need for revising current irrigation scheduling practices.

Within the context of policy/crop changes, the following scenarios were conceptualized:

- Scenario A represents policy conditions *before* the mid 1990s when alfalfa was cultivated in rotation with cotton.
- Scenario B represents policy conditions *after* the 1990s when winter wheat replaced alfalfa and double cropping was restricted by the policy to "save" irrigation water for the cultivation of cotton.
- Scenario C analyzes the potential *future* water use of a double cropping system, i.e., a policy option currently under consideration, but still inactive in the region.

RESULTS AND DISCUSSION

We modeled three cropping scenarios, three alternative irrigation water management regimes and rainfed cropping conditions, and four positions of the groundwater table, as outlined above. Our goal was to evaluate the impact of different cropping scenarios on irrigation water requirements and water use in order to identify the pathways and policy options for improving water productivity and enhancing food security. The results for various cropping scenarios are discussed below.

Water resources available for reallocation

Estimates of actual evapotranspiration (ET_a) as affected by the alternative cropping systems are given in Table 4. The estimates for alfalfa show that actual evapotranspiration ($ET_{a,a}$) is in the range of 792–905 mm under FI, 760–880 mm under LDI, 690–837 mm under HDI, and 444–654 mm for rainfed conditions. Higher values of $ET_{a,a}$ were obtained for shallow water table conditions and lower values for deep water table conditions (Scenario A). Under shallow groundwater conditions, crop roots are expected to obtain more water due to capillary rise. This is supported by, among others, a lysimeter study by Soppe and Ayars (2002) who found that a small portion of the root zone of safflower closest to the water table extracted a significant amount of groundwater. Higher soil moisture contents in the crop root zone under shallow water table conditions, as compared to deep groundwater conditions, lead hence to higher transpiration and evapotranspiration rates, especially for alfalfa with their deep dense rooting system.

For the winter wheat/fallow system, differences in crop $ET_{a,wf}$ for different groundwater depths were less obvious under full irrigation, but increased with more deficit irrigation. Changes in ET_a were the result of increasing evaporation from the fallowed land after winter wheat harvesting. From June 15 through September 30, higher evaporation losses were estimated under shallow groundwater conditions than for deep water tables. Liu and Luo (2011) similarly found that ET_a of winter wheat declined with a lowering of the water table. Differences in ET_a for different water table depths were due to the contributions of groundwater to evapotranspiration.

Overall, the shift from alfalfa to the winter wheat/fallow system (Scenario B) reduced ET_a by 216–283 mm under FI, by

Table 4. Released water resources available for reallocation.

Scenario	GWL[1]	$ET_{a,a}$[2]	$ET_{a,wf}$[3]	$ET_{a,wg}$[4]	$WA_{a.wf}$[5]	$WA_{a.wg}$[6]
	m	mm	mm	mm	Mm	mm
Full irrigation	3	792	576	647	216	145
	2.5	787	592	668	195	119
	2	888	592	674	297	214
	1.5	905	622	705	283	200
Low deficit irrigation	3	760	529	618	231	142
	2.5	760	551	636	209	124
	2	855	558	647	297	208
	1.5	880	624	714	256	166
High deficit irrigation	3	690	496	599	194	91
	2.5	708	530	633	178	75
	2	797	547	642	250	155
	1.5	837	599	697	238	140
Rainfed	3	444	371	475	73	–31
	2.5	515	437	540	78	–25
	2	572	496	600	76	–28
	1.5	654	601	700	53	–46

[1]Groundwater table depth, [2]actual evapotranspiration from the alfalfa field, [3]actual evapotranspiration from the winter wheat/fallow field, [4]actual evapotranspiration from the winter wheat/green gram double cropping field, [5]water resources released by shifting from alfalfa to the winter wheat/fallow system, [6]water resources released by shifting from alfalfa to the winter wheat/green gram double cropping.

Table 5. Water savings and changes in productive water use achieved by replacing alfalfa with the winter wheat/fallow system or the winter wheat/green gram double cropping.

Scenario	GWL[1]	E_a[2]	$WS_{a.wf}$[3]	$WS_{a.wg}$[4]	T_a[5]	$PW_{a.wf}$[6]	$PW_{a.wg}$[7]
	m	mm	mm	mm	mm	mm	mm
Full irrigation	3	341	101	120	451	116	25
	2.5	338	85	116	449	110	2
	2	258	0	50	630	297	164
	1.5	253	–30	59	652	313	141
Low deficit irrigation	3	327	130	131	433	100	10
	2.5	319	86	108	441	123	16
	2	248	14	57	607	283	150
	1.5	246	–40	43	634	295	123
High deficit irrigation	3	304	116	100	386	78	–10
	2.5	297	82	86	411	96	–11
	2	231	2	40	566	248	115
	1.5	226	–60	14	611	298	126
Rainfed	3	195	27	10	249	46	–41
	2.5	206	13	17	309	66	–41
	2	223	4	32	349	72	–60
	1.5	235	–53	20	419	106	–66

[1]Groundwater table depth, [2]evaporation from the alfalfa field, [3]water savings achieved by replacing alfalfa with the winter wheat/fallow system, [4]water saving achieved by replacing alfalfa with winter wheat/green gram double cropping, [5]crop transpiration from the alfalfa field, [6]productive water use change after replacing alfalfa with the winter wheat/fallow system, [7]productive water use change after replacing alfalfa with winter wheat/green gram double cropping.

231–256 mm under LDI, by 192–235 mm under HDI, and 53–73 mm under rainfed conditions. Higher reductions in ET_a were estimated again for shallow groundwater conditions. Total water resources released in the Fergana Valley by shifting from alfalfa to winter wheat/fallow were estimated at 468, 470, 396, and 132 million m^3/yr for FI, LDI, HDI, and rainfed conditions, respectively, with the released amounts then becoming available for instream and downstream users.

For winter wheat/green gram double cropping, crop $ET_{a.wg}$ gradually increased with an increase in the water table depth from 3 m to 1.5 m below the soil surface and gradually decreased with an increase in the irrigation water deficit. As compared to winter wheat/fallow system, these ET_a changes were associated mainly with an increase in crop transpiration. Overall, the shift from alfalfa to winter wheat/green gram double cropping (Scenario C) reduced ET_a by 119–214 mm under FI, by 124–208 mm under LDI, and by 75–155 mm under HDI. More substantial reductions in ET_a were obtained again for shallow water table conditions. ET_a was found to increase by 25–46 mm under rainfed conditions. Total water resources of the Fergana Valley, which can be released by shifting from alfalfa to winter wheat/green gram double cropping, were estimated at 320, 302, and 218 million m^3/yr for FI, LDI, and HDI regimes. Reducing both evaporation losses (E) and crop transpiration under the studied irrigation regimes releases water resources for other uses. No water was available for reallocation under rainfed conditions.

Water savings

Estimates of changes in non-productive evaporation (E) as affected by the alternative cropping systems are given in Table 5. The estimates for alfalfa show that non-productive evaporation is 253–341 mm under full irrigation, 246–327 mm under LDI, 226–304 mm under HDI, and 235–195 mm under rainfed conditions. Higher irrigation applications for deep groundwater conditions resulted in higher water contents in the topsoil and higher evaporation losses. Lower irrigation applications for shallow groundwater conditions and a higher crop soil cover produced lower values of E for all irrigation conditions.

The shift from alfalfa to winter wheat/fallow for deep groundwater table conditions (2.5–3 m below the soil surface) reduced E by 85–101 mm under FI, by 89–130 mm under LDI, by 77–114 mm under HDI, and by 13–27 mm under rainfed conditions. There were no significant water savings under shallow groundwater table conditions for the considered irrigation options. Under shallow groundwater conditions, evaporation losses had the same magnitudes for the alfalfa field and winter wheat/fallow systems. In the case of alfalfa, evaporation losses occurred mainly during the irrigations, and in the case of the winter wheat/fallow system when the land was fallowed. Total water savings due to shifting from alfalfa to the winter wheat/fallow system in the Fergana Valley were estimated at 74, 90, and 66 million m^3/yr for FI, LDI, and HDI scenarios, respectively, which is enough for irrigation of 8,000–10,000 ha of the irrigated land. These water savings comprise a minor part of water resources available for reallocation, while a major part is associated with reductions in productive water use (i.e., crop transpiration).

The shift from alfalfa to the winter wheat/green gram double cropping for deep groundwater table conditions (2.5–3 m below the soil surface) reduced E by 116–120 mm under FI, by 108–131 mm under LDI, by 86–100 mm under HDI, and by 10–17 mm under rainfed conditions, respectively. There were less significant water savings under shallow groundwater table conditions for all considered irrigation regimes. Total water savings due to shifting from alfalfa to winter wheat/green gram double cropping in the Fergana Valley were estimated at 163, 160, 114, and 38 million m^3/yr for the FI, LDI, HDI and rainfed regimes, respectively. These water savings are enough for crop production on 14,000–20,000 ha of irrigated land. The estimates indicate that water savings with wheat/green gram double cropping are higher than for the winter wheat/fallow system for all irrigation scenarios. Water savings with winter wheat/green gram double cropping make up most of the water resources available for reallocation as compared to the winter wheat/fallow system, where water available for reallocation originates mainly from reductions in productive water use.

Productive water use

Estimates of changes in productive water use (*PW*) as affected by alternative cropping systems are given in Table 5. The estimates for alfalfa show that productive transpiration was 451–652 mm for FI, 433–634 mm for LDI, 386–611 mm for HDI, and 249–419 mm for the rainfed conditions. Higher values of T_c were obtained for shallow groundwater tables as compared to deep groundwater conditions. Modeling results indicate that the shift from alfalfa to the winter wheat/fallow system causes a significant decrease in crop transpiration for all irrigation regimes, irrespective of the water table location. Crop transpiration was reduced by 110–313 mm for FI, 100–295 mm for LDI, 78–298 mm for HDI, and 46–106 mm for the rainfed system, respectively, indicating ineffective water use. Higher reductions in T_c were estimated for shallow groundwater conditions as compared to deeper water tables. Total reductions in productive water use, as a result of the shifts from alfalfa to the winter wheat/fallow system, were estimated to be 395, 379, 340 and 139 million m^3/yr for FI, LDI, HDI, and the rainfed conditions, respectively.

The shift from alfalfa to the winter wheat/green gram double cropping reduced productive water use by 141–164 mm for FI, 123–150 mm for LDI, and 115–126 mm for HDI for shallow groundwater conditions. Crop transpiration was reduced by 2–25 mm for FI and 10–16 mm for LDI, but increased by 10–11 mm for HDI under deep groundwater conditions. Crop transpiration was increased by 41 and 60–66 mm under rainfed conditions for shallow and deep groundwater conditions, respectively. Total reductions in productive water use in the Fergana Valley as a result of the shift from alfalfa to winter wheat/green gram double cropping were found to be 156, 141, and 104 million m^3/yr for the FI, LDI, and HDI scenarios, respectively. There are potential gains in productive water use of 99 million m^3/yr for the rainfed scenario. Thus, double cropping for all irrigation scenarios promoted more productive water use instead of unproductive losses from fallow lands.

Table 6 compares estimates of water available for reallocation, water savings, and changes in productive water use as a result of shifting from alfalfa to the winter wheat/fallow and winter wheat/green gram double cropping systems. The estimates show that in areas with shallow groundwater, the shift from alfalfa to the winter wheat/fallow system releases water resources mainly by reducing productive water use. In areas with deep groundwater, free water resources become available thanks to both water savings and reductions in productive water use. These findings indicate that the winter wheat/fallow system is not a suitable water saving alternative for alfalfa for areas with shallow and deep groundwater tables. However, the winter wheat/fallow system might be a suitable alternative cropping system for areas with deep groundwater and high-deficit irrigation conditions.

Water resources available for reallocation as a result of shifting from alfalfa to winter wheat/green gram double cropping are smaller as compared to the winter wheat/fallow system. Free water resources originate in areas with deep groundwater mainly as a result of reducing evaporation, and in areas with shallow groundwater mainly as a result of reducing productive transpiration. Our results show that winter wheat/green gram double cropping is a less suitable cropping system compared to alfalfa in areas with shallow groundwater, while it is a suitable alternative to alfalfa for areas with deep groundwater tables subject to full (FI) and low deficit (LDI) irrigations. The winter wheat/fallow system may be a more suitable cropping system for areas having deep groundwater tables and subject to high deficit irrigation (HDI).

Water productivity

Estimated alfalfa yields (the above ground biomass) was found to be in the range of 28.5 to 33.0 t/ha for full irrigation, 27.2–32.0 t/ha for LDI, 24.4–30.3 t/ha for HDI, and 7.3–11.5 t/ha for rainfed conditions for deep and shallow water table conditions, respectively (Table 7). As expected, higher values of the biomass were obtained for shallow water table conditions. For the winter wheat/fallow system, the yield of winter wheat was in the range of 5.08–5.5 t/ha for full irrigation, 4.96–5.18 t/ha for LDI, 4.91–5.13 t/ha for HDI, and 1.81–2.52 t/ha for rainfed conditions. These estimates did not account for the effects of soil and groundwater salinity, which may affect the yield of winter wheat. The yield of the winter wheat/green gram system, in wheat equivalents, was 8.3–10.1 t/ha for full irrigation, 8.0–10.2 t/ha for LDI, 7.7–10.0 t/ha for HDI, and 3.2–5.0 t/ha for rainfed conditions, respectively.

Table 6. Water available for reallocation, water savings, and changes in productive water use after replacing alfalfa by the winter wheat/fallow system or the winter wheat/green gram double cropping.

Scenario	GWL[1]	$WA_{a.wf}$[2]	$WS_{a.wf}$[3]	$PW_{a.wf}$[4]	$WA_{a.wg}$[5]	$WS_{a.wg}$[6]	$PW_{a.wg}$[7]
	m	mm	mm	mm	mm	mm	mm
Full irrigation	3	216	101	116	145	120	25
	2.5	195	85	110	119	116	2
	2	297	0	297	214	50	164
	1.5	283	–30	313	200	59	141
Low deficit irrigation	3	231	130	100	142	131	10
	2.5	209	86	123	124	108	16
	2	297	14	283	208	57	150
	1.5	256	–40	295	166	43	123
High deficit irrigation	3	194	116	78	91	100	–10
	2.5	178	82	96	75	86	–11
	2	250	2	248	155	40	115
	1.5	238	–60	298	140	14	126
Rainfed	3	73	27	46	–31	10	–41
	2.5	78	13	66	–25	17	–41
	2	76	4	72	–28	32	–60
	1.5	53	–53	106	–46	20	–66

[1]Groundwater table depth, [2]water resources released by shifting from alfalfa to the winter wheat/fallow system, [3]water savings achieved by replacing alfalfa with the winter wheat/fallow system, [4]productive water use change after replacing alfalfa with the winter wheat/fallow system, [5]water resources released by shifting from alfalfa to the winter wheat/green gram double cropping, [6]water saving achieved by replacing alfalfa with winter wheat/green gram double cropping, and [7]productive water use change after replacing alfalfa with winter wheat/green gram double cropping.

Table 7. Revenue and water productivity for the alfalfa, winter wheat/fallow and winter wheat/green gram double cropping systems.

Scenario	Groundwater depth	Yield			Revenue			Economic water productivity		
		Alfalfa	WWF[1]	WWGG[2]	Alfalfa	WWF	WWGG	Alfalfa	WWF	WWGG
	m		kg/ha			$/ha			$/m^3	
FI	3	28.5	5.45	8.33	1838	900	1375	0.23	0.16	0.21
	2.5	28.3	5.50	8.78	1825	908	1449	0.23	0.15	0.22
	2	32.3	5.25	9.18	2083	866	1514	0.23	0.15	0.22
	1.5	33	5.08	10.08	2129	838	1663	0.24	0.13	0.24
LDI	3	27.2	5.17	7.98	1754	853	1317	0.23	0.16	0.21
	2.5	27.2	5.15	8.41	1754	850	1388	0.23	0.15	0.22
	2	31	4.96	8.87	2000	818	1464	0.23	0.15	0.23
	1.5	32	5.18	10.17	2064	855	1678	0.23	0.14	0.23
HDI	3	24.4	5.00	7.72	1574	825	1274	0.23	0.17	0.21
	2.5	25.1	5.13	8.36	1619	846	1379	0.23	0.16	0.22
	2	28.7	4.91	8.80	1851	809	1453	0.23	0.15	0.23
	1.5	30.3	5.01	9.96	1954	826	1643	0.23	0.14	0.24
RF	3	7.3	1.81	3.16	471	299	521	0.11	0.08	0.11
	2.5	8.7	2.04	3.66	561	337	604	0.11	0.08	0.11
	2	9.8	2.22	4.16	632	367	687	0.11	0.07	0.11
	1.5	11.5	2.52	5.00	742	416	824	0.11	0.07	0.12

[1]Winter wheat/fallow system; [2]winter wheat/green gram double cropping

The cultivation of alfalfa ensures high revenues for farmers, at \$1838–2129/ha under FI, \$1754–2064/ha under LDI, \$1574–1974/ha under HDI, and \$471–742/ha under rainfed conditions. Lower revenues were obtained for deep groundwater conditions and higher revenues for shallow groundwater conditions. The shift from alfalfa to winter wheat, with an aim toward food independency and social benefits, reduced the revenues of local farmer communities but enhanced food security. For the winter wheat/fallow scenario, revenues of farmers were estimated at \$838–908/ha for FI, \$818–855/ha for LDI, \$809–846/ha for HDI, and \$299–416/ha for rainfed conditions. The cultivation of green gram after winter wheat harvesting significantly adds to the revenues of farmers by generating new income from land and water resources that would otherwise remain underutilized during fallow periods. The revenues were estimated at \$1375–1663/ha for FI, \$1317–1678/ha for LDI, \$1274–1643/ha for HDI, and \$521–824/ha for rainfed conditions.

The economic water productivity for alfalfa is estimated to be \$0.23–0.24/m^3 under irrigation and \$0.11/m^3 under rainfed conditions. The economic water productivity for the winter wheat/fallow system is appraised at \$0.13–0.16/m^3, \$0.14–0.16/m^3, \$0.14–0.17/m^3 for FI, LDI, and HDI, respectively, and \$0.07–0.08/m^3 for rainfed conditions. The economic water productivity for winter wheat/green gram double cropping is estimated to be \$0.21–0.24/m^3 for irrigation and \$0.11–0.12/m^3 for rainfed conditions.

It is expected that with adjustments to the area under alfalfa and winter wheat/green gram double cropping, in accordance with the market opportunities and economics that capture relative commodity prices, the yield stability and effects of legume double cropping on subsequent crop performance will bring together higher revenues to farmers cultivating these two alternative crops. This will also improve the economic productivity of winter wheat/green gram double cropping. However, from a broader perspective, public policies should also provide incentives for value chain development and risk management, and for the establishment of multi-commodity farmer groups and related support measures.

SOCIOECONOMIC GAINS FROM CROPPING POLICY CHANGES

Our HYDRUS-1D modeling results show that Scenario C pertaining to the *potential future* water use of a double cropping system produces notable water savings by transforming non-productive evaporation into productive transpiration and enhancing crop water productivity. Indeed, double cropping by growing green gram/food legumes after harvesting winter wheat instead of leaving crop fields fallow, also improves the economic water productivity (\$/m^3) and crop revenue (\$/ha) for all irrigation regimes. The HYDRUS simulations indicate that the more productive water use leads to gains in water productivity and generates new income and higher economic benefits for farmers, thus clearly offering incentives to support double cropping through policy reforms. However, the successful integration of gram/pulse crops into wheat-based systems depends upon economic, social, and policy drivers (Maaz et al., 2017).

Apart from gains in water savings, shifting from alfalfa to winter wheat-green gram double cropping has several socioeconomic benefits and implications, including gains in income, consumption, employment, and rural livelihoods, and contributions to national and regional food security. For example, consider Scenario B that represents the policy conditions *after* the 1990s when winter wheat replaced alfalfa. While shifting to wheat cultivation by itself did not bring higher income to farmers of the Fergana Valley, there were several socioeconomic benefits for the wider population and the national economy. First, major benefits were associated with an increase in food production and improvements in consumption patterns in the region. Based on data from the food balance sheets of the Food and Agricultural Organization (FAO) of the United Nations, wheat provides about 53% of the dietary caloric intake in Uzbekistan, and thus is a major source of calorie consumption by the population. In Central Asia, in general, the consumption of wheat-based food is higher compared to other regions of the world. The wheat-equivalent consumption across Central Asian countries ranges from 138 to 174 kg capita^{-1} year^{-1} as compared to 66 kg capita^{-1} year^{-1} for Asian region as a whole (Chabot and Tondel, 2011). The additional 14,000–20,000 ha of irrigated area and the production of winter wheat under Scenario C can make a significant contribution to food security.

Increasing gram/legume production may also contribute to more balanced nutrition of the population in rural and urban areas and thus improve food security and nutrition outcomes (Pingali, 2015; Verkaart et al., 2017). For example, the potential future double cropping green gram option in areas where alfalfa was replaced by winter wheat on 189,000 ha can produce about 250–280 thousand tons of green gram. Although

data on green gram consumption are lacking, FAO Stat (2017) shows that the annual pulse consumption per capita in Uzbekistan, Tajikistan, and Kyrgyzstan is quite low (less than 3 kg), while the pulse consumption is higher in neighboring countries, including Bangladesh (5.3 kg), China (9.4 kg), India (13.6 kg), Pakistan (6.2 kg), and Sri Lanka (9.3 kg), which all have unmet local demand for pulses. Using an average annual gross pulse consumption at 10 kg per capita, this gram production may serve the pulse consumption needs of about 20 million people in these countries, while generating millions of dollars in export earnings.

The consumption norm *recommended* by the Ministry of Health of Uzbekistan for meat and meat products is around 46.1 kg, whereas the *actual* meat consumption was about 28.4 kg per capita per annum in 2009, indicating a deficit in the meat consumption of about 17.7 kg per capita. Green gram has only a slightly lower protein content (24%) than meat (26%), which suggests that gram production could supplement the meat consumption deficit for about 10 million people in Uzbekistan. In terms of supplying the daily protein needs solely from non-meat alternative sources of protein, this gram production may be sufficient to serve the meat/protein needs of about 6 million people. However, since meat is a high quality complete protein, while gram is an incomplete protein, the meat/protein equivalent estimate should be interpreted cautiously. Also, people tend to substitute pulse-based protein with meat as incomes grow (Stokstad et al., 2010). However, green gram can supply vegetable-based protein at a much lower unit cost ($3.6/kg protein) than meat-based protein ($12.4/kg), and is a lean source of protein with a high fiber and nutrient content that offers multiple health benefits.

The higher food production will help stabilize the food supply and market prices to benefit both farmers and consumers. One of the important issues for the wheat supply in Uzbekistan is that trainfed wheat production in neighboring Kazakhstan shows a considerable degree of inter-annual variability. Export of wheat varies from 4% to 22% of total wheat available for consumption. In poor wheat-production years, such as in 2008-2009 during the global food, wheat export from Kazakhstan dropped by 30% (Chabot and Tondel, 2011). In spite of this, prices remained low in the local market of Uzbekistan, even as prices on the international market increased substantially. Therefore, due to the increased wheat and legume production in the valley, farmers may benefit from the higher output and additional economic activity in rural areas, while consumers benefit from increased food consumption and lower food prices (Hussain et al., 2004). The increased food production makes food available and affordable for millions of consumers, thus improving their dietary intake, nutrition, and cognitive skills, and contributing towards sustainable human development (Conceiçao et al., 2016). There are also wider benefits in irrigation value chains (agro-processing, cereal products, value addition) and markets (domestic, urban, export) since wheat and green gram can economically support nutritional changes since feeding humans on a cereal- and legumes-based diet requires far fewer resources in terms of water, energy, and land, than meat based diets (Hanjra and Qureshi, 2010; Keyzer et al., 2005; Stokstad, 2010).

The second major impact is a gain in employment. Labor requirements for wheat production in the Fergana Valley are high at 24 person-day ha^{-1} as compared to 5 person-day ha^{-1} for alfalfa (World Bank, 2009). Increasing employment is especially important for the region where the rural population comprises 80% to 90% of the total, and district-wise out-migration for job opportunities is quite high and ranges from 2.5–4.5% (World Bank, 2009).

Farmers' incomes can grow by adopting a double cropping system combining winter wheat with gram/legumes and vegetables. Year-round production with a higher cropping intensity and a more diversified cropping pattern helps to attenuate intra-seasonal variability in employment, output, income, and prices while improving livelihoods and reducing the risks that are so pervasive in agriculture. For example, the production of vegetables can provide much higher incomes for farmers as compared to alfalfa, while employment will increase from 5 to 200–286 person-day ha^{-1} (World Bank, 2009), i.e., to an almost full-time and year-round employment. Rough estimates indicate that the production of vegetables after harvesting winter wheat on the entire wheat production area may create full-time employment for 200,000 people in the Fergana Valley. Vegetables have a higher water productivity (Al-Said et al., 2012) and are also an important part of a nutritious and healthy diet and contribute to export earnings; public policies and investments that support double cropping hence offer high social benefits.

The proposed crop and water management practices also enhance the sustainability of irrigation systems and benefit instream and downstream users. Reduced irrigation water diversions from the Syrdarya River and its tributaries in the Fergana Valley will reduce groundwater recharge and gradually lower the groundwater table, thereby reducing the return flow to the river. This may improve the quality of both groundwater and river flow. Lowering the water table often results in gradual reductions in the area of salt-affected soils and enhance the sustainability of irrigated agriculture (Kijne, 2006).

However, the main socioeconomic gains of water savings in the Fergana Valley are expected to be in downstream sub-regions, such as the Mirzachul and Djizak steppes of the Syrdarya River basin. Irrigation in these semi-desert zones fully relies on water from the river. Between 1990 and 2000, cotton yields in the Mirzachul steppe located on the left bank downstream of the river plummeted by 46%, while some of the land was taken out of production due to irrigation water shortages and increasing salinity (Kushiev et al., 2005). This had a direct impact on agricultural production, with estimated losses of around $90.4 million on 555,000 ha (Keith and McKinney, 1997). Cotton yields declined in this area below 2t ha^{-1} due to a shortage of irrigation water and salinity buildup in the topsoil. A sustainable water supply is a precondition in these areas to arrest soil salinization, which is the main limitation for crop production. Reduced water diversions for irrigation also offer major energy cost savings, for example in lift irrigation schemes (Karimov et al., 2017), with associated reductions in carbon emissions.

In addition to guaranteeing the continued buildup of the national revenue of the newly independent states, the double cropping policy change could be an approach for increasing rural incomes and enhancing food security. The cotton policy changes increased food production. Increasing green gram production in Uzbekistan may also enhance the export of agricultural products to India, Pakistan, and Afghanistan. The implications of increasing wheat and legumes production and policy changes extend hence well beyond irrigated agriculture in the Fergana Valley to countries in the region facing similar water scarcity and agricultural policy reform challenges. Since the benefit accrues to the public at large and even beyond the national boundaries, the incidence analysis of costs and benefits is quite complex, and benefit-sharing models and policy reforms also require further research.

CONCLUSIONS AND POLICY IMPLICATIONS

This paper showed that national policy reforms in Uzbekistan since the 1990s led to changes in the cropping pattern that aimed for greater food security, social benefits, and water savings. A case in point was the analysis of replacing alfalfa with a winter wheat/fallow system and then transitioning to wheat-gram double cropping that currently remains inactive in the agricultural policy. Modeling estimates using HYDRUS-1D suggest that:

- The shift from alfalfa to the winter wheat/fallow system released about 400–470 million m^3/yr of water resources in the Fergana Valley for instream and downstream uses. However, these water resources became available mainly as a result of reducing productive crop transpiration. Water savings associated with reductions in nonproduction evaporation from the change in the cropping pattern are estimated to be only about 66–90 million m^3/yr.
- Winter wheat is not a suitable water-saving alternative crop to replace alfalfa under shallow groundwater conditions due to significant upward fluxes from the water table. As a result, total evaporation losses are of the same magnitude for the alfalfa and winter wheat/fallow systems at different levels of deficit irrigation, while productive transpiration is significantly higher for alfalfa as compared to winter wheat. Shifting from alfalfa to winter wheat on 200,000 ha (or 22% of the irrigated land in the Fergana Valley with a shallow water table) did not produce water savings but enhanced the wheat output and food security. Yet, the current practice of restricting double cropping under shallow groundwater conditions causes additional evaporation losses from land fallowed after winter wheat harvesting. This implies that further policy reforms and liberalizations that incentivize better land and water management practices could produce water savings and socioeconomic gains for the nation.
- Shifting from alfalfa to winter wheat followed by green gram in areas with groundwater deeper than 2 m below the land surface can reduce evaporation losses without changes in crop productive transpiration. This double cropping in the Fergana Valley can produce water savings of 114–163 million m^3/yr compared to alfalfa at different levels of deficit irrigation, and can increase green gram grain production by 250–280 thousand tons.
- When only the use of water in agriculture is considered, free water resources gained through the change in the cropping pattern can be reallocated within the Fergana Valley, which has a more productive agriculture as compared to downstream systems. Improving the water supply downstream, which faces water shortages, may be possible through a set of water saving technologies which do not affect crop productive transpiration. When other uses, including environmental, industrial, and instream users, are considered, then water released through the change in the cropping pattern can be considered for reallocation within the river system.

To conclude, double cropping with summer green gram represents an advantageous option for crop intensification and widely-shared socioeconomic gains that may justify public policy support. The cultivation of alfalfa in areas with a shallow groundwater table can be continued, or the ground water table can be lowered in areas with winter wheat/green gram, by extracting groundwater for irrigation of the second crop and promoting the conjunctive use of surface water and groundwater.

*Acknowledgements.*The authors would like to express their thanks to the OPEC Fund for International Development and the CGIAR Research Program on Water, Land and Ecosystems for financing this work and Dr. Ravza Mavlyanova, Regional Coordinator of the World Vegetable Center for Central Asia for promoting the adoption of green gram among farming communities.

REFERENCES

Allen, R.G., Pereira, L.S., Raes, D., Smith, M., 1998. Crop evapotranspiration. Guidelines for computing crop water requirements. FAO Irrigation and Drainage Paper 56. FAO, Rome, 300 p.

Allen, R.G., Pereira, L.S., Smith, M., Raes, D., Wright, J.L., 2005. FAO-56 dual crop coefficient method for estimating evaporation from soil and application extensions. J. Irrig. Drain. Eng., 131, 2–13.

Al-Said, F.A., Ashfaq, M., Al-Barhi, M., Hanjra, M.A., Khan, I. A., 2012. Water productivity of vegetables under modern irrigation methods in Oman. Irrigation and Drainage (ICID Journal), 61, 4, 477–489.

Anderson, K., 2007. Agricultural trade liberalisation and the environment: a global perspective. World Economy, 15, 153–172.

Awan, U.K., Ibrakhimov, M., Benli, B., Lamers, J.P.A., Liaqat, U.W., 2017. A new concept of irrigation response units for effective management of surface and groundwater resources: a case study from the multi-country Fergana Valley, Central Asia. Irrigation Science, 35, 1, 55–68.

Borisov, V.A., 2007. Groundwater Resources and Their Use in Uzbekistan. Fan, Tashkent, Uzbekistan. (In Russian.)

Cai, X., McKinney, D.C., Rosegrant, M.W., 2002. Sustainability analysis for irrigation water management in the Aral Sea region. Agricultural Systems, 76, 1–24.

Chabot, Ph.,Tondel, F., 2011. A regional view of wheat markets and food security in Central Asia with a focus on Afghanistan and Tajikistan. USAID. http://www.fews.net/docs/Publications/Regional View of Wheat... (Accessed on 25.12.14).

Conceiçao, P., Levine, S., Lipton, M., Warren-Rodríguez, A., 2016. Toward a food secure future: Ensuring food security for sustainable human development in Sub-Saharan Africa. Food Policy, 60, 1–9.

Doorenbos, J., Kassam, A.H., 1979. Yield response to water. FAO Irrigation and Drainage Paper No. 33. FAO, Rome.

Edgorov, D., Ikramova, M., Azimov, S., 2006. Crop rotation and role of alfalfa on salinity control. Bukhara Branch of the Uzbek Research Institute of Cotton Growing. Bukhara. 64 p.

Evans, A.E. V., Hanjra, M.A., Jiang, Y., Qadir, M., Drechsel, P., 2012. Water quality: assessment of the current situation in Asia. International Journal of Water Resources Development, 28, 195–216.

Feddes, R.A., Kowalik, P.J., Zaradny, H., 1978. Simulation of Field Water Use and Crop Yield. John Wiley & Sons, New York.

Forkutsa, I., Sommer, R., Shirokova, Y.I., Lamers, J.P., Kienzler, K., Tischbein, B., Martius, C., Vlek, P.L.G., 2009. Modeling irrigated cotton with shallow groundwater in the Aral Sea Basin of Uzbekistan: I. Water dynamics. Irrig. Sci., 27, 331–346. DOI: 10.1007/s00271-009-0148-1.

Foxx, T.S., Tierney, G.D., Williams, J.M., 1982. Rooting depths of plants relative to biological and environmental factors. Los Alamos National Laboratory, 28 p. https://www.iaea.prg/inis/collection/NCLCollectionStore/_Public/16/061/16061888.pdf.

Grismer, M.E., 2015. Use of shallow groundwater for crop production. ANR Publication., 6 p. http://anrcatalog.ucanr.edu.

Gan, Y.T., Warkentin, T.D., Bing, D.J., Stevenson, F.C., McDonald, C.L., 2010. Chickpea water use efficiency in relation to cropping system, cultivar, soil nitrogen and Rhizobial inoculation in semiarid environments. Agricultural Water Management, 97, 1375–1381.

Ganiev, K.G., 1979. Evaporation and Infiltration Recharge of Groundwater. Fan, Tashkent, Uzbekistan (In Russian.)

Giordano, M., Turral, H., Scheierling, S.M., Tréguer, D.O., McCornick, P.G., 2017. *Beyond 'More Crop per Drop*'. Research Report 169. International Water Management Institute (IWMI), Colombo, Sri Lanka; The World Bank, Washington, DC, USA.

Hanjra, M.A., Qureshi, M.E., 2010. Global water crisis and future food security in an era of climate change. Food Policy 35, 2, 365–377.

He, K., Yang, Y., Yang, Y., Chen, S., Hu, Q., Liu, X., Gao, F., 2017. HYDRUS simulation of sustainable brackish water irrigation in a winter wheat-summer maize rotation system in the North China Plain. Water, 9, 536.

Hernandez, T.X., 2001. Rainfall-runoff modeling in humid shallow water table environments. MSc Thesis. University of South Florida.

Hussain, I., Mudasser, M., Hanjra, M.A., Amrasinghe, U., Molden, D., 2004. Improving wheat productivity in Pakistan: econometric analysis using panel data from Chaj in the upper Indus Basin. Water International, 29, 189–200.

Huang, J., Xu, C., Ridoutt, B.G., Wang, X., Ren, P., 2017. Nitrogen and phosphorus losses and eutrophication potential associated with fertilizer application to cropland in China. Journal of Cleaner Production, 159, 171–179.

Jalilov, S.M., Amer, S.A., Ward, F.A., 2013. Water, food, and energy security: an elusive search for balance in Central Asia. Water Resources Management, 27, 11, 3959–3979.

Karimov, A., Molden, D., Khamzina, T., Platonov, A., Ivanov, Y., 2012. A water accounting procedure to determine the water savings potential of the Fergana Valley. Agricultural Water Management, 108, 61–72.

Karimov, A.K., Šimůnek, J., Hanjra, M.A., Avliyakulov, M., Forkutsa, I., 2014. Effects of the shallow water table on water use of winter wheat and ecosystem health: Implications for unlocking the potential of groundwater in the Fergana Valley (Central Asia). Agricultural Water Management, 131, 0, 57–69.

Karimov, A.K., Smakhtin, V., Karimov, A.A., Khodjiev, Kh., Yakubov, S., Platonov, A., Avliyakulov, M., 2017. Reducing the energy intensity of lift irrigation schemes of Northern Tajikistan- potential options. Renewable and Sustainable Energy Reviews. doi.org/10.1016/j.rser.2017.06.107

Keith, J.E., McKinney, D.C., 1997. Option analysis of the operation of the Toktogul reservoir. Issue Paper No. 7. www.ce.utexas.edu/prof/mckinney/ce397/Topics/Options Toktogul 3.pdf. (Accessed on 20.02.2014).

Keyzer, M.A., Merbis, M.D., Pavel, I.F.P.W., van Wesenbeeck, C.F.A., 2005. Diet shifts towards meat and the effects on cereal use: can we feed the animals in 2030? Ecological Economics, 55, 187–202.

Khan, S., Hanjra, M. A. 2008. Sustainable land and water management policies and practices: A pathway to environmental sustainability in large irrigation systems. Land Degradation and Development, 19, 469–487.

Kijne, J.W., 2006. Salinisation in irrigated agriculture in Pakistan: mistaken predictions. Water Policy, 8, 325–38.

Kushiev, K., Noble, A.D., Abdullaev, I., Toshbekov, U., 2005. Remediation of abandoned saline soils using *Glycyrrhiza glabra*: A study from the Hungry Steppes of Central Asia. Int. J. Agric. Sustain., 3, 2, 102–113.

Li, H., Yi, J., Zhang, J., Zhao, Y., Si, B., Lee, R., Cui, L., Liu, X., 2015. Modeling of soil water and salt dynamics and its effects on root water uptake in Heihe Arid Wetland, Gansu, China. Water, 7, 2382–2401. DOI: 10.3390/w7052382.

Liu, T., Luo, Y., 2011. Effect of shallow water tables on the water use and yield of winter wheat (*Triticum aestivum L.*). AJCS, 5, 13, 1692–1697.

Maaz, T., Wulfhorst, J.D., McCracken, V., Kirkegaard, J., Huggins, D.R., Roth, I., Kaur, H., Pan, W., 2017. Economic, policy, and social trends and challenges of introducing oilseed and pulse crops into dryland wheat cropping systems. Agriculture, Ecosystems & Environment, doi.org/10.1016/j.agee.2017.03.018.

Mavlyanova, R., Sharma, R.C., 2015. High quality seed production of wheat and mungbean in Kuva, Fergana. Report. ICARDA, Tashkent. www.cac-program.org/files/ec9f7aca08a1460f0debbbab0399c61c.pdf

Mirzaev, S.Sh., 1974. Groundwater Storages of Uzbekistan . Fan, Tashkent, Uzbekistan. (In Russian.)

Molden, D., 1997. Accounting for water use and productivity. SWIM Paper 1. International Water Management Institute, Sri Lanka.

Molden, D., Sakthivadivel, R., 1999. Water accounting to assess use and productivity of water. International Journal of Water Resources Development, 15, 1&2, 55–71.

Molden, D., Oweis, T., Steduto, P., Bindraban, P., Hanjra, M.A., Kijne, J., 2010. Improving agricultural water productivity: Between optimism. Agric. Water Manage., 97, 4, 528–535.

Nandalal, W., Hipel, W., 2007. Strategic decision support for resolving conflict over water sharing among countries along the Syr Darya River in the Aral Sea Basin. Journal of Water Resources Planning and Management, 133, 289–299.

Pingali, P., 2015. Agricultural policy and nutrition outcomes – getting beyond the preoccupation with staple grains. Food Security, 7, 3, 583–591.

Reddy, J.M., Muhammedjanov, Sh., Jumaboev, K., Eshmuratov, D., 2012. Analysis of cotton water productivity in Fergana Valley. Agricultural Science, 3, 6, 822–834.

Sanchez, C.A., Zerihun, N.I., Warrick, A.W., Furman, A., 2003. Efficient surface fertigation of high value horticulture crops. In: Western Nutrient Management Conference, Salt Lake City, UT, pp. 77–82.

Seckler, D., 1996. The New Era of Water Resources Management: From "Dry" To "Wet" Water Savings. Research Report 1. International Irrigation Management Institute (IIMI), Colombo, Sri Lanka.

Šejna, M., Šimůnek, J., van Genuchten, M.Th., 2012. The Hydrus software package for simulating the two- and three-dimensional movement of water, heat, and multiple solutes in variably-saturated media. HYDRUS User manual, Version 2. PC-Progress, Prague, Czech Republic. 287 p.

Shouse, P.J., Ayars, E., Šimůnek, J., 2011. Simulating root uptake from a shallow saline groundwater resource. Agricultural Water Management, 98, 784–790.

Shreder, V.R., Vasiliev, I.K., Trunova, T.A., 1977. Hydromodul zoning for calculation of the irrigation rates for cotton under arid environments. In: Proceedings of the

Middle Asia Research Institute of Irrigation. No. 8. Middle Asia Research Institute of Irrigation, Tashkent, pp. 28–41.

Shultsc, V.L., 1949. Rivers of Middle Asia. State Publishing House of Geographic Literature, Moscow, 196 p. (In Russian.)

Šimůnek, J., Šejna, M., Saito, H., Sakai, M., van Genuchten M.Th., 2008. The HYDRUS-1D Software Package for Simulating the Movement of Water, Heat, and Multiple Solutes in Variably Saturated Media, Version 4.0, HYDRUS Software Series 3. Department of Environmental Sciences, University of California Riverside, Riverside, California, USA, 315 p.

Šimůnek, J., van Genuchten, M.Th., Šejna, M., 2016. Recent developments and applications of the HYDRUS computer software packages. Vadose Zone Journal, 15, 7, 25 p., DOI: 10.2136/vzj2016.04.0033.

Smeal, D., Kallsen, C.E., Sammis, T.W., 1991. Alfalfa yield as related to transpiration, growth stage and environment. Irrig. Sci., 12, 79–86.

Sommer, R., Glazirina, M., Yuldashev, T., Otarov, A., Ibraeva, M., Martynova, L., Bekenov, M., Kholov, B., Ibragimov, N., Kobilov, R., Karaev, S., Sultonov, M., Khasanova, F., Esanbekov, M., Mavlyanov, D., Isaev, S., Abdurahimov, S., Ikramov, R., Shezdyukova, L., de Pauw, E., 2013. Impact of climate change on wheat productivity in Central Asia. Agriculture, Ecosystems & Environment, 178, 78–99.

Soppe, R.W., Ayars, J.E., 2002. Crop water use by safflower in weighing lysimeters. Agricultural water management, 69, 59–71.

Soylu, M.E., Istanbulluoglu, E., Lenters, J.D., Wang, T., 2011. Quantifying the impact of groundwater depth on evapotranspiration in a semi-arid grassland region. Hydrol. Earth Syst. Sci., 15, 787–806. www.hydrol-earth-syst-sci.net/15/787/2011/doi:10.5194/hess-15-787-2011.

Spoor, M., 1998. The Aral Sea Basin crisis: Transition and environment in former Soviet Central Asia. Development and Change, 29, 409–435.

Stokstad, E., 2010. Could less meat mean more food? Science, 327, 810–811.

Sumochkina, T.E., Konovalova, N.S., Ivanova, D.A., Kapner, D.Ya., Muminov, F.A., Reizvih, O.N., Abdullaev, Kh.M., Gorelysheva, Z.M., Titova, M.M., 1977. Agroclimatic resources of Namangan, Andijan and Fergana provinces (Fergana Valley) of Uzbekistan. Gidrometeoizdat, Leningrad, 194 p. (In Russian.)

Talipov, G.A., 1992. Land resources of Uzebkistan and problems of their rational use. Uzbek Research Institute of Cotton Growing, Tashkent, 232 p. (In Russian.)

Taylor, S.A., Ashcroft, G.M., 1972. Physical Edaphology. W.H. Freeman and Co., San Francisco, pp. 434–435.

Verkaart, S., Munyua, B.G., Mausch, K., Michler, J.D. 2017. Welfare impacts of improved chickpea adoption: A pathway for rural development in Ethiopia? Food Policy, 66, 50–61.

van Genuchten, M.Th., 1980. A closed-form equation for predicting the hydraulic conductivity of unsaturated soils. Soil Sci. Soc. Am. J., 44, 5, 892–898.

Ward, F.A., Booker, J.F., 2003. Economic costs and benefits of instream flow protection for endangered species in an international basin. Journal of the American Water Resources Association, 427–440.

Ward, F.A., Pulido-Velazquez, M., 2008. Water conservation in irrigation can increase water use. PNAS 105, 18215–18220.

Webber, H.A., 2008. Improving irrigated agriculture in the Fergana Valley, Uzbekistan. PhD Thesis. McGill University. 188 p.

Wesseling, J.G., Elbers, J.A., Kabat, P., van den Broek, B.J., 1991. SWATRE; Instructions for Input. Internal Note. Winand Staring Centre, Wageningen.

World Bank, 2009. Uzbekistan - First phase of the Ferghana Valley Water Resources Management Project: Resettlement policy framework and specific resettlement action plan. http://documents.worldbank.org/curated/en/200907/10849223/uzbekistan-first-phase-ferghana-valley-water-resources-management-project-resettlement-policy-framework-specific-resettlement-action-plan. (Accessed on 18.12.2014).

Received 7 August 2017
Accepted 20 October 2017

Note: Colour version of Figures can be found in the web version of this article.

J. Hydrol. Hydromech., 66, 2018, 2, 202–210
DOI: 10.1515/johh-2017-0047

Reassessment of the Goiânia radioactive waste repository in Brazil using HYDRUS-1D

Elizabeth M. Pontedeiro[1, 2*], Paulo F. Heilbron[3], Jesus Perez-Guerrero[3], Jian Su[1], Martinus Th. van Genuchten[2, 4]

[1] Department of Nuclear Engineering, Federal University of Rio de Janeiro, UFRJ, Rio de Janeiro, RJ, Brazil.
[2] Department of Earth Sciences, Utrecht University, Utrecht, Netherlands.
[3] Brazilian Nuclear Energy Commission, CNEN, Rio de Janeiro, RJ, Brazil.
[4] Center for Environmental Studies, CEA, São Paulo State University, UNESP, Rio Claro, SP, Brazil.
[*] Corresponding author. E-mail: bettinadulley@hotmail.com

Abstract: In September 1987 an accident occurred with a cesium chloride (CsCl) teletherapy source taken from a cancer therapy institute in Goiânia, Brazil. Misuse of the abandoned source caused widespread contamination of radioactive material (about 50 TBq of ^{137}Cs) in the town of Goiânia. Decontamination of affected areas did lead to about 3,500 m^3 of solid radioactive wastes, which were disposed in two near-surface repositories built in concrete in 1995. This paper documents a safety assessment of one of the low-level radioactive waste deposits containing ^{137}Cs over a time period of 600 years. Using HYDRUS-1D, we first obtained estimates of water infiltrating through the soil cover on top of the repository into and through the waste and its concrete liners and the underlying vadose zone towards groundwater. Calculations accounted for local precipitation and evapotranspiration rates, including root water uptake by the grass cover, as well as for the effects of concrete degradation on the hydraulic properties of the concrete liners. We next simulated long-term water fluxes and ^{137}Cs transport from the repository towards groundwater. Simulations accounted for the effects of ^{137}Cs sorption and radioactive decay on radionuclide transport from the waste to groundwater, thus permitting an evaluation of potential consequences to the environment and long-term exposure to the public. Consistent with previous assessments, our calculations indicate that very little if any radioactive material will reach the water table during the lifespan of the repository, also when accounting for preferential flow through the waste.

Keywords: Cs-137 transport; Goiânia radioactive waste repository; HYDRUS-1D; Safety assessment.

INTRODUCTION

In September 1987 a major accident occurred with an old Cesium teletherapy source taken from an abandoned cancer therapy institute (Instituto Goiano de Radioterapia) in the Brazilian town of Goiânia. Misuse of the source caused widespread contamination of radioactive material (about 1375 Ci of ^{137}Cs, or 5 x 10^{13} Bq), leading to four deaths and about 250 people showing significant levels of internal or external contamination (Heilbron et al., 2002; IAEA, 1988; Paschoa et al., 1993; Roberts, 1987). Subsequent cleanup of ^{137}Cs contaminated areas generated about 3,500 m^3 of solid radioactive waste totaling some 6,000 tons of material. The waste was disposed in two near-surface low-level radioactive waste repositories built in reinforced concrete. Previously, two safety assessments were carried out, in 1995 and 2002, to evaluate the performance of the repositories over a 400-year time period (Heilbron et al., 2002). The studies were mandated by the Brazilian Nuclear Regulatory Agency (CNEN) as part of their regular assessments of the long-term effects of the Goiânia waste repositories on the environment and human health.

Numerical models have long been recognized to be important tools for radioactive waste repository design, operation and environmental regulation (e.g., Pontedeiro et al., 2010; Robinson et al., 2012; Tsang (Ed.), 1987). They are important to understand the long-term subsurface fate and transport of contaminants leached from solid waste disposal sites as a function of climatologic conditions, local hydrogeologic conditions, and repository design. Performance assessments are especially important to evaluate the future safety of installations containing radioactive materials with long-lived radionuclides. This may need to include evaluations of how gradual processes of degradation of engineered and natural barriers of the repositories after their closure would affect the environment (Jacques et al., 2013, 2014; Pabalan et al., 2009). Other events or processes could also compromise the integrity of a repository, such as intrusion by humans and animals (Naveira-Cotta et al., 2013; Yu et al., 2007).

The current study was carried out to provide a mandatory five-year reassessment of the possible future impacts of the Goiânia radioactive waste repositories on the environment and biosphere, as requested by the Brazilian Nuclear Regulatory Agency. While many models potentially could be used for such an analysis (e.g., as inventoried by Mallants et al., 2011), we used in our study the HYDRUS-1D software of Šimůnek et al. (2016). Below we first give a brief description of the Goiânia waste disposal site, including a synopsis of previous assessments, then discuss HYDRUS-1D as used to evaluate ^{137}Cs transport from the waste site to the underlying vadose zone and groundwater, and provide results of the calculations.

THE GOIÂNIA RADIOACTIVE WASTE REPOSITORY

To facilitate the safe disposal of radioactive waste generated during decontamination in Goiânia, two near-surface repositories were constructed. The first one was a near-surface repository for disposal of very low-activity wastes (40% in volume, with specific ^{137}Cs activities less than 87 Bq/g), while the second repository (also a near-surface type) was constructed for higher-activity wastes (60% in volume, with specific activities above 87 Bq/g). This second repository, being the focus of this study, was built in concrete, having dimensions of 19.6 m

Fig. 1. View of the Goiânia near-surface repositories. The repository in the front contains relatively low-activity ^{137}Cs waste (specific activities less than 87 Bq/g), and the repository in the back higher-activity waste (specific activities above 87 Bq/g).

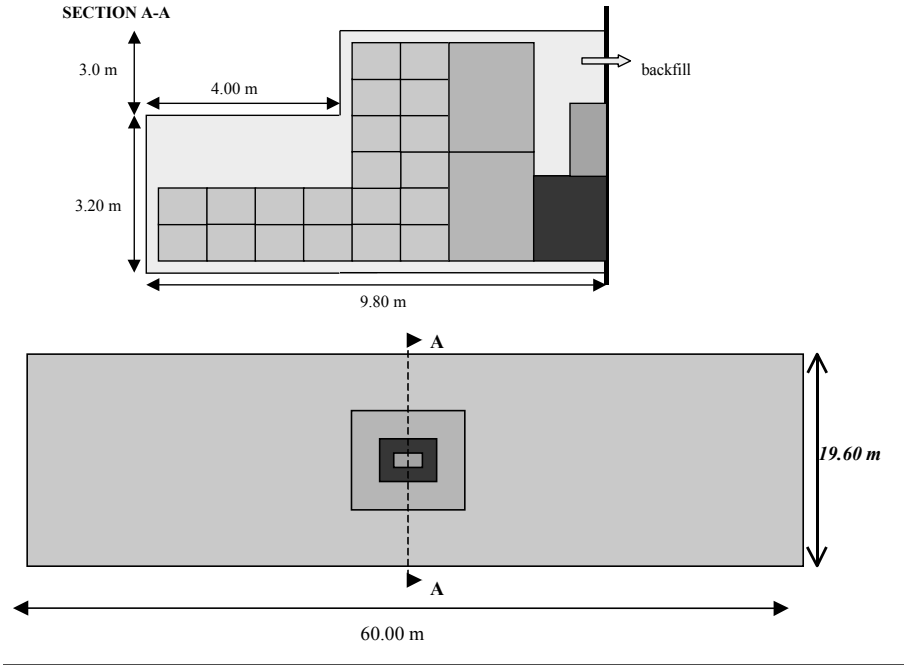

Fig. 2. Schematic internal cross-section (a) and areal view (b) of the Goiânia near-surface higher-activity radioactive waste repository (Heilbron et al., 2002).

length, 60 m width and 6.20 m height, and with 20-cm thick concrete walls along all sides of the facility, including the top and bottom. A 50-cm thick uniform soil cover was placed on top of the repository and vegetated with grass. Figure 1 gives an above-ground view of the two constructed repositories.

Waste inside the second repository considered here consisted mostly of compacted soil contaminated with ^{137}Cs, covering a height of about 4.38 m. A schematic of the design of the facility is shown in Figure 2. The concrete deposit contained inside various types of containers filled with waste having diverse activity levels. Void spaces between the containers were filled and compacted with natural material, composed of sand and clay. While macroscopically quite heterogeneous, for the purpose of this study we considered the resulting waste material to be distributed in a homogeneous manner, with the hydraulic characteristics of the waste being the same as those of the compacted soil. The repository is located at 16° 45′ 32″ S, 49° 26′ 16″ W, about 770 m above sea level. Depth to groundwater below the lower concrete liner during the year fluctuated between 4 and 5 m, with 4.5 m being a good average value.

PREVIOUS ASSESSMENTS

In 1995 the first environmental safety assessment of the Goiânia radioactive waste disposal site was conducted by the Brazilian Nuclear Energy Commission (CNEN) using a screening model (Heilbron et al., 1995, 1996). The assessment considered one of the main scenarios of the possible impact of the repository to be the water pathway, mostly involving the ingestion of water or vegetable and animal products contaminated by irrigation water from a nearby contaminated well. Also considered was an agricultural pathway in which an inadvertent intruder mixes contaminated soil with native garden soil, as well as a scenario where the intruder during digging encounters an intact engineered barrier that is not further penetrated. Another conservative scenario considered rapid natural degradation of

the repository cap until complete failure after only 30 years, at which time the contaminant is allowed to move freely to the water table and then to migrate laterally by groundwater to a well only 2 m downgradient. This last scenario, which allowed water from the well to be used in a vegetable garden, resulted in a transit time for ^{137}Cs through the 4 to 5 m thick unsaturated zone of at least 423 years, and concentrations that produced potential doses that remained always below the lower limit of 0.25 mSv allowed by CNEN. Since the calculated maximum concentrations in groundwater below the repository always remained below the allowed concentrations at any time, the groundwater pathway was not considered important.

A reassessment of the Goiânia repository was carried out in 2002 using a hybrid numerical-analytical approach based on the standard advection-dispersion equation assuming steady-state downward flow through the repository, with the contaminant subject to equilibrium sorption and radioactive decay, and with a certain fraction of the waste being stable and not subject to leaching (Heilbron et al., 2002). The 2002 reassessment confirmed the 1995 results in that the ^{137}Cs water pathways related to a possible residential scenario near the site were found to be negligible, mostly again because of the long residence time in the unsaturated zone below the repository, which hence served as a natural barrier. The maximum ^{137}Cs concentration at any time below the repository was again found to be below the maximum value of 25,000 Bq/m^3 (about 6.8 x10^{-7} Ci/m^3), which would result in a dose for an individual of 0.25 mSv/y. The 2002 reassessment also found that of the three intrusion scenarios considered in 1995, the potentially most hazardous case would be the agriculture scenario. But since this would occur only after the assumed complete degradation of the concrete (300 to 500 years), the results would still not be important since after 280 years the doses would be lower than the allowed limit of 1 m Sv/y due to natural decay of ^{137}Cs. If one were to neglect this possibility (i.e., degradation of concrete during a period of time less than 300 years), the most important scenario would be the post-drilling scenario after an institutional control period of 50 years. The calculations were consistent with a 7-year environment monitoring plan (EMP) of the site, which showed that it was very unlikely to find in the future dangerous concentrations of ^{137}Cs in the aquifer for population living near the site. All concentrations were found to be below the detection limit of 200 Bq/m^3 (about 5.4x10^{-9} Ci/m^3).

In this paper we provide another reassessment, as mandated by CNEN, in which HYDRUS-1D is used to follow ^{137}Cs transport from the repository through the unsaturated zone to underlying groundwater. An important part of the current study is an assessment of the possible effects of degradation of the concrete cap on transient infiltration into and through the repository. Modeling of fluid flow through the entire repository assembly was done in two steps. The first step focused on fluid flow through the cover over a period of 600 years, rather than only 400 years as in the first two assessments, as well as partial degradation of the upper concrete liner covering the waste. In a second step, water flow and ^{137}Cs transport through the waste, the lower concrete liner and the vadose zone was followed using the infiltration rates obtained from the first step. We also briefly considered the effects of possible preferential flow through the waste.

SIMULATION METHODOLOGY

Simulations using HYDRUS-1D assumed applicability of the Richards equation for flow in variably-saturated media as follows:

$$\frac{\partial \theta(h)}{\partial t} = \frac{\partial}{\partial z}\left[K(h)\left(\frac{\partial h}{\partial z} - 1\right)\right] - S(h) \tag{1}$$

where θ is the volumetric water content, h is the pressure head, K is the unsaturated hydraulic conductivity, $S(h)$ is a water sink term (in our study associated with root water uptake), z is the vertical coordinate (positive downwards), and t is time. The soil hydraulic functions $\theta(h)$ and $K(h)$ in Eq. (1) were described using the original constitutive relationships of van Genuchten (1980):

$$S_e(h) = \frac{\theta(h) - \theta_r}{\theta_s - \theta_r} = \left(1 + |\alpha h|^n\right)^{-m} \qquad (m = 1 - 1/n) \tag{2}$$

$$K(h) = K_s S_e^{0.5}[1 - (1 - S_e^{1/m})^m]^2 \tag{3}$$

where S_e is effective saturation, θ_r and θ_s are the residual and saturated water contents, respectively, K_s is the saturated hydraulic conductivity, and α and n are quasi-empirical shape parameters.

The root water uptake term $S(h)$ in Eq. (1) was described with the equation (Feddes et al., 1978)

$$S(h) = \alpha_w(h)\beta(z)T_p \tag{4}$$

in which $\alpha_w(h)$ is the water stress response function ($0 \le \alpha \le 1$), $\beta(z)$ represents the normalized root density distribution in the profile, and T_p is the potential transpiration rate. For $\alpha_w(h)$ we used the piecewise linear reduction function by Feddes et al. (1978) using the default parameter values of grass as embedded within HYDRUS-1D.

Transport of the Cs radionuclide was modeled at first using the equilibrium advection-dispersion equation accounting for decay in both the liquid and solid phases:

$$\frac{\partial(\theta RC)}{\partial t} = \frac{\partial}{\partial z}(\theta D \frac{\partial C}{\partial z}) - \frac{\partial qC}{\partial z} - \mu RC \tag{5}$$

where C is the solution concentration, R is the solute retardation factor, D is the solute dispersion coefficient, q is the volumetric fluid flux, and μ is the radionuclide decay rate coefficient. The retardation factor R for linear equilibrium sorption is given by

$$R = 1 + \frac{\rho K_d}{\theta} \tag{6}$$

in which ρ is the dry soil bulk density and K_d the distribution coefficient of ^{137}Cs between the liquid and solid phases. For the dispersion coefficient D we used the standard equation

$$D = D_o\tau + \lambda\left|\frac{q}{\theta}\right| \tag{7}$$

in which D_o is the diffusion coefficient of ^{137}Cs in water, τ is the tortuosity factor described here as a function of the water content using the equation of Millington and Quirk (1961), and λ the dispersivity.

Tables 1 and 2 summarize the main soil physical and chemical parameters, respectively, used in the simulations. For the soil cover we used soil hydraulic parameters from a typical Cerrado soil in the Goiânia area of Brazil (Batalha et al., 2010) containing 53% of sand, 10% of silt and 37% clay. The initial

Table 1. Soil physical properties of the repository system used in the simulations.

Layer	Depth (m)	θ_r ($cm^3\ cm^{-3}$)	θ_s ($cm^3\ cm^{-3}$)	α (cm^{-1})	n (–)	K_s ($cm\ day^{-1}$)
Top soil	0–0.50	0.067	0.386	0.0267	1.31	13.2
Upper concrete liner	0.50–0.70	0.000	0.204	0.00142	1.52	0.000864*
Waste layer	0.70–5.08	0.070	0.365	0.0281	1.18	5.99
Lower concrete liner	5.08–5.28	0.000	0.306	0.00142	1.52	0.0864
Vadose zone	5.28–10.28	0.078	0.409	0.0232	1.29	7.47

*Initial value before degradation

Table 2. Soil chemical properties of the repository system used in the simulations.

Layer	Depth below upper concrete liner (m)	D_o ($cm^2\ day^{-1}$)	ρ_b ($cm^3\ g^{-1}$)	λ (cm)	K_d ($cm^3\ g^{-1}$)	μ_w, μ_s (day^{-1})
Waste layer	0–4.38	1.0	1.72	25.0	463	6.33×10^{-5}
Lower concrete liner	4.38–4.58	1.0	1.60	25.0	10.0	6.33×10^{-5}
Vadose zone	4.58–9.58	1.0	1.30	25.0	430	6.33×10^{-5}

hydraulic parameters for the upper reinforced concrete liner were taken from literature values, mostly those by Schneider et al. (2012). We assumed that degradation of the concrete occurred slowly but steadily, starting after 10 years of operation of the repository. The main effect of concrete degradation, in terms of the long-term flow rates through the repository system and underlying vadose zone, is the change in the saturated hydraulic conductivity, K_s, of the liner. We assumed that after 10 years of operation, K_s would increase slowly but continuously in a logarithm manner from the initial value of 10^{-10} m/s (0.000864 cm/day, or 0.315 cm/year) after 10 years to 10^{-9} m/s after 225 years and 10^{-8} m/s after 400 years, to approximately the same value as for the waste.

The contaminated waste layer in the repository was taken to be 4.38 m thick, situated over a 20-cm thick concrete liner and a 5-m thick vadose zone to the average water table. Hydraulic properties of the waste layer were measured (Pereira, 1996), including the bulk density (average value of 1.70 g/cm^3) and a value of 463 cm^3/g for the K_d of that layer. The relatively high bulk density of the waste reflected compaction of the ^{137}Cs contaminated soils. The concrete liner below the waste was assumed to have the same unsaturated hydraulic properties as the degraded upper concrete liner, except for a slightly higher porosity and higher conductivity. Our reasoning here was that the flow rate into and through the repository was controlled mostly only by the very low fluid flow rate through the upper liner into the waste, with the conductivity of the lower liner not having not much of an effect anymore so that a constant value could be uses (equal to K_s of the upper liner after degradation). We further used a partitioning coefficient (K_d) of 10 cm^3/g for the concrete (Aguiar, 2006). Hydraulic properties and K_d of the vadose zone were measured (Pereira, 1996), with a bulk density of 1.30 g/cm^3 and a mean value of 430 cm^3/g for the distribution coefficient, K_d.

Potential evapotranspiration (E_p) rates needed for the simulations were obtained with the equation of Hargreaves (1975) using 10 years of temperature and precipitation data from a local weather station. Results are shown in Figure 3. The E_p data were repeated several times as needed for longer-term calculations.

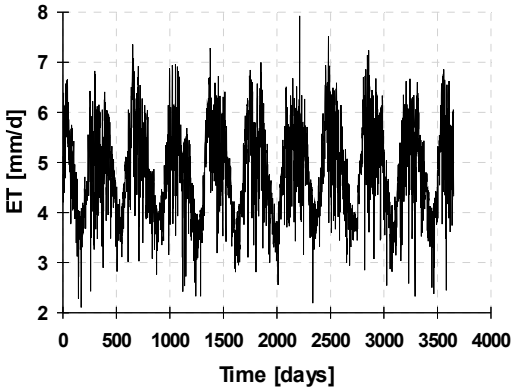

Fig. 3. Calculated potential evapotranspiration (E_p) rates during a ten-year time period at Goiânia.

WATER FLOW SIMULATIONS

Modeling of the repository was done in two steps (Fig. 4). First flow rates through the tops soil cover and upper concrete liner into the repository were studied, assuming some degradation of the concrete liner, during a time period of 600 years. Fluxes through the upper liner into the repository obtained in this manner were used next to estimate ^{137}Cs transport rates from the waste vertically down towards the water table.

A major challenge was to accurately estimate downward infiltration rates into the waste through the 70-cm cap of the repository, i.e., 50 cm topsoil covered by grass and the upper concrete liner that presumably undergoes decay. Degradation of the concrete would have mostly an effect on the saturated hydraulic conductivity (K_s), with the effects on porosity (or θ_s) and the other hydraulic parameters (notably θ_r, α and n) being far less important in terms of affecting fluid flow rates through the repository. Figure 5 shows how the K_s value of the upper concrete liner affected infiltration rates into the waste. Infiltration rates up to about 15 cm/year were determined nearly exclusively by the permeability of the liner, while at higher K_s values the local atmospheric conditions and moisture dynamics in the top soil determined the infiltration rate. The final asymptotic value for the flow rate was about 65 cm/year when the conductivity of the upper liner approached the value of the waste after 400 years (not further shown in Fig. 5).

The calculations for Fig. 5 were carried out using a seepage face as the lower boundary of the cap, thus assuming limited direct capillary contact between the waste and the upper liner. The seepage face boundary at the bottom of the concrete liner was set at zero pressure head, which hence allowed water

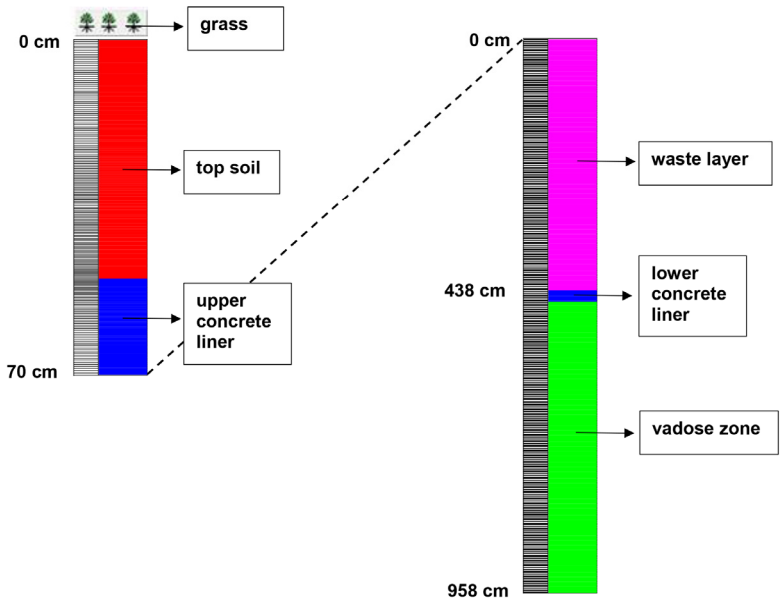

Fig. 4. Assumed profiles for simulations of flow through the soil cover and upper concrete liner (left plot), and of flow and Cs transport through the waste and underlying vadose zone (right plot), including the adopted finite element discretizations (please note that the left and right plot have different spatial scales).

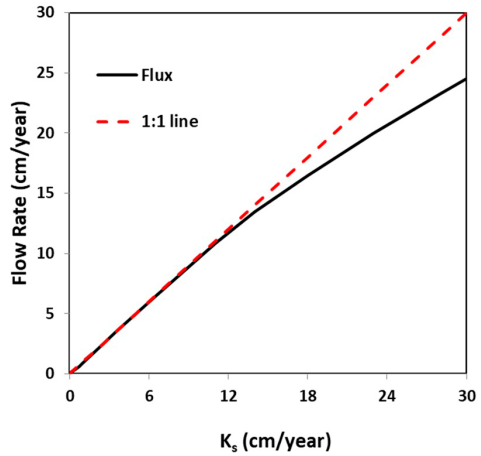

Fig. 5. Effect of the saturated hydraulic conductivity (K_s) of the upper concrete liner on the rate of infiltration into the waste.

to slowly move (drip) from the liner into the waste (or allowing water to evaporate from the liner). Using boundary pressure head values of –10 or –60 cm for the seepage face did not have much effect on the infiltration rates, as did not any changes in the values of θ_r, θ_s, α and n, generally leading to only a few percentages higher (notably with higher θ_s values) or lower (with higher α values) flow rates. The results in Figure 4 were obtained with a root distribution that declined linearly from the soil surface to zero at the soil-liner interface at a depth of 50. Changing the root distribution to only the upper 30 cm also did not materially affect the comparison between K_s and net infiltration, except for very small increases in the extremely low rates (those less than about 1 cm/year in Fig. 5).

Once the results in Fig. 5 were established, we calculated the flow regime through the waste, the lower concrete liner and the underlying vadose zone. Figure 6 shows the simulated pressure head and water content distributions during the assumed 600-year life span of the repository. As initial condition for the pressure head we used the steady-state profile calculated with an upper boundary flux approximately equal to the saturated hydraulic conductivity (K_s) of the upper liner before degradation, consistent with Fig. 4. Figure 6 shows that, as the upper liner slowly degraded, more moisture would enter the repository and increase the water contents and fluid flow rates.

CESIUM TRANSPORT SIMULATIONS

Estimated infiltration rates into the repository were used next for the ^{137}Cs transport calculations. Figure 7 shows calculated ^{137}Cs concentrations of fluid leaving the waste and the lower concrete liner into the underlying vadose zone. Notice that the concentrations are already very much lower than those in the waste layer, mostly because of the very low fluid flow rates and the relatively high K_d value (463 cm^3/g) for ^{137}Cs in the waste. Figure 8 further shows the Cesium distributions at three locations below the lower concrete liner, i.e., at locations N1 (12 cm), N2 (23 cm) and N3 (34 cm) below the liner. Notice that concentrations considerable decreased in time because of slow movement and radioactive decay. ^{137}Cs concentrations eventually approach zero because of the decay.

For completeness we also present, in Fig. 9 on a semi-log scale, the entire ^{137}Cs concentration profiles in the waste and underlying vadose zone. Notice again the slowly moving concentration front due to the high K_d value of the soil below the repository (Table 2), with the retardation factor being about 1530, as well as rapidly decreasing concentrations due to radioactive decay. Radionuclides hence remained restricted nearly entirely to the upper 50 cm of the vadose zone. These results suggest that very little if any radioactive material will reach the water table during the life span of the repository.

All of the calculations thus far assumed applicability of the standard Richards equation for flow in variably-saturated media, the equilibrium advection-dispersion equation for Cesium transport, and the presence of slowly degrading concrete liners.

These relatively ideal conditions may not necessarily be met in practice. For this reason we also considered two scenarios that would alter the above standard approach: More rapidly degrading concrete liners, and preferential flow through the waste layer and underlying vadose zone.

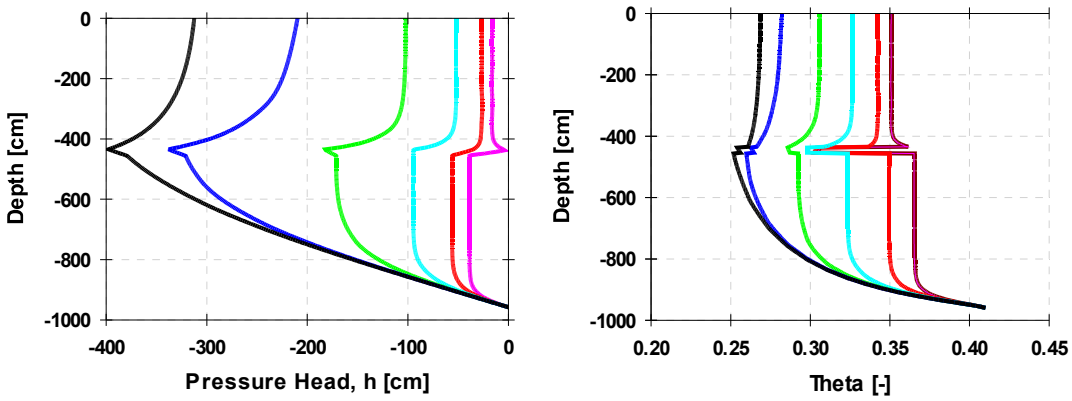

Fig. 6. Calculated pressure head and water content distributions in the repository (below the upper concrete liner) and underlying vadose zone. Distributions are given at every 100 years from left (t = 0, representing the initial conditions) to right (t = 600 years). The distributions after 500 and 600 years on the right were essentially identical.

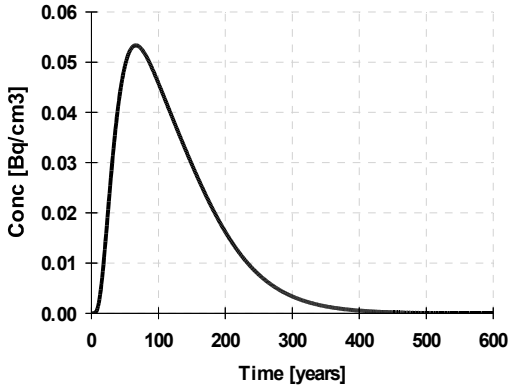

Fig. 7. Calculated ^{137}Cs concentrations just below the lower concrete liner at the bottom of the waste layer.

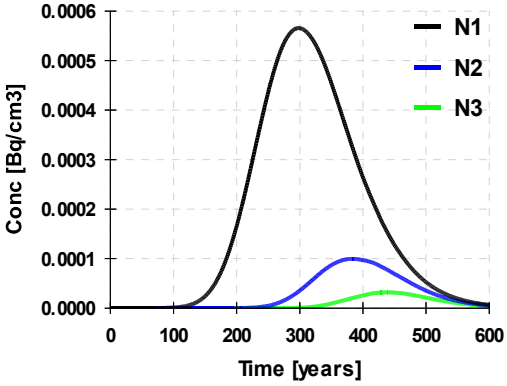

Fig. 8. Calculated ^{137}Cs concentrations in the vadose zone 12, 23 and 34 cm below the lower concrete liner of the Goiânia repository.

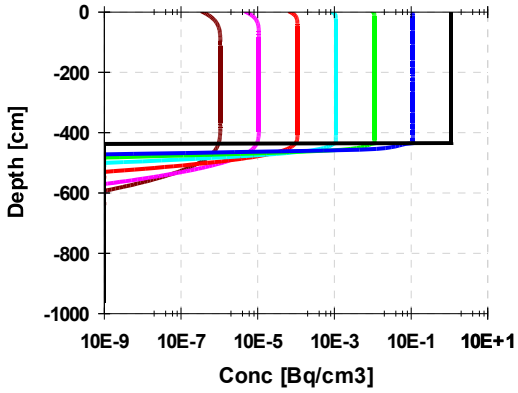

Fig. 9. Calculated ^{137}Cs concentration within the waste, the lower concrete liner and underlying vadose zone. Distributions are given every 100 years from right (t = 0, representing the initial condition) to left (t = 600 years).

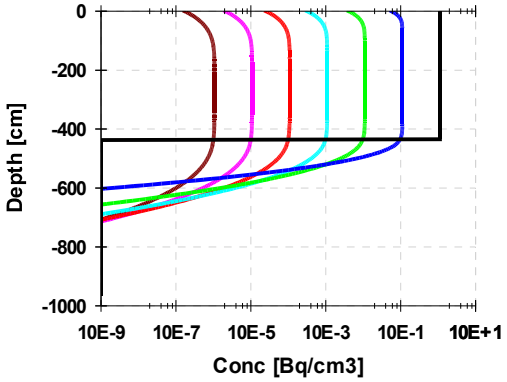

Fig. 10. Calculated ^{137}Cs concentration at three locations in the vadose zone below the lower concrete liner. Distributions are given every 100 years from right (t = 0, representing the initial condition) to left (t = 600 years).

For the first scenario we assumed that the concrete liners completely failed after installation, possible due to the development of cracks and/or dissolution or other alterations of the upper liner due to repeated wetting and drying cycles and perhaps the effect of plant roots. We used for these calculations a net infiltration rate of 65 cm/year (0.187 cm/day), which we obtained for the case when the saturated hydraulic conductivity (K_s) of the upper liner would not limit the long-term downward infiltration rate as derived from the atmospheric boundary conditions (Fig. 3). Figure 10 shows the resulting ^{137}Cs distribution in the profile below the upper concrete liner. The calculations indicate that the concentration front now moves slightly deeper into the vadose zone, but still not to depths and at concentrations that should be a concern.

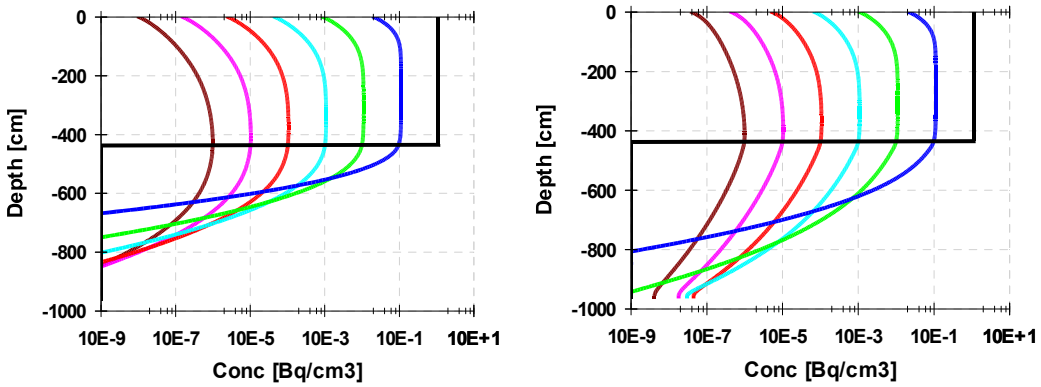

Fig. 11. Mobile concentration distributions in the repository and underlying vadose zone obtained with the dual porosity model using the parameters listed in Table 3 for Case A (left plot) and Case B (right plot). Distributions are given every 100 years from right (t = 0, representing the initial condition) to left (t = 600 years).

Table 3. Dual-porosity model parameter values used for the simulation in Figure 10.

Layer	Depth below upper concrete liner (m)	Case A			Case B		
		θ_{im} (–)	f (–)	α_s (year^{-1})	θ_{im} (–)	f (–)	α_s (year^{-1})
Waste layer	0–4.38	0.20	0.20	0.01	0.20	0.20	0.1
Lower concrete liner	4.38–4.58	0.20	0.50	0.1	0.20	0.20	1.0
Vadose zone	4.58–9.58	0.20	0.50	0.1	0.20	0.20	1.0

For the second scenario we superimposed on the first scenario the effects of possible preferential flow in both the waste layer and vadose zone. This since the waste layer was very heterogeneous by containing separate drums with the ^{137}Cs contaminated material, which likely caused infiltrating water to bypass much of the radioactive waste. Preferential transport was simulated using a mobile-immobile type dual-porosity model of the form (van Genuchten and Wagenet, 1989)

$$\frac{\partial \beta \theta R C_m}{\partial t} = \frac{\partial}{\partial x}\left(\theta_m D_m \frac{\partial C_m}{\partial z}\right) - \frac{\partial q c_m}{\partial z} - \alpha_s (c_m - c_{im}) - \beta \theta R \mu C_m \tag{8}$$

$$\frac{\partial (1-\beta)\theta R C_{im}}{\partial t} = \alpha_s (c_m - c_{im}) - (1-\beta)\theta R \mu C_{im} \tag{9}$$

in which

$$\beta = \frac{\theta_m + f \rho_b K_d}{\theta + \rho_b K_d} \tag{10}$$

where the subscripts m and im refer to the mobile and immobile regions of the soil (or concrete) such that $\theta_m + \theta_{im} = \theta$, f is the fraction of ^{137}Cs sorption sites located in the mobile region, and α_s is a first-order mass transfer coefficient governing the rate of solute exchange between the mobile and immobile liquid regions.

Figure 11 gives two plots based on dual-porosity simulations using the parameters listed in Table 3. For θ_{im} we selected a reasonably large (and hence conservative) value that always remained below the minimum water contents in the three layers. The value of f similarly is a fairly conservative value suggesting that 80% of the sorption sites are not in direct contact with the moving fluid. This again appears very reasonable for the heterogeneous waste material where water likely will bypass the containers filled with contaminated material. Finally, two values for the mass transfer coefficient α_s were used to cover relatively fast and slow solute exchange between the mobile and immobile liquid domains (Cases A and B in Fig. 11), based in part by an inventory by Maraqa (2001) of previously published values. The lower value of α_s for the waste layer (as compared to the vadose zone) was again motivated by the likely imperfect contact between the waste and presumed preferential fluid paths through the repository.

The results in Fig. 11 indicate that preferential flow in certain situations will lead to faster movement of the concentration front through the vadose one, and hence earlier breakthrough at the water table. However, the concentrations, as obtained especially for Case B in Fig. 11, are extremely low and well below the detection limit for ^{137}Cs. Also, interestingly, is the effect of preferential flow in the waste layer as predicated by the selected values of f and α_s, leading to considerable bypassing of the waste. Preferential flow in that layer causes less rapid transport of ^{137}Cs out of the contaminated waste, and hence less pollution of underlying layers. These results are consistent with an earlier study (Pontedeiro et al., 2010) showing that preferential flow through a mining waste disposal site will lead to less rapid pollution of the subsurface by considerably lowering the concentrations leaving the disposal site. This is in contrast to situations where contaminated water originates at the soil surface, for example through some industrial accident or as part of agricultural practices such as the surface application of pesticides, in which case preferential flow will lead to more rapid downward transport and contamination of the vadose zone and underlying groundwater (e.g., Jarvis et al. 2016; Mallants et al., 2011).

CONCLUSIONS

Decontamination of areas affected by the Goiânia radiation accident produced about 3,500 m^3 of solid radioactive wastes, which were disposed of in two near-surface low-level repositories built in concrete in 1995. In this paper we presented an analysis over a time period of 600 years of the repository containing the higher ^{137}Cs levels. Using HYDRUS-1D, we first obtained estimates of water infiltrating through the soil cover on top of the repository into and through the waste and its concrete liners and the underlying vadose zone towards groundwater. For the calculations we used atmospheric boundary conditions accounting for local precipitation and evapotranspiration rates, including root water uptake by the grass cover. Special concern was possible degradation of the concreate liners on top and below the waste material. We used HYDRUS-1D next to simulate long-term water fluxes and ^{137}Cs transport from the repository towards groundwater, thus providing an assessment of potential consequences to the environment and long-term exposure to the public. Results indicate that very little if any radioactive material will reach the water table during the lifespan of the repository.

Complete failure of the concrete liners from the very beginning also would not lead to any significant ^{137}Cs movement to groundwater below the repository. We note that recent tests (in 2017) revealed no noticeable degradation of the concrete liners, thus indicating that the adopted approach with concrete degradation was a very conservative scenario that may well have overestimated actual flow rates through the repository. Additional simulations assuming preferential flow caused faster transport to the groundwater table, but at concentrations far below the detection limit. In all, the current study confirms previous assessments by the Brazilian Nuclear Energy Commission (Heibron et al., 1996, 2002) that it is very unlikely to find in the future any unsafe concentrations of ^{137}Cs in the aquifer for populations living near the site.

REFERENCES

Aguiar, L.A., 2006. Avaliação de Risco de um Repositório Próximo à Superfície na Fase Pós – Fechamento em Cenários de Liberação de Radionuclídeos por Infiltração de Água. DSc Thesis, Department of Nuclear Engineering, COPPE, Federal University of Rio de Janeiro, UFRJ, Rio de Janeiro, Brazil, http://antigo.nuclear.ufrj.br/DScTeses/Lais/tese_doutorado_lais.pdf (In Portuguese.)

Batalha, M.S., Bezerra, C.R., Pontedeiro, E.M., van Genuchten, M.Th., 2010. Environmental fate of natural radioactive contaminants in fertilizers and phosphogypsum. In: Proc. ENCIT 2010, 13th Brazilian Congress of Thermal Sciences and Engineering, Dec. 5–10, 2010, Uberlandia, MG, Brazilian Soc. Mech. Sci. & Eng., ABCM, Brazil.

Feddes, R.A., Kowalik, P.J., Zaradny, H., 1978. Simulation of Field Water Use and Crop Yield. John Wiley & Sons, New York, NY.

Hargreaves, G.H., 1975. Moisture availability and crop production. Trans. Am. Soc. Agric. Eng., 18, 5, 980–984.

Heilbron, P.F.L, Tranjan Filho, A., Xavier, A.M., 1995. Safety Analysis Report (SAR) of the Concrete Waste Container (CGP). Internal Report. Brazilian Nuclear Energy Commission (CNEN), Rio de Janeiro, Brazil.

Heilbron, P.F.L., Rochedo, E., Xavier, A.M., 1996. Preliminary safety assessment of the first Brazilian repository. In: Proc. Int. Symp. Experience in the Planning and Operation of Low Level Waste Disposal Facilities. Int. Atomic Energy Agency (IAEA), Vienna, 17–21 June 1996, IAEA-SM-341/8, pp. 395–404.

Heilbron, P.F.L, Pontedeiro, E.M., Cotta, R.M., Pérez-Guerrero, J., Ruperti, N.J., 2002. Reassessment of the safety of the Goiânia repositories. Internal Report. Brazilian Nuclear Energy Commission (CNEN), Rio de Janeiro, Brazil, http://www.crcn-co.cnen.gov.br/documentos/anaseg-repo-1995-2002.pdf.

IAEA, 1988. The Radiological Accident in Goiânia. Int. Atomic Energy Agency (IAEA), Vienna, Austria, STI/PUB/815, 152 p. http://www-pub.iaea.org/mtcd/publications/pdf/ pub815_web.pdf.

Jacques, D., Maes, N., Perko, J., Seetharam, S.C., Phung, Q.T., Patel, R., Soto, A., Liu, S., Wang, L., De Schutter, G., Ye, G., van Breugel, K., 2013. Concrete in engineered barriers for radioactive waste disposal facilities - Phenomenological study and assessment of long term performance. In: Proc. ASME 2013 15th International Conference on Environmental Remediation and Radioactive Waste Management, pp. 1–10.

Jacques, D., Perko, J., Seetharam, S.C., Mallants, D., 2014. A cement degradation model for evaluating the evolution of retardation factors in radionuclide leaching models. Applied Geochemistry, 49, 143–158.

Jarvis, N., Koestel, J., Larsbo, M., 2016. Understanding preferential flow in the vadose zone: Recent advances and future prospects. Vadose Zone J., 15, 12. DOI: 10.2136/vzj2016.09.0075.

Mallants, D., van Genuchten, M.Th., Šimůnek, J., Jacques, D., Seetharam, S., 2011. Leaching of contaminants to groundwater. In: Swartjes, F.A. (Ed.): Dealing with Contaminated Sites; from Theory to Practical Application. Chapter 18. Springer Verlag, Dordrecht, The Netherlands, pp. 787–850.

Maraqa, M.A., 2001. Prediction of mass-transfer coefficient for solute transport in porous media. J. Contam. Hydrol., 53, 153–171.

Millington, R.J., Quirk, J.M., 1961. Permeability of porous solids. Trans. Faraday Soc., 57, 1200–1207.

Naveira-Cotta, C.P., Pontedeiro, E.M., Cotta, R.M., Su, J., van Genuchten, M.Th., 2013. Environmental impact assessment of liquid waste ponds in uranium milling installations. Waste Biomass Valor., 4, 197–211. DOI: 10.1007/s12649-012-9156-0.

Pabalan, R.T., Glasser, F.P., Pickett, D.A., Walter, G.R., Biswas, S., Juckett, M.R., Sabido, L.M., Myers, J.L., 2009. Review of literature and assessment of factors relevant to performance of grouted systems for radioactive waste disposal. CNWRA 2009-001. Center for Nuclear Waste Regulatory Analyses (CNWRA), San Antonio, Texas.

Pashoa, A.S., Tranjan Filho, A., Rosenthal, J.J., 1993. Revisiting Goiânia: Toward a final repository for radioactive waste. Topical Report. IAEA Bulletin 1/1993, pp. 28–31.

Pontedeiro, E.M., van Genuchten, M.Th., Cotta, R.M., Šimůnek, J., 2010. The effects of preferential flow and soil texture on risk assessments of a NORM waste disposal site. J. Hazard. Mater., 174, 648–655. DOI: 10.1016/j.jhazmat.2009.09.100.

Pereira, J.C.A., 1996. Determinação da Velocidade de Migração e das Razões de Partição de 137Cs em Solos da Região do Futuro Repositório de Rejeitos de Abadia de Goiás, Goiás. MS. Thesis, Departamento de Química, Pontifícia Universidade Católica do Rio de Janeiro, Brazil. (In Portuguese.)

Roberts, L., 1987. Radiation accident grips Goiânia. Science, 238, 4830, 1028–1031. DOI: 10.1126/science.3685964.

Robinson, B.A., Chu, S., Lu, Z., 2012. Simulation of radionuclide transport through unsaturated fractured rock: Application to Yucca Mountain, Nevada. Vadose Zone J., 11, 4. DOI: 10.2136/vzj2011.0142

Schneider, S., Jacques, D., Mallants, D., 2012. Estimating unsaturated hydraulic properties of concrete C-15-A and mortar M1. Mater. Res. Soc. Symp. Proc., Vol. 1475. DOI: 10.1557/opl.2012.601.

Šimůnek, J., van Genuchten, M.Th., Šejna, M., 2016. Recent developments and applications of the HYDRUS computer software packages. Vadose Zone J., 15. DOI: 10.2136/vzj2016.04.0033.

Tsang, C.-F. (Ed.), 1987. Coupled Processes Associated with Nuclear Waste Repositories. Academic Press, London, UK.

van Genuchten, M.Th., 1980. A closed-form equation for predicting the hydraulic conductivity of unsaturated soils. Soil Sci. Soc. Am. J., 44, 5, 892-898.

van Genuchten, M.Th., Wagenet, R.J., 1989. Two-site/two-region models for pesticide transport and degradation: Theoretical development and analytical solutions. Soil Sci. Soc. Am. J., 53, 5, 1303–1310.

Yu, C., Gnanapragasam, E., Biwer, B.M., Kamboi, S., Cheng, J.-J., Yuan, Klett, T., LePoire, D., Ziele, A.J., Chen, S.Y., Williams, W.A., Wallo, A., Domotor, S., Mo, T., Schwartzman, A., 2007. User's manual for RESRAD-OFFSITE. Version 2. ANL/EVS/TM/07-1. Argonne National Laboratory, Argonne, IL.

Received 9 May 2017
Accepted 31 August 2017

Note: Colour version of Figures can be found in the web version of this article.

J. Hydrol. Hydromech., 66, 2018, 2, 211–226
DOI: 10.1515/johh-2017-0049

The HPx software for multicomponent reactive transport during variably-saturated flow: Recent developments and applications

Diederik Jacques[1*], Jiří Šimůnek[2], Dirk Mallants[3], Martinus Th. van Genuchten[4, 5]

[1] Engineered and Geosystems Analysis Unit, Belgian Nuclear Research Centre, 2400 Mol, Belgium.
[2] Department of Environmental Sciences, University of California Riverside, Riverside, CA 92521, USA. E-mail: jsimunek@ucr.edu
[3] CSIRO, Urrbrae, SA 5064, Australia. E-mail: dirk.mallants@csiro.au
[4] Center for Environmental Studies, CEA, São Paulo State University, Rio Claro, SP 13506-900, Brazil.
E-mail: rvangenuchten@hotmail.com
[5] Department of Nuclear Engineering, Federal University of Rio de Janeiro, Rio de Janeiro, RJ, 21945-970, Brazil.
[*] Corresponding author. E-mail: diederik.jacques@sckcen.be

Abstract: HPx is a multicomponent reactive transport model which uses HYDRUS as the flow and transport solver and PHREEQC-3 as the biogeochemical solver. Some recent adaptations have significantly increased the flexibility of the software for different environmental and engineering applications. This paper gives an overview of the most significant changes of HPx, such as coupling transport properties to geochemical state variables, gas diffusion, and transport in two and three dimensions. OpenMP allows for parallel computing using shared memory. Enhancements for scripting may eventually simplify input definitions and create possibilities for defining templates for generic (sub)problems. We included a discussion of root solute uptake and colloid-affected solute transport to show that most or all of the comprehensive features of HYDRUS can be extended with geochemical information. Finally, an example is used to demonstrate how HPx, and similar reactive transport models, can be helpful in implementing different factors relevant for soil organic matter dynamics in soils. HPx offers a unique framework to couple spatial-temporal variations in water contents, temperatures, and water fluxes, with dissolved organic matter and CO_2 transport, as well as bioturbation processes.

Keywords: HYDRUS; HPx; Numerical modeling; Reactive transport; Organic matter; Bioturbation.

INTRODUCTION

Mathematical, process-based simulation models are indispensable tools for elucidating the role of coupled processes in soil systems, including their functioning and providing ecosystem services (Vereecken et al., 2016). Coupled multicomponent reactive transport models for the so-called critical zone (Brantley et al., 2007) are essential tools to analyze nonlinear interactions between hydrological, geochemical and (micro)biological processes and to link the critical zone to other spheres of the earth system such as the hydrosphere, atmosphere, biosphere, and geosphere (Li et al., 2017; Steefel et al., 2005). During the last two decades, a number of tools have been developed to simulate such coupled processes in natural subsurface and engineered systems (Steefel et al., 2015). Numerous applications illustrate the enormous possibilities of these codes (e.g., see references in Li et al. (2017), Steefel et al. (2015)). They typically couple a water flow equation (such as the Richards equation for the vadose zone) with transport equations for heat and solutes based on the advection-dispersion equation, a thermodynamically based geochemical solver, and a kinetic reaction solver, while allowing for the coupling of multiple parameters with a series of state variables (Figure 1). Because of the generic nature of such codes, they provide a flexible (in terms of model formulations) and extendible (in terms of model components) problem-solving environment to tackle important environmental and engineering problems. This paper focuses on the HPx simulator as developed within the HYDRUS computer software packages (Šimůnek et al., 2016). In this introduction we first introduce briefly two aspects which illustrate the need for such modeling tools.

Reactive transport models allow for the direct coupling of time-varying geochemical state variables with transport properties. In addition to the coupling of microstructural changes due to mineral dissolution and precipitation to porosity and hydraulic properties (Freedman et al. (2004), Wissmeier and Barry (2009), Xie et al. (2015)), fluid properties such as viscosity and density, which are linked to the hydraulic properties of porous media, depend upon the composition of the aqueous solution (Laliberté (2007), Laliberté and Cooper (2004), Sharqawy et al. (2010)). Biomass accumulation or biofilm production during microbiological reactions can also induce changes in hydraulic properties, which may potentially influence the coupled hydrological-physical-geochemical-biological processes operative in porous media and, consequently, such processes as flow paths, the performance of biofilters, and the transport of colloids (e.g., Bozorg et al. (2015a), Bozorg et al. (2015b), Carles Brangarí et al. (2017), Or et al. (2007), Rockhold et al. (2002), Yarwood et al. (2006)). The processes of precipitation and dissolution of minerals may be affected by microbiological processes, such as in the engineering practice of microbially induced calcium carbonate precipitation (Hommel et al., 2015; Martinez et al., 2014). Another process that can produce changes in porosity and the hydraulic properties is the migration of fines (solid mineral particles), which is influenced by both hydrodynamic and chemical factors (Bennacer et al., 2017; Mays and Hunt, 2007; Yu et al., 2013). Again, this process is relevant in many engineering applications, but also within the field of soil development. Finally, under saturated conditions, biogenic processes such as methanogenesis and denitrification may result in the formation of gas bubbles, which may result in a reduction of the hydraulic conductivity due to blocking of pore spaces (Amos and Mayer, 2006).

Organic matter dynamics in soils is a crucial process affecting many environmentally-related issues. Degradation produces inorganic carbon, which can be released into the atmosphere.

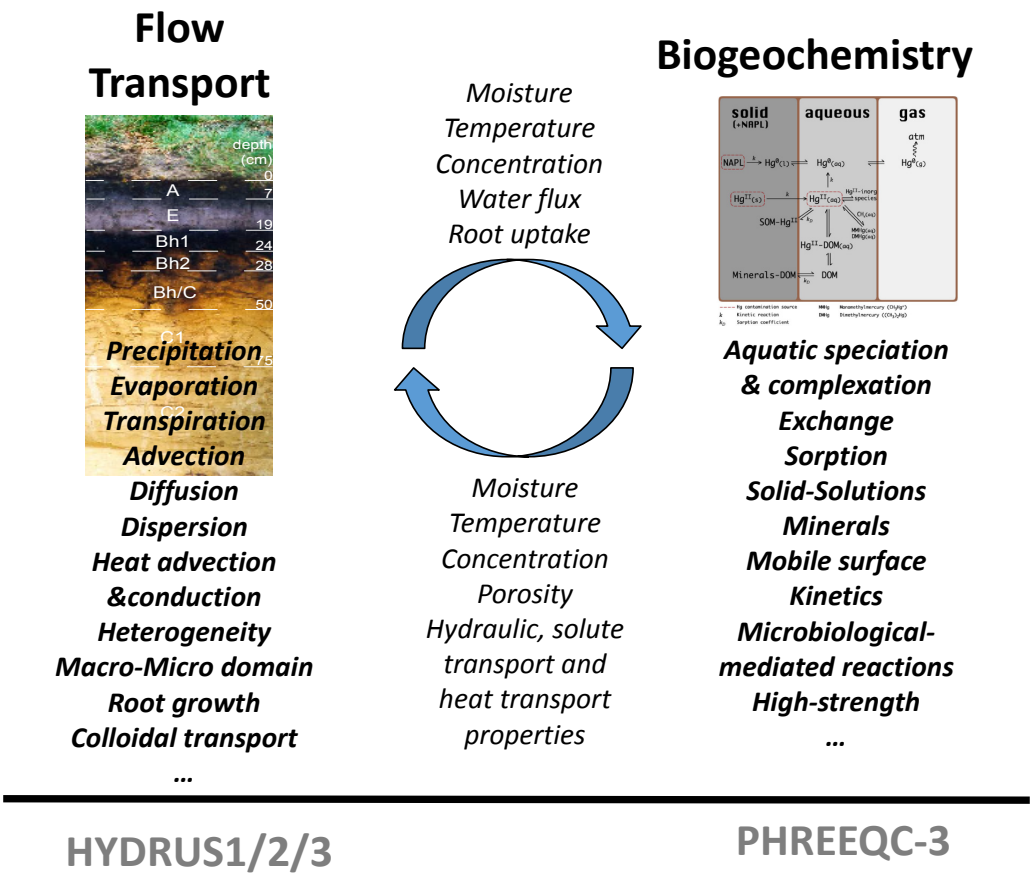

Fig. 1. Reactive transport models coupling water flow and solute transport with biogeochemical processes.

Consequently, CO_2 sequestration in soils may be a factor in controlling atmospheric CO_2, and thus climate change (Todd-Brown et al., 2013). And vice versa, climate change, together with land use, influences soil organic matter (SOM) dynamics (e.g. Batlle-Aguilar et al. (2011)). Dissolved organic matter (DOM) plays also an important role in many soil processes including contaminant transport (e.g., Maes et al. (2006), Paradelo et al. (2012)). For example, Leterme and Jacques (2015) showed that DOM concentrations are among the most sensitive factors in simulating Hg fate in soil systems.

As reported by Manzoni and Porporato (2009), a large number of models exist for simulating SOM dynamics. Many SOM models are so-called compartment models, which divide the heterogeneous nature of SOM into a number of homogeneous pools, and then simulate the fluxes between these pools. Some of these models have a rigid structure in the sense that the number of pools, the abiotic factors that must be considered, their functional forms, and the extent of biotic-abiotic interactions, are fixed. It is therefore not always possible to perform a structured comparison between different types of model formulations. Reactive transport models, on the other hand, provide a flexible structure that enables the introduction of different SOM degradation networks within the same simulation framework. In addition, existing compartment models sometimes strongly simplify flow and transport processes and/or the geochemistry involved, such as simplifying or ignoring pH and buffering effects on degradation or CO_2 geochemistry. For predictions that are more accurate, also within the framework of climate predictions, SOM models should consider temporarily and spatially variable abiotic factors such as temperature and moisture, nutrient dynamics, microbial activity, solid-water interactions, and transport processes of solid and dissolved organic matter and/or inorganic carbon (e.g., Schmidt et al. (2011), Tang and Riley (2015)). Reactive transport models should account for these factors and effects, such as illustrated in recent studies by Tang et al. (2013) and Riley et al. (2014).

The main objective of this paper is to give an overview of new capabilities of the HPx codes compared to the model descriptions given previously by Jacques et al. (2006) and Jacques et al. (2008a). We also wanted to illustrate some of these capabilities as used in several recent studies, as well as present an example involving different SOM degradation networks and bioturbation processes.

THE HPX REACTIVE TRANSPORT CODE

The HPx codes couple the HYDRUS-1D and HYDRUS (2D/3D) software packages (Šimůnek et al., 2016) with PHREEQC (Parkhurst and Appelo, 2013) using a sequential non-iterative coupling approach as explained by Jacques et al. (2006). HYDRUS-1D or HYDRUS (2D/3D) act as the solver for the hydrological and physical processes, including variable-saturated water flow, solute transport, diffusion in the gas phase, and heat transport, whereas PHREEQC is the solver for thermodynamic and kinetic geochemical processes. While the first versions of HPx used PHREEQC-2.4 (Jacques and Šimůnek, 2005; Jacques et al., 2006), the most recent versions 2.4 of HPx use PHREEQC 3.1. Two- and three dimensional flow and transport is included as well (Šimůnek et al., 2012).

Coupling with PHREEQC is performed using so called "hard coupling", which is in principle similar to the procedures available in the more recently developed wrappers iPhreeqc

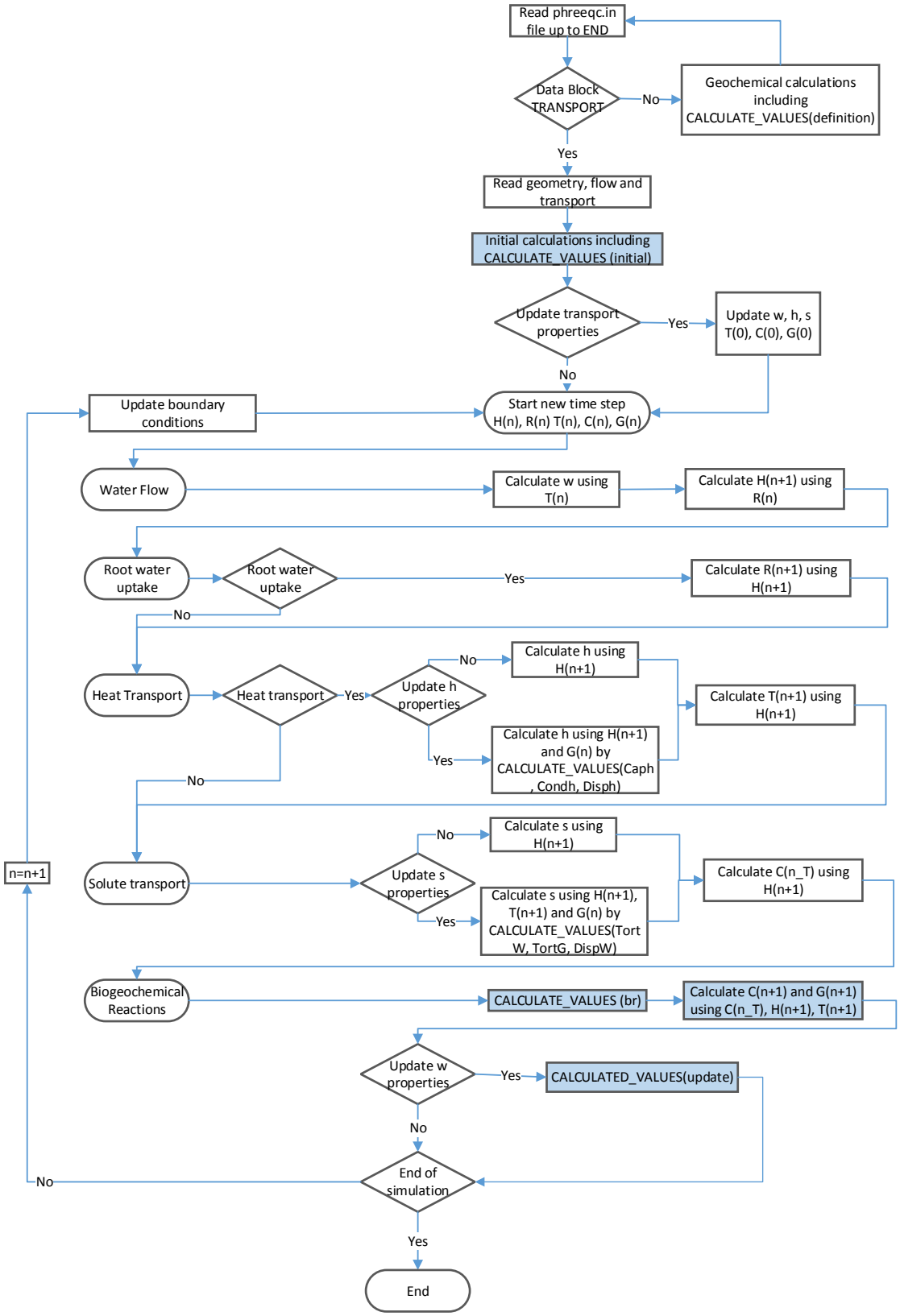

Fig. 2. Flow chart of HPx. The letters w, h, and s indicate parameters for water flow, heat transport, and solute transport, respectively. The variables H, R, T, C, and G indicate state variables for water flow, root water uptake, heat transport, solute transport, and biogeochemical processes, respectively. The boxes with blue background are steps run in parallel using OpenMP. CALCULATED_VALUE(type) indicates the execution of scripts labeled with type.

(Charlton and Parkhurst, 2011) and RMPhreeqc (Parkhurst and Wissmeier, 2015). Due to the hard coupling, HPx does not always include the latest version of PHREEQC. However, HPx includes additional flexibilities compared to the original PHREEQC, such as linking geochemical definitions (e.g., solution compositions, exchange sites, minerals, kinetic reactants) to the material distribution, or exchanging information between the flow model and the BASIC scripts (e.g., pressure heads,

velocities, and scaling factors). The geochemical input is defined using the standard PHREEQC input conventions using data blocks and identifiers, thereby allowing a direct implementation of the PHREEQC models into HPx. The scripting possibilities are now enhanced by introducing global variables or data tables, which can be used as inline variables or as BASIC scripting variables, using different types of scripting blocks to perform specific calculations, and introducing a specific version of BASIC (such as MyBasic; https://github.com/paladin-t/my_basic) with structured grammar for some specific calculations). Templates for generic types of problems can be generated in advance and then imported into additional input files that can be created during project execution using the INCLUDE$ statement. Geochemical calculations are performed in parallel using the OpenMP (www.openmp.org) shared memory approach and PHREEQC objects. The main object reads then the input and performs all initial calculations. The information (thermodynamic data and geochemical models) is copied to a user-defined number of additional objects representing chunks in the OpenMP formalism. The nodes are assigned evenly between the chunks. A dynamic schedule controls the calculations of the nodes in a chunk on the available threads on a computer. After the geochemical calculations, the information from different chunks is assembled and sent to the transport calculations or to the model output files. Because of the OpenMP implementation and the enhanced scripting possibilities, the current flow chart of HPx (see Figure 2) is an extended version of the chart described in Jacques et al. (2006).

Simulation output data now also contain variables, which are integrated over a part of the domain, such as over a particular soil material. HP2 makes it possible to obtain geochemical information along mesh lines or cross-sections at different times as defined in the standard HYDRUS (2D/3D) graphical user interface.

FLOW, TRANSPORT, AND BIOGEOCHEMICAL PROCESSES

Conceptual models

Figure 3 shows schematically the different physical water flow and solute transport models implemented in HPx. The software considers flow, transport, and the prevailing biogeo-

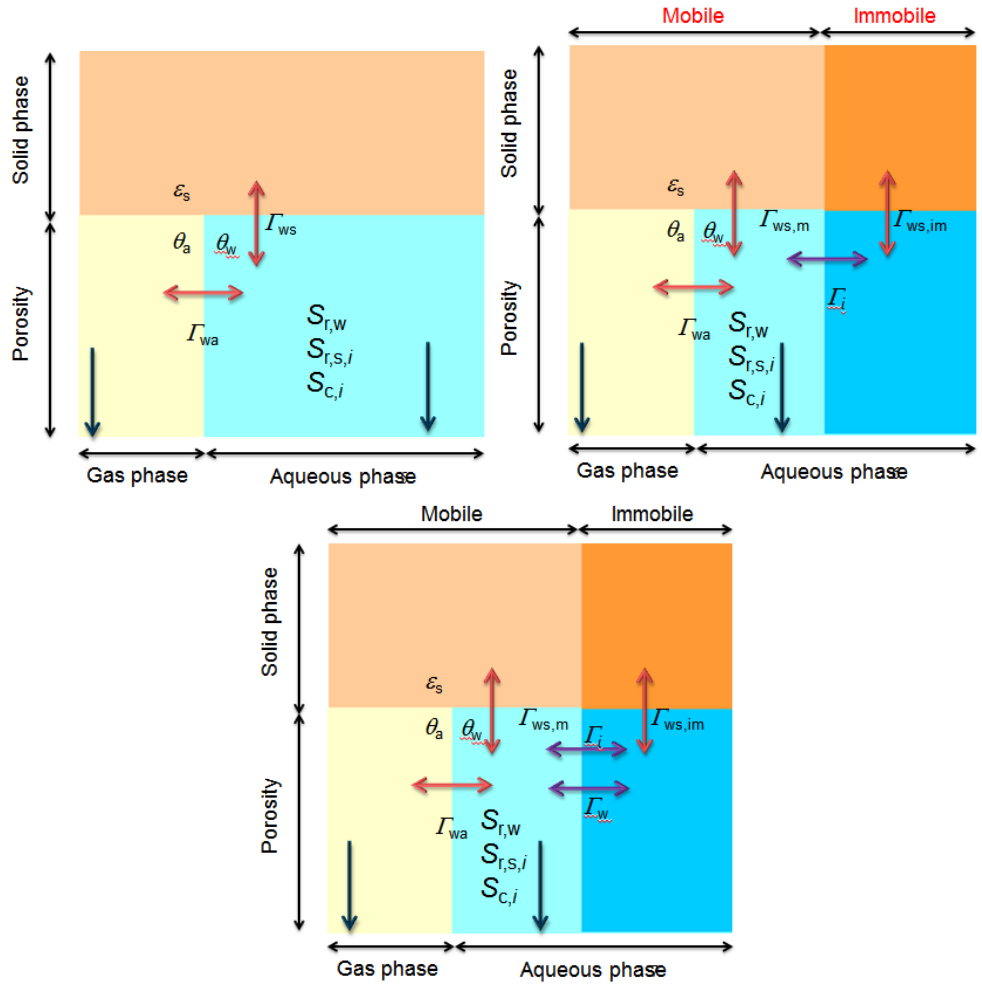

Fig. 3. Conceptual physical and geochemical models implemented in HPx. Black arrows represent transport processes within a single phase, and red arrows exchange processes between different phases. The top left, top right, and bottom plots indicate water flow, solute transport, and biogeochemical reactions in a single-porosity continuum, in a single-porosity continuum with an immobile solute domain, and in a dual-porosity model, respectively (ε_s - the solid content [dm^3 dm^{-3}], θ_a - the air content [dm^3 dm^{-3}], θ_w - the water content [dm^3 dm^{-3}], Γ_w - the water exchange between the immobile and mobile domains [dm^3 dm^{-3} T^{-1}]Γ_{wa} - the solute exchange between the aqueous phase and the gas phase [mol dm^{-3}T^{-1}], Γ_{ws} - the solute exchange between the aqueous phase and the solid phase [mol dm^{-3}T^{-1}], $\Gamma_{ws,m}$ - the solute exchange between the mobile aqueous phase and the solid phase [mol dm^{-3}T^{-1}], $\Gamma_{ws,im}$ - the solute exchange between the immobile aqueous phase and the solid phase [mol dm^{-3}T^{-1}], Γ_i - the solute exchange between the immobile and mobile domains [mol dm^{-3}T^{-1}], $S_{r,w}$ - root water uptake [dm^3 dm^{-3}T^{-1}], $S_{r,s,i}$ – root solute uptake [mol dm^3 T^{-1}], $S_{c,,i}$ – kinetic transformations in the aqueous phase [mol dm^{-3} T^{-1}]).

chemical processes at the continuum scale with three main phases being water (θ_w), air (θ_a) and the solid phase (ε_s) as shown in the figure. The water and solid phases in the dual porosity modeling options of the code are divided into two parts, with one part comprising the mobile phase in which water, heat and solutes are allowed to move, and another part being the immobile domain where water is assumed to be stagnant.

Variably-saturated water flow, multicomponent solute transport and heat transport are described using the Richards equation, the advection-dispersion equations (for multiple solutes), and (neglecting energy transported by vapor transport) the convection-dispersion equation, respectively. Transport of reactive gases, which is crucial for simulating biological processes or solid phase alterations such as carbonation of concrete (e.g., Phung et al., 2016) or weathering (Li et al., 2017), is either only by diffusion or advection. The latter is based on the assumptions of negligible air compressibility due to the fast exchange with the atmosphere, zero air flux at the bottom of the profile, and immediate matching of volume changes in the total water content by volume changes in the gas content.

Possible sinks of water in the flow domain are uptake by plants roots ($S_{r,w}$) and exchange between the mobile and immobile water phases (Γ_w), the latter only if dual-porosity water exchange is considered. Sinks or sources of solutes from the aqueous phase are via (i) exchange with roots ($S_{r,i}$ with i referring to a solute component), (ii) kinetic transformations such as radioactive decay, degradation, or redox reactions ($S_{c,i}$), (iii) exchange between the mobile and immobile water phases (Γ_i), and (iv) exchange with the gaseous (Γ_{wa}) or solid phases ($\Gamma_{ws,m}$ and $\Gamma_{ws,im}$) via thermodynamic speciation reactions or kinetic rate equations. The latter reactions represent processes such as sorption, ion exchange, surface complexation, gas-aqueous phase equilibria, and mineral dissolution and precipitation.

Mathematical models

Water flow in its most general form is described using a dual-porosity formulation of the Richards equation (Šimůnek and van Genuchten, 2008):

$$\frac{\partial \theta_m}{\partial t} = \frac{\partial}{\partial x_i}\left[K\left(K_{ij}^A \frac{\partial h}{\partial x_j} + K_{iz}^A \right)\right] - S_{r,w} - \Gamma_w \qquad (1)$$

$$\frac{\partial \theta_{im}}{\partial t} = \Gamma_w$$

where θ_m is the volumetric water content in the mobile domain [L^3L^{-3}], θ_{im} is the volumetric water content in the immobile domain [L^3L^{-3}], h is the pressure head [L], x_i (i = 1, 2, 3) are the spatial coordinates [L], t is time [T], $S_{r,w}$ is the root water uptake term [T^{-1}], Γ_w is the water exchange term [T^{-1}] driven by a first-order rate equation proportional to the difference in water contents or pressure heads between the mobile and immobile domains, K_{ij}^A are components of a dimensionless anisotropy tensor $\boldsymbol{K}^A$, and K is the unsaturated hydraulic conductivity function [LT^{-1}]. The single-porosity models assume that θ_m is equal to the total water content θ, in which case θ_{im} and Γ_m become equal to zero. The second part of Eq. (1) for the immobile region then does not apply.

Several analytical forms are available to describe the unsaturated soil hydraulic properties $\theta(h)$ and $K(h)$ including Brooks and Corey (1964), van Genuchten (1980), Kosugi (1996), and Durner (1994). Root water uptake is driven by potential transpiration. Actual transpiration is calculated based on the spatial-temporal root distribution, while stress factors in the soil are linked to local water contents and salinities. The codes may be used to account for root water uptake compensation by allowing the roots to take up more water in less stressed soil zones (Šimůnek and Hopmans, 2009). Boundary conditions are either system-independent (e.g., constant or variable pressure head (Dirichlet), flux (Neumann), or gradient boundary conditions) or system-dependent by considering atmospheric conditions involving time-dependent precipitation, potential evaporation, and potential transpiration rates.

Heat transport is described as:

$$C_s(\theta)\frac{\partial T}{\partial t} = \frac{\partial}{\partial x_i}\left(\lambda_{ij}(\theta)\frac{\partial T}{\partial x_i}\right) - C_w q_i \frac{\partial T}{\partial x_i} \qquad (2)$$

where C_s and C_w are volumetric heat capacities [$ML^{-1}T^{-2}K^{-1}$] of soil and water, respectively, and λ_{ij} is the apparent thermal conductivity of the soil [$MLT^{-3}K^{-1}$]. The reactive module uses temperature to correct equilibrium constants or change rate coefficients as desired using user-defined relations. Equation (2) is valid for both single- and dual-porosity flow models when assuming local temperature equilibrium, i.e., that temperature is the same in the solid phase, as well as in the mobile and immobile liquid phases.

Solute concentrations in the aqueous phase are expressed in terms of total concentrations for a given primary species C_k (mol/kgw), which includes the concentration of all aqueous equilibrium species, c_l (mol/kgw) or so-called secondary species:

$$C_k = c_k + \sum_{l=1}^{N_a} \upsilon_{lk} c_l \qquad (3)$$

where υ_{lk} is the stoichiometric coefficient of species k in secondary species l, k = 1,…, N_c (N_c is the number of primary species) and l = 1,…, N_a (N_a is the number of secondary species). For each primary species, solute transport in the aqueous phase is described using advection-dispersion-reaction equations of the form:

$$\frac{\partial \theta_m C_{m,k}}{\partial t} = \frac{\partial}{\partial x_i}\left(\theta_m D_{ij}^w \frac{\partial C_{m,k}}{\partial x_i}\right) - \frac{\partial q_i C_k}{\partial x_i} - S_{r,w} C_{r,k}$$
$$- \Gamma_k - \Gamma_{wa,k} - R_{m,k}^{eq} - R_{m,k}^{kin} \qquad (4)$$
$$\frac{\partial \theta_{im} C_{im,k}}{\partial t} = \Gamma_k - R_{im,k}^{eq} - R_{im,k}^{kin}$$
$$\Gamma_k = \omega\left(C_{m,k} - C_{im,k}\right) + \Gamma_w \left(H\left(\Gamma_w\right) C_{m,k} + H(-\Gamma_w) C_{im,k}\right)$$

where $C_{m,k}$ and $C_{im,k}$ are the total concentrations of the k species in the mobile and immobile domains [mol/dm^3], respectively, θ_m and θ_{im} have the unit [dm^3/dm^3], D^w_{ij} is the dispersion coefficient tensor [L^2T^{-1}], q_i is the ith component of the Darcian fluid flux density [LT^{-1}], $C_{r,k}$ is the concentration of the sink term [mol/dm^3], Γ_k represents solute exchange between the immobile and mobile domains [mol/dm^3T^{-1}], $\Gamma_{wa,k}$ accounts for the exchange between the aqueous and the gas phase [mol/dm^3T^{-1}], $R_{m,k}^{eq}$, $R_{im,k}^{eq}$, $R_{m,k}^{kin}$ and $R_{im,k}^{kin}$ are aqueous sink/source terms [mol/dm^3T^{-1}], with the superscripts eq and kin referring to equilibrium and kinetic reactions, respectively, and subscripts m and im to the mobile and immobile domains, respectively, ω is the mass transfer coefficient [T^{-1}] and H() is the Heaviside step function.

Reactive gases such as O_2 and CO_2 play important roles in many soil processes (e.g., pyrite oxidation, Mayer et al. (2015), and hence must form an integral part of reactive transport models. Diffusion in the gas phase is described as:

$$\frac{\partial \theta_a C_{a,k}}{\partial t} = \frac{\partial}{\partial x_i}\left(\theta_a D_{ij}^a \frac{\partial C_{a,k}}{\partial x_i} \right) + \Gamma_{wa,k} \tag{5}$$

where $C_{a,k}$ is the concentration in the gas phase of component k [mol/dm^3], D^a_{ij} is the gaseous diffusion tensor [L^{2}T^{-1}], and other symbols as defined before.

The geochemical model calculates aqueous concentrations of the primary and secondary species using an aqueous equilibrium chemical model written as:

$$A_l \rightleftharpoons \sum_{k=1}^{N_c} \nu_{lk} A_k \tag{6}$$

where A_l and A_k are the chemical formulae of the species, ν_{lk} are stoichiometric coefficients and N_c is the number of primary species. Mass action laws permit calculations of the aqueous concentrations as follows:

$$c_l = \frac{\prod_{k=1}^{N_c} (\gamma_k c_k)^{\nu_{lk}}}{K_l \gamma_l} \tag{7}$$

where K_l is the equilibrium constant for the reaction, defined as product of the activities of the reaction products divided by the product of the activities of the reactants, and γ_i and γ_j are the activity correction coefficients to obtain activity a [–] when multiplied with c. The thermodynamic constants are adapted for temperature using the enthalpy of the reaction in the van't Hoff equation or by a six-term analytic equation as a function of temperature (Parkhurst and Appelo (2013), see e.g. also Eq. (2) in the appendix). Some of the parameters of this equation can be linked to thermodynamic variables, such as the change of entropy, enthalpy and heat capacity of reaction, at least for relatively small temperature variations (e.g., Puigdomènech et al. (1997), Jacques (2009)) that are expected for soil conditions. Several activity correction models are implemented, such as ion-association models (Davies equation, extended Debye-Hûckel equation), Pitzer model, and a model based on specific ion interaction theory (SIT). Ion exchange, surface complexation, mineral, gas-aqueous phase and solid solutions equilibrium models are available heterogeneous reactions to calculate the $\Gamma_{wa,k}$, $R^{eq}_{m,k}$ and $R^{eq}_{im,k}$, terms in Eq. (4).

Equilibrium between the gas and aqueous phases is given as:

$$G_l \rightleftharpoons A_l \tag{8}$$

where G_l is the chemical formula of the gaseous component. The equilibrium constant of the reactions is the ratio of the activity of A_l over the fugacity of G_l. With the assumption of an ideal gas phase, which is valid for low total gas phase pressures, the fugacity coefficient is 1 in which case the fugacity equals the partial pressure of G_l. Fugacity correction factors can be calculated with the Peng and Robinson equation of state (Peng and Robinson, 1976). However, for total gas phase pressures lower than 10 atm, the fugacity coefficient will be close to 1 (Appelo et al., 2014).

A general ion exchange reaction in which the site capacity is always occupied by ions of the opposite charge (i.e., a charge neutral reaction) is given as:

$$\nu_{X_k} X_k + \upsilon_l A_l \rightleftharpoons \nu_{X_l} X_l + \nu_k A_k \tag{9}$$

where X denotes the chemical formula of an exchange species and ν is the stoichiometric coefficient, which is linked to a thermodynamic constant using different conventions for the activity correction of the exchange species including Gaines-Thomas, Gapon, and Vanselow convention. The Rothmund-Kornfeld equations (Bloom and Mansell, 2001; Bond, 1995), allows one to consider the effects of a changing selectivity with site occupancy (e.g., Jacques et al. (2012)). Different exchange sites can be combined to define a multisite exchange model (e.g., Jacques et al. (2008b)).

A general equation for surface complexation is:

$$S^{z_s}(A_k^{z_k})_{\nu_k} + \nu_l A_l^{z_l} \rightleftharpoons S^{z_s}(A_l^{z_l})_{\nu_l} + \nu_k A_k^{z_k} \tag{10}$$

where S represents the chemical formula of a surface master species, and z the charge of the surface master species, the aqueous species, or the complexed species. Chemical equilibrium is obtained when the ratio of the activity product is equal to the equilibrium reaction constant, possibly corrected for electrostatic effects. These effects can be either neglected using a non-electrostatic model or incorporated by using a diffuse double layer model (Dzombak and Morel, 1990) or the CD-MUSIC model (Hiemstra and VanRiemsdijk, 1996). The composition of the double layer to counterbalance the surface is estimated by explicitly calculating the charge distribution in the layer (Borkovec and Westall, 1983) or by the Donnan model (Appelo and Wersin, 2007).

A general mineral dissolution/precipitation reaction is of the form:

$$M_l \rightleftharpoons \sum_{k=1}^{N_l} \nu_{kl} A_k \tag{11}$$

where M represents the chemical formula of the mineral and N_l the number of aqueous species in the reaction equation. Since the activity of a pure phase (mineral) is assumed to be equal to 1, the equilibrium constant is the activity product of the aqueous species. In ideal solid solutions, which are homogeneous mixtures of different minerals, the activity of the phase is less than 1, leading to a more stable phase compared to the pure phase. For non-ideal binary solid solutions, described using the Guggenheim series expansion model (Guggenheim, 1937), a mechanical mixture may sometimes be more stable than the homogeneous mixture, resulting in an immiscibility gap or phase separation.

The $R^{kin}_{m,k}$ and $R^{kin}_{im,k}$ terms in Eq. (4) represents homogeneous and heterogeneous kinetically controlled reactions, respectively. Homogeneous reaction networks may involve redox, degradation or decay reactions. Each species in such a degradation network must be treated as primary species for which a separate transport equation is required. Typical heterogeneous reactions are dissolution and precipitation of minerals, for which different kinetic expressions exist. One group is based on transition state theory (Aagaard and Helgeson, 1982), which allows for irreversible reactions; the rate parameter may depend on solution composition variables such as pH or activities of other species, which could act as catalyzer or inhibitor. However, irreversible rate equations based on a shrinking core model (e.g., Liu et al. (2014)) or equations in which reaction rates are controlled by microbiological processes can be described as

well. Monod terms for electron acceptors and donors can act as catalytic and inhibitory terms in the microbially-mediated rate equations. Mayer et al. (2002) gave a general rate equation for both surface and transport controlled kinetics for mineral dissolution and precipitation. The scripting possibilities in HPx and PHREEQC permit users to incorporate these or alternative rate equations. In addition, rate equations can be defined for sorption processes when implemented as exchange or surface complexation reactions.

Flow-transport-geochemistry interactions

The concept of scaling hydraulic properties (Vogel et al., 1991), which is typically used in soil sciences to describe their spatial variability, provides a flexible framework for describing the temporal changes of these properties as well. Changes in porosity are then linked to a scaling factor of the water content, α_θ [–], as:

$$\alpha_\theta(t,x) = \frac{\theta_s(t,x) - \theta_r^*}{\theta_s^* - \theta_r^*} \tag{12}$$

where θ_s is the time- and space-variable saturated water content (or the porosity) [L^3 L^{-3}], and θ_s^* [L^3 L^{-3}] and θ_r^* [L^3 L^{-3}] are the reference saturated and residual water contents, respectively, for a specific material. Variations in the hydraulic conductivity in time and space, $K(x,t)$ [L T^{-1}], are described by a scaling factor of the hydraulic conductivity, a_K [–], as follows

$$\alpha_K(t,x) = \frac{K_s(t,x)}{K_s^*} \tag{13}$$

where K_s^* is the reference saturated hydraulic conductivity for a specific material [L T^{-1}]. This formulation enables one to include the effects of temperature and geochemistry on viscosity and density, as well as of precipitation/dissolution/clogging processes on the microstructure. Also, changes in the apparent air-entry value can be described using a scaling factor for the pressure head, α_h [–], such that h/α_h rather than h (for the reference hydraulic properties) is used to obtain the water content and hydraulic conductivity. HPx does not provide any functional relation for calculating the scaling factors. Via the input file, users can implement their preferred model relating geochemical variables to the scaling factors. In the current implementation, change of porosity and scaling factor for the pressure head (in the dual porosity model with water exchange driven by pressure head gradient) are limited to the mobile domain. Assuming a constant porosity of the immobile domain, the change in θ_s^* reflects a change in porosity of the mobile domain only. One limitation is that the scaling factors only describe linear changes in the hydraulic properties. For example, they do not allow for capturing a model for hydraulic property changes which assumes that precipitation and dissolution reactions occur only in the fully water-saturated part of the pore space (e.g., the model of Wissmeier and Barry (2009)). However, when the reactions take place in all of the pore space, the linear scaling model is applicable (Wissmeier and Barry, 2010).

HPx can also update solute and heat transport properties such as the tortuosity of the aqueous and gaseous phases, and the dispersivity, heat capacity, heat conductivity, and heat dispersivity. Tortuosity is often linked to porosity using Archie's law or the model of Millington and Quirk (1961). For cement systems, some models discriminate between the types of porosity (gel versus capillary porosity) and associated cement phases (Patel et al., 2016). The heat capacity can be linked to individual heat capacities of the minerals in the system. However, not much literature evidence exists for a model linking dispersivity and conductivity to geochemical state variables.

Root solute uptake

Kinetic uptake and exudation processes can be implemented in HPx using rate expressions defined in the input files. Examples of PHREEQC implementations of these types of processes were given by Seuntjens et al. (2004) and Nowack et al. (2006). Compared to the HYDRUS implementations, also available in HPx, some additional features can be taken into account when the rate equations $R_{m,k}^{kin}$ in Eq. (4) are used, such as species-specific uptake rather than uptake of an element irrespective of the distribution among different aqueous species, inclusion of counter-ions, root exudation, and uptake parameters depending upon soil geochemistry. It is also possible to incorporate the term $S_{r,w}C_{r,k}$ in Eq. (4) in $R_{m,k}^{kin}$. Following Silberbush et al. (2005), a general formulation of root solute uptake that combines passive and active uptake is given by

$$\begin{aligned} r_l &= p_l + a_l \\ &= p_l + A_{root} J_{l,max}(\omega_{gc}) \frac{c_l - c_{l,min}}{K_{l,m}(\omega_{gc}) + (c_l - c_{l,min})} \end{aligned} \tag{14}$$

$$\begin{aligned} p_{a,l} &= \min[S_{w,r} \min[c_l, c_{max,l}], \\ &\quad A_{root} J_{p,max,l}(\omega_{gc}), \\ &\quad p_{p,l}] \qquad \text{if } c_l > c_{r,l} \\ &= 0 \quad \text{otherwise} \end{aligned} \tag{15}$$

where r_l refers to the uptake of a species l, p_l and a_l are passive and active uptake rates [mol/dm^3 T^{-1}], $c_{max,l}$ is the maximum allowed concentration for passive uptake [mol/dm^3], A_{root} is the root surface area [L^2/dm^3], $J_{p,max,l}$ is the maximum allowed passive nutrient uptake rate [mol L^{-2} T^{-1}], ω is the current geochemical condition, $p_{p,l}$ is the potential passive nutrient uptake rate [mol/dm^3 T^{-1}], $c_{r,l}$ is the critical concentration below which passive root uptake is zero [mol/dm^3], $J_{l,max}$ is the maximum active nutrient uptake which may depend on geochemical conditions or the maximum potential active uptake [T^{-1}], $K_{l,m}$ is the Michaelis-Menten parameter [mol/dm^3], and $c_{l,min}$ is the minimum nutrient concentration below which active uptake is zero. The expression for passive uptake is generic as it limits uptake by (i) a maximum allowable concentration for uptake, (ii) a maximum nutrient uptake flux, and (iii) the maximum potential root uptake rate. It is important to note that it is not straightforward to implement active and passive uptake processes as discussed by Šimůnek and Hopmans (2009), in which active uptake is only invoked when passive uptake does not meet a maximum nutrient plant demand.

OVERVIEW OF RECENT APPLICATIONS

The early studies of Jacques et al. (2008a, 2008b) illustrated the coupled effects of water flow dynamics and geochemistry on the mobility and availability of various contaminants. Since water content variations due to the temporal nature of precipitation, infiltration, and evapotranspiration continually change concentrations in the aqueous phase, other chemical factors and processes such as ionic strength, pH, and aqueous complexation are affected as well. Differences in component mobility result in changes in aqueous speciation and, consequently, both

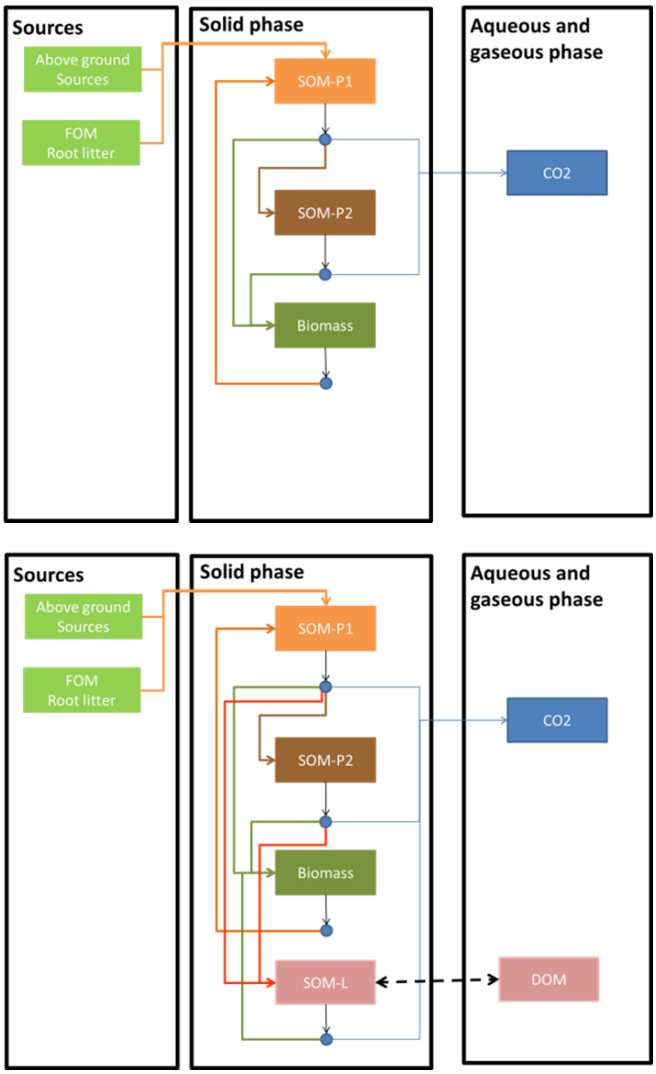

Fig. 4. Organic matter decomposition networks: (top) a scheme without leachable soil organic matter, (bottom) a scheme with leachable soil organic matter. Orange lines indicate decomposition to easily decomposable soil organic matter (SOM-P1), brown lines indicate decomposition to slowly decomposable soil organic matter (SOM-P2), green lines indicate assimilation into biomass (Biomass), blue lines indicate respiration and production of inorganic carbon species (CO_2), and red lines indicate decomposition towards leachable soil organic matter (SOM-L). The dashed black line represents kinetic exchange between leachable soil organic matter and dissolved organic matter.

mineral dissolution/precipitation and sorption can be affected by the temporal-spatial variability of water contents and water fluxes. Comprehensive studies and/or assessments of fate and transport of contaminants in soil systems need to take into account these types of variations. HPx already has been applied in many studies, including for evaluation of Hg fate in soil systems (Bessinger and Marks, 2010; Leterme and Jacques, 2015; Leterme et al., 2014) or, more recently, scenario analyses involving the transport of trace metals in a soil leached with coal seam gas produced water (Mallants et al., 2017). The benchmark study of Greskowiak et al. (2015), in which HPx was used as one of several reactive transport models they evaluated, illustrated the applicability of HPx to describe U transport using a multi-rate mass transfer model (MRMT, e.g., Haggerty and Gorelick (1995)).

Another benchmark study was used to verify the implementation of changes in the porosity, diffusion coefficient and hydraulic conductivity as a consequence of mineral precipitation and dissolution in multiple reactive transport models (Xie et al., 2015), including HP1. Valdes-Abellan et al. (2017) developed a model (using HP1) to simulate the spatial-temporal evolution of soil hydraulic properties during non-conventional water irrigation during non-isothermal transient flow. In addition to linking the porosity, a_h, and the saturated hydraulic conductivity to the amount of precipitated or dissolved minerals, soil hydraulic properties were also linked to changes in the soil water composition, salinity, and temperature. Valdes-Abellan et al. (2017) in their study indicated that a close interplay exist between gypsum-calcite dissolution/precipitation, evaporation fronts, and the key role of the partial pressure of CO_2. While the partial pressure of CO_2 was linked only to calcite equilibria, the role of organic matter degradation (and corresponding CO_2 production) could potentially be incorporated within the HPx framework as well (see below).

HYDRUS in its specialized C-Ride add-on module solves a set of equations describing the transport of colloid and colloid-facilitated solute transport (Šimůnek et al., 2006). A similar set of equations can be implemented in HPx, thus allowing one to consider the effects of geochemistry on various parameters such as attachment efficiency or competitive sorption on the transport of colloids. Zhou et al. (2016) developed a model simulating the transport of three antibiotics in the presence of different kinds of natural organics originating from manure. Compared to the comprehensive capabilities in the standard HYDRUS code, HPx can account for competitive sorption of antibiotics to the soil using a Langmuir competitive kinetic adsorption model in conjunction with competitive kinetic sorption on mobile and immobile organic colloids. The role of geochemistry on colloid mobility was described in a study by Makselon et al. (2017) who modeled the transport of silver nanoparticles in an experiment with flow interruption, evaporation, and ionic strength changes. Ionic strength, and hence the general aqueous geochemical conditions, determined the value of the attachment efficiency, which can be calculated using DVLO theory. A lower ionic strength results in a lower attachment efficiency because of a higher energy barrier and a smaller secondary minimum. BASIC scripts in the input file included root finding algorithms to identify the primary and secondary minima to obtain the attachment efficiency as a function of the changing geochemical conditions during the transport experiment.

EXAMPLES

Organic matter dynamics

As an illustration of the flexible framework of HPx to define reaction networks in general, and for soil organic matter (SOM) degradation in particular, a reaction network loosely based on a study by Porporato et al. (2003) was implemented for this example (HPx projects are available at https://www.pc-progress.com/en/Default.aspx?h1d-library). For convenience, the single-porosity model formulation is used in this example. Figure 4 shows the network with three organic matter pools: (i) a fast decomposable SOM pool (SOM-P1) with concentration $C_{\text{SOM-P1}}$, (ii) a slow decomposable SOM pool (SOM-P2) with concentration $C_{\text{SOM-P2}}$, and (iii) a biomass pool (Biomass) with concentration C_B. In addition, inorganic carbon is released in the aqueous and gaseous soil phases during decomposition, C_I.

This decomposition is described in terms of four ordinary differential equations:

$$\frac{\mathrm{d}C_{\text{SOM-P1}}}{\mathrm{d}t} = i_{\text{F}} + d_{\text{B}} - d_{\text{SOM-P1}} \tag{16}$$

$$\frac{\mathrm{d}C_{\text{SOM-P2}}}{\mathrm{d}t} = r_{\text{SOM-P1}\to\text{P2}} d_{\text{SOM-P1}} - d_{\text{SOM-P2}} \tag{17}$$

$$\frac{\mathrm{d}C_{\text{B}}}{\mathrm{d}t} = r_{\text{SOM-P1}\to\text{B}} d_{\text{SOM-P1}} + r_{\text{SOM-P2}\to\text{B}} d_{\text{SOM-P2}} - d_{\text{B}} \tag{18}$$

$$R^{\text{kin}}_{\text{m,C(4)}} = r_{\text{SOM-P1}\to\text{I}} d_{\text{SOM-P1}} + r_{\text{SOM-P2}\to\text{I}} d_{\text{SOM-P2}} \tag{19}$$

where d_X refers to the decomposition rates, $r_{x\to y}$ denotes the fraction of the decomposition products of pool x going to pool y, and i_{F} denotes the addition of fresh organic matter as litter fall on top of the soil profile or as root decay. Wutzler and Reichstein (2008) discussed different model formulations that can be used to include decomposer biomass into the decomposition rates: (i) no representation of the biomass using equations that are based only on the substrate, (ii) a linear representation of biomass, and (iii) a nonlinear representation of biomass. These models differ in the scaling behavior with the substrate and how they represent priming effects. Although all of these formulations could be included in HPx, the example given below is limited to a non-explicit representation of the biomass and a linear model of the available substrate, i.e.,

$$d_X = k_X C_X \tag{20}$$

where k_X is the first-order decomposition term [T^{-1}], C_X is the concentration of the substrate [ML^{-3}], and X denotes a soil organic matter pool. The value of the rate parameter k_X may depend on temperature $f_{\text{T}}(T)$ [–] and soil moisture $f_{\text{M}}(S_\theta)$ [–] as follows:

$$k_X = k_{X,0} f_T(T) f_M(S_\theta) \tag{21}$$

where $k_{X,0}$ is the reference rate [T^{-1}]. Sierra et al. (2012) gave an overview of different functions to account for the effects of environmental factors on the degradation rate. Here we describe $f_{\text{M}}(S_\theta)$ using the equations of Porporato et al. (2003):

$$f_{\text{M}}(S_\theta) = \begin{cases} \dfrac{S_\theta}{S_{\text{fc}}} & S_\theta \le S_{\text{fc}} \\ \dfrac{S_{\text{fc}}}{S_\theta} & S_\theta > S_{\text{fc}} \end{cases} \tag{22}$$

where S_θ is the degree of saturation ($=\theta/\theta_{\text{s}}$) [–] and S_{fc} is the saturation degree at field capacity [–]. The temperature dependency is described using the formulation from ROTC (Jenkinson et al., 1990):

$$f_{\text{T}}(T) = \frac{47.9}{1+\exp\left(\dfrac{106}{T+18.3}\right)} \tag{23}$$

Still needed to complete the description of the organic matter decomposition network is an aqueous speciation model for inorganic C species. We refer to the Appendix for details. Table 2 further gives the parameters used in a transient flow simulation for a meteorological time series representative of Belgium conditions.

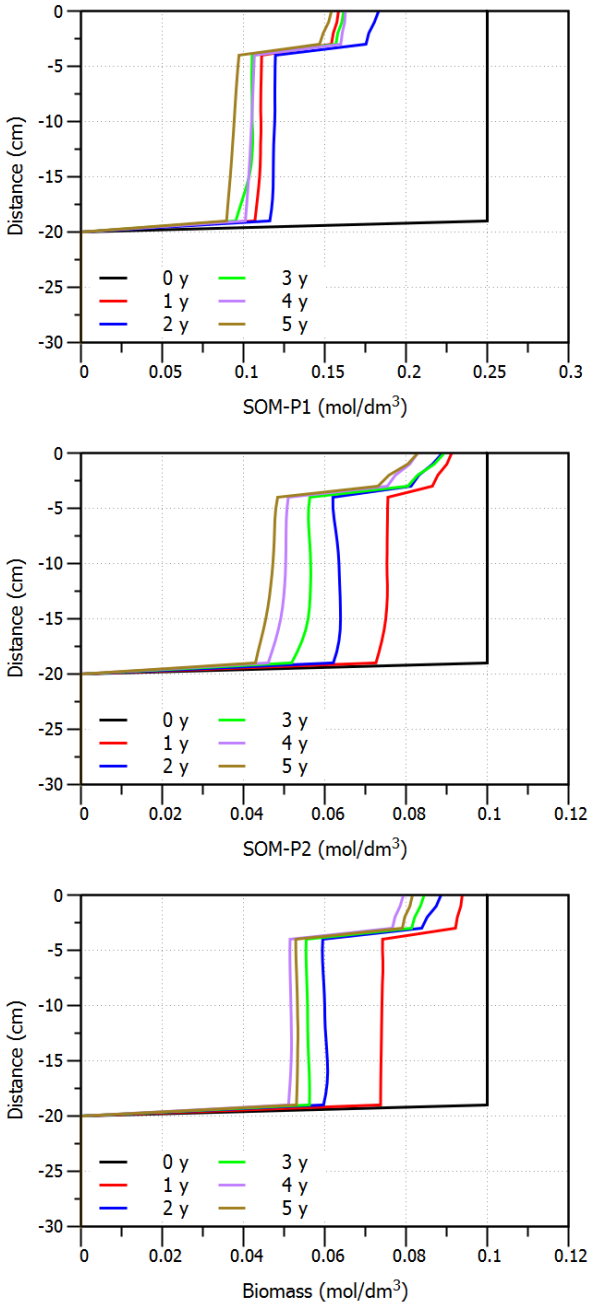

Fig. 5. Profiles of SOM-P1 (top), SOM-P2 (middle), and Biomass (bottom) for network 1.

Figure 5 shows the computed distributions versus depth of the various pools of soil organic matter and biomass during five consecutive years. Large changes during the first few years indicate that selected initial and production terms are not in long-term equilibrium with the degradation processes. The current set of parameters and meteorological variables do not produce much variability in the vertical direction. The relative enrichment of the top 5 cm is due to SOM-P1 originating both from litter fall and root decay whereas deeper in the profile, only root decay contributes to the SOM-P1 pool. A more throughout analysis of the model setup using a sensitivity analysis of the model parameters is beyond the scope of the current paper but could be done straightforwardly with HPx as was illustrated by Leterme and Jacques (2015).

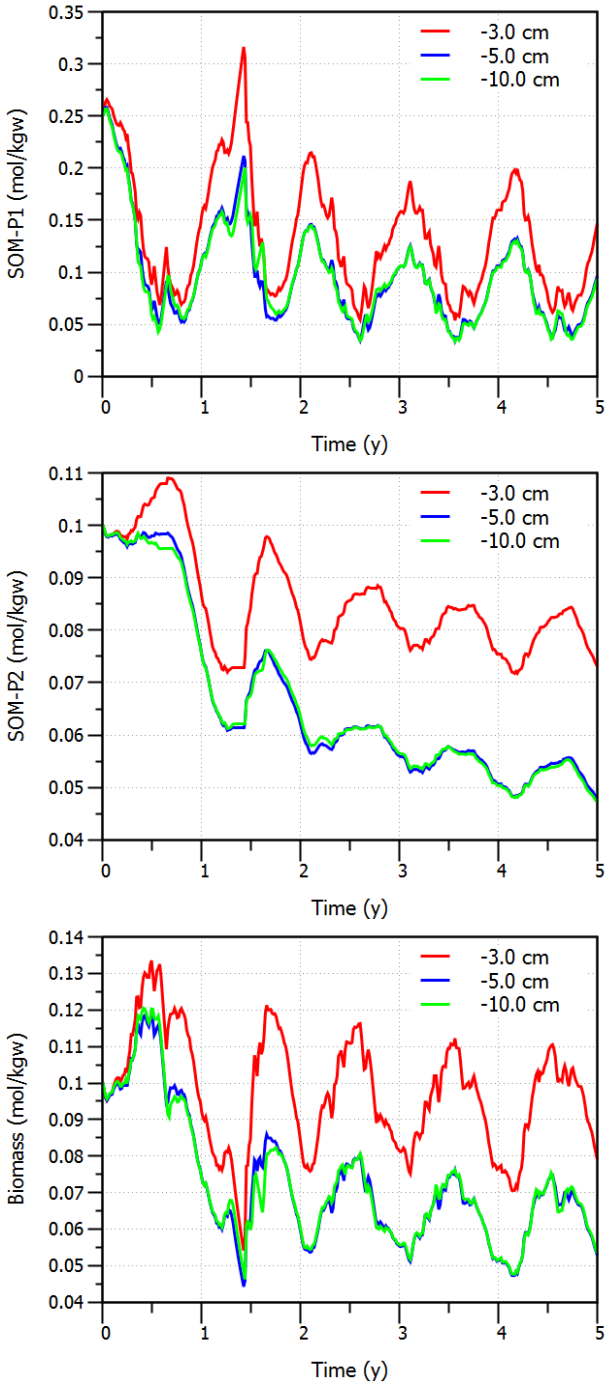

Fig. 6. Time series of SOM-P1 (top), SOM-P2 (middle), and Biomass (bottom) for network 1.

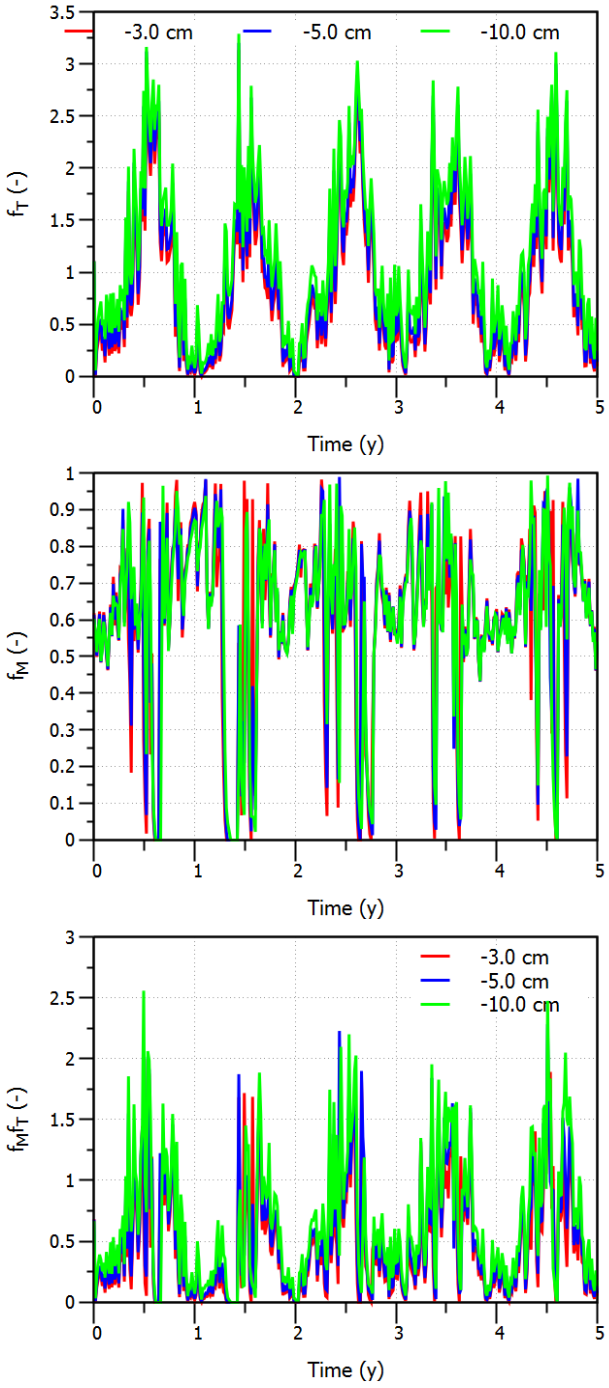

Fig. 7. Time series of f_M (top), f_T (middle), and $f_M f_T$ (bottom) for network 1.

Figure 6 shows time series of various pools of SOM and Biomass at several depths. The strong seasonal fluctuations in these pools are due to variations in soil water contents and temperatures, leading to changes in the environmental factors on the degradation rates as expressed by Eqs. (21)–(23). As shown in Figure 7, variations in f_M and f_T are similar at different soil depths, which explain the relatively uniform distribution of various organic pools (Figure 5). HPx in general provides geochemical information of the system such as pH (not further shown here) and inorganic aqueous and gaseous C concentrations, the latter shown in Figure 8 in terms of the partial pressure of CO_2 in the soil air phase. In this example C was the only aqueous species and no pH controlling components or processes were included. Figure 8 also shows the cumulative flux of CO_2 from the soil to the atmosphere, which is a critical variable in soil-plant-atmosphere and regional or global climate studies (e.g., Thaysen et al. (2014)).

Dissolved organic matter

The previous organic matter degradation model is further extended in this example by including a leachable organic matter pool (SOM-L) and a dissolved organic matter pool (DOM), which are both kinetically exchanged. The formulation, loosely based on the model of Braakhekke et al. (2011), allows for

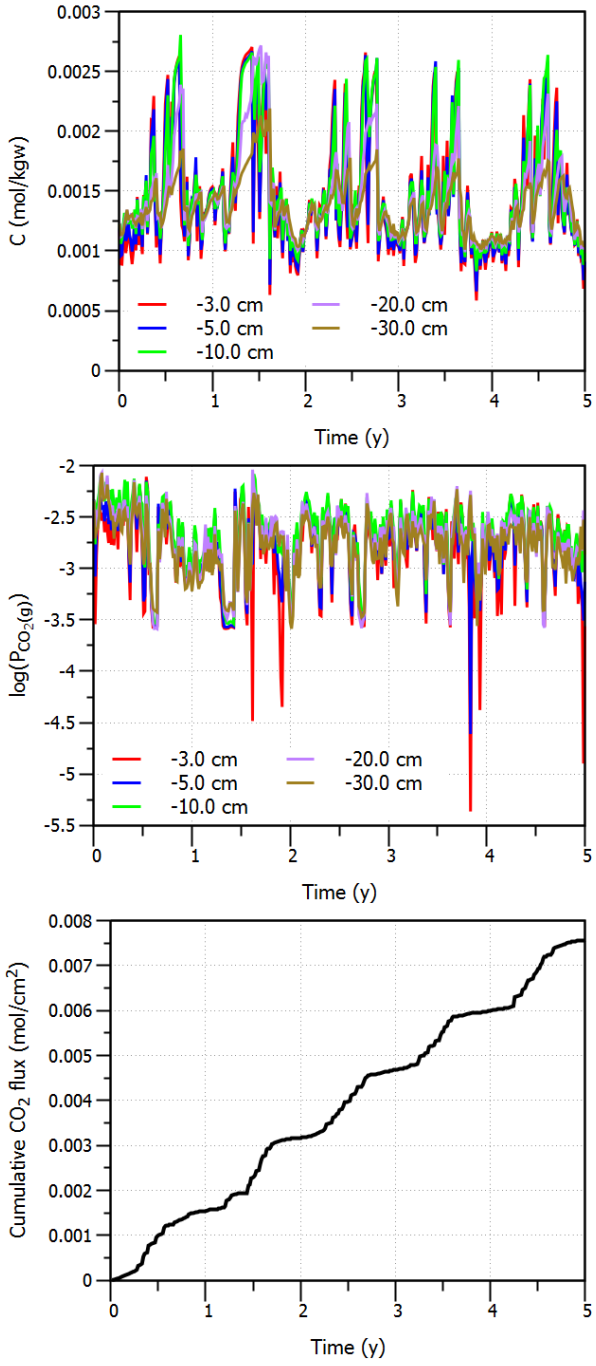

Fig. 8. Time series of C concentration (mol/kgw) (top), P_{CO2} (middle) and cumulative CO_2 flux to the atmosphere (bottom) for network 1.

advective-dispersive transport of DOM. The set of governing ordinary-differential equations is as follows:

$$\frac{\mathrm{d}C_{\text{SOM-P1}}}{\mathrm{d}t} = i_{\text{F}} + d_{\text{B}} - d_{\text{SOM-P1}} \tag{24}$$

$$\frac{\mathrm{d}C_{\text{SOM-P2}}}{\mathrm{d}t} = r_{\text{SOM-P1}\to\text{P2}} d_{\text{SOM-P1}} - d_{\text{SOM-P2}} \tag{25}$$

$$\frac{\mathrm{d}C_{\text{B}}}{\mathrm{d}t} = r_{\text{SOM-P1}\to\text{B}} d_{\text{SOM-P1}} + r_{\text{SOM-P2}\to\text{B}} d_{\text{SOM-P2}} + r_{\text{SOM-L}\to\text{B}} d_{\text{SOM-L}} - d_{\text{B}} \tag{26}$$

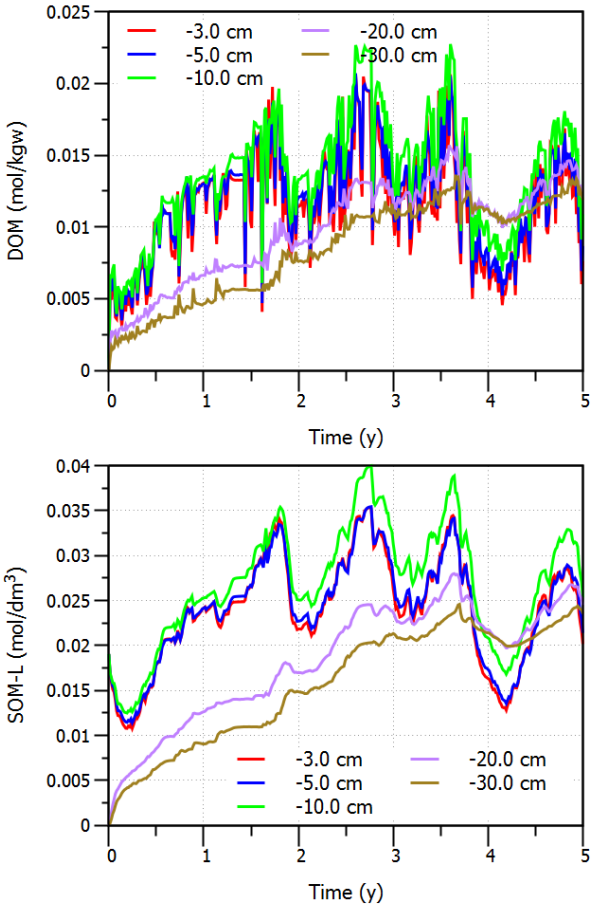

Fig. 9. Time series of DOM (top) and SOM-L (bottom) for network 2.

$$\frac{\mathrm{d}C_{\text{SOM-L}}}{\mathrm{d}t} = r_{\text{SOM-P1}\to\text{SOM-L}} d_{\text{SOM-P1}} + r_{\text{SOM-P2}\to\text{SOM-L}} d_{\text{SOM-P2}} - d_{\text{SOM-L}} - d_{\text{S}} \tag{27}$$

$$R^{\text{kin}}_{\text{m,C(4)}} = r_{\text{SOM-P1}\to\text{I}} d_{\text{SOM-P1}} + r_{\text{SOM-P2}\to\text{I}} d_{\text{SOM-P2}} + r_{\text{SOM-L}\to\text{I}} d_{\text{SOM-L}} \tag{28}$$

$$R^{\text{kin}}_{\text{m,DOM}} = d_{\text{s}} \tag{29}$$

where d_{S} is the desorption term:

$$d_{\text{s}} = k_{\text{S}}(C_{\text{SOM-L}} - C^{\text{eq}}_{\text{SOM-L}}) = k_{\text{S}}\left(C_{\text{SOM-L}} - \frac{K_{\text{L}} S_{\max} C_{\text{DOM}}}{1 + K_{\text{L}} C_{\text{DOM}}}\right) \tag{30}$$

in which K_{L} is the coefficient of binding affinity [$\text{dm}^3\text{gC}^{-1}$] and $S_{\max}$ the maximum adsorption capacity [gC dm^{-3}]. Time series of the new two pools, SOM-L and DOM, are shown in Figure 9. DOM shows short-scale temporal variations due to changes in the water content. These variations are less pronounced for SOM-L due to the kinetics of the sorption process. The advection and dispersion of DOM result in an increase in both DOM and SOM-L at depths below the initial source of soil organic matter between 0 and 20 cm below the soil surface. Note that the other pools potentially will develop also below the 20-cm depth when this degradation scheme is used, but their amounts remain very small for the chosen set of parameters.

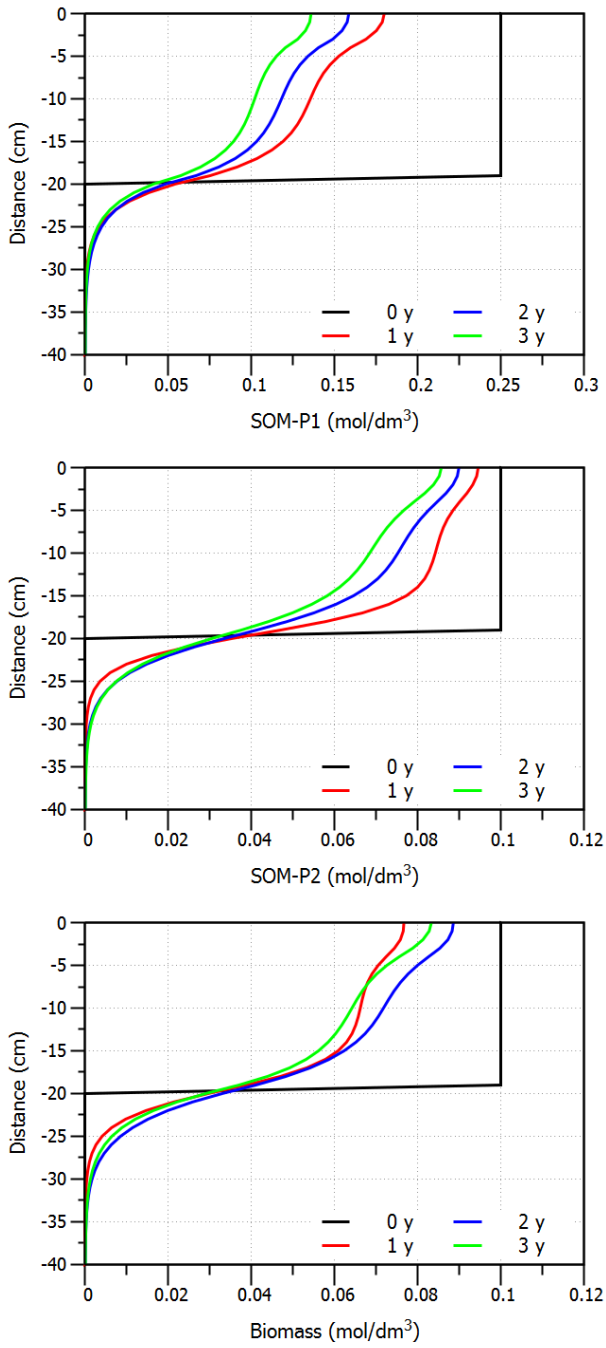

Fig. 10. Profiles of SOM-S1 (top), SOM-S2 (middle) and Biomass (bottom) for a simulation with network 1 including biodiffusion.

Bioturbation

The long term prediction of soil carbon cycling requires an explicit representation of the vertical distribution of soil organic matter, and hence a model able to represent processes leading to the vertical distribution of SOM such as the root litter distribution and the transport of soil organic matter (Braakhekke et al., 2011). The biological transport of soil solid phases, often referred to as bioturbation, depends strongly on the behavior of the biological community species, which necessitated the development of different modeling approaches (Meysman et al., 2003a). Models based on Fick's law are local random models (Meysman et al., 2005), whereas non-local models need to be employed when ingestion and egestion processes of SOM by bio fauna are vertically separated (Jarvis et al., 2010).

As an example, a biodiffusion model was implemented within the input files of HPx:

$$J_{s,X} = -D_{B,X} \frac{\partial C_X}{\partial x} \tag{31}$$

where $J_{s,X}$ is the solid phase diffusive flux of the Xth pool [mol T^{-1} L^{-2}], $D_{B,X}$ is the effective solid phase diffusion coefficient [L^2 T^{-1}], and C_X is the solid phase concentration [mol L^{-3}]. The biodiffusion model was applied to organic network 1 described above with SOM-P1, SOM-P2, and biomass. We assumed rather arbitrarily that $D_{B,X} = 10^{-10}$ m^2/s. As shown in Figure 10, a smooth profile of the three organic pools developed over the course of 3 years to about 15 cm below the initial layer with organic matter.

CONCLUSIONS

The original HP1 model (Jacques and Šimůnek, 2005; Jacques et al., 2006) has seen many extensions during the past 10 years or more. The most important changes were the development of two- and three-dimensional versions (HPx), and the incorporation of the software PHREEQC-3, OpenMP, enhanced scripting possibilities, diffusion in the gas phase of reactive gases in the software, and linking geochemical state variables to transport properties. Using the terminology of Meysman et al. (2003b), HPx is now moving towards a more flexible and extendible problem-solving environment to allow users to incorporate a range of user-defined conceptual models to tackle their specific projects. Flexibility and extendibility are discussed in this manuscript with respect to coupling geochemistry with transport properties, colloid and colloid-affected transport, bioturbation, and root solute uptake. Recent applications show that HPx, and similar reactive transport codes, are useful tools to evaluate many environmental and engineering problems both from a scientific as well as from an application point of view, thus underpinning the main statement from Li et al. (2017).

In this paper, we illustrated the capabilities and flexibility of HPx by developing a reaction-transport model for soil organic matter, in which we included different factors important in soil organic matter degradation. Only a few SOM degradation models can similarly consider spatial-temporal variations in water contents, water fluxes, and temperatures, as well as different conceptual models for SOM degradation networks, advection-dispersive transport of DOM, CO_2 transport, and bioturbation in one modeling framework. Within the scope of this paper, the role of microbial processes together with the transport of oxygen were not addressed, but conceptually could be implemented in a very similar way. We also acknowledge that further parameter sensitivity studies and validation of these models are crucial in further model applications.

Acknowledgement. The first author acknowledges the support of the Belgian Nuclear Research Centre for developing, maintaining, and applying the HPx code.

REFERENCES

Aagaard, P., Helgeson, H.C., 1982. Thermodynamic and kinetic constraints on reaction rates among minerals and aqueous solutions, 1. Theoretical considerations. Am. J. Sci., 282, 237–285.

Amos, R.T., Mayer, K.U., 2006. Investigating the role of gas bubble formation and entrapment in contaminated aquifers: Reactive transport modelling. J. Cont. Hydrol., 87, 123–154.

Appelo, C.A.J., Parkhurst, D.L., Post, V.E.A., 2014. Equations for calculating hydrogeochemical reactions of minerals and gases such as CO_2 at high pressures and temperatures. Geochim. Cosmochim. Acta, 125, 49–67.

Appelo, C.A.J., Wersin, P., 2007. Multicomponent diffusion modeling in clay systems with application to the diffusion of tritium, iodide, and sodium in Opalinus Clay. Env. Sci. Tech., 41, 5002–5007.

Batlle-Aguilar, J., Brovelli, A., Porporato, A., Barry, D.A., 2011. Modelling soil carbon and nitrogen cycles during land use change: A review. Agron. Sust. Devel., 31, 251–274.

Bennacer, L., Ahfir, N.D., Alem, A., Wang, H.Q., 2017. Coupled effects of ionic strength, particle size, and flow velocity on transport and deposition of suspended particles in saturated porous media. Transp. Por. Med., 118, 251–269.

Bessinger, B.A., Marks, C.D., 2010. Treatment of mercury-contaminated soils with activated carbon: A laboratory, field, and modeling study. Remed., 21, 115–135.

Bloom, S.A., Mansell, R.S., 2001. An algorithm for generating cation exchange isotherms from binary selectivity coefficients. Soil Sci. Soc. Am. J., 65, 1426–1429.

Bond, W.J., 1995. On the Rothmund-Kornfeld description of cation exchange. Soil Sc. Soc. Am. J., 59, 436–443.

Borkovec, M., Westall, J., 1983. Solution of the Poisson-Boltzmann equation for surface excesses of ions in the diffuse layer at the oxide electrolyte interface. J. Elect. Chem., 150, 325–337.

Bozorg, A., Gates, I.D., Sen, A., 2015a. Impact of biofilm on bacterial transport and deposition in porous media. J. Cont. Hydrol.,183, 109–120.

Bozorg, A., Gates, I.D., Sen, A., 2015b. Using bacterial bioluminescence to evaluate the impact of biofilm on porous media hydraulic properties. J. Microb. Meth., 109, 84–92.

Braakhekke, M.C., Beer, C., Hoosbeek, M.R., Reichstein, M., Kruijt, B., Schrumpf, M., Kabat, P., 2011. SOMPROF: A vertically explicit soil organic matter model. Ecol. Mod., 222, 1712–1730.

Brantley, S., Goldhaber, M.B., Ragnarsdottir, K.V., 2007. Crossing disciplines and scales to understand the critical zone. Elements, 3, 307–314.

Brooks, R.H., Corey, A., 1964. Hydraulic properties of porous media. Hydrol. Paper No. 3, Colorado State Univ., Fort Collins, CO.

Carles Brangarí, A., Sanchez-Vila, X., Freixa, A., M. Romaní, A., Rubol, S., Fernàndez-Garcia, D., 2017. A mechanistic model (BCC-PSSICO) to predict changes in the hydraulic properties for bio-amended variably saturated soils. Water Resour. Res., 53, 93–109.

Charlton, S.R., Parkhurst, D.L., 2011. Modules based on the geochemical model PHREEQC for use in scripting and programming languages. Comp. & Geosc., 37, 1653–1663.

Durner, W., 1994. Hydraulic conductivity estimation for soils with heterogeneous pore structure. Water Resour. Res., 30, 211–223.

Dzombak, D.A., Morel, F.M.M., 1990. Surface Complexation Modeling – Hydrous Ferric Oxide. John Wiley, New York.

Freedman, V.L., Bacon, D.H., Saripalli, K.P., Meyer, P.D., 2004. A film depositional model of permeability for mineral reactions in unsaturated media. Vadose Zone J., 3, 1414–1424.

Greskowiak, J., Gwo, J., Jacques, D., Yin, J., Mayer, K.U., 2015. A benchmark for multi-rate surface complexation and 1D dual-domain multi-component reactive transport of U(VI). Comp. Geosc., 19, 585–597.

Guggenheim, E.A., 1937. Theoretical basis of Raoult's law. Trans. Faraday Soc., 33, 151–159.

Haggerty, R., Gorelick, S.M., 1995. Multiple-rate mass transfer for modeling diffusion and surface reactions in media with pore-scale heterogeneity. Water Resour. Res., 31, 2383–2400.

Hiemstra, T., VanRiemsdijk, W.H., 1996. A surface structural approach to ion adsorption: The charge distribution (CD) model. J. Col. Int. Sci., 179, 488–508.

Hommel, J., Lauchnor, E., Phillips, A., Gerlach, R., Cunningham, A.B., Helmig, R., Ebigbo, A., Class, H., 2015. A revised model for microbially induced calcite precipitation: Improvements and new insights based on recent experiments. Water Resour. Res., 51, 3695–3715.

Jacques, D., 2009. Benchmarking of the cement model and detrimental chemical reactions including temperature dependent parameters. Project near surface disposal of category A waste at Dessel, NIRAS-MP5-03 DATA-LT(NF) Version 1.

Jacques, D., Šimůnek, J., 2005. User Manual of the Multicomponent Variably- Saturated Flow and Transport Model HP1. SCK•CEN-BLG-998.

Jacques, D., Šimůnek, J., Mallants, D., van Genuchten, M.T., 2006. Operator-splitting errors in coupled reactive transport codes for transient variably saturated flow and contaminant transport in layered soil profiles. J. Contam. Hydrol., 88, 197–218.

Jacques, D., Šimůnek, J., Mallants, D., van Genuchten, M.T., 2008a. Modeling coupled hydrologic and chemical processes: Long-term uranium transport following phosphorus fertilization. Vadose Zone J., 7, 698–711.

Jacques, D., Šimůnek, J., Mallants, D., van Genuchten, M.T., 2008b. Modelling coupled water flow, solute transport and geochemical reactions affecting heavy metal migration in a podzol soil. Geoderma, 145, 449–461.

Jacques, D., Smith, C., Simůnek, J., Smiles, D., 2012. Inverse optimization of hydraulic, solute transport, and cation exchange parameters using HP1 and UCODE to simulate cation exchange. J. Contam. Hydrol., 142–143, 109–125.

Jarvis, N.J., Taylor, A., Larsbo, M., Etana, A., Rosen, K., 2010. Modelling the effects of bioturbation on the re-distribution of ^{137}Cs in an undisturbed grassland soil. Eur. J. Soil Sci., 61, 24–34.

Jenkinson, D.S., Andrew, S.P.S., Lynch, J.M., Goss, J.M., Tinker, P.B., 1990. The turnover of organic carbon and nitrogen in soil. Philosoph. Trans., 329, 361–368.

Kosugi, K., 1996. Lognormal distribution model for unsaturated soil hydraulic properties. Water Resour. Res., 32, 2697–2703.

Laliberté, M., 2007. Model for calculating the viscosity of aqueous solutions. J. Chem. Eng. Data, 52, 321-335.

Laliberté, M., Cooper, W.E., 2004. Model for calculating the density of aqueous electrolyte solutions. J. Chem. Eng. Data, 49, 1141–1151.

Leterme, B., Blanc, P., Jacques, D., 2014. A reactive transport model for mercury fate in soil—application to different anthropogenic pollution sources. Environ. Sci. Pollut. Res., 12279–12293.

Leterme, B., Jacques, D., 2015. A reactive transport model for mercury fate in contaminated soil-sensitivity analysis. Environ. Sci. Pollut. Res., 22, 16830–16842.

Li, L., Maher, K., Navarre-Sitchler, A., Druhan, J., Meile, C., Lawrence, C., Moore, J., Perdrial, J., Sullivan, P., Thompson, A., Jin, L., Bolton, E.W., Brantley, S.L., Dietrich, W.E., Mayer, K.U., Steefel, C.I., Valocchi, A.,

Zachara, J., Kocar, B., McIntosh, J., Tutolo, B.M., Kumar, M., Sonnenthal, E., Bao, C., Beisman, J., 2017. Expanding the role of reactive transport models in critical zone processes. Earth Sci. Rev., 165, 280–301.

Liu, S., Jacques, D., Govaerts, J., Wang, L., 2014. Conceptual model analysis of interaction at a concrete-Boom Clay interface. Phys. Chem. Earth, 70–71, 150–159.

Maes, N., Wang, L., Hicks, T., Bennett, D., Warwick, P., Hall, T., Walker, G., Dierckx, A., 2006. The role of natural organic matter in the migration behaviour of americium in the Boom Clay - Part I: Migration experiments. Phys. Chem. Earth, 31, 541–547.

Makselon, J., Zhou, D., Engelhardt, I., Jacques, D., Klumpp, E., 2017. Experimental and numerical investigations of silver nanoparticle transport under variable flow and ionic strength in soil. Envir. Sci. Techn., 51, 2096–2104.

Mallants, D., Šimůnek, J., van Genuchten, M.T., Jacques, D., 2017. Simulating the fate and transport of coal seam gas chemicals in variably-saturated soils using HYDRUS. Water, 9, 6, 385.

Manzoni, S., Porporato, A., 2009. Soil carbon and nitrogen mineralization: Theory and models across scales. Soil Biol. Biochem., 41, 1355–1379.

Martinez, B.C., DeJong, J.T., Ginn, T.R., 2014. Bio-geochemical reactive transport modeling of microbial induced calcite precipitation to predict the treatment of sand in one-dimensional flow. Comp. Geotech., 58, 1–13.

Mayer, K.U., Alt-Epping, P., Jacques, D., Arora, B., Steefel, C.I., 2015. Benchmark problems for reactive transport modeling of the generation and attenuation of acid rock drainage. Comp. Geosci., 19, 599–611.

Mayer, K.U., Frind, E.O., Blowes, D.W., 2002. Multicomponent reactive transport modeling in variably saturated porous media using a generalized formulation for kinetically controlled reactions. Water Resour. Res., 38, 1174, DOI: 1110.1029/2001WR000862.

Mays, D.C., Hunt, J.R., 2007. Hydrodynamic and chemical factors in clogging by montmorillonite in porous media. Envir. Sci. Techn., 41, 5666–5671.

Meysman, F.J.R., Boudreau, B.P., Middelburg, J.J., 2003a. Relations between local, nonlocal, discrete and continuous models of bioturbation. J. Mar. Res., 61, 391–410.

Meysman, F.J.R., Boudreau, B.P., Middelburg, J.J., 2005. Modeling reactive transport in sediments subject to bioturbation and compaction. Geochim. Cosmochim. Acta, 69, 3601–3617.

Meysman, F.J.R., Middelburg, J.J., Herman, P.M.J., Heip, C.H.R., 2003b. Reactive transport in surface sediments. I. Model complexity and software quality. Comp. Geosci., 29, 291–300.

Millington, R.J., Quirk, J.P., 1961. Permeability of porous solids. Trans. Faraday Soc., 57, 1200–1206.

Nowack, B., Mayer, K.U., Oswald, S.E., van Beinum, W., Appelo, C.A.J., Jacques, D., Seuntjens, P., Gérard, F., Jaillard, B., Schnepf, A., Roose, T., 2006. Verification and intercomparison of reactive transport codes to describe root-uptake. Plant and Soil, 285, 305–321.

Or, D., Smets, B.F., Wraith, J.M., Dechesne, A., Friedman, S.P., 2007. Physical constraints affecting bacterial habitats and activity in unsaturated porous media – a review. Adv. Wat. Res., 30, 1505–1527.

Paradelo, M., Perez-Rodriguez, P., Fernandez-Calvino, D., Arias-Estevez, M., Lopez-Periago, J.E., 2012. Coupled transport of humic acids and copper through saturated porous media. Eur. J. Soil Sci., 63, 708–716.

Parkhurst, D.L., Appelo, C.A.J., 2013. Description of Input and Examples for PHREEQC Version 3 – A Computer Program for Speciation, Batch-Reaction, One-Dimensional Transport, and Inverse Geochemical Calculations. Chapter 43 of Section A. Groundwater Book 6, Modeling Techniques.

Parkhurst, D.L., Wissmeier, L., 2015. PhreeqcRM: A reaction module for transport simulators based on the geochemical model PHREEQC. Adv. Wat. Res., 83, 176–189.

Patel, R., Phung, Q.T., Seetharam, S.C., Perko, J., Jacques, D., Maes, N., De Schutter, G., Ye, G., van Breugel, K., 2016. Diffusivity of saturated ordinary Portland cement- based materials: A critical review of experimental and analytical modelling approaches. Cem. Con. Res., 90, 52–72.

Peng, D.-Y., Robinson, D.B., 1976. A new two-constant equation of state. Ind. Eng. Chem. Fund., 15, 59–64.

Phung, Q.T., Maes, N., Jacques, D., De Schutter, G., Ye, G., Perko, J., 2016. Modelling the carbonation of cement pastes under a CO2 pressure gradient considering both diffusive and convective transport. Const. Build. Mat., 114, 333–351.

Porporato, A., D'Odorico, P., Laio, F., Rodriguez-Iturbe, I., 2003. Hydrologic controls on soil carbon and nitrogen cycles. I. Modeling scheme. Adv. Wat. Res., 26, 45–58.

Puigdomènech, I., Rard, J.A., Plyasunov, A.V., Grenthe, I., 1997. Temperature corrections to thermodynamic data and enthalpy calculations. In: Grenthe, I., PuigdomSnech, I. (Eds.): OECD Nuclear Chemistry, Paris, pp. 427–493.

Riley, W.J., Maggi, F., Kleber, M., Torn, M.S., Tang, J.Y., Dwivedi, D., Guerry, N., 2014. Long residence times of rapidly decomposable soil organic matter: application of a multi-phase, multi-component, and vertically resolved model (BAMS1) to soil carbon dynamics. Geosci. Model Dev., 7, 1335–1355.

Rockhold, M.L., Yarwood, R.R., Niemat, M.R., Bottomley, P.J., Selker, J.S., 2002. Considerations for modeling bacterial-induced changes in hydraulic properties of variably saturated porous media. Adv. Wat. Res., 25, 477–495.

Schmidt, M.W.I., Torn, M.S., Abiven, S., Dittmar, T., Guggenberger, G., Janssens, I.A., Kleber, M., Kogel-Knabner, I., Lehmann, J., Manning, D.A.C., Nannipieri, P., Rasse, D.P., Weiner, S., Trumbore, S.E., 2011. Persistence of soil organic matter as an ecosystem property. Nature, 478, 49–56.

Seuntjens, P., Nowack, B., Schulin, R., 2004. Root-zone modeling of heavy metal uptake and leaching in the presence of organic ligands. Plant and Soil, 265, 61–73.

Sharqawy, M.H., Lienhard V, J.H., Zubair, S.M., 2010. Thermophysical properties of seawater: A review of existing correlations and data. Desal. Wat. Treat., 16, 354–380.

Sierra, C.A., Müller, M., Trumbore, S.E., 2012. Models of soil organic matter decomposition: the SoilR package, version 1.0. Geosci. Model Dev., 5, 1045–1060.

Silberbush, M., Ben-Asher, J., Ephrath, J.E., 2005. A model for nutrient and water flow and their uptake by plants grown in a soilless culture. Plant and Soil, 271, 309–319.

Šimůnek, J., He, C., Pang, L., Bradford, S.A., 2006. Colloid-facilitated solute transport in variably saturated porous media: Numerical model and experimental verification. Vadose Zone J., 5, 1035–1047.

Šimůnek, J., Hopmans, J.W., 2009. Modeling compensated root water and nutrient uptake. Ecol. Mod., 220, 505–521.

Šimůnek, J., Jacques, D., Šejna, M., van Genuchten, M.T., 2012. The HP2 Program for HYDRUS (2D/3D). A Coupled Code for Simulating Two-Dimensional Variably-Saturated Water Flow, Head Transport, Solute Transport Flow, and

Biogeochemistry in Porous Media. (HYDRUS+PHREEQC+2D), Version 1.

Simunek, J., Sejna, M., Saito, H., Sakai, K., van Genuchten, M.T., 2013. The HYDRUS-1D Software Package for Simulating the Movement of Water, Heat, and Multiple Solutes in Variably Saturated Media. Version 4.17. HYDRUS Software Series 3. Department of Environmental Sciences, University of California Riverside, Riverside, California, USA.

Šimůnek, J., van Genuchten, M.T., 2008. Modeling nonequilibrium flow and transport processes using HYDRUS. Vadose Zone J., 7, 782–797.

Šimůnek, J., van Genuchten, M.T., Šejna, M., 2016. Recent developments and applications of the HYDRUS Computer Software Packages. Vadose Zone J., 15, DOI: 10.2136/vzj2016.04.0033.

Steefel, C.I., Appelo, C.A.J., Arora, B., Jacques, D., Kalbacher, T., Kolditz, O., Lagneau, V., Lichtner, P.C., Mayer, K.U., Meeussen, J.C.L., Molins, S., Moulton, D., Shao, H., Šimůnek, J., Spycher, N., Yabusaki, S.B., Yeh, G.T., 2015. Reactive transport codes for subsurface environmental simulation. Comp. Geosci., 19, 445–478.

Steefel, C.I., DePaolo, D.J., Lichtner, P.C., 2005. Reactive transport modeling: An essential tool and a new research approach for the Earth sciences. Earth Plan. Sci. Let., 240, 539–558.

Tang, J., Riley, W.J., 2015. Weaker soil carbon-climate feedbacks resulting from microbial and abiotic interactions. Nature Clim. Change, 5, 56–60.

Tang, J.Y., Riley, W.J., Koven, C.D., Subin, Z.M., 2013. CLM4-BeTR, a generic biogeochemical transport and reaction module for CLM4: model development, evaluation, and application. Geosci. Model Dev., 6, 127–140.

Thaysen, E.M., Jacques, D., Jessen, S., Andersen, C.E., Laloy, E., Ambus, P., Postma, D. and Jakobsen, I., 2014. Inorganic carbon fluxes across the vadose zone of planted andunplanted soil mesocosms. Biogeosci., 11, 7179–7192.

Todd-Brown, K.E.O., Randerson, J.T., Post, W.M., Hoffman, F.M., Tarnocai, C., Schuur, E.A.G., Allison, S.D., 2013. Causes of variation in soil carbon simulations from CMIP5 Earth system models and comparison with observations. Biogeosci., 10, 1717–1736.

Valdes-Abellan, J., Jiménez-Martínez, J., Candela, L., Jacques, D., Kohfahl, C., Tamoh, K., 2017. Reactive transport modelling to infer changes in soil hydraulic properties induced by non-conventional water irrigation. J. Hydrol., 549, 114–124.

van Genuchten, M.T., 1980. Closed-form equation for predicting the hydraulic conductivity of unsaturated soils. Soil Sci. Soc. Am. J., 44, 892–898.

Vereecken, H., Schnepf, A., Hopmans, J.W., Javaux, M., Or, D., Roose, T., Vanderborght, J., Young, M.H., Amelung, W., Aitkenhead, M., Allison, S.D., Assouline, S., Baveye, P., Berli, M., Brüggemann, N., Finke, P., Flury, M., Gaiser, T., Govers, G., Ghezzehei, T., Hallett, P., Hendricks Franssen, H.J., Heppell, J., Horn, R., Huisman, J.A., Jacques, D., Jonard, F., Kollet, S., Lafolie, F., Lamorski, K., Leitner, D., McBratney, A., Minasny, B., Montzka, C., Nowak, W., Pachepsky, Y., Padarian, J., Romano, N., Roth, K., Rothfuss, Y., Rowe, E.C., Schwen, A., Šimůnek, J., Tiktak, A., Van Dam, J., van der Zee, S.E.A.T.M., Vogel, H.J., Vrugt, J.A., Wöhling, T., Young, I.M., 2016. Modeling soil processes: Review, key challenges, and new perspectives. Vadose Zone J., 15, 1–57.

Vogel, T., Cislerova, M., Hopmans, J.W., 1991. Porous media with linearly variable hydraulic properties. Water Resour. Res., 27, 2735–2741.

Wissmeier, L., Barry, D.A., 2009. Effect of mineral reactions on the hydraulic properties of unsaturated soils: Model development and application. Adv. Wat. Res., 32, 1241–1254.

Wissmeier, L., Barry, D.A., 2010. Implementation of variably saturated flow into PHREEQC for the simulation of biogeochemical reactions in the vadose zone. Env. Mod. Soft., 25, 526–538.

Wutzler, T., Reichstein, M., 2008. Colimitation of decomposition by substrate and decomposers - a comparison of model formulations. Biogeosci., 5, 749–759.

Xie, M., Mayer, K.U., Claret, F., Alt-Epping, P., Jacques, D., Steefel, C., Chiaberge, C., Šimůnek, J., 2015. Implementation and evaluation of permeability-porosity and tortuosity-porosity relationships linked to mineral dissolution-precipitation. Comp. Geosci., 19, 655–671.

Yarwood, R.R., Rockhold, M.L., Niemet, M.R., Selker, J.S., Bottomley, P.J., 2006. Impact of microbial growth on water flow and solute transport in unsaturated porous media. Water Resour. Res., 42, W10405, 1–11.

Yu, C., Muñoz-Carpena, R., Gao, B., Perez-Ovilla, O., 2013. Effects of ionic strength, particle size, flow rate, and vegetation type on colloid transport through a dense vegetation saturated soil system: Experiments and modeling. J. Hydrol., 499, 316–323.

Zhou, D., Thiele-Bruhn, S., Arenz-Leufen, M.G., Jacques, D., Lichtner, P., Engelhardt, I., 2016. Impact of manure-related DOM on sulfonamide transport in arable soils. J. Contam. Hydrol., 192, 118–128.

Received 12 July 2017
Accepted 21 September 2017

APPENDIX – Details about the organic matter degradation model.

The aquatic geochemical reactions within the adopted modeling approach are limited to the inorganic carbon reactions, as given in Table 1. For all aqueous species, the activity correction model of WATEQ is used:

$$\log \gamma = \frac{-Az^2\sqrt{\mu}}{1+Ba\sqrt{\mu}} + b\mu \quad (1)$$

where γ is the activity correction coefficient, z is the charge, μ is the ionic strength, A and B are constants at a given temperature, and a and b are species-dependent parameters, except for CO_2 for which the activity coefficient is obtained as $\log \gamma = 0.1\,\mu$. The temperature dependence of the mass action constant is given as:

$$\log_{10} K = A_1 + A_2 T + \frac{A_3}{T} + A_4 \log_{10} T + \frac{A_5}{T^2} + A_6 T^2 \quad (2)$$

where $A_1, \ldots, A_6$ are parameters and T is temperature in Kelvin. The relevant temperature range is limited between ~0 to ~30°C.

Tables 2 through 5 provide a list of parameter definitions and values used in the simulations of the organic matter degradation networks.

Table 1. Overview of species, geochemical reactions, and thermodynamic parameters (values are from the phreeqc.dat database as incorporated in PHREEQC-3).

Species	Reaction	Activity correction		Temperature dependence					
		a	*b*	A_1	A_2	A_3	A_4	A_5	A_6
H^+		9.0	0						
CO_3^{2-}		5.4	0						
OH^-	$H_2O = OH^- + H^+$	3.5	0	293.29	0.1361	–10576.9	–123.73	0	–6.996e–5
HCO_3^-	$CO_3^{2-} + H^+ = HCO_3^-$	5.4	0	107.89	0.0325	–5151.8	–38.93	563713.9	
CO_2	$CO_3^{2-} + 2H^+ = CO_2 + H_2O$	–	–	464.20	0.0934	–26986.2	–165.76	2248628.9	
$CO_{2(g)}$	$CO_2 = CO_2$	–	–	119.87	2.19e-2	–7337.8	–44.77	669371	

Table 2. Parameter values for network 1 (Eqs. (16)–(19)). Parameter values are for illustrative purpose.

Symbol	Parameter description	Value	Unit
i_F	Addition of fresh organic matter	0.0015	gC/d/dm^3 bulk
k_B	Decay rate for biomass pool	8.5×10^{-3}	1/d
$r_{SOM\text{-}P1\rightarrow P2}$	Transformation factor from SOM-P1 to SOM-P2	0.1	–
$r_{SOM\text{-}P1\rightarrow B}$	Transformation factor from SOM-P1 to B	0.3	–
$r_{SOM\text{-}P1\rightarrow I}$	Transformation factor from SOM-P1 to I	0.6	–
$r_{SOM\text{-}P2\rightarrow B}$	Transformation factor from SOM-P2 to B	0.4	–
$r_{SOM\text{-}P2\rightarrow I}$	Transformation factor from SOM-P2 to I	0.6	–
ρ_b	Bulk density	1.43	kg/dm^3 bulk
$k_{SOM\text{-}P1}$	Rate constant for SOM-P1 degradation	3.00×10^{-2}	1/d
$k_{SOM\text{-}P2}$	Rate constant for SOM-P2 degradation	5.00×10^{-3}	1/d

Table 3. Parameter values for network 2 (Eqs. (24)–(30)). Parameter values are for illustrative purpose.

Symbol	Parameter description	Value	Unit
i_F	Addition of fresh organic matter	0.0015	gC/d/dm^3 bulk
k_B	Decay rate for biomass pool	8.5×10^{-3}	gC/d/dm^3 bulk
$r_{SOM\text{-}P1\rightarrow P2}$	Transformation factor from SOM-P1 to SOM-P2	0.1	–
$r_{SOM\text{-}P1\rightarrow B}$	Transformation factor from SOM-P1 to B	0.3	–
$r_{SOM\text{-}P1\rightarrow I}$	Transformation factor from SOM-P1 to I	0.55	–
$r_{SOM\text{-}P1\rightarrow L}$	Transformation factor from SOM-P1 to SOM-L	0.05	–
$r_{SOM\text{-}P2\rightarrow B}$	Transformation factor from SOM-P2 to B	0.4	–
$r_{SOM\text{-}P2\rightarrow I}$	Transformation factor from SOM-P2 to I	0.5	–
$r_{SOM\text{-}P2\rightarrow L}$	Transformation factor from SOM-P2 to SOM-L	0.1	–
$r_{SOM\text{-}L\rightarrow B}$	Transformation factor from SOM-P2 to B	0.1	–
$r_{SOM\text{-}L\rightarrow I}$	Transformation factor from SOM-P2 to I	0.9	–
K_L	Binding affinity of DOM	5	dm^3/gC
S_{max}	Binding capacity for DOM	0.4	gC/dm^3 bulk
ρ_b	Bulk density	1.43	kg/dm^3
k_{sor}	First-order kinetic sorption term	0.05	d^{-1}
$k_{SOM\text{-}P1}$	Rate constant for SOM-P1 degradation	3.0×10^{-2}	1/d
$k_{SOM\text{-}P2}$	Rate constant for SOM-P2 degradation	5.0×10^{-3}	1/d
$k_{SOM\text{-}L}$	Rate constant for SOM-L degradation	2.0×10^{-6}	1/d

Table 4. Initial organic matter pools.

Organic Pool	Value	Unit
SOM-P1	1.75×10^{-4}	kgC/kg soil
SOM-P2	7.00×10^{-5}	kgC/kg soil
SOM-L1[*$]	0.019	gC/dm^3 bulk
B	7.00×10^{-5}	kgC / kg soil
DOM[$]	0.01	gC/dm^{3}soil

[$] only for reaction network 2 [*] Calculated in equilibrium with DOM

Table 5. Soil hydraulic parameters for the van Genuchten (1980) soil hydraulic functions, solute transport parameters, and plant uptake parameters (for the S-shape water uptake reduction model – see the HYDRUS-1D manual for more information Simunek et al. (2013)) for single porosity model implementation.

Symbol	Parameter description	Value	Unit
θ_r	Residual water content	0.08	dm^3/dm^3
θ_s	Saturated water content	0.45	dm^3/dm^3
α	Shape parameter of the water retention function	0.05	cm^{-1}
n	*S*hape parameter of the water retention functions	1.6	–
K_s	Saturated hydraulic conductivity	25	cm day^{-1}
D^w	Diffusion coefficient in the aqueous phase	2	cm^2 day^{-1}
D^a	Diffusion coefficient in the air phase	20,000	cm^2 day^{-1}
λ	Dispersivity	10	cm
P_{50}	Pressure head at which 50% reduction in water uptake occur	–500	cm
P_3	*E*xponent in the root water uptake response function	3	–

J. Hydrol. Hydromech., 66, 2018, 2, 227–231
DOI: 10.1515/johh-2017-0053

Simulating vertical flow wetlands using filter media with different grain sizes with the HYDRUS Wetland Module

Bernhard Pucher*, Guenter Langergraber

Institute of Sanitary Engineering and Water Pollution Control, University of Natural Resources and Life Sciences Vienna (BOKU), Muthgasse 18, A-1190 Vienna, Austria.
* Corresponding author. E-mail: bernhard.pucher@boku.ac.at

Abstract: In this study, the simulation results of four vertical flow wetland systems using the HYDRUS Wetland Module are presented. The four wetland systems comprise three single-stage pilot scale systems and one full-scale two-stage system. The main difference between these systems is the filter media used, referred to as fine media, i.e., sand with a grain size distribution 0.063–4 mm, or coarse media, i.e., sand with grain size distributions between 1–4 mm, respectively. The water-flow simulation of each system is carried out using the single porosity van Genuchten-Mualem model. A good match between measured and simulated volumetric effluent flow rates could be achieved for all wetland systems. For reactive transport simulations, the CW2D biokinetic model was applied. First, simulations were run using the standard CW2D parameter set. For some systems, adjustments of the parameter set were needed in order to avoid unlimited bacteria growth. To better fit measured COD, NH_4-N, and NO_3-N effluent concentrations, adjustments of few parameters of the standard parameter set were required. The results show that for the VF wetlands with fine sand, no adjustments of the CW2D standard parameter set were needed, while for systems with coarser filter media as the main layer, the standard parameter set had to be adjusted to match simulated and measured effluent concentrations.

Keywords: Treatment wetlands; Vertical flow; French VF wetland; HYDRUS Wetland Module; CW2D.

INTRODUCTION

In order to improve the understanding of water flow and solute transport, including biological and chemical processes within the soil matrix, the use of software tools like HYDRUS is steadily increasing. With the basic description of water flow in variably-saturated conditions coupled with solute transport, adsorption/desorption processes, geochemical reactions, and biokinetic degradation, a very broad range of applications is available and furthermore extended by various scientific communities (Šimůnek et al., 2016). One implemented module, the HYDRUS Wetland Module (Langergraber and Šimůnek, 2012), was developed in order to simulate the governing biological and chemical transformation and degradation processes of wastewater constituents in subsurface flow treatment wetlands (SSF TW). The field of TW simulation grew consistently over the last decades and has evolved from looking at such systems as a black box to the use of process-based models describing the simultaneous occurring processes responsible for the degradation of various pollutants in the wastewater (Langergraber, 2017; Meyer et al., 2015).

For the treatment of domestic wastewater, SSF TWs are generally applied. Furthermore, SSF TWs can be divided into horizontal flow (HF) and vertical flow (VF) wetlands, whereby in HF wetlands mainly anaerobic and in VF wetlands mainly aerobic processes occur (Kadlec and Wallace, 2009). Two biokinetic model formulations are implemented in the HYDRUS Wetland Module: CW2D (Langergraber and Šimůnek, 2005) that describes aerobic and anoxic processes and is mostly used for simulating VF wetlands and CWM1 (Langergraber et al., 2009a) that additionally describes anaerobic processes and is also applicable for HF wetlands. Their mathematical formulation is based on the IWA Activated Sludge Models (Henze et al., 2000).

In this study, simulation results of four different VF TWs are presented and discussed. Two systems are classical single-stage VF TWs (pilot-scale), one is a full-scale two-stage VF wetland system, and one is a French single-stage VF TW system (pilot-scale).

The two-stage VF wetland system is intermittently loaded with mechanically pre-treated wastewater. The first stage consists of a coarse filter media (sand 1–4 mm) for the main layer and has an impounded drainage layer, while the second stage uses a finer sand (0.063–4 mm) as the main filter layer. This system is designed for full nitrification and high nitrogen elimination. The design is based on the specific area needed with 1 m² per people equivalent (PE) for each stage, i.e., in total 2 m² per PE (Langergraber et al., 2008; Langergraber et al., 2009b; Langergraber et al., 2014).

The French VF wetland is also a two-stage VF wetland system but is intermittently loaded with raw wastewater. The main layer of the first stage consists of gravel. The loading of the first stage filter lasts for three to four days and is followed by a resting period twice this time. This is important for the degradation of organic matter and the drying of the sludge layer. The main layer of the second stage consists of sand and treats the percolating water from the first stage (Molle et al., 2005; Paing and Voisin, 2005).

Simulation for the four systems is carried out following the same procedure. Simulation results are compared to measured data and the need for adjustments of model parameter is discussed in relation to the different wetland parameters, i.e., sand used for the main layer, loading regime, etc.

MATERIALS AND METHODS

VF wetlands

A general description of the systems modeled is given in Table 1. Systems 1, 2, and 3 are based on the Austrian system where System 1 (Langergraber, 2001) and 2 (Pucher, 2015) represent the first stage of a 1m² pilot-scale system operated in the technical lab hall at the Institute of Sanitary Engineering at

Table 1. General description of the simulated systems.

	Size	Wastewater	Filter media	Depth*	Grain size*	Area	Drainage
Single-stage VF wetlands							
System 1	Pilot-scale	Primary treated	Sand	50cm	0.063–4 mm	1 m²	Free
System 2	Pilot-scale	Primary treated	Sand	50cm	1–4 mm	1 m²	Impounded
Two-stage VF wetland							
System 3	Full-scale	Primary treated	Sand	50cm	2–3 mm	50 m^2	Impounded
French VF wetland							
System 4	Pilot-scale	Raw	Pea gravel	40cm	2–4mm	2.3 m²	Free

* of the main layer

Table 2. CW2D processes (Langergraber and Šimůnek, 2012).

Heterotrophic bacteria		
1	Hydrolysis	Conversion of CS into CR
2	Aerobic growth of XH on CR	Mineralization of OM
3	Anoxic growth of XH on CR	Denitrification on NO_2-N
4	Anoxic growth of XH on CR	Denitrification on NO_3-N
5	Lysis of XH	Production of OM
Autotrophic bacteria		
6	Aerobic growth of XANs on NH_4-N	First step of nitrification
7	Lysis of XANs	Production of OM
8	Aerobic growth of XANb on NO_2-N	Second step of nitrification
9	Lysis of XANb	Production of OM

BOKU University. The third system (Langergraber et al., 2014) is a full-scale two-stage VF wetland system located on a mountain. System 4 (Ruiz et al., 2016) is a single-stage wetland based on the French system.

HYDRUS Wetland Module

HYDRUS (Šimůnek et al., 2016) numerically solves variably saturated water-flow and solute-transport equations. The water-flow equation incorporates a sink term to account for water uptake by plant roots. The solute-transport equations consider convective-dispersive transport in the liquid phase, diffusion in the gaseous phase, as well as nonlinear non-equilibrium reactions between the solid and liquid phases (Šimůnek et al., 2016). Version 2 of the HYDRUS Wetland Module includes two biokinetic model formulations to simulate the biochemical transformation and degradation processes in TWs: CW2D and CWM1 (Langergraber and Šimůnek, 2012). Up to now, only the single-porosity water-flow model can be used together with the HYDRUS Wetland Module although dual-porosity water-flow models are available within the standard HYDRUS software.

For the simulation of VF wetlands with aerobic conditions, the CW2D biokinetic model is commonly applied (Langergraber, 2017) and therefore CW2D is also chosen for this work. The mathematical formulation of CW2D includes 12 components and nine processes. The components are dissolved oxygen (O_2), organic matter (OM) divided into readily available (CR), slowly available (CS), and inert organic matter (CI), heterotrophic microorganisms (XH), autotrophic microorganisms (XANs, XANb), nitrogen compounds as ammonium (NH_4-N), nitrite (NO_2-N), and nitrate (NO_3-N) nitrogen, and nitrogen gas (N_2), as well as inorganic phosphorous (PO_4-P) (Langergraber and Šimůnek, 2005). The nine processes described in CW2D are related to the activities of the heterotrophic and autotrophic bacteria groups, respectively (Table 2).

Simulation procedure

For the two-stage system, each plot was simulated on its own. The simulated effluent concentrations of the first stage have been used as influent concentrations of the second stage (Hochfeldt, 2017). All four VF wetland systems have been calibrated following the same workflow. The water flow was modeled using the standard van Genuchten-Mualem soil hydraulic model (Mualem, 1976; van Genuchten, 1980). Measured soil hydraulic parameters, namely the hydraulic conductivity K_s, and the saturated water content θ_s, as well as the measured boundary flux of each system were used to determine the missing parameters, namely the residual water content θ_r and the form parameters α and n, using the inverse solution implemented in HYDRUS, leading to the calibration of the water-flow model.

The reactive transport simulation, including the biokinetic model, was carried out first using the soil and solute specific parameters proposed by Langergraber and Šimůnek (2011) and the standard parameter set of the CW2D module (Langergraber and Šimůnek, 2005). No adsorption processes were considered. The effects of plants, like nutrient uptake, were neglected and a root model was not implemented within the Wetland Module. The influent concentration of COD was fractionalized as follows: CI (inert organic matter) was set to the measured effluent COD concentration while the ratio of readily to slowly biodegradable organic matter, i.e., CR:CS, was 2:1 (Toscano et al., 2009). The adjustment of the biokinetic model parameters was done as follows:

(a) The first adjustment of the parameter set addresses the unlimited growth of the two bacterial groups, XH and XANs/XANb, as no growth limiting function is implemented. Therefore the lysis rates [d^{-1}] (b_h, b_{ANs}, b_{ANb}) were increased proportionally until a steady state within the model domain was reached (Pálfy et al., 2016; Pucher et al., 2017).
(b) In order to fit the simulated and measured NH_4-N effluent concentrations, the maximum aerobic growth rate μ_{ANs} [d^{-1}] of XANs was adjusted.

(c) In the impounded drainage layer, denitrification occurred. To fit the measured and simulated NO_3-N effluent concentrations, two parameters needed to be changed. First, the hydrolyses rate K_h [d^{-1}] was decreased so that less OM had been degraded in the main layer and more was available for denitrification in the impounded layer as electron donor. Secondly, the maximum denitrification rate μ_{DN} [d^{-1}] was changed addressing the growth of XH in the impounded layer under anoxic conditions.

RESULTS AND DISCUSSION

For all systems, a good match between measured and simulated flow data could be reached (results not shown here but can be found in Hochfeldt (2017), Langergraber (2017), and Pucher et al. (2017)).

Table 3 shows measured and simulated influent and effluent concentrations for all four VF wetland systems. In the first step, simulations were carried out using the standard parameter set of the CW2D biokinetic model (Langergraber and Šimůnek, 2005). These results are referred to as the "standard" parameter set in Table 3. When the match between the simulated and measured effluent concentrations was not sufficient, adjustments to the biokinetic model parameter set were carried out. The adjusted parameters are listed in Table 4 and simulation results are referred to as the "adjusted" parameter set in Table 3. For system 4, no parameter adjustments were performed. For more information on System 4, readers are referred to Pucher et al. (2017).

The fitting procedure was carried out using a trial-and-error approach starting with the growth of the three bacterial groups, namely XH and XANs/b, in order to get steady-state conditions (Figure 1). System 1 only needed to be adjusted for XH, while System 2 was adjusted for all three. For System 3, no adjustment to the lysis rate was needed (Figure 2). This is explained by the low hydraulic loading based on the event driven operation (Langergraber et al., 2014).

Table 3. Measured and simulated influent and effluent concentrations as mean values; *measurements taken only on the third day of loading.

			Parameter set	COD [$mg.L^{-1}$]	NH_4-N [$mg.L^{-1}$]	NO_3-N [$mg.L^{-1}$]
System 1	Influent	Measured		300	60	0.1
	Effluent	Measured		20	0.1	37
		Simulated	Standard	29	0.1	56
		Simulated	Adjusted	No adjustment required		
System 2	Influent	Measured		394	93	0.59
	Effluent	Measured		35	14.5	70.8
		Simulated	Standard	29	0.1	85.0
		Simulated	Adjusted	35	13.6	83.6
System 3	Influent	Measured		351	52.9	< 0.1
	Effluent Stage 1	Measured		42	14.1	0.6
		Simulated	Standard	33	0.9	54.7
		Simulated	Adjusted	32	16.3	5.0
	Effluent Stage 2	Measured		<10	<0.03	12.2
		Simulated	Standard	7	0.09	12.9
		Simulated	Adjusted as for stage 1	7	12.9	<0.01
System 4*	Influent	Measured		850	94	2
	Effluent	Measured		171	30	38
		Simulated	Standard	141	3	83
		Simulated	Adjusted	No adjustments performed		

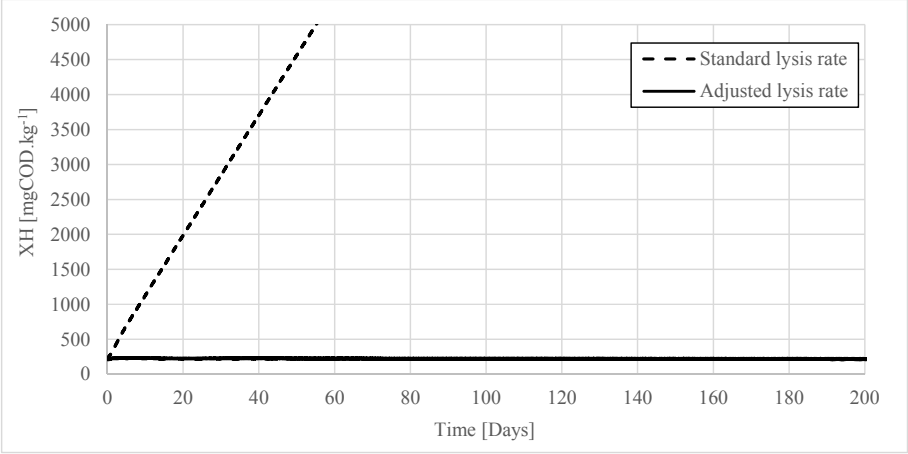

Fig. 1. Effect of the lysis rate adjustment for XH of System 2.

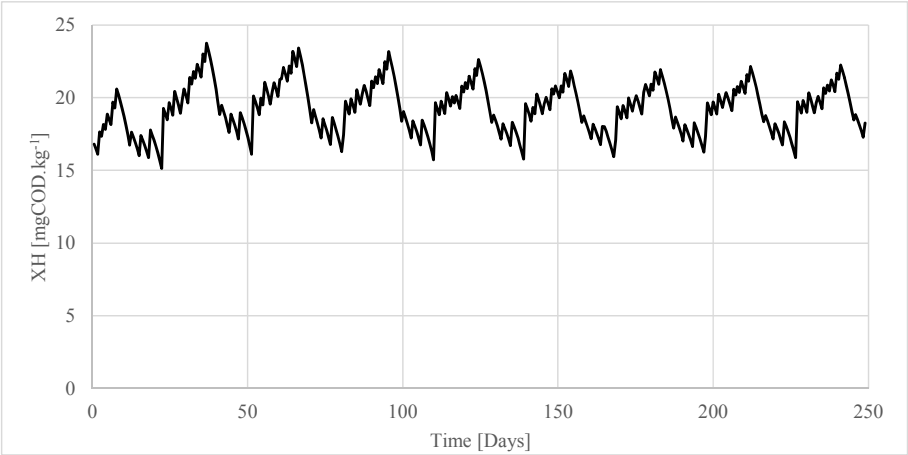

Fig. 2. Steady state conditions of XH growth in Stage 1 of System 3 with the standard value for the lysis rate b_H.

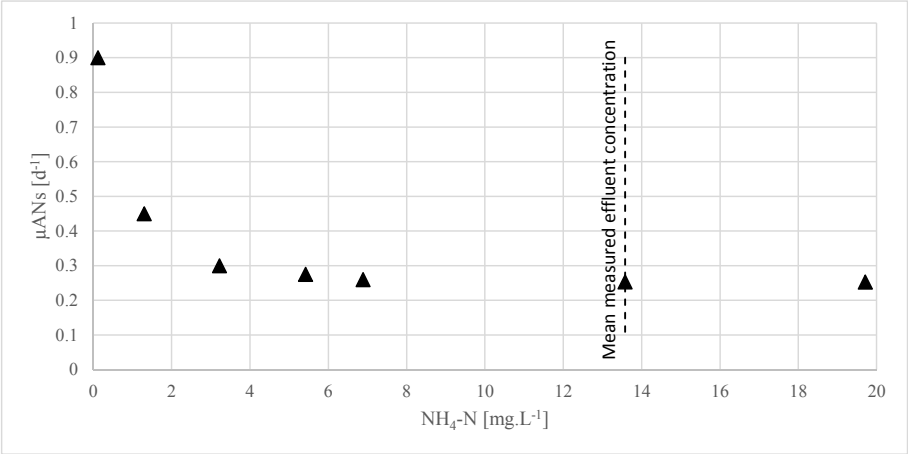

Fig. 3. Effect of decreasing μ_{ANs} on the simulated NH_4-N effluent concentration during the fitting procedure of System 2.

Table 4. Comparison of the parameter adjustments required for the CW2D biokinetic model parameters.

Parameter	Description		Standard	System 1	System 2	System 3 Stage 1
K_h	Hydrolysis rate	[d^{-1}]	3		–	0.59
b_h	Lysis rate for XH	[d^{-1}]	0.4	0.9	0.96	–
$b_{ANs/b}$	Lysis rate for XANs/b	[d^{-1}]	0.15		0.216	–
μ_{ANs}	Maximum aerobic growth rate of XANs	[d^{-1}]	0.9		0.2538	0.18
μ_{DN}	Maximum denitrification rate of XH	[d^{-1}]	4.8		–	60

The fitting of measured and simulated NH_4-N was carried out by decreasing the maximum nitrifier growth rate μ_{ANs}. The effect of this adjustment is illustrated in Figure 3 for System 2 as an example.

The simulation results for System 1 show that, for systems using the fine-filter material, sand with grain size distribution 0.063–4 mm, no parameter adjustments are needed, while for System 2, using the coarser sand (grain size distribution 1–4 mm), the CW2D standard parameter set overestimates the treatment performance. The same effect can be observed within System 3 using coarser sand with grain size distribution 2–3 mm. When applying the adjusted parameter set from the first stage of System 3 to its second stage (using fine sand with grain size distribution 0.063–4 mm), the simulated treatment performance is underestimated. By using the CW2D standard parameter set, a good fit can be achieved for the second stage of System 3.

The difference in the simulation performance between fine and coarse filter media can be explained by the available water-flow model when using the HYDRUS Wetland Module. A comparison between the classical equilibrium flow model and a non-equilibrium model (dual-porosity model) was carried out by Morvannou et al. (2013). When simulating a tracer experiment for the first stage of a French VF wetland system, the dual-porosity model fitted the experiment well, while with the standard equilibrium water-flow model, the tracer couldn't be fitted. These results can be directly compared with the simulation of the treatment performance carried out in this study, as for coarse media a higher performance was simulated than measured. This is explained by the longer contact time between wastewater and biofilm due to the equilibrium flow model.

CONCLUSION

Based on the simulation results the following conclusions can be drawn:

- Despite differences in construction and operational conditions of the presented systems, the simulation using the HYDRUS Wetland module gives good results when adjustments to the standard parameter set of the CW2D biokinetic model (Langergraber and Šimůnek, 2005) have been made.
- The most limiting factor in achieving good simulation results using the CW2D standard parameter set is related to the grain size of the filter material used. For fine filter media, the CW2D standard parameter set provides sufficient results, while for coarser media, the treatment performance is overestimated.
- As only single-pore water-flow models can be used with the HYDRUS Wetland Module, only equilibrium-matrix flow is described. Preferential flow paths occurring in coarser media cannot be described and therefore the simulated hydraulic retention time (HRT) is too high, resulting in an overestimation of the pollutant removal.
- It is expected that when coupling a dual-porosity water-flow model with the HYDRUS Wetland Module, better description of the actual water flow, especially preferential flow path and simulated HRT, can be achieved and thus excessive changes of the biokinetic model parameters can be avoided. Finally, it should become possible to simulate measured effluent concentrations for VF wetlands with coarse sand as the main layer using the standard parameter set of the biokinetic model.

REFERENCES

Henze, M., Gujer,W., Mino, T., Loosdrecht, M., 2000. Activated Sludge Models ASM1, ASM2, ASM2d and ASM3. IWA Publishing, London, UK

Hochfeldt, V., 2017. Numerical simulation of a full-scale two-stage constructed wetland system. Master Thesis. University of Applied Sciences Höxter, Germany and University of Natural Resources and Life Sciences, Vienna (BOKU University), Austria.

Kadlec, R.H., Wallace, S.D., 2009. Treatment Wetlands. 2nd ed. CRC Press, Boca Raton, FL, USA.

Langergraber, G., 2001. Development of a Simulation Tool for Subsurface Flow Constructed Wetlands. Ph.D. Thesis. University of Natural Resources and Applied Life Sciences, Vienna (BOKU University), Austria.

Langergraber, G., 2017. Applying process-based models for subsurface flow treatment wetlands: recent developments and challenges. Water, 9, 1, 5.

Langergraber, G., Šimůnek, J., 2005. Modeling variably saturated water flow and multicomponent reactive transport in constructed wetlands. Vadose Zone Journal, 4, 4, 924–938.

Langergraber, G., Šimůnek, J., 2011. HYDRUS Wetland Module Manual - Version 2. HYDRUS Software Series 4. Department of Environmental Sciences, University of California Riverside, Riverside, CA, USA, 56 p.

Langergraber, G., Šimůnek, J., 2012. Reactive transport modeling of subsurface flow constructed wetlands using the HYDRUS Wetland Module. Vadose Zone Journal, 11, 2.

Langergraber, G., Leroch, K., Pressl, A., Rohrhofer, R., Haberl, R., 2008. A two-stage subsurface vertical flow constructed wetland for high-rate nitrogen removal. Water Science and Technology, 57, 12, 1881–1887.

Langergraber, G., Rousseau, D.P.L., García, J., Mena, J. 2009a. CWM1: A general model to describe biokinetic processes in subsurface flow constructed wetlands. Water Science and Technology, 59, 9, 1687–1697.

Langergraber, G., Leroch, K., Pressl, A., Sleytr, K., Rohrhofer, R., Haberl, R., 2009b. High-rate nitrogen removal in a two-stage subsurface vertical flow constructed wetland. Desalination, 246, 1–3, 55–68.

Langergraber, G., Pressl, A., Haberl, R., 2014. Experiences from the full-scale implementation of a new two-stage vertical flow constructed wetland design. Water Science and Technology, 69, 2, 335–342.

Meyer, D., Chazarenc, F., Claveau-Mallet, D., Dittmer, U., Forquet, N., Molle, P., Morvannou, A., Pálfy, T., Petitjean, A., Rizzo, A., Samsó Campà, R., Scholz, M., Soric, A., Langergraber, G., 2015. Modelling constructed wetlands: Scopes and aims – a comparative review. Ecological Engineering, 80, 205–213.

Molle, P., Liénard, A., Boutin, C., Merlin, G., Iwema, A., 2005. How to treat raw sewage with constructed wetlands: an overview of the French systems. Water Science and Technology, 51, 9, 11–21.

Morvannou, A., Forquet, N., Vanclooster, M., Molle, P., 2013. Which hydraulic model to use for vertical flow constructed wetlands? In: Šimůnek, J., van Genuchten, M.T., Kodešová, R. (Eds.): Proc. 4th Int. Conf. HYDRUS Software Applications to Subsurface Flow and Contaminant Transport Problems. Dept. of Soil Science and Geology, Czech University of Life Sciences, Prague, pp. 247–257.

Mualem, Y., 1976. A new model for predicting the hydraulic conductivity of unsaturated porous media. Water Resources Research, 12, 3, 513–522.

Paing, J., Voisin, J., 2005. Vertical flow constructed wetlands for municipal wastewater and septage treatment in French rural area. Water Science and Technology, 51, 9, 145–155.

Pálfy, T.G., Molle, P., Langergraber, G., Troesch, S., Gourdon, R., Meyer, D., 2016. Simulation of constructed wetlands treating combined sewer overflow using HYDRUS/CW2D. Ecological Engineering, 87, 340–347.

Pucher, B., 2015. Simulation of vertical flow filters for the treatment of domestic wastewater using sand and zeolite as filter materials. Master Thesis. University of Natural Resources and Applied Life Sciences, Vienna (BOKU University), Austria.

Pucher, B., Ruiz, H., Paing, J., Chazarenc, F., Molle, P., Langergraber, G., 2017. Using numerical simulation of a one stage vertical flow wetland to optimize the depth of a zeolite layer. Water Science and Technology, 75, 3, 650–658.

Šimůnek, J., van Genuchten, M.T., Šejna, M., 2016. Recent developments and applications of the HYDRUS Computer Software Packages. Vadose Zone Journal, 15, 7, 25 p.

Toscano, A., Langergraber, G., Consoli, S., Cirelli, G.L., 2009. Modelling pollutant removal in a pilot-scale two-stage subsurface flow constructed wetlands. Ecological Engineering, 35, 2, 281–289.

van Genuchten, M.T., 1980. A closed-form equation for predicting the hydraulic conductivity of unsaturated soils. Soil Science Society of America Journal, 44, 5, 892–898.

Received 29 June 2017
Accepted 7 September 2017

J. Hydrol. Hydromech., 66, 2018, 2, 232–245
DOI: 10.1515/johh-2017-0055

Coupling DSSAT and HYDRUS-1D for simulations of soil water dynamics in the soil-plant-atmosphere system

Vakhtang Shelia[1*], Jirka Šimůnek[2], Ken Boote[1], Gerrit Hoogenbooom[1]

[1] Department of Agricultural and Biological Engineering & Institute for Sustainable Food Systems, University of Florida, Gainesville, FL 32611, USA.
[2] Department of Environmental Sciences, University of California Riverside, Riverside, CA, USA.
[*] Corresponding author. Tel.: (1) 352-392-1864 ext 259. E-mail: vakhtang.shelia@ufl.edu

Abstract: Accurate estimation of the soil water balance of the soil-plant-atmosphere system is key to determining the availability of water resources and their optimal management. Evapotranspiration and leaching are the main sinks of water from the system affecting soil water status and hence crop yield. The accuracy of soil water content and evapotranspiration simulations affects crop yield simulations as well. DSSAT is a suite of field-scale, process-based crop models to simulate crop growth and development. A "tipping bucket" water balance approach is currently used in DSSAT for soil hydrologic and water redistribution processes. By comparison, HYDRUS-1D is a hydrological model to simulate water flow in soils using numerical solutions of the Richards equation, but its approach to crop-related process modeling is rather limited. Both DSSAT and HYDRUS-1D have been widely used and tested in their separate areas of use. The objectives of our study were: (1) to couple HYDRUS-1D with DSSAT to simulate soil water dynamics, crop growth and yield, (2) to evaluate the coupled model using field experimental datasets distributed with DSSAT for different environments, and (3) to compare HYDRUS-1D simulations with those of the tipping bucket approach using the same datasets. Modularity in the software design of both DSSAT and HYDRUS-1D made it easy to couple the two models. The pairing provided the DSSAT interface an ability to use both the tipping bucket and HYDRUS-1D simulation approaches. The two approaches were evaluated in terms of their ability to estimate the soil water balance, especially soil water contents and evapotranspiration rates. Values of the *d* index for volumetric water contents were 0.9 and 0.8 for the original and coupled models, respectively. Comparisons of simulations for the pod mass for four soybean and four peanut treatments showed relatively high *d* index values for both models (0.94–0.99).

Keywords: System Modeling; Crop Growth; Soil water; Unsaturated zone; DSSAT; HYDRUS-1D.

INTRODUCTION

Accurate estimation of the soil water balance is important for determining the availability of water resources and their optimal management in agriculture, the major consumer of water. Process-based simulation models of complex systems such as the soil-plant-atmosphere continuum are invaluable tools for this purpose. They may be used to simulate in detail multiple processes of the real system to predict various state variables at every time step during the simulations. The processes of evapotranspiration and leaching are the main sinks of water in the soil-plant-atmosphere system affecting soil water status. Their correct simulation is a prerequisite for successful simulations of crop growth and yield since the accuracy of soil water content and evapotranspiration simulations affect the accuracy of simulated plant processes and crop yield. Comparing model simulation results with field observations, or with results of other models based on different conceptual approaches, may provide invaluable information on the performance of the model and reveal their strong and weak parts. This is an essential step also when selecting appropriate models for practical applications in water resources analyses and for estimation of crop yield components. Comparing a physically-based soil-plant-atmosphere model with a simpler model may provide information on how the models perform compared to each other. If a simpler model can simulate the required processes with sufficient accuracy, that model should be an attractive alternative to a more data-intensive, complex simulation model. Using a simple model may also minimize the need for a comprehensive data collection effort (Ines at al., 2001; Pachepsky et al., 2006).

Crop simulation models usually are based on mathematical equations that describe the basic flow and conversion processes of carbon, water, and nitrogen, and that are integrated hourly or daily to predict the time course of crop growth, nutrient uptake, and water use, and to predict final yield and other plant traits (e.g., Boote et al., 2010). The Cropping System Models (CSM) in the DSSAT software (Decision Support System for Agrotechnology Transfer) are particularly well suited for simulating various agricultural practices (Jones et al., 2003). DSSAT (version 4.6) integrates several crop system models, soil carbon and nitrogen models, a daily water dynamic model, and a range of crop/land management options to simulate crop growth/yield and environmental impacts. DSSAT has been used widely and successfully for crop yield simulations under different management strategies, for optimizing the use of various resources, for yield trend simulations under different soil and climate scenarios, for crop yield risk analysis (Gijsman et al., 2002b; Sarkar, 2009), for simulating corn yield and nitrogen cycling in a 50-year corn production experiment (Liu et al., 2010), and for many other applications. The software has also been applied to controlled tile drainage-subsurface irrigation systems (Liu et al., 2011). Hence, DSSAT is particularly useful for predicting the short-, medium-, and long-term impacts of specific land management practices on crop yield, soil water storage, and nitrate-N leaching losses (Boote et al., 2010; Gheysari et al., 2009; Mullen et al., 2009).

The DSSAT Cropping System Model (CSM) (Jones et al., 2003; Hoogenboom et al., 2015) is a suite of field-scale, process-based crop models that have the capacity to simulate both crop and soil processes. They include the phenological devel-

opment of crops and detailed growth components from emergence until harvest maturity on the basis of crop genetic coefficients, environmental (weather, soil) conditions, and management options. To simulate soil water flow and root water uptake in each individual soil layer, DSSAT CSM uses a one-dimensional tipping bucket approach (Ritchie, 1998) that considers the soil profile to consist of a number of soil layers that are all homogeneous horizontally. The soil water balance model currently uses a tipping bucket approach for simulating soil hydrologic cycle and water redistribution for all crop models in CSM. The time step for the soil water balance and evapotranspiration (*ET*) calculations is daily, which matches the timing of weather data inputs and daily plant dry matter growth (Ritchie, 1998). Boote et al. (2008) concluded that the tipping bucket soil water balance model in DSSAT generally works satisfactorily when the soil water-holding properties (a drained upper limit, *DUL*, and a lower limit of plant-extractable soil water, *LL*) are estimated properly, and when the rooting depth and root length distribution are predicted adequately. Nevertheless, the approach is inherently more approximate than the soil water flow calculations used in many hydrological models such as HYDRUS-1D, which can estimate soil moisture distribution in the soil profile with higher accuracy (Scanlon et al., 2002).

HYDRUS-1D (Šimůnek et al., 2008; 2016) is a widely used hydrological model that simulates water flow in one-dimensional variably-saturated soils using numerical solutions of the Richards equation. The water flow equation incorporates a sink term to account for water uptake by plant roots. Root water uptake and transpiration are calculated using the formulation of Feddes et al. (1978). Evapotranspiration can be calculated using the Penman-Monteith equation. As compared to DSSAT, calculations in HYDRUS-1D are more physically based by allowing flow to be driven by pressure head differences, thus allowing for capillary flow and hence both upward or downward flow in the soil profile. The runoff calculations in HYDRUS-1D are also less empirical than in DSSAT. While DSSAT uses the modified curve number method of the United States Department of Agriculture, Soil Conservation Service (USDA-SCS) (Williams, 1991), HYDRUS-1D determines runoff as infiltration-excess water that is obtained by the numerical solution of the Richards equation for specified precipitation rates and soil hydraulic properties.

HYDRUS-1D has been used widely in many industrial and environmental applications, as well as for addressing many agricultural problems (Šimůnek et al., 2016). Examples of existing agricultural applications include irrigation management (Bristow et al., 2002; Dabach et al., 2015), drip and sprinkler irrigation design (Bristow et al., 2002; Gärdenäs et al., 2005; Hanson et al., 2008; Kandelous et al., 2012), studies of root water and nutrient uptake (Šimůnek and Hopmans, 2009; Vrugt et al., 2001a,b), among many others.

Both DSSAT and HYDRUS-1D have been used widely and tested separately, as well as coupled with other models. Several crop models describing relevant crop growth processes have been integrated successfully with hydrological models, such as DSSAT-RZWQM (Ma et al., 2006), DSSAT-SWAP (Dokoohaki et al., 2016), SWAT-MODFLOW (Sophocleous et al., 1999), and WOFOST-SWAP (van Walsum, 2011). Similarly, HYDRUS have been coupled successfully with existing crop and root growth models (e.g., Groenendyk et. al., 2012; Han et al., 2015; Hartmann et al., 2017; Li et al., 2014; Peña-Haro et al., 2012; Wang et al., 2014; Zhou et al., 2012). For example, Peña-Haro et al. (2012) integrated WOFOST, a crop growth and production model, with HYDRUS-1D as well as with MODFLOW-2000 (Harbaugh et al., 2000), the latter being a saturated flow model. The coupling was done using a combination of two different approaches: external coupling (through input/output data manipulation) and by using code wrapping. Peña-Haro et al. (2012) used OMS3 for wrapping WOFOST and PYTHON to write scripts. Groenendyk et al. (2012) coupled HYDRUS-1D with a generic crop growth model based on the plant growth module used in the WEPP model and then used the Ensemble Kalman Filter for assimilation of soil water content observations into the hydrologic model. The coupled approach was then tested for an irrigated wheat cropping experiment conducted at Maricopa, Arizona. Similarly, Hydrus-1D was coupled with MODFLOW-2000 for simulating hydrological processes at the large scale (Seo et al., 2007; Twarakavi et al., 2008).

The main objectives of this study were: a) to implement the flow routines from HYDRUS-1D into the DSSAT CSM crop models as a new option for simulating soil water dynamics, b) to evaluate the coupled model using field experimental datasets distributed with DSSAT for different environments, and c) to compare the performance of the HYDRUS-1D approach with the tipping bucket approach in DSSAT CSM using the same measured datasets. By integrating DSSAT with HYDRUS-1D, crop production simulations of DSSAT can be improved by using more accurate calculations of actual evaporation, transpiration, root water uptake, drainage, and water distributions in the soil profile using the Richards equation.

MATERIALS AND METHODS

DSSAT CSM

The Cropping System Model (CSM) within DSSAT V4.6 (Hoogenboom et al., 2015; Jones et al., 2003) contains various crop models that are executed under the DSSAT shell. The crop models available are the CERES models for cereals (barley, maize, sorghum, millet, rice, and wheat), the CROPGRO models for legumes (dry bean, soybean, peanut, and chickpea), and additional models for root crops (cassava, potato) and other crops (sugarcane, tomato, sunflower, and pasture). The architecture differs from one model to another. Various controls and management scenarios can be invoked within the shell to simulate crop growth. The crop models can simulate single cropping, seasonal and sequential cropping systems.

The soil water balance in DSSAT is based on a formulation by Ritchie (1972, 1981a,b) using the concept of a drained upper limit (*DUL*) and drained lower limit (*LL*) for available soil water. The approach applies a simple water accounting procedure to each layer in the soil profile (Porter et al., 2004; Ritchie, 1985; 1998). Water from an upper layer cascades to lower layers, thereby mimicking the process of a series of linear reservoirs. Infiltration is calculated as the difference between rainfall/irrigation and runoff. Drainage between layers takes place if soil water present in the layer exceeds its water holding capacity. Drainage at the bottom of the soil profile is equal to the drainage flux from the bottom layer. Upward flow can be caused by root water uptake due to transpiration and by soil evaporation. Potential root water extraction depends on available soil water and the root length density of each layer in the soil. Actual transpiration is calculated using reduction factors as a function of the leaf area index and an energy extinction coefficient. Infiltration and runoff from rainfall or irrigation water are calculated using the USDA Soil Conservation Service runoff curve number method (Williams, 1991). The profile is assumed to be well drained and without any interaction with groundwater. Ritchie (1998) recommended the use of more appropriate modeling approaches for poorly

drained conditions where the oxygen stress may affect crop growth.

Soil water balance processes include infiltration of rainfall and irrigation, runoff, soil evaporation, crop transpiration, root water uptake from the various soil layers, and drainage of water from the soil profile below the root zone (Boote et al., 2008). The soil is divided into a number of computational layers, up to a maximum of 20. The water content of each layer varies between the lower limit of plant extractable soil water [*LL*(*j*)], the drained upper limit [*DUL*(*j*)], and the saturated soil water content [*SAT*(*j*)], where *j* is a soil layer number. If the water content of a given layer is above *DUL*, water will drain to the next layer based on the tipping bucket approach, using a profile-wide drainage coefficient (*SWCON*). If available, the saturated hydraulic conductivity (K_s) of each soil layer can be entered to control vertical drainage from one layer to the next. This feature allows the soil to retain water above *DUL* in layers that have a sufficiently low K_s, and which case soil layers may remain saturated long enough to cause root damage, reduced root water uptake, anoxia-induced stress, and lower N fixation. Water between *SAT* and *DUL* is available for root water uptake, subject to the anoxia-induced restriction that is triggered when the air-filled pore space falls below 2% of porosity (this value can be species-dependent). The DSSAT V4.6 software includes pedotransfer functions that compute *LL*, *DUL*, and *SAT* from sand, silt, clay, soil organic carbon content, and bulk density. The pedotransfer functions are mostly those by Saxton et al. (1986) as described by Gijsman et al. (2002a).

The default option for computing potential evapotranspiration (*PET*, equivalent to ET_O) is the Priestley-Taylor method (Priestley and Taylor, 1972; Ritchie, 1985), primarily because it is less demanding for weather data and does not require daily wind speed or dewpoint temperature data as inputs. The FAO-56 Penman-Monteith method is available if wind speed and dewpoint temperature are provided. The DSSAT crop models partition *PET* into potential plant transpiration (EP_O) and potential soil evaporation (ES_O) following Ritchie's (1972, 1985) approach, which considers the portion of net radiation that reaches the soil surface and can be used as latent energy to evaporate water from the soil surface if the soil is wet.

Actual soil evaporation (*ES*) and plant transpiration (*EP*) depend on the availability of water to meet potential rates. The current DSSAT CSM models allow calculations of *ES* using two soil evaporation methods: Suleiman-Ritchie (Ritchie et al., 2009) and the two-stage soil evaporation method of Ritchie (1985). The first approach is based on an equation derived from diffusion theory by Suleiman and Ritchie (Suleiman and Ritchie, 2003). The method is currently the default option for *ES* computations in DSSAT CSM. The two-stage soil evaporation method computes *ES* by assuming a constant rate during the energy-limited stage (Stage 1) and a falling-rate stage (Stage 2) that begins after the first stage loss has been met, during which *ES* declines with the square root of time. Since neither the Suleiman-Ritchie method nor the two-stage soil evaporation method are considered to particularly accurate, improvements are still being considered.

Root water uptake must be computed before actual canopy transpiration (*EP*) is computed. Potential root water uptake, *RWU*(*j*), from each soil layer is a function of the root length density (*RLD*) and the soil water content of that layer, and is calculated using a simplified approximation of radial flow to roots (Ritchie, 1985). The total soil water content (*SWTD*) and the total extractable water content (*SWXD*) in the soil profile, among other variables, are calculated in the soil water balance module. *SWTD* is equal to the water contents summed over all soil layers, i.e., $SWTD = \Sigma SW(j) \times DLAYR(j)$, where *SW*(*j*) is the volumetric water content in the *j*th layer and *DLAYR*(*j*) is the thickness of the *j*th layer. *SWXD* is similarly equal to the extractable water contents summed over all soil layers, i.e., $SWXD = \Sigma(SW(j) - LL(j)) \times DLAYR(j)$.

HYDRUS-1D

HYDRUS-1D is a physically-based, detailed hydrological model that simulates the relationships between soil, water, and weather, while using a sink term to account for water uptake by plant roots. The core of the model is the Richards one-dimensional equation, which combines the Darcy-Buckingham law for the fluid flux with the continuity equation as follows:

$$\frac{\partial \theta}{\partial t} = \frac{\partial}{\partial z}\left[K(h)\frac{\partial h}{\partial z} - K(h) \right] - S \qquad (1)$$

where θ is the volumetric water content [L^3L^{-3}], h is the pressure head [L], K is the unsaturated hydraulic conductivity [LT^{-1}], z is the vertical coordinate positive upward [L], t is time [T], and S is root water uptake [T^{-1}].

HYDRUS-1D simulates soil water movement by considering spatial differences in the soil water potential in the soil profile. The governing equation is solved numerically using an implicit finite element scheme, which can be applied to both saturated and unsaturated conditions. The soil hydraulic functions are described using the analytical functions of van Genuchten-Mualem (Mualem, 1976; van Genuchten, 1980), among other formulations. HYDRUS-1D also considers, as needed, the effects of heat on water flow and the fate and transport of solutes in soils. Numerical solutions are provided for both flux or pressure head controlled boundary conditions at the top and bottom boundaries. The Penman-Monteith equation can be used to estimate potential evapotranspiration, ET_p. The HYDRUS-1D model uses the leaf area index (*LAI*) or the soil cover fraction (*SC*) to separate potential evapotranspiration (ET_p) into potential plant transpiration (T_p) and potential evaporation (E_p) of a partially covered soil. Reductions in T_p and E_p are calculated using a physically-based approach. Reductions in T_p are obtained by using the Feddes et al. (1978) approach involving stress response functions, which depend on the type of crop. Reductions in E_p are obtained directly from the numerical solution of the Richards equation by switching from a flux to a pressure head boundary condition when some limiting minimum pressure head is reached (e.g., –150 m). The effects of salinity and water/oxygen stress on actual transpiration can be considered to be either additive or multiplicative. Surface runoff is evaluated as infiltration-excess water calculated using the Richards equation for specified precipitation rates and soil hydraulic properties. Alternatively, infiltration-excess water can accumulate on the soil surface until a specified limit is reached, after which surface runoff is initiated. Field drainage to tile drains can be simulated using the Hooghoudt or Ernst equations for homogeneous and heterogeneous soil profiles, respectively. The bottom flux is calculated according to the selected bottom boundary conditions. Several water management scenarios can be modeled with HYDRUS-1D. For example, irrigation scheduling can be considered at fixed times or using a number of criteria that can trigger irrigation, such as its timing and depth of application.

Coupling the two models

Accurate simulations of crop growth require proper integration of models for crop growth and water flow in the unsaturated zone. There are at least three different approaches for integrating independent external programs (Peña-Haro et al., 2012):

1) One could modify the original source code of the two models in order to have the coupled model within the same executable file.

2) The models could interact through their input/output files. However, if the variables of interest are not included in the default input or output files, this approach requires modifications to the original source codes of the two models.

3) The original code can be wrapped using a specialized software such as OMS3 (David et al., 2002), OpenMI (Gregersen, 2007), or PYTHON (www.python.org). This approach allows one to have access to all variables stored in a memory that is common to all programs.

In order to implement the HYDRUS-1D water flow routines into DSSAT, the routines were simplified first by removing the source code related to other processes, such as vapor flow and solute transport. After some reorganization, the remaining source code was then included directly into DSSAT CSM (both models are written in the Fortran language) to obtain one single executable program. The modular structure of DSSAT CSM (Jones et al., 2003) requires that all rate processes are calculated each day based on the state variables from the previous day, using a daily time step. Corresponding changes were implemented to inputs/outputs from HYDRUS-1D to DSSAT. Some variables had to be passed between the main program and the new subsystem. These data types were defined inside a new module and passed between the models.

Data transfer between the models can be summarized as follows (Fig. 1): DSSAT CSM calculates crop growth by taking as input the crop parameters and weather data. Among the output that DSSAT CSM generates, the following parameters were transferred to HYDRUS-1D as input: rooting depth, potential transpiration and evaporation, and irrigation and precipitation. Although DSSAT calculates root length distributions also, the current version of the coupled model assumes the HYDRUS-1D approach in which the root distribution decreases linearly with depth from the soil surface to the bottom of the root zone. HYDRUS-1D then calculates soil water contents and actual transpiration and evaporation rates, integrated to a daily basis using the variable time-steps of HYDRUS-1D, which are then sent back to DSSAT CSM. Temporal and spatial discretizations are different in the two models and thus had to be synchronized. While HYDRUS-1D uses variable time steps and water stress periods are used, the structure of DSSAT CSM allows only daily time steps. Consequently, the two models exchange information on a daily time interval, while HYDRUS-1D carried out multiple time steps during this interval. Similarly as for the temporal discretization, HYDRUS-1D usually uses a much finer spatial discretization than DSSAT CSM. HYDRUS-1D outputs thus had to be averaged over multiple nodes, before information could be entered into DSSAT CSM.

The coupled DSSAT-HYDRUS-1D model is now able to simulate water flow using both the original tipping bucket approach as well as the HYDRUS-1D based numerical solution of the Richards equation. While HYDRUS-1D still focuses mostly on soil water, the Cropping System Model (CSM) from DSSAT deals nearly exclusively with plant related processes.

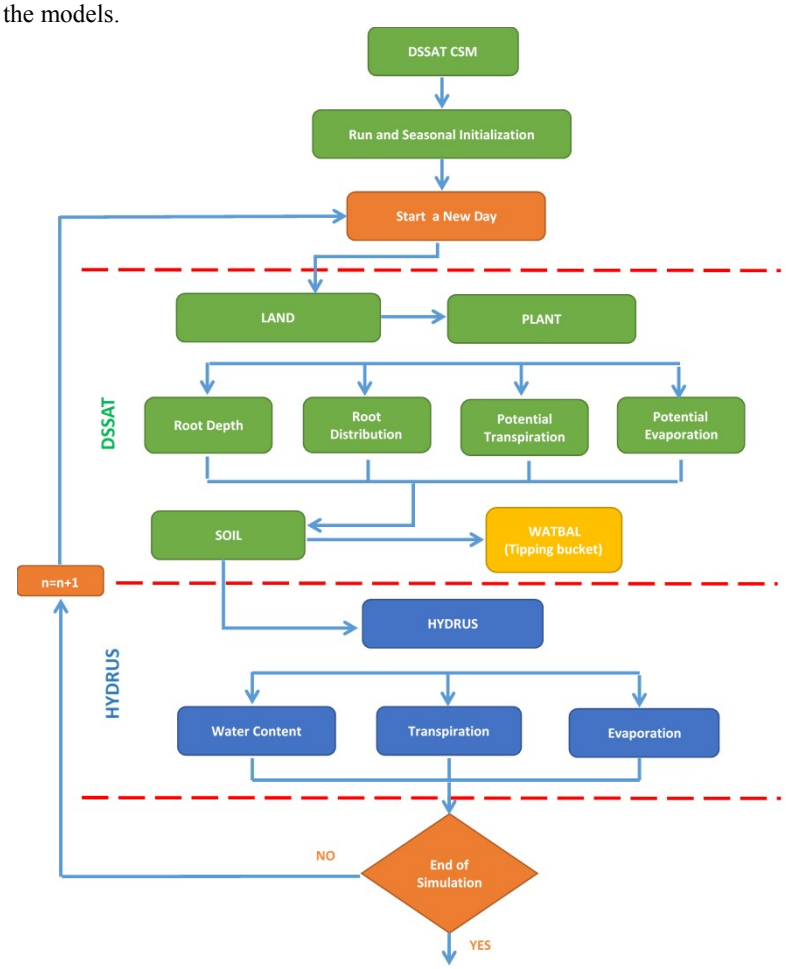

Fig. 1. Flowchart of the coupled DSSAT and HYDRUS-1D model.

Field experiments and data

We used data from eight treatments of six experiments released with DSSAT V4.6 (Hoogenboom et al., 2015) for soybean and peanut to evaluate the coupled model. The field experiments were conducted between 1978 and 1990 by the University of Florida (UF), Gainesville, Florida, and Iowa State University (ISU), Ames, Iowa. The experimental field at UF was located at the campus far, with soil being characterized as a Millhopper fine sand soil (loamy, siliceous, hyperthemic Grossarenic Paleudults). The soil profiles in the DSSAT soil dataset (the SOIL.SOL file) are identified as IBSB910015 and IBPN910015 for the soybean and peanut experiments, respectively. Table 1 shows the soil physical and hydraulic properties of nine layers of the soil profile. These data are needed along with other soil properties such as soil albedo (*SALB*, fraction), the evaporation limit (*SLU1*, mm), the drainage rate (*SLDR*, fraction day^{-1}), and the runoff curve number (*SLRO*) to simulate soil water dynamics in DSSAT. The drainage rate, *SLDR*, represents the fraction of water between the actual water content and the drained upper limit that drains from a soil layer in one day. For the given soil, these values were *SALB* = 0.18, *SLU1* = 5.0 mm, *SLDR* = 0.5 day^{-1}, and *SLRO* = 66.

Based on the particle size distribution and soil bulk density data in Table 1, two soil layers 0–15 cm and 15–180 cm were distinguished for the experimental field at UF, Gainesville, consisting of sand and loamy sand, respectively. Parameters for the van Genuchten-Mualem soil water retention functions (van Genuchten, 1980) for these two soil textures were taken from the HYDRUS-1D soil catalog and then used in the DSSAT-HYDRUS-1D coupled model (Table 2).

The soil of the second experimental field at ISU was characterized as Nicollet clay loam (fine-loamy, mixed, Mesic Aquic). This soil profile in the DSSAT soil dataset was identified as IBSB910049. Since the IBSB910049 soil profile contains only data necessary to run DSSAT, while lacking data on soil texture and the saturated hydraulic conductivity, we assumed that the entire soil profile was homogeneous and used the HYDRUS-1D default parameters for a clay loam soil (Table 2).

The soybean varieties "BRAGG" and "Williams-82" were used in the field experiments at UF and ISU, respectively. Their default cultivar coefficients are given in the soybean cultivar file SBGRO046.CUL in DSSAT. The cultivar coefficients for BRAGG are shown in Table 3. The peanut experiments were carried out using the variety "Florunner". Its cultivar-specific parameters as used in the DSSAT CSM and coupled DSSAT-HYDRUS-1D simulations are also listed in Table 3. Several parameters of the soybean and peanut varieties had been calibrated earlier for the DSSAT CSM simulations. Specifically, the BRAGG and Florunner cultivar coefficients were taken from the standard DSSAT V4.6 release, as previously calibrated for DSSAT V4.6 based on a full set of 7 and 18 treatments, respectively. The peanut variety Florunner was calibrated for the coupled DSSAT-HYDRUS-1D model using data from the field experiment conducted at UF in 1989. Modified values of several cultivar coefficients of this variety for the coupled model are given in Table 3, together with those used for DSSAT CSM.

The datasets, distributed with DSSAT V4.6 and used for evaluation of the coupled model, were from a) soybean experiments UFGA7801 (1978, treatment 1, irrigated, 206 mm in 21 applications, and treatment 2, rainfed), IUAM8801 (1988, treatment 1, rainfed) and IUAM9001 (1990, treatment 1, rainfed), and b) peanut experiments UFGA8401 (1984, treatment 1, irrigated, 365 mm in 16 applications, and treatment 2, rainfed, except irrigation, 243 mm in 9 applications, after water deficit period was relieved), UFGA8601 (1986, treatment 1, rainfed), and UFGA8701 (1987, treatment 1, irrigated, 115 mm in 8 applications). The names of the experiments follow the DSSAT file name convention and are constructed from 8 characters that include an institute code (2 characters), a site code (2 characters), the year of the experiment (2 characters), and an experiment number (2 characters). For example, UFGA7801 is an experiment (01) conducted by the University of Florida (UF) at Gainesville (GA) in 1978 (78) and IUAM8801 is an experiment (01) conducted by the Iowa State University (IU) at Ames (AM) in 1988 (88). Available measurements included total crop mass, leaf mass, stem mass, pod mass, grain mass, leaf area index (*LAI*), the V-stage (leaf number on main axis), specific leaf area, leaf nitrogen concentration, grain number, unit grain mass, pod number, shelling % and dates for anthesis, first pod, first seed, and physiological maturity.

Table 1. Soil physical and hydraulic properties of the experimental field at the University of Florida, Gainesville.

Depth	Particle size distribution, %			Bulk density	Lower limit	Upper limit, drained	Upper limit, saturated	Saturated hydraulic conductivity	Organic carbon	Root growth factor
cm	clay	silt	sand	g cm^{-3}	cm^3 cm^{-3}	cm^3 cm^{-3}	cm^3 cm^{-3}	cm h^{-1}	%	
0–5	0.9	11.8	87.3	1.36	0.023	0.086	0.230	7.40	0.9	1.00
5–15	0.9	11.8	87.3	1.40	0.023	0.086	0.230	7.40	0.69	1.00
15–30	4.6	6.4	89	1.46	0.023	0.086	0.230	15.80	0.28	0.55
30–45	5.8	5.4	88.8	1.46	0.023	0.086	0.230	28.00	0.20	0.32
45–60	5.8	5.4	88.8	1.47	0.023	0.086	0.230	28.00	0.20	0.32
60–90	9.6	4.2	86.2	1.43	0.021	0.076	0.230	27.60	0.09	0.38
90–120	9.6	4.2	86.2	1.48	0.020	0.076	0.230	17.50	0.03	0.40
120–150	8.3	3.6	88.1	1.57	0.027	0.13	0.230	0.30	0.03	0.30
150–180	8.3	3.6	88.1	1.79	0.070	0.258	0.360	0.10	0.03	0.20

Table 2. Values of the van Genuchten-Mualem soil hydraulic parameters as obtained from the HYDRUS-1D Soil Catalog (Carsel and Parrish, 1988) for two experimental fields soils (θ_r is the residual water content, θ_s is the saturated water content, α, n, and l are empirical parameters, and K_s is the saturated soil hydraulic conductivity).

Soil ID	Depth cm	Soil type by texture	θ_r cm^3/cm^3	θ_s cm^3/cm^3	α 1/cm	n	l	K_s m/day
IBPN910015,IBSB910015	0–15	Fine sand	0.045	0.43	0.145	2.68	0.5	7.13
IBPN910015, IBSB910015	15–180	Loamy fine sand	0.057	0.41	0.124	2.28	0.5	3.50
IBSB910049	0–202	Clay loam	0.079	0.442	0.016	1.414	0.5	0.082

Table 3. Cultivar coefficients for the soybean variety BRAGG (SB) and the peanut variety Florunner (PN) used in the DSSAT-CSM and the coupled DSSAT-HYDRUS-1D simulations.

#	Coeff.	SB	PN	Definitions	#	Coeff.	SB	PN	Definitions
1	CSDL	12.33	11.84	Critical short-day length, hour	10	SIZLF	170	18.0	Maximum size of full leaf (three leaflets), cm^2
2	PPSEN	0.32	0.00	Slope of the relative response of development to photoperiod with time, 1/hour	11	XFRT	1.0	0.92	Maximum fraction of daily growth that is partitioned to seed + shell
3	EM-FL	19.5	21.2, 20.2	Time between plant emergence and flower appearance (R1), photothermal days	12	WTPSD	0.17	0.69, 0.65	Maximum weight per seed, g
4	FL-SH	10.0	9.2, 8.2	Time between first flower and first pod (R3), photothermal days	13	SFDUR	24	40	Seed filling duration for pod cohort at standard growth conditions, photothermal days
5	FL-SD	15.2	18.8, 24.8	Time between first flower and first seed (R5), photothermal days	14	SDPDV	2	1.65, 1.6	Average seed per pod under standard growing conditions, #/pod
6	SD-PM	37.6	74.3, 77.3	Time between first seed (R5) and physiological maturity (R7), photothermal days	15	PODUR	10	24, 26	Time required for cultivar to reach final pod load under optimal conditions, photothermal days
7	FL-LF	19	88, 90	Time between first flower (R1) and end of leaf expansion, photothermal days	16	THRSH	78	80	Maximum ratio of (seed/(seed+shell)) at maturity, Threshing percentage
8	LFMAX	1.0	1.4	Maximum leaf photosynthesis rate at 30^0 C, 350 vpm CO_2, and high light, mg CO_2/m^2-s	17	SDPRO	0.40	0.27	Fraction protein in seeds, g(protein)/g(seed)
9	SLAVR	355	260, 264	Specific leaf area of cultivar under standard growth conditions, cm^2/g	18	SDLIP	0.20	0.51	Fraction oil in seeds, g(oil)/g(seed)

The numerical time steps of HYDRUS-1D in the coupled model varied between 10^{-3} and 1 day, while the time step in DSSAT CSM was always 1 day. The soil profile in HYDRUS-1D was discretized into 1-cm soil layers in the top 30 cm, 2-cm soil layers down to a depth of 150 cm, and 3-cm soil layers until a depth of 180 or 202 cm.

Statistical indicators

Several statistical indicators were used to compare the performance of the original and coupled models and their capability to describe the experimental data. The indicators included the Mean, the Root Mean Square Error (*RMSE*), the normalized Root Mean Square Error (*nRMSE*) (Loague and Green, 1991), the index of agreement (*d*) (Willmott et al., 1985), the Model Efficiency (*EF*) (Nash and Sutcliffe, 1970), and the Mean Error (*E*).

The *RMSE* was computed using

$$RMSE = \sqrt{\frac{\sum_{i=1}^{n}\left(P_i - O_i\right)^2}{n}} \tag{2}$$

where P_i and O_i are the simulated and observed values for the *i*th measurement, respectively, and *n* is the number of observations.

The *nRMSE* was computed as:

$$nRMSE = \frac{RMSE}{\bar{O}} \times 100\% \tag{3}$$

where $\bar{O}$ is the overall mean of observed values.

The *d* index was calculated using the equation:

$$d = 1 - \frac{\sum_{i=1}^{n}\left(P_i - O_i\right)^2}{\sum_{i=1}^{n}\left(\left|P_i - \bar{O}\right| + \left|O_i - \bar{O}\right|\right)^2} \tag{4}$$

while the Model Efficiency (*EF*) was computed using

$$EF = 1 - \frac{\sum_{i=1}^{n}\left(P_i - O_i\right)^2}{\sum_{i=1}^{n}\left(\left|O_i - \bar{O}\right|\right)^2} \tag{5}$$

and the Mean Error (*E*) as

$$E = \frac{\sum_{i=1}^{n}\left(P_i - O_i\right)}{n} \tag{6}$$

A high value of the *d* index ($0 \le d \le 1$) and a low value of *RMSE* indicate a good fit between the simulated and observed values. Since *EF* has no unit, this criterion can be used to compare the accuracy of model outputs for different variables. Its value can range from $-\infty$ to 1. The closer the model efficiency is to 1, the more accurate the model, with $EF = 1$ corresponding to a perfect match between simulated values and observed data. A value of zero for the efficiency *E* indicates that the predictions are as accurate as the mean of the observed data, whereas an efficiency less than zero suggests that the observed mean is a better predictor than the model. *E* is an indicator of whether the model predictions tend to underestimate (if negative) or overestimate (if positive) the measured data.

RESULTS AND DISCUSSION

The two approaches for soil water modeling in DSSAT were evaluated based on their ability to accurately estimate the soil water balance, the soil water content by soil layer, potential and actual evapotranspiration rates and, subsequently, crop growth, which was characterized using both total and individual organ biomass accumulation.

Soil water balance

Since coupling added new functionality to the soil water simulations in DSSAT, the performance of the original and coupled models was evaluated first in terms of their ability to predict soil water contents (total and extractable) in the entire soil profile and particular soil layers during the crop growing season. Both irrigated or rainfed treatments were considered in the analysis.

For the UFGA7801 soybean experiment, the initial total water content in the soil profile 180 cm deep was 214 mm (equivalent to field Capacity in DSSAT-CSM) for both treatments (treatment 1 was irrigated and treatment 2 was rainfed). Simulations with both models showed a similar tendency of describing the dynamics of the total soil water content (*SWTD*) (Fig. 2a,b). Similar simulated trends can also be seen for extractable amount of soil water (*SWXD*) (Fig. 2c,d). The extractable soil water as obtained with the coupled model was in general higher than when simulated with the original model. For example, one can see that the SWXDs simulated using both models were higher than those measured in treatment 2 of the 1978 soybean experiment (Fig. 2d). Values of the *d* index were 0.95 and 0.90 and those of *RMSE* were 26.5 mm and 41.3 mm for the original and coupled models, respectively.

The soybean experiments at Ames, Iowa in 1988 and 1990 included data about the Williams-82 soybean variety grown under rainfed conditions. The 1988 season showed a major drought, which allowed us to contrast its results with the cool and rainy season of 1990. Soil water contents during the 1988 experiment were measured with a neutron probe. Initial conditions and water content distributions with depth were different in the 202-cm deep soil profile for these soybean experiments. For treatment 1 of the IUAM8801 experiment and treatment 1 of the IUAM9001 experiment, the total water contents (*SWTD*) were 628 mm and 574 mm, respectively, with water contents in different layers being close to the drained upper limit.

Simulations by both models showed a similar tendency of describing soil water content dynamics for the Iowa experiments (Fig. 3). On 103 DAP (days after planting) of the 1988 growing season, a large 142-mm rainfall event occurred (Fig. 3a). The original and coupled models reacted from this by increasing the total water content by 80 mm and 136 mm, respectively (Fig. 3a). While the tipping bucket approach limited infiltration as determined by the SCS curve number, the water content of the near-surface soil layer, and the total soil drainage coefficient (SWCON) (see Table 2), the HYDRUS-1D approach, which considers not only gravity but also capillarity, allowed larger infiltration. Both modeling approaches produced similar results for the cool and rainy season of 1990, while the coupled model slightly overpredicted water contents during most of the season (Fig. 3b,d).

Comparisons between volumetric water contents measured in the different layers during the 1988 soybean experiment and simulated using the DSSAT CSM and the DSSAT-HYDRUS-1D models are illustrated in Fig. 4. In most cases, the *d* index was approximately 0.9 for the original model and 0.8 for the coupled model. The *RMSE* values for the original and coupled models were 0.08 and 0.05, respectively. The coupled model simulated more soil water depletion in the deeper layers during the early part of the season. The two modeling approaches again showed different responses to a large rainfall amount (142 mm) on 103 DAP. The original model failed to re-saturate the soil profile because of excessively high runoff caused by incorrect application of the SCS runoff number to a cracking clay soil, while the coupled model simulated a much large increase in the total water content on day 103 due to better simulations of infiltration.

The initial total water content (214 mm) of the 180-cm deep soil profile, and the water contents at depths of 5, 15, 30, 45, 60, 90, 120, 150, and 180 cm, were the same in all three peanut (UFGA8401, UFGA8601, and UFGA8701) experiments at Gainesville, FL when the simulations started on 19, 5, and 2 days before planting, respectively. The coupled model showed lower water contents at the beginning of all simulations through about 40–50 days after planting (DAP) in both treatments of the UFGA8401 experiment (Fig. 5a,b). This was expected for sandy soils that have very low water retention properties.

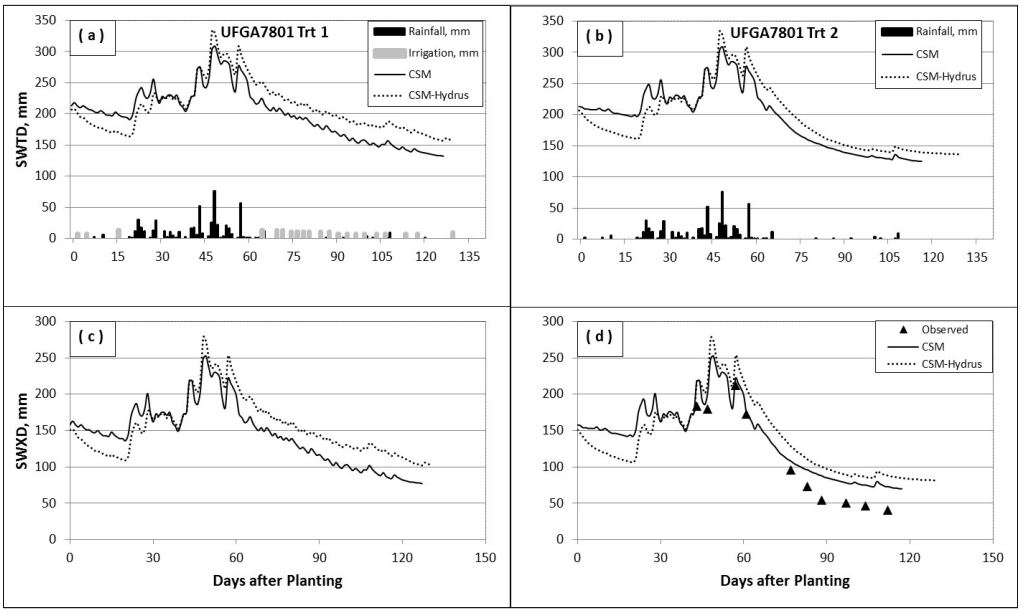

Fig. 2. Total water contents (*SWTD*) (a,b) and extractable water contents (*SWXD*) (c,d) in the 0–180 cm soil profile as simulated with the DSSAT CSM and DSSAT-HYDRUS-1D models for an irrigated treatment 1 (left) and rainfed treatment 2 (right). Also shown are measured total plant extractable soil water (d) and irrigation and rainfall amounts (a, b) during the BRAGG soybean growing season at Gainesville, FL, in 1978.

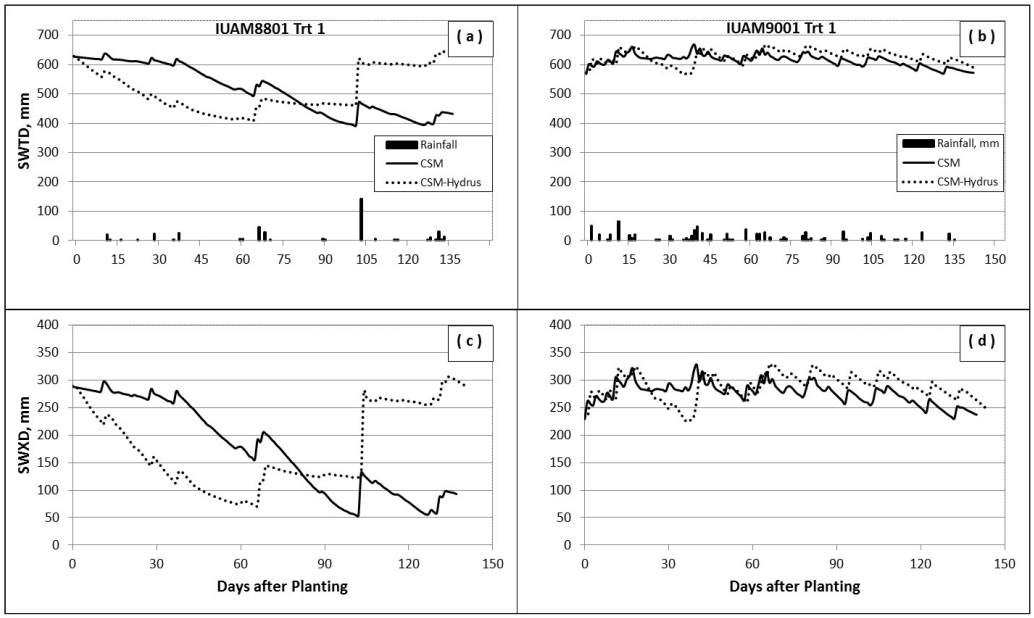

Fig. 3. Total water contents (*SWTD*) (a,b) and extractable water contents (*SWXD*) (c,d) in the 0–202 cm soil profile as simulated with the DSSAT CSM and DSSAT-HYDRUS-1D models for 1988 (left) and 1990 (right). Also shown are rainfall amounts during the Williams-82 soybean growing season at Ames, IA, in 1988 (a) and 1990 (b).

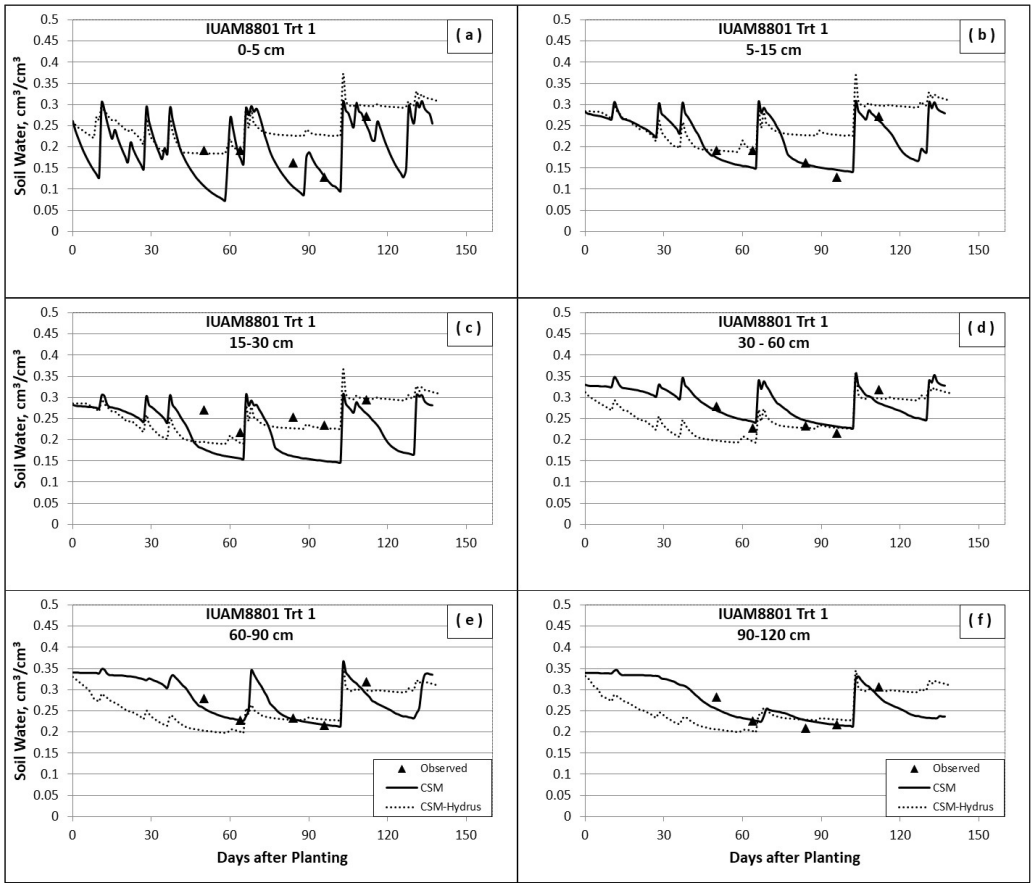

Fig. 4. Measured and simulated water contents of six soil layers as simulated with the DSSAT CSM and DSSAT-HYDRUS-1D models during the Williams-82 soybean growing season at Ames, IA, in 1988.

After this initial period, water contents simulated with the coupled model were slightly higher than those simulated with the original model. The two models adequately reacted to precipitation and showed similar water content dynamics, albeit at different levels (Fig. 5).

Daily and seasonal evapotranspiration

The performance of the two models was also evaluated in terms of their ability to predict potential and actual evapotranspiration rates. Potential evapotranspiration dynamics and their values were the same for both models (Figs. 6a,b and 7a,b).

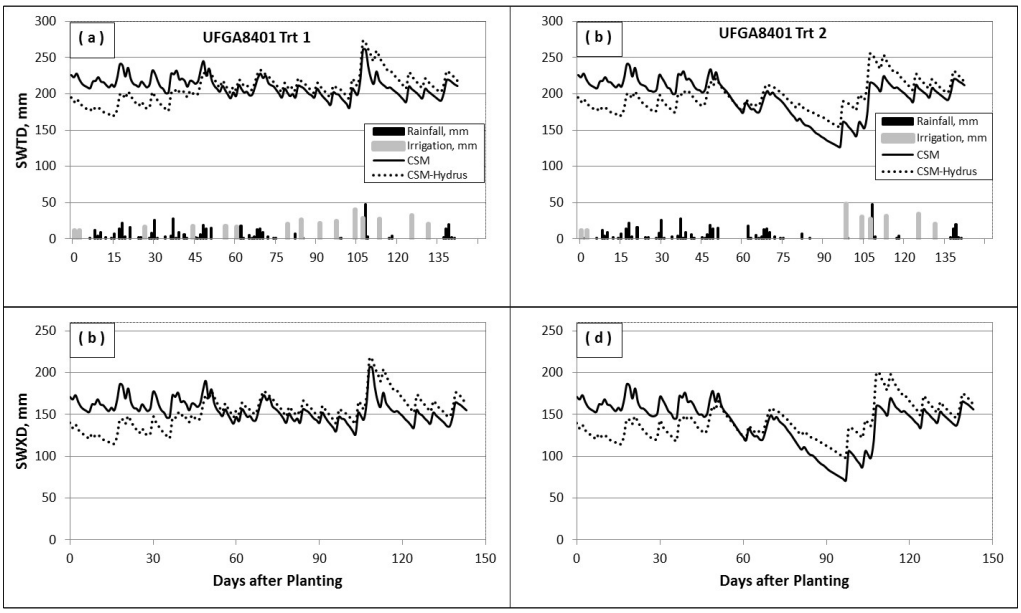

Fig. 5. Total water contents (*SWTD*) (a,b) and extractable water contents (*SWXD*) (c,d) as simulated with the DSSAT CSM and DSSAT-HYDRUS-1D models for treatments 1 (left) and 2 (right). Also shown are rainfall and irrigation amounts for the two treatments of the Florunner peanut experiment at Gainesville, FL in 1984 (a,b).

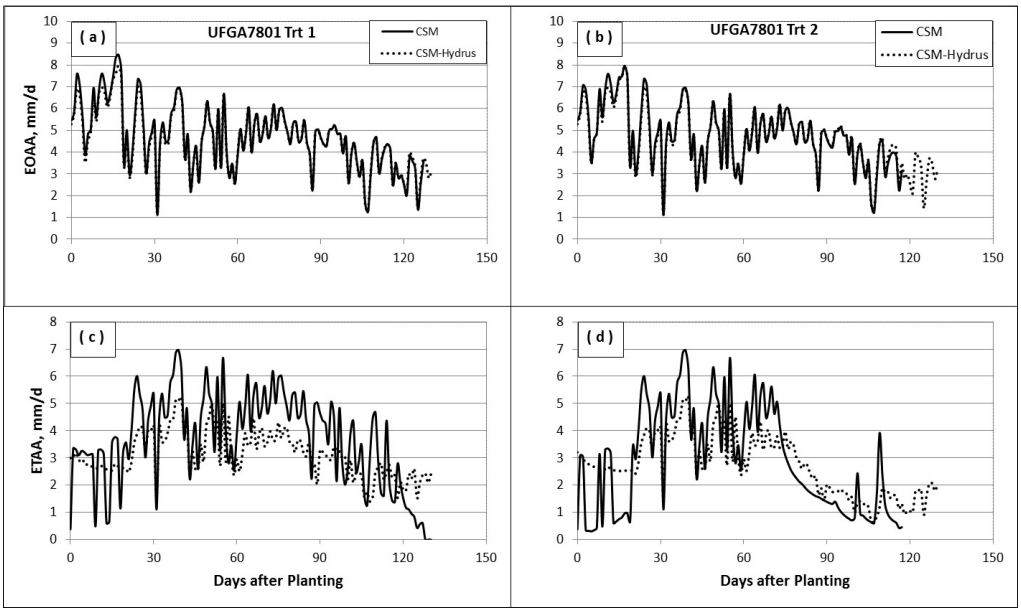

Fig. 6. Potential evapotranspiration (*EOAA*) (a,b) and actual evapotranspiration (*ETAA*) (c,d) rates as simulated with the DSSAT CSM and the DSSAT-HYDRUS-1D models for Treatment 1 (left, irrigated) and Treatment 2 (right, rainfed) of the BRAGG soybean experiment at Gainesville, FL, in 1978.

Actual evapotranspiration rates differed significantly between the two models. The coupled model showed less variations in its predictions, although the trend was similar compared to the original model (Figs. 6c,d and 7c,d). For both UFGA7801 soybean treatments during full canopy, evapotranspiration values varied between 2.5–5 mm/day and 3–7 mm/day for the coupled and the original models, respectively.

The coupled and original models produced comparable values for the evapotranspiration rate at the beginning of the growing season (about 3 mm and 3.5 mm, respectively) and at the end of the season (1.5–2.5 mm and 1–3 mm, respectively), for irrigated treatment 1 (Fig. 6c). Differences were more significant in the case of the treatment 2 (rainfed): about 2.5 mm and 0.5–1 mm at the beginning of the season and 1–2 mm and 0.5–1 mm at the end of the season for the coupled and original models, respectively (Fig. 6d). However, the seasonal patterns of the coupled model differed from the original CSM. The coupled model had higher evapotranspiration (*ETAA*) rates during the early season when *LAI* values were still low, but lower *ETAA* rates in mid-season with its higher *LAI* values.

DSSAT CSM results showed differences in the average daily evapotranspiration rates between for the irrigated and rainfed treatments of the UFGA8401 peanut experiment (Fig. 7c,d), for only 24 out of 143 days of simulations, with differences that varied between 1.4–3 mm/day. The coupled model showed differences in evapotranspiration between the two treatments during 80 days of the 143 simulation days, with maximum differences of about 2 mm (Fig. 7c,d). By comparison,

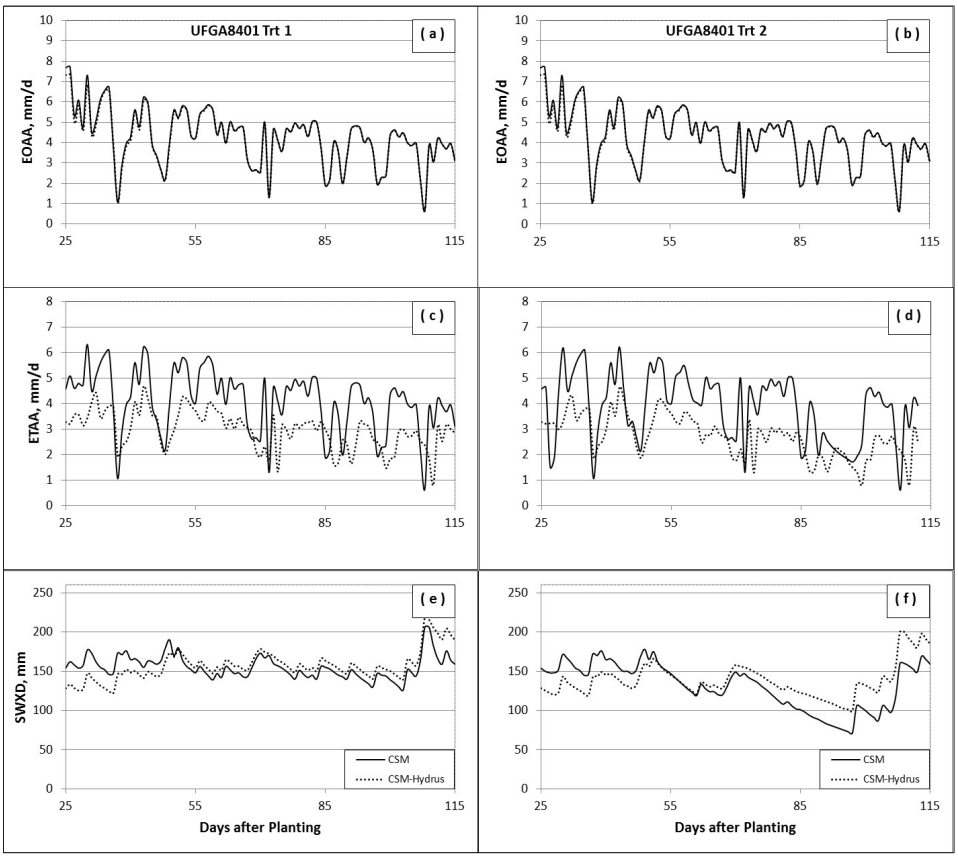

Fig. 7. Potential (*EOAA*) (a,b) and actual (*ETAA*) (c,d) evapotranspiration rates and extractable soil water (*SWXD*) (e,f) as simulated with the DSSAT CSM and the DSSAT-HYDRUS-1D models for Treatment 1 (left, irrigated) and Treatment 2 (right, rainfed) of the Florunner peanut experiment at Gainesville, FL, in 1984.

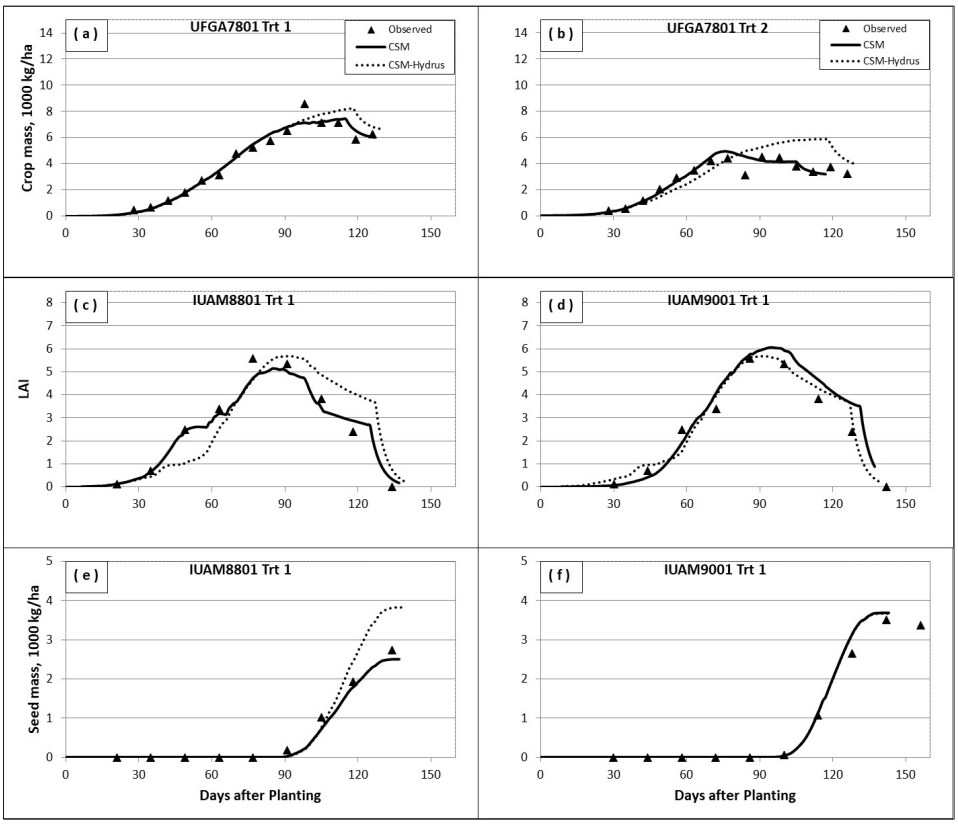

Fig. 8. Simulated and observed crop mass for the BRAGG (a,b) soybean experiments at Gainesville, FL in 1978, and *LAI*s and seed mass for the Williams 82 (c–f) soybean experiments at Ames, IA in 1988 and 1990, respectively. Simulations were carried out using the DSSAT CSM model with its tipping bucket approach and the coupled DSSAT-HYDRUS-1D model.

the original model did not show any differences for the two treatments after 98 DAP, although 48 mm irrigation was applied on day 98 after planting and 139 mm during the period of 98–114 DAP, while the coupled model simulated more evapotranspiration for irrigated treatment 1 until 115 DAP.

Fig. 7 shows results obtained with the two modeling approaches for the time interval of 25–115 DAP out of 0–143 DAP when differences were found between the irrigated and rainfed treatments. Similarly as for the soybean example, the coupled model tended to produce lower values than the CSM approach during much of the season.

Crop growth simulations

The comparison between simulated and observed yield components during the growing season indicated the different performance of the DSSAT-HYDRUS-1D and original CSM models. Of the three soybean experiments, the coupled model performed worst for treatment 2 of the UFGA7801 experiment, which showed a very low value of the *d* index (0.47) for pod mass, compared to 0.91 for the original model (Table 4).

The *EF* values were negative for this treatment as well. The original and coupled models performed well for treatment 1, producing relatively high values (0.99) of the *d* index for pod and stem mass, and with slightly better *d* index values for the original model for crop mass and *LAI* (0.99 and 0.95, respectively) than the coupled model (0.98 and 0.95, respectively). The coupled model performed better for the IUAM9001 experiment (Table 4, Fig. 8d,f) in terms of all statistical measures than for the IUAM8801 soybean experiment (Table 4, Fig. 8c,e).

Table 4. Comparisons of observed and simulated crop mass, pod mass, stem mass, and *LAI* using the original DSSAT CSM model (CSM) and the coupled DSSAT-HYDRUS-1D model (HYD) for three soybean experiments and their statistical indicators.

			Mean (Sim.)		*RMSE*		*nRMSE*		*d*		*EF*		*E*	
Biomass component	Trt #	Mean (Obs.)	CSM	HYD	CSM	HYD	CSM	HYD	CSM	HYD	CSM	HYD	CSM	HYD
UFGA7801														
Crop mass, kg/ha	1	4485	4501	4722	478	731	10.7	16.3	0.99	0.98	0.96	0.83	16	236
Pod mass, kg/ha	1	2336	2280	2514	227	317	9.7	13.6	0.99	0.99	0.98	0.94	–56	178
Stem mass, kg/ha	1	2069	2099	2107	220	273	10.6	13.2	0.99	0.99	0.96	0.96	30.87	38.6
LAI	1	2.85	2.89	3.1	0.4	0.6	14.3	22.6	0.98	0.95	0.93	0.92	0.04	0.22
Crop mass, kg/ha	2	2960	3054	3541	468	1191	15.8	39.3	0.97	0.86	0.89	0.20	94.3	510
Pod mass, kg/ha	2	655	851	2510	263	2010	40.1	232.4	0.91	0.47	0.57	–13.38	196.4	1644
Stem mass, kg/ha	2	1714	1714	2093	253	596	14.8	34.6	0.98	0.91	0.92	0.47	0	374
LAI	2	2.61	2.68	3.0	0.56	1.2	21.3	51.1	0.96	0.85	0.84	0.4	0.07	0.74
IUAM8801														
Crop mass, kg/ha	1	4220	3854	4280	525	872	12.4	20.6	0.99	0.98	0.97	0.91	–366	59.8
Pod mass, kg/ha	1	2043	1568	2340	530	678	26.0	33.2	0.96	0.96	0.86	0.78	–474	297
Stem mass, kg/ha	1	1966	1888	1769	216	301	10.9	15.3	0.99	0.99	0.98	0.95	–78.6	–197
LAI	1	2.98	2.81	2.94	0.39	0.98	13.3	32.7	0.99	0.94	0.95	0.72	–0.17	–0.04
IUAM9001														
Crop mass, kg/ha	1	4267	4511	4553	454	478	10.6	11.2	0.99	0.99	0.98	0.98	244	285
Pod mass, kg/ha	1	2304	2577	2575	396	393	17.2	17.1	0.99	0.98	0.95	0.95	272	270
Stem mass, kg/ha	1	2001	2055	2082	184	196	9.2	9.8	0.99	0.99	0.98	0.98	53.7	80.5
LAI	1	3.33	3.31	3.36	0.23	0.22	6.9	6.7	0.99	0.99	0.99	0.99	–0.03	0.03

Table 5. Comparisons of observed and simulated crop mass, pod mass, stem mass, and *LAI* using the original DSSAT CSM model (CSM) and the coupled DSSAT-HYDRUS-1D model (HYD) for three peanut experiments and their statistical indicators.

			Mean (Sim.)		*RMSE*		*nRMSE*		*d*		*EF*		*E*	
Biomass component	Trt #	Mean (Obs.)	CSM	HYD	CSM	HYD	CSM	HYD	CSM	HYD	CSM	HYD	CSM	HYD
UFGA84001														
Crop mass, kg/ha	1	6781	5806	6035	1197	974	17.7	14.4	0.98	0.99	0.92	0.95	–975	974
Pod mass, kg/ha	1	3290	2738	2544	728	1029	22.1	31.2	0.97	0.94	0.89	0.78	–552	–746
Stem mass, kg/ha	1	2588	2236	2445	472	388	18.2	15.0	0.97	0.98	0.89	0.93	–351	–143
LAI	1	3.74	3.39	3.71	0.54	0.41	14.6	11.1	0.97	0.99	0.91	0.95	–0.35	–0.04
Crop mass, kg/ha	2	6686	5370	6031	1654	1076	24.7	16.1	0.96	0.98	0.85	0.93	–1316	–654
Pod mass, kg/ha	2	3079	2406	2522	838	862	27.2	28.0	0.95	0.96	0.84	0.83	–673	–558
Stem mass, kg/ha	2	2697	2146	2452	799	478	29.6	17.7	0.92	0.98	0.72	0.90	–552	–245
LAI	2	3.59	3.08	3.7	0.75	0.67	20.9	18.8	0.94	0.96	0.81	0.85	–0.52	0.11
UFGA86001														
Crop mass, kg/ha	1	8363	6991	8251	1641	734	19.6	8.8	0.96	0.99	0.87	0.97	–1371	–112
Pod mass, kg/ha	1	2711	2853	3187	288	628	10.7	23.2	0.99	0.98	0.98	0.91	141	475
Stem mass, kg/ha	1	3694	2675	3281	1164	631	31.5	17.1	0.87	0.96	0.57	0.87	–1019	–413
LAI	1	5.19	3.82	4.9	1.77	1.11	34.1	21.5	0.81	0.92	0.41	0.77	–1.37	–0.3
UFGA8701														
Crop mass, kg/ha	1	7336	7175	8011	514	890	7.0	12.1	0.99	0.99	0.98	0.95	–161	675
Pod mass, kg/ha	1	3103	2873	2675	458	649	14.8	20.9	0.99	0.98	0.95	0.90	–230	–427
Stem mass, kg/ha	1	2649	2826	3454	300	973	11.3	36.7	0.99	0.89	0.94	0.32	177	805
LAI	1	3.89	4.13	5.1	0.61	1.37	15.7	35.2	0.96	0.86	0.83	0.16	0.24	1.23

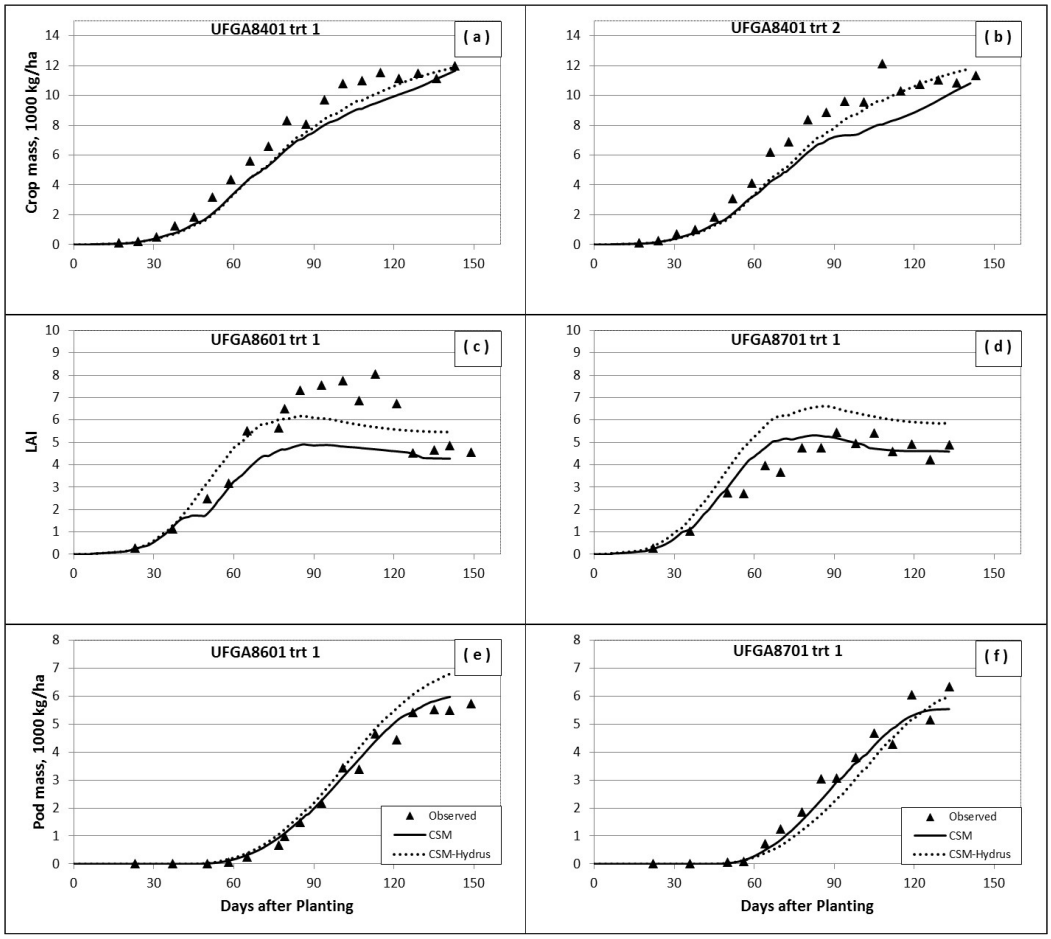

Fig. 9. Simulated and observed crop mass (a,b), *LAI*s (c,d) and pod mass (e,f) for the Florunner peanut experiments at Gainesville, FL in 1984, 1986, and 1987. Simulations were carried out using the DSSAT CSM model with its tipping bucket approach and the coupled DSSAT-HYDRUS-1D model.

In both treatments of the UFGA8401 peanut experiment, the coupled model performed better with higher values of both the *d* index and *EF*, and lower values of *nRMSE,* as compared to the original model (Table 5, Fig. 9a,b). Treatment 1 of the UFGA8601 peanut experiment showed again better performance of the coupled model for crop mass, stem mass, and *LAI*. But the coupled model performed slightly worse for pod mass, for which the *d* index of 0.98 was a fraction lower than 0.99 for the original model, while the *EF* of 0.91 was also lower than 0.98 for the original model (Table 5, Fig. 9c,e). For treatment 1 of the UFGA8701 peanut experiment, the original model performed better with higher values of the *d* index and *EF*. Both models had the same *d* index value (0.99) for crop mass, although the *RMSE* for the original model was better as compared to the coupled model: 514 kg/ha and 890 kg/ha, respectively (Table 5 and Fig 9d,f).

The various DSSAT CSM and DSSAT-HYDRUS-1D simulations of soybean and peanut crop production overall showed differences when applied to water-limiting conditions using several different datasets for two locations. As shown above, the coupled model in general predicted less evapotranspiration and higher water contents in the soil profile, which resulted in less water stress, higher *LAI* values and more biomass than the original DSSAT CSM model. While the simulations as such showed the great potential of the coupled model, several improvements may be possible in the analysis of the experiments discussed in this study. These include getting better soil texture data (and hydraulic property information) especially for the soybean experiment at ISU, improving root length distribution data, and improving the partitioning of potential *ET* into potential evaporation (E_p) and transpiration (T_p). Availability of such information should further improve the reliability and accuracy of the predictions.

CONCLUSIONS

HYDRUS-1D was coupled in this study with the Cropping System Model (CSM) of DSSAT V4.6 to simulate soil water dynamics. Simulations with the coupled model were compared with results obtained with the original model that uses a tipping bucket approach for soil water modeling. Performance of the two models was evaluated in terms of simulated soil water contents, evapotranspiration, and various crop yield components. Results showed that the coupled model provided satisfactory simulations of soil water content changes as well as the plant growth. However, the two models provided different predictions for crop, pod, seed, and stem mass, and the crop *LAI*, especially under water-limited conditions for soybean in Iowa and Florida and peanut in Florida. The coupled model, in that case, simulated insufficient yield reductions under drought, possibly related to its lower evapotranspiration rate during the full canopy phase. The coupled model produced significantly different results for actual evapotranspiration rates, being higher during an early canopy phase, but lower during the full cano-

py phase when LAI was high. These differences in evapotranspiration rates contributed to differences in simulated soil water contents at different times of the season, even though the dynamics of water movement by the coupled model was simulated well. Each of the two approaches to soil water modeling has particular advantages and disadvantages, which should be tested in further studies against more comprehensive datasets related to the soil and plant water regimes.

REFERENCES

Boote, K. J., Sau, F., Hoogenboom, G., Jones, J.W., 2008. Experience with Water Balance, Evapotranspiration, and Predictions of Water Stress Effects in the CROPGRO Model. Response of crops to limited water: Understanding and modeling water stress effects on plant growth processes. Advances in Agricultural Systems Modeling Series 1. ASA, CSSA, SSSA, 677 S. Segoe Rd., Madison, WI 53711, USA. pp. 59–103.

Boote, K.J., Jones, J.W., Hoogenboom, G., White, J.W., 2010. The role of crop systems simulation in agriculture and environment. Int. J. Agric. Environ. Inf. Syst., 1, 41–54.

Bristow, K.L., Hopmans, J.W., Cote, C.M., Charlesworth, P.B., Thorburn, P.J., Cook, F.J., 2002. Development of improved water and nutrient management strategies through strategic modeling. In: Proc. 17th WCSS, Thailand, pp. 14–21.

Dabach, C., Shani, U., Lazarovitch, N., 2015. Optimal tensiometer placement for high-frequency subsurface drip irrigation management in heterogeneous soils. Agric. Water Manag., 152, 91–98.

David, O., Markstrom, S.L., Rojas, K.W., Ahuja, L.R., Schneider, I.W., 2002. The Object Modeling System. In: Ahuja, L.R., Ma, L., Howell, T.A. (Eds): Agricultural System Models in Field Research and Technology Transfer. Lewis Publishers, Boca Raton, FL, 317–330.

Dokoohaki, H., Gheysari, M., Mousavi, S., Zand-Parsa, S., Miguez, F., Archontoulis, S., Hoogenboom, G., 2016. Coupling and testing a new soil water module in DSSAT CERES-Maize model for maize production under semi-arid condition. Agric. Water Manag., 163, 90–99.

Feddes, R. A., Kowalik, P. J., Zaradny, H., 1978. Simulation of field water use and crop yield. In: Simulation Monograph, Pudoc, Wageningen, The Netherlands, pp. 9–30.

Gärdenäs, A.I., Hopmans, J.W., Hanson, B. R., Šimůnek, J., 2005. Two-dimensional modeling of nitrate leaching for various fertigation scenarios under micro-irrigation. Agric. Water Manag., 74, 219–242.

Gheysari, M., Mirlatifi, S.M., Homaee, M., Asadi, M.E., Hoogenboom, G., 2009. Nitrate leaching in a silage maize field under different irrigation and nitrogen fertilizer rates. Agric. Water Manag., 96, 946–954.

Gijsman, A.J., Jagtap, S.S., Jones, J.W., 2002a. Wading through a swamp of complete confusion: How to choose a method for estimating soil water retention parameters for crop models. Eur. J. Agron., 18, 75–105.

Gijsman, A.J., Hoogenboom, G., Parton, W.J., Kerridge, P.C., 2002b. Modifying DSSAT crop models for low-input agricultural systems using a soil organic matter residue module from CENTURY. Agron. J., 94, 462–474.

Gregersen, J.B., Gijsbers, P.J., Westen, S.J., 2007. OpenMI: open modeling interface. J. Hydroinf., 9, 3, 175–191.

Groenendyk, D., Thorp, K.R., Ferre, P.A., Crow, W.T., 2012. Testing an Ensemble Kalman Filter for assimilation of soil moisture into HYDRUS 1D and Coupled Crop Model. In: American Geophysical Union, Fall Meeting 2012, Abstract #H33F-1382.

Han, M., Zhao, C., Šimůnek, J., Feng, G., 2015. Evaluating the impact of groundwater on cotton growth and root zone water balance using Hydrus-1D coupled with a crop growth model. Agric. Water Manag., 160, 64–75, DOI: 10.1016/j.agwat.2015.06.028.

Hanson, B.R., Šimůnek, J., Hopmans, J.W., 2008. Leaching with subsurface drip irrigation under saline, shallow groundwater conditions. Vadose Zone Journal, 7, 2, 810–818, DOI: 10.2136/VZJ2007.0053.

Harbaugh, A.W., Banta, E.R., Hill, M.C., McDonald, M.G., 2000. MODFLOW-2000, the U.S. Geological Survey modular ground-water model user guide to modularization concepts and the ground-water flow process. USGS, Denver, CO.

Hartmann, A., Šimůnek, J., Aidoo, M.K., Seidel, S. J., Lazarovitch, N., 2017. Modeling root growth as a function of different environmental stresses using HYDRUS. Vadose Zone Journal, 16, DOI: 10.2136/vzj2017.02.0040, (accepted June 13 2017).

Hoogenboom, G., Jones, J.W., Wilkens, P.W., Porter, C.H., Boote, K.J., Hunt, L.A., Singh, U., Lizaso, J.I., White, J.W., Uryasev, O., Ogoshi, R., Koo, J., Shelia, V., Tsuji, V., 2015. Decision Support System for Agrotechnology Transfer (DSSAT) Version 4.6 (www.DSSAT.net). DSSAT Foundation, Prosser, Washington.

Ines, A.V.M., Droogers, P., Makin, I.W., Das Gupta, A., 2001. Crop growth and soil water balance modeling to explore water management options. IWMI Working Paper 22. Colombo, Sri Lanka: International Water Management Institute. 26 p.

Jones, J.W., Hoogenboom, G., Porter, C.H., Boote, K.J., Batchelor, W.D., Hunt, L.A., Wilkens, P.W., Singh, U., Gijsman, A.J., Ritchie, J.T., 2003. DSSAT Cropping System Model. Europ. J. Agron., 18, 235–265.

Kandelous, M.M., Kamai, T., Vrugt, J.A., Šimůnek, J., Hanson, B.R., Hopmans, J.W., 2012. Evaluation of subsurface drip irrigation design and management parameters for alfalfa. Agric. Water Manag., 109, 81–93.

Li, Y., Zou, Q., Zhou, J., Zhang, G., Chen, C., Wang, J., 2014. Assimilating remote sensing information into a coupled hydrology-crop growth model to estimate regional maize yield in arid regions. Ecological Modelling, 291, 15–27.

Liu, H.L., Yang, J.Y., Drury, C.F., Reynolds, W.D., Tan, C.S., Bai, Y.L., He, P., Jin, J., Hoogenboom, G., 2010. Using the DSSAT-CERES-Maize model to simulate crop yield and nitrogen cycling in fields under long-term continuous maize production. Nutr. Cycl. Agroecosys., 1–16, DOI: 10.1007/s10705-010-9396-y.

Liu, H.L., Yang, J.Y., Tan, C.S., Drury, C.F., Reynolds, W.D., Zhang, T.Q., Bai, Y.L., Jin, Y.L., He, P., Hoogenboom, G., 2011. Simulating water content, crop yield and nitrate-N loss under free and controlled tile drainage with subsurface irrigation using the DSSAT model. Agric. Water Manage., 98, 1105–1111.

Loague, K., Green, R.E., 1991. Statistical and graphical methods for evaluating solute transport models: overview and application. J. Contam. Hydrol., 7, 51–73.

Nash, J.E., Sutcliffe, J.V., 1970. River flow forecasting through conceptual models. part I - A discussion of principles. J. Hydrol., 10, 282–290.

Mualem, Y., 1976. A new model for predicting the hydraulic conductivity of unsaturated porous media. Water Resources Research, 12, 3, 513-522.

Mullen, J.D., Yu, Y., Hoogenboom, G., 2009. Estimating the demand for irrigation water in a humid climate: A case study from the southeastern United States. Agric. Water Manage., 96, 1421–1428.

Pachepsky, Y., Guber, A., Jacques, D., Šimůnek, J., van Genuchten, M.Th., Nicholson, T., Cady, R., 2006. Information content and complexity of simulated soil water fluxes. Geoderma, 134, 253–266.

Peña-Haro, S., Zhou, J., Zhang, G.F., Chen, C., Stauffer, F., Kinzelbach W., 2012. A multi-approach framework to couple independent models for simulating the interaction between crop growth and unsaturated-saturated flow processes. In: Seppelt, R., Voinov, A.A., Lange, S., Bankamp D. (Eds.): International Environmental Modelling and Software Society (iEMSs) 2012 International Congress on Environmental Modelling and Software. Managing Resources of a Limited Planet: Pathways and Visions under Uncertainty. Sixth Biennial Meeting, Leipzig, Germany, pp. 1224–1231. http://www.iemss.org/society/index.php/iemss-2012-proceedings. ISBN: 978-88-9035-742-8.

Porter, C.H., Jones, J.W., Hoogenboom, G., Wilkens, P.W., Ritchie, J.T., Pickering, N.B., Boote, K.J., Baer, B., 2004. DSSAT v4 soil water balance module. In: Jones, J.W. et al. (Eds.): Decision support system for agrotechnology transfer Version 4.0, Vol. 4 DSSAT v4: Crop model documentation. Univ. of Hawaii, Honolulu, HI, pp. 1–23.

Priestley, C.H.B., Taylor. R.J., 1972. On the assessment of surface heat and evaporation using large scale parameters. Mon. Weather Rev., 100, 81–92.

Ritchie, J.T., 1972. A model for predicting evaporation from a row crop with incomplete cover. Water Resources Research, 8, 1204–1213.

Ritchie, J.T., 1981a. Water dynamics in the soil-plant-atmosphere. Plants and Soil, 58, 81–96.

Ritchie, J.T., 1981b. Soil water availability. Plants and Soil, 58, 327–338.

Ritchie, J.T., 1985. A user–oriented model of the soil water balance in wheat. p. 293–305. In: Fry, E., Atkin, T.K. (Eds): Wheat Growth and Modeling. NATO-ASI Series, Plenum Press.

Ritchie, J.T., 1998. Soil water balance and plant water stress. In Tsuji, G.Y., Hoogenboom, G., Thornton, P.K. (Eds): Understanding Options of Agricultural Production. Kluwer Academic Publishers and International Consortium for Agricultural Systems Applications, Dordrecht, The Netherlands, pp. 41–54.

Ritchie, J.T., Porter, C.H., Judge, J., Jones, W.J., Suleiman, A.A., 2009. Extension of an existing model for soil water evaporation and redistribution under high water content conditions. Soil Sci. Soc. Am. J., 73, 792–801.

Sarkar, R., 2009. Use of DSSAT to model cropping systems. CAB Reviews: Perspectives in Agriculture, Veterinary Science, Nutrition and Natural Resources, 4, No. 025.

Saxton, K.E., Rawls, W.J., Romberger, J.S., Papendick, R.I., 1986. Estimating generalized soil–water characteristics from texture. Soil Sci. Soc. Am. J., 50, 1031–1036.

Scanlon, B.R., Christman, M., Reedy, R.C., Porro, I., Šimůnek, J., Flerchinger, G.F., 2002. Intercode comparisons for simulating water balance of surficial sediments in semiarid regions. Water Resources Research, 38, 12, 1323, 59.1-59.16. DOI: 10.1029/2001WR001233.

Seo, H., Šimůnek, J., Poeter, E., 2007. Documentation of the HYDRUS package for MODFLOW-2000, the US Geological Survey modular ground-water model. GWMI 2007-01. Int. Ground Water Modeling Ctr, Colorado School of Mines, Golden, pp. 1–98.

Šimůnek, J., Hopmans, J.W., 2009. Modeling compensated root water and nutrient uptake. Ecological Modeling, 220, 4, 505–521. DOI:10.1016/j.ecolmodel.2008.11.004.

Šimůnek, J., van Genuchten, M.T., Šejna, M., 2008. Development and applications of the HYDRUS and STANMOD software packages and related codes. Vadose Zone Journal, 7, 2, 587–600. DOI: 10.2136/vzj2007.0077.

Šimůnek, J., van Genuchten, M.Th., Šejna, M., 2016. Recent developments and applications of the HYDRUS computer software packages. Vadose Zone Journal, 15, 7, pp. 25. DOI: 10.2136/vzj2016.04.0033.

Sophocleous, M., Koelliker, J.K., Govindaraju, R.S., Birdie, T., Ramireddygari, S.R., Perkins, S.P., 1999. Integrated numerical modeling for basin-wide water management: The case of the Rattlesnake Creek basin in south-central Kansas. Journal of Hydrology, 214, 1–4, 179–196.

Suleiman, A.A., Ritchie J.T., 2003. Modeling soil water redistribution during second-stage evaporation. Soil Sci. Soc. Am. J., 67, 377–386.

Twarakavi, N.K.C., Šimůnek, J., Seo, S., 2008. Evaluating interactions between groundwater and vadose zone using the HYDRUS-Based Flow Package for MODFLOW. Vadose Zone Journal, 7, 757–768.

van Genuchten, M. Th., 1980. A closed-form equation for predicting the hydraulic conductivity of unsaturated soils. Soil Sci. Soc. Am. J., 44, 892-898.

van Walsum, P.E.V., 2011. Influence of feedbacks from simulated crop growth on integrated regional hydrologic simulations under climate scenarios. Hydrol. Earth Syst. Sci. Discuss., 8, 10151–10193.

Vrugt, J. A., Hopmans, J. W., Šimůnek, J., 2001a. Calibration of a two-dimensional root water uptake model, Soil Science Society of America Journal, 65, 4, 1027–1037.

Vrugt, J.A., van Wijk, M.T., Hopmans, J.W., Šimůnek, J., 2001b. One-, two-, and three-dimensional root water uptake functions for transient modeling. Water Resources Research, 37, 10, 2457–2470.

Wang, J., Huang, G, Zhan, B., Mohanty, P., Zheng, J., Huang, Q., Xu, X., 2014. Evaluation of soil water dynamics and crop yield under furrow irrigation with a two-dimensional flow and crop growth coupled model. Agric. Water Manag., 141, 10–22.

Williams, J.R. 1991. Runoff and water erosion. In: Hanks, R.J., Richie, J.T. (Eds): Modeling Soil and Plant Systems. Agronomy Monograph 31. Madison, Wisconsin, USA: American Society of Agronomy, pp. 439–455.

Willmott, C.J., Ackleson, S.G., Davis, R.E., Feddema, J.J., Klink, K.M., Legates, D.R., O'Donnell, J., Rowe, C.M., 1985. Statistics for the evaluation and comparison of models. J. Geophys. Res., 90, 8995–9005.

Zhou, J., Cheng, G., Li, X., Hu, B. X., Wang, G., 2012. Numerical modeling of wheat irrigation using coupled HYDRUS and WOFOST models. Soil Sci. Soc. Am. J., 76, 2, 648–662. DOI: 10.2136/sssaj2010.0467.

Received 23 September 2017
Accepted 11 December 2017

Note: Colour version of Figures can be found in the web version of this article.

J. Hydrol. Hydromech., 66, 2018, 2, 246–256
DOI: 10.2478/johh-2018-0005

Simulations of freshwater lens recharge and salt/freshwater interfaces using the HYDRUS and SWI2 packages for MODFLOW

Adam Szymkiewicz[1*], Anna Gumuła-Kawęcka[1], Jirka Šimůnek[2], Bertrand Leterme[3], Sahila Beegum[2], Beata Jaworska-Szulc[1], Małgorzata Pruszkowska-Caceres[1], Wioletta Gorczewska-Langner[1], Rafael Angulo-Jaramillo[4], Diederik Jacques[3]

[1] Gdańsk University of Technology, Faculty of Civil and Environmental Engineering, ul. Narutowicza 11, 80-233 Gdańsk, Poland.
[2] University of California Riverside, 900 University Ave., Riverside, CA 92521, USA.
[3] Engineered and Geosystems Analysis, Institute for Environment, Health and Safety, Belgian Nuclear Research Centre, Boeretang 200, 2400 Mol, Belgium.
[4] Laboratoire d'Ecologie des Hydrosystèmes Naturels et Anthropisés (LEHNA) UMR 5023, 3, rue Maurice Audin, 69518 Vaulx-en-Velin, France.
[*] Corresponding author. E-mail: adams@pg.gda.pl

Abstract: The paper presents an evaluation of the combined use of the HYDRUS and SWI2 packages for MODFLOW as a potential tool for modeling recharge in coastal aquifers subject to saltwater intrusion. The HYDRUS package for MODFLOW solves numerically the one-dimensional form of the Richards equation describing water flow in variably-saturated media. The code computes groundwater recharge to or capillary rise from the groundwater table while considering weather, vegetation, and soil hydraulic property data. The SWI2 package represents in a simplified way variable-density flow associated with saltwater intrusion in coastal aquifers. Combining these two packages within the MODFLOW framework provides a more accurate description of vadose zone processes in subsurface systems with shallow aquifers, which strongly depend upon infiltration. The two packages were applied to a two-dimensional problem of recharge of a freshwater lens in a sandy peninsula, which is a typical geomorphologic form along the Baltic and the North Sea coasts, among other places. Results highlighted the sensitivity of calculated recharge rates to the temporal resolution of weather data. Using daily values of precipitation and potential evapotranspiration produced average recharge rates more than 20% larger than those obtained with weekly or monthly averaged weather data, leading to different trends in the evolution of freshwater-saltwater interfaces. Root water uptake significantly influenced both the recharge rate and the position of the freshwater-saltwater interface. The results were less sensitive to changes in soil hydraulic parameters, which in our study were found to affect average yearly recharge rates by up to 13%.

Keywords: Groundwater recharge; Freshwater lenses; HYDRUS; SWI2; MODFLOW; Vadose zone.

INTRODUCTION

Groundwater recharge through the vadose zone is an important factor affecting salinity patterns in coastal aquifers. In particular, in view of possible climate change, increased water demands and sea level rise, the development of freshwater lenses supplied with infiltrated rainwater on top of saline aquifers is a subject of intense research (e.g., Werner et al., 2013). A large number of contributions have focused on freshwater lenses in deltaic regions, as well as on islands, peninsulas, or sandbars located in tropical, arid, and temperate climatic zones (e.g., Comte et al., 2014; Contractor and Jenson, 2000; Chang et al., 2016; De Louw et al., 2011; Eeman et al., 2017; Holding and Allen, 2015; Houben and Post, 2016; Illangasekare et al., 2006; Jocson et al., 2002; Mahmoodzadeh et al., 2014; Sadurski et al., 1987; Sinclair et al., 2016; Stuyfzand, 2016; Sulzbacher et al., 2012).

The actual amount of recharge reaching the groundwater table depends on several factors, including time-variable weather conditions, land use, hydraulic properties of the vadose zone, topographic relief, and the groundwater table depth. Thus, recharge is inherently variable in space and time and this variability may have a significant influence on freshwater-saltwater dynamics in shallow coastal aquifers (Mollema and Antonelli, 2013; Trglavcnik et al., 2016; Vandenbohede et al., 2014). Other studies highlighted the importance of such factors as water uptake by tree roots (Comte et al., 2014) or hydraulic properties and water storage in the vadose zone (Contractor and Jenson, 2000; Jocson et al., 2002). There is thus a need to include seasonal fluctuations of recharge in groundwater models for coastal aquifers (Eeman et al., 2012; Mollema and Antonellini, 2013; Oude Essink et al., 2010) and to integrate vadose zone processes more fully into groundwater models.

Vadose zone models transform weather data that are provided as input (precipitation and potential evapotranspiration) into recharge fluxes arriving at the groundwater table. The choice of the temporal resolution of weather data (hourly, daily, monthly, yearly) can significantly affect time distribution and values of recharge. This problem was investigated previously mainly within the context of solute transport through the unsaturated zone (e.g. Foussereau et al., 2001; Persson and Saifadeen, 2016; Vero et al., 2014), with results showing that using longer averaging periods (e.g., daily vs. hourly) of weather data leads to less recharge and longer solute travel times. A systematic study by Batalha et al. (2018) evaluated groundwater recharge in different climatic regions of Brazil. They found that recharge rates calculated using daily climatological data were up to 9 times larger than those obtained using yearly averages. On the other hand, saltwater intrusion studies are often performed using monthly (e.g., Mollema and Antonellini, 2013; Prieto et al., 2006) or yearly (e.g., Oude Essink et al., 2010) weather data. Thus, the question arises about the possible influence of the temporal resolution of weather data on modeling results.

It is generally accepted that comprehensive representations of water flow in the vadose zone can be obtained using the Richards equation (e.g., Healy, 2010), although this approach generally does not account for some processes that may be important at the local scale, such as preferential flow (e.g., Šimůnek et al., 2003) or air entrapment (e.g., Szymańska et al., 2016). An extended form of the Richards equation can be used to describe flow under both unsaturated and saturated conditions, thereby offering a unified three-dimension (3D) description of flow for the entire subsurface domain. Numerical codes such as SUTRA (Voss and Provost, 2010), or HydroGeoSphere (Therrien et al., 2010) are based on this approach and include the capability to simulate density-dependent flow essential for saltwater intrusion modeling. However, due to high nonlinear nature of the Richards equation and the need for fine spatial discretizations close to the land surface, the requirements for computational power and time are often prohibitive for fully coupled saturated-unsaturated 3D models.

Alternatively, less complex models can be used also to describe flow in the vadose zone, especially close to the land surface. These models are often based on relatively simple water balance principles (e.g., SWAT (Neitsch et al., 2011) or HELP (Schroeder et al., 1994)) or kinematic wave routing (e.g., the UZF1 package for MODFLOW (Niswonger et al., 2006)). The usefulness of these type of models has been confirmed in a number of studies (e.g., Chang et al., 2016; Holding and Allen, 2015; Luoma and Okkonen, 2014). They are typically very efficient computationally. However, due to their simplified nature, they may not be able to represent properly some important features of unsaturated flow. For example, neither UZF1 nor HELP allows for upward flow due to capillary action, while SWAT greatly simplifies water flow below the root zone. Additionally, the kinematic wave model used in UZF1 is based on the assumption of a homogeneous soil profile, which is often not the case.

In addition to the above two groups of models, another possible modeling approach of intermediate complexity would be to couple a 3D (or 2D horizontal) model for flow in the saturated zone with one or more 1D models for flow in representative unsaturated zone soil profiles, based on the Richards equation. Such an intermediate approach would still allow for a wide range of unsaturated zone processes, but with less computational overhead compared to the complete 3D variably-saturated flow models. The intermediate concept was implemented in the HYDRUS package for MODFLOW (Beegum et al., 2018; Seo et al., 2007; Twarakavi et al., 2008), which is based on the widely-used standalone numerical HYDRUS-1D code (Šimůnek et al., 2008ab, 2016). HYDRUS-1D simulates the transient movement of water, solute, and heat in variably-saturated soil profiles using finite element discretization in space and fully implicit discretization in time. The model has been validated in a large number of applications (Šimůnek et al., 2008b, 2016), including several related to recharge (e.g., Scanlon et al., 2002; Šimůnek et al., 2016) and saltwater intrusion (Werner and Lockington, 2004).

The HYDRUS package for MODFLOW was originally written for MODFLOW-2000 (Seo et al., 2007). Its evaluation and comparison with other MODFLOW-related packages for vadose zone flow was presented by Twarakavi et al. (2008) and Bailey et al. (2013). Applications to regional scale groundwater flow, as well as comparisons with the UZF1 package, are described in Leterme et al. (2013, 2015). Currently, the package is being developed further in cooperation between research groups from the University of California Riverside, the Belgian Nuclear Research Centre (SCK•CEN), and the Gdańsk University of Technology (Beegum et al., 2018). The most recent version of the HYDRUS package is compatible with MODFLOW-2005 (Harbaugh, 2005). So far, only a fraction of the processes implemented in the original standalone HYDRUS-1D program has been ported to HYDRUS for MODFLOW. Much potential exists for further enhancements, including features such as contaminant transport, macropore flow, or improved models of the hydraulic functions.

The SWI2 package (Bakker et al., 2013) is the latest release of the Seawater Intrusion (SWI) Package for MODFLOW. This package allows simulations of variable-density groundwater flow and seawater intrusion in multi-aquifer coastal systems. Vertically integrated variable-density flow is based on the Dupuit approximation in which an aquifer is vertically discretized into zones of differing densities, separated from each other by defined surfaces representing interfaces (Bakker et al., 2013). The simplified, sharp-interface approach to density-dependent flow implemented in the SWI and SWI2 packages allows for considerable savings of computer time, as compared to solutions of the coupled variable-density flow and salt transport equations. In fact, each aquifer can be represented by only a single layer of cells. However, the sharp-interface model neglects diffusion and dispersion processes, which may be important in some circumstances. Numerical tests (Dausman et al., 2010) showed that the sharp-interface models may not be realistic when considerable dispersion occurs across the interface, when the anisotropy ratio is very small, or in some systems where inversion occurs and a significant amount of vertical fingering is present.

Our research reported in this contribution has two main goals. The first objective is to carry out an evaluation of the HYDRUS package for MODFLOW as a tool for simulating recharge in conjunction with the SWI2 package (Bakker et al., 2013) for saltwater intrusion modeling. While HYDRUS-1D has been used previously in studies related to saltwater intrusion, the HYDRUS package for MODFLOW has to the best of our knowledge not yet been applied in this particular context. The second objective is to investigate the influence of selected factors on the amount of recharge as well as evolutions of the groundwater table and the saltwater-freshwater interface during the simulations. These factors include uncertainty in soil hydraulic parameters (describing the retention and hydraulic conductivity functions of unsaturated soils), the presence of vegetation, and the temporal resolution of weather data (precipitation and reference evapotranspiration).

MATERIALS AND METHODS

HYDRUS code

Numerical simulations were performed using a modified version of MODFLOW-OWHM (Hanson et al., 2014), which includes both the SWI2 (Bakker et al., 2013) and HYDRUS packages for MODFLOW (Twarakavi et al., 2008). We used the updated version of HYDRUS for MODFLOW (Beegum et al., 2018), which represents an improvement over the original version as described by Seo et al. (2007) and Twarakavi et al. (2008), and which is compatible with MODFLOW-2005 and MODFLOW-OWHM. Here, we provide a more detailed description of the current version of the HYDRUS package, while details about MODFLOW-OWHM and SWI2 can be found in Hanson et al. (2014) and Bakker et al. (2013), respectively.

The HYDRUS package performs simulations of vertical flow in the vadose zone overlying the MODFLOW model domain. Simulations are carried out for a number of user-defined soil profiles. In principle, it is possible to associate a

separate soil profile with each cell of the MODFLOW horizontal grid, but this approach may lead to unacceptably long simulation times for larger problems. Thus, it is recommended to divide the flow domain into a number of regions in such a way that each region encompasses several MODFLOW cells having approximately the same vadose zone flow and transport parameters. The division into regions should be based on such criteria as soil type, vegetation, depth to groundwater, and weather data. It is also possible to define HYDRUS profiles only for a part of the MODFLOW cells for which a more detailed description of unsaturated flow is required, while using alternative methods to specify recharge rates for the remaining cells.

The top of each HYDRUS profile corresponds with the soil surface, while the bottom should be located within the uppermost aquifer defined in MODFLOW, below the expected water table fluctuation zone. Each profile may consist of an arbitrary number of soil layers having different hydraulic properties. The number and position of nodes used to discretize each vadose zone profile are specified by the user. For reasons of numerical stability and efficiency, small nodal spacings (on the order of 1 cm) close to the soil surface are recommended. Details of the numerical scheme used to solve the Richards equation in HYDRUS are given by Šimůnek et al. (2008a).

Boundary conditions at the soil surface are implemented as so-called atmospheric conditions, which can be described by the following set of inequalities (Neuman et al., 1974; Šimůnek et al., 2008a):

$$I_{\max} \le -K\frac{\partial h}{\partial z} - K \le E_{\max} \tag{1a}$$

$$h_{dry} \le h \le h_{pond} \tag{1b}$$

where $I_{\max}$ is the maximum possible infiltration rate (equal to precipitation if interception is neglected), given as a negative number, K is the soil hydraulic conductivity at the surface, h is the pressure head, z is the vertical coordinate (oriented positively upwards), $E_{\max}$ is the maximum possible evaporation rate (potential evaporation), h_{pond} is the maximum ponding depth at the soil surface, and h_{dry} is the minimum allowed value of the pressure head at the surface. These values are provided by users at an arbitrary temporal resolution, and not related to the stress periods defined in MODFLOW. The type of the boundary condition at the soil surface is automatically switched between the flux and pressure head boundary conditions, depending upon the prevailing weather and soil conditions. When the pressure head boundary condition is used, the potential flux is reduced to the actual flux (e.g., actual infiltration and/or evaporation). Details about the numerical implementation of the atmospheric boundary conditions can be found in Šimůnek et al. (2008a).

Another important feature of the HYDRUS package is an explicit representation of water uptake by plant roots. The root zone depth and root density distribution is specified for each soil profile, according to available data on vegetation. The maximum potential transpiration rates are specified by the user at a temporal resolution matching the precipitation and evaporation data. At each HYDRUS time step, the current maximum transpiration rate is distributed among the nodes in the root zone, proportionally to the defined root density distribution, to calculate the nodal potential root water uptake. Actual root water uptake, appearing as a source term in the Richards equation, is obtained by multiplying potential root water uptake using a stress response function, which in turn depends on the soil water pressure head. For our simulations we used a simplification of the well-known stress response function of Feddes et al. (1978), as given by Huang et al. (2011). Resulting values of root water uptake are either equal to or smaller than the potential root water uptake.

HYDRUS-MODFLOW coupling

The sequential coupling of MODFLOW and HYDRUS involves exchanging information about the recharge rates and the position of the groundwater table. During each MODFLOW time step, the HYDRUS package is called to solve the 1D Richards equation for each defined soil profile. Due to the variability and nonlinearity of flow in the unsaturated zone, the HYDRUS solution is generally performed using much smaller time steps than the MODFLOW solution. HYDRUS time steps are adjusted automatically within a user-defined range according to the performance of the iterative solver. The initial condition for each soil profile is specified by users for the first MODFLOW time step. The atmospheric boundary condition at the top of each profile is used to represent precipitation, irrigation and/or evaporation as described above. The boundary condition at the bottom of each profile is given as the average value of the groundwater head in the uppermost aquifer, calculated for all MODFLOW cells associated with a particular soil profile.

The unsaturated flow simulation is performed for a time period corresponding to the current MODFLOW time step. Average flow through the bottom of the vadose zone profile during a particular MODFLOW time step is then used as the average recharge (or capillary rise) rate for a particular time step. This recharge rate is then included into the discretized equations for the MODFLOW cells corresponding to a given profile (in the same manner as recharge values defined in the RCH package). Next, the solution for saturated zone flow is obtained with MODFLOW for the new time level, thus providing new values of groundwater heads in the upper aquifer, with the solution proceeding to the next time step. Pressure head and water content distributions in each HYDRUS profile are updated next to reflect the new position of the water table and the vertical flux in the considered HYDRUS profile at the end of the previous MODFLOW time step (Beegum et al., 2018).

Note that the HYDRUS package for MODFLOW does not consider full coupling of saturated and unsaturated flow, such as in the VSF (Thoms et al., 2006), VS2DI (Healy, 2008), or SUTRA (Voss and Provost, 2010) codes. Rather, the HYDRUS package is now merely a tool to facilitate and improve estimations of infiltration and evapotranspiration fluxes, which otherwise could be achieved using the standalone HYDRUS-1D code or other codes solving the 1D Richards equation, as implemented for example by Contractor and Jenson (2000) and Kamps et al. (2008). The applied loose coupling scheme does not allow complete consistency between the HYDRUS and MODFLOW solutions due to the three reasons, First, during each MODFLOW time step, the HYDRUS simulation is performed with a constant groundwater head at the bottom of the profile, which is subsequently updated instantaneously at the beginning of a new time step. In reality, the groundwater table varies continuously in time in response to vadose zone flow and other processes such as pumping. Second, the groundwater head at the bottom of each HYDRUS profile represents an average for all MODFLOW cells associated with a particular soil profile, while in reality it is spatially variable. And third, MODFLOW solves the groundwater flow equation for an unconfined aquifer using a value of specific yield (S_y),

which is defined by the user independently of the vadose zone simulations. The value of S_y determines the change in the groundwater table position in response to the specified recharge flux. Consequently, the specific yield also determines the updated boundary condition at the bottom of each HYDRUS profile during the next time step. We are aware that the value of specific yield should be strongly related to the vadose zone conditions above the water table; this issue is a subject of ongoing research.

The simplifications mentioned above result of the need to compromise between accuracy and computational efficiency in the proposed approach. As a consequence, it is not possible to calculate a global mass balance for both the saturated and unsaturated zones. The mass balance should be considered separately for the MODFLOW groundwater domain (taking into account the coupled fluxed) and for each HYDRUS profile at each MODFLOW time step. In the simulations described below the HYDRUS and MODFLOW mass balance errors for all time steps were below 1%.

Simulation setup

Simulations were carried out for a 2D cross-section through a sandy peninsula along the Polish Baltic coast, as shown in Fig. 1. Although the width of the peninsula was 600 m, the solution domain extended offshore 200 m on each side. The elevation of the ground surface varied from –5 m at the edges of the domain to +5 m in the center of the peninsula, while the bottom of the aquifer was assumed to be horizontal at an elevation of –40 m. The MODFLOW grid consisted of a single row of 100 cells in a single layer representing the unconfined aquifer. The vertical boundaries and the bottom of the domain were assumed impermeable. A third-type boundary condition (a general head boundary, GHB) was prescribed on those parts of the soil surface that were below the sea level, similarly as in the examples described by Bakker et al. (2013), using the GHB package of MODFLOW. The total freshwater head, $H = h+z$, was assumed to be 0 m for the GHB cells, while the conductivity was set to 100 m^2/d. The SWI2 option ISOURCE was set to –2 for the GHB cells so that any water infiltrating into the aquifer was considered to be seawater, while water exfiltrating to the sea had the salinity corresponding to the upper part of the cell. In all simulations, the number of salinity zones in the SWI2 package was set to 2 (i.e., a single zeta-surface was defined). The density of freshwater (ρ_f) was 1 g/cm^3, and the density of saltwater (ρ_s) was 1.0065 g/cm^3, typical for south Baltic sea water. The aquifer was assumed to be isotropic and homogeneous with a saturated conductivity (K_s) of 10 m/day and a specific yield (S_y) of 0.25.

The central (land) part of the aquifer was subject to recharge from precipitation. Simulations of vadose zone flow were carried out using the HYDRUS package. Two regions with representative soil profiles were defined based on the average depth to the groundwater (GW) table. Region 1 included two 200-m wide strips of land parallel to the shoreline on each side of the peninsula where the GW table was up to 2 m deep on average. Region 2 consisted of the central 200 m of land where the GW table was expected to be about 4 to 5 m deep. The soil profiles were discretized using 41 nodes in Region 1 and 81 nodes in Region 2. The vertical node spacing was non-uniform, ranging from 1 cm close to the ground surface to 9 cm at the bottom of the profile.

The simulations were performed for three types of sand, characterized by the van Genuchten-Mualem hydraulic functions of the following form:

$$\theta(h) = \theta_R + (\theta_S - \theta_R)\left[1+\left(\alpha|h|\right)^n\right]^{-m} \tag{2a}$$

$$K(h) = K_S K_R(h) = K_S \frac{\left\{1-\left(\alpha|h|\right)^{n-1}\left[1+\left(\alpha|h|\right)^n\right]^{-m}\right\}^2}{\left[1+\left(\alpha|h|\right)^n\right]^{m/2}} \tag{2b}$$

where θ is the volumetric water content, θ_S is the water content at field saturation, θ_R is the residual water content, h is the soil water pressure head (negative in the unsaturated zone), K is the hydraulic conductivity, K_S is the hydraulic conductivity at field saturation, K_R is the relative hydraulic conductivity, and α, n and m are fitting parameters (with $m = 1–1/n$). Values of the soil hydraulic parameters are listed in Table 1. The first set, with a relatively high saturated conductivity (400 m/d), is denoted as medium sand in the database of VS2DTI and VS2DHI codes (Hsieh et al., 1999) and was used e.g. by Dan et al. (2012). While such a high hydraulic conductivity is not typical for vertical flow in the vadose zone (except macropore flow), we include this set as an example of highly permeable material. The second set, denoted here as fine sand, is reported by Carsel and Parrish (1988) as an average set of parameters for sand according to the USDA textural division. Similarly, the third set represents an average set of parameters for a loamy sand according to the USDA classification (Carsel and Parrish, 1988). In the following section, we report results obtained for each of these three soil types. Note that the change in hydraulic

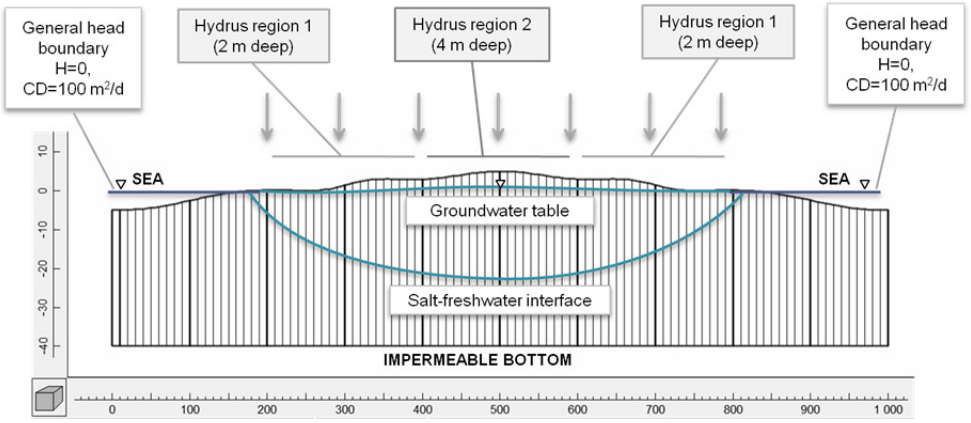

Fig. 1. Assumed flow domain and specified boundary conditions (CD = conductance).

parameters affected only the HYDRUS simulations for the vadose zone. The values of specific yield and the horizontal hydraulic conductivity in the aquifer were kept the same for all simulations. Thus, we neglected the influence of unsaturated flow on the specific yield, as explained above.

The initial condition for each simulation was obtained by running the MODFLOW/HYDRUS simulation for a period of 40 000 days with a constant value of the infiltration flux (equal to the assumed recharge rate) imposed at the soil surface. The infiltration flux was specified as 300 mm/yr, based on estimates given by Dyck and Chardabellas (1963) (cited in Hölting and Coldewey, 2013) for sands with a sparse plant cover (about 60% of yearly precipitation). A long warm-up period was used because of the need to obtain the steady position of the interface with the SWI2 package, which generally requires more than 100 years (see Examples 3 and 4 in the documentation of SWI2). A warm-up period for the vadose zone simulations was also necessary, but it is much shorter, on the order of a single year. As a basic check, we compared the steady-state results obtained with the HYDRUS package with a constant infiltration rate to the results obtained with the RCH MODFLOW package. This package allows one to input a user-specified rate of recharge at the water table. While the results are not shown here, the agreement in terms of both the groundwater table elevation and the saltwater-freshwater interface position was very good (differences in the position of the groundwater table and the fresh-salt interface in the center of the domain were less that 1.5 cm, while the elevations agreed with the Ghyben-Herzberg formula (Verruijt, 1968)).

Simulations were performed for a 5-year period using the available weather data from Gdańsk (2011–2015), starting from the initial steady-state conditions. Daily values of the reference potential evapotranspiration (ET_0) for the simulation period are shown in Figure 2, while the daily precipitation values are shown in Figs. 3, 5 and 7. Average annual precipitation during the 5-year period was 550 mm/yr and the average annual ET_0 317 mm/yr. ET_0 was estimated using the method of Grabarczyk, developed in Poland (Grabarczyk and Żarski, 1992), which gives evapotranspiration values somewhat lower

Table 1. Parameters of the van Genuchten - Mualem hydraulic model for the soils used in this study.

Parameter	Medium sand	Fine sand	Loamy sand
θ_R	0.022	0.045	0.057
θ_S	0.375	0.430	0.410
K_S [m/d]	400	10	3.5
α [1/m]	4.31	14.50	12.40
n = 3.08	3.10	2.68	2.28

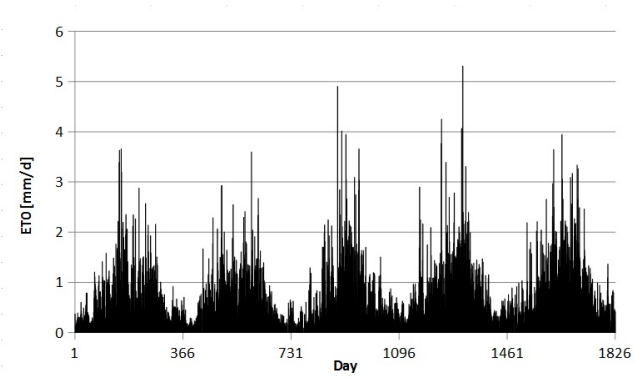

Fig. 2. Daily reference evapotranspiration rates for the 5-year simulation period.

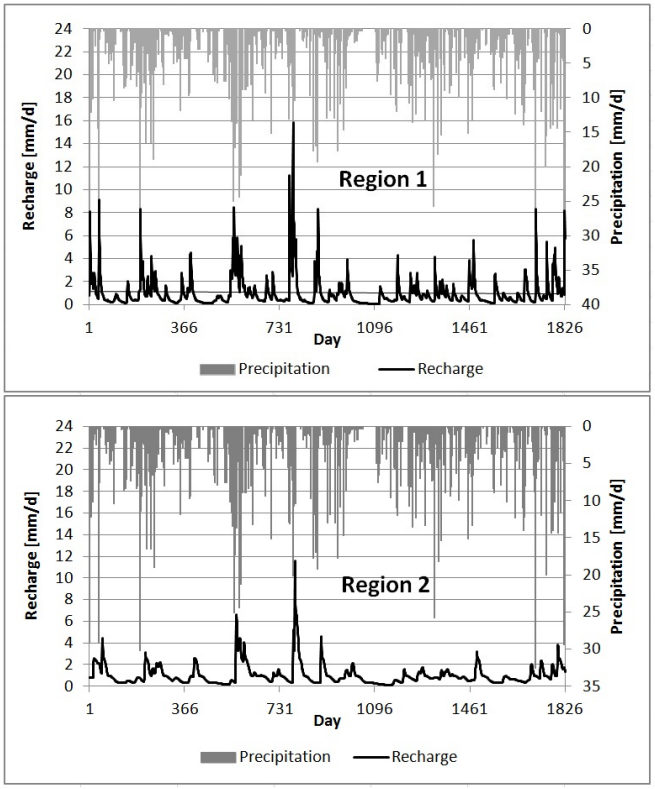

Fig. 3. Daily values of recharge for fine sand without vegetation, calculated using daily weather data; top: HYDRUS region 1, bottom: HYDRUS region 2.

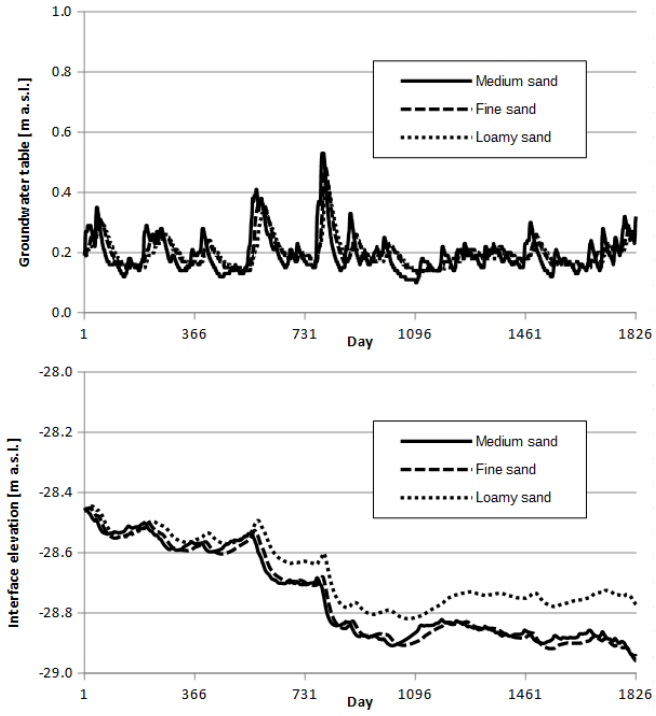

Fig. 4. Evolution of the water table position (top) and the freshwater/saltwater interface for different types of sand, using daily weather data and assuming no vegetation.

than the widely used Penman-Monteith FAO equation. The formula requires only daily values of the average air temperature and the average vapor pressure deficit.

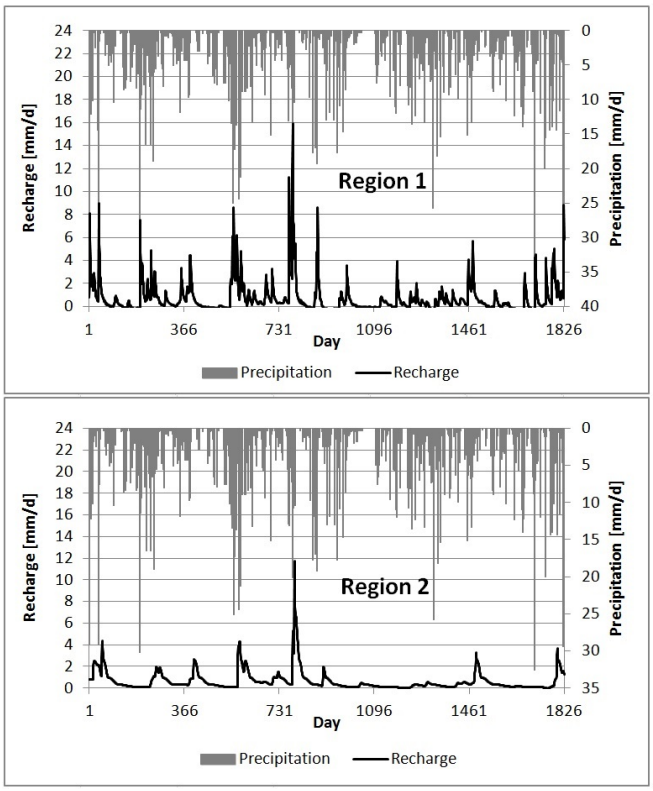

Fig. 5. Daily values of recharge for fine sand with vegetation, calculated using daily weather data in two HYDRUS regions; top: HYDRUS region 1, bottom: HYDRUS region 2.

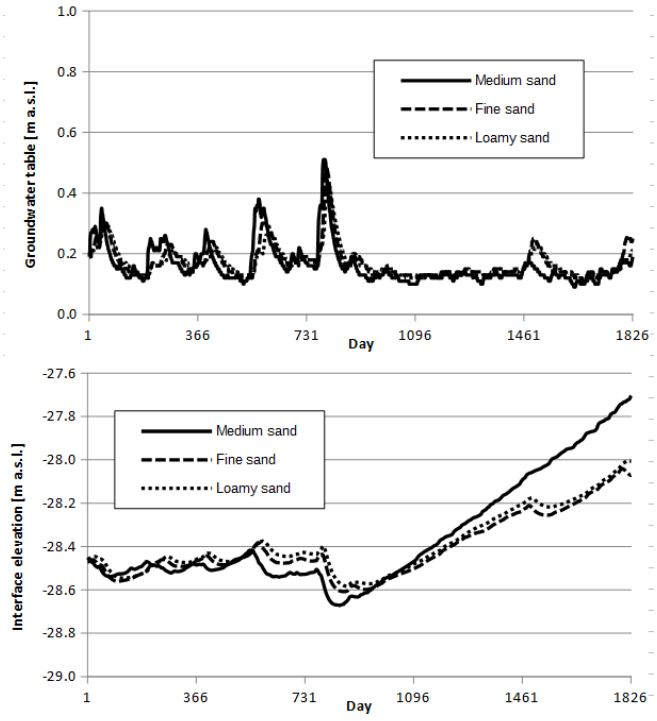

Fig. 6. Evolution of the water table position (top) and the freshwater/saltwater interface for different types of sand, using daily weather data and assumed the presence of vegetation.

The total evapotranspiration flux includes both evaporation from the soil surface and transpiration of water taken up by plant roots from deeper soil layers. Several studies (e.g., Comte at al., 2014; Kamps et al., 2008) reported that water uptake

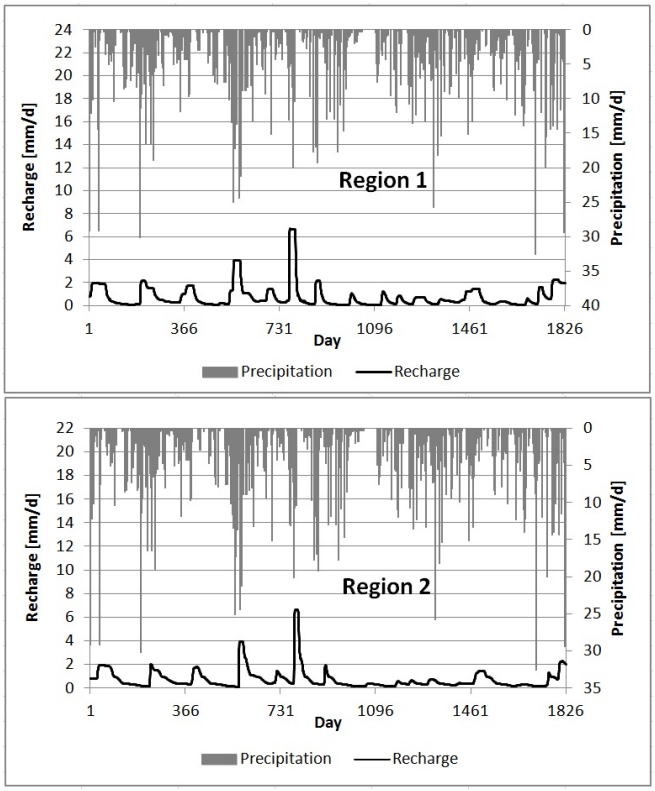

Fig. 7. Daily values of recharge for fine sand without vegetation, calculated using monthly weather data; top: HYDRUS region 1, bottom: HYDRUS region 2.

by vegetation is an important factor influencing groundwater resources of freshwater lenses. In order to account for this, we performed two series of simulations. In the first series, we neglected the presence of plants and assumed that ET_0 was equal to potential evaporation. In the second series, the reference evapotranspiration was distributed as a source term over the root zone, i.e., ET_0 corresponded to potential transpiration (interception was not considered). While both of these cases were significant simplifications of reality, they can be considered as indicators for the possible range of variability of recharge for a varying soil cover by vegetation. We assumed that the depth of the root zone was 2 m, with the root density distribution decreasing linearly from a maximum value at the soil surface to zero at a depth of 2 m. For the stress response function, which describes the reduction in water uptake due to decreasing pressure heads in unsaturated soil, we used the model of Huang et al. (2011), which is a simplified version of the well-known formulation by Feddes et al. (1978). In this approach, root water uptake is assumed to be maximum for pressure heads larger than h_1 (equal to –3 m in our study), zero for pressure heads less than the wilting point (assumed at h_2 = –150 m), and changing linearly for pressure heads between these two values. Such a model is considered representative of coniferous forests (see Huang et al., 2011, and references therein). More details on the implementation of root water uptake in HYDRUS-1D can be found in Šimůnek et al. (2008a). The two scenarios represent typical conditions of coastal sandbars of the Baltic coast, which can be covered by bare dunes, grassland, or sparse pine forests.

The coupled codes were also used to investigate the effect of the temporal resolution of weather data. We used either daily, weekly, or monthly averages of the precipitation and evapotranspiration rates. Regardless of the temporal resolution of the

weather data, we used a constant MODFLOW time step of 1 day and allowed the time steps in HYDRUS to vary within a range from 10^{-5} to 1 day. All simulations assumed a ponding depth of zero and a minimum soil water pressure head at the soil surface of –10000 m. The input data for the groundwater model were partly prepared using the ModelMuse interface (Winston, 2009). Since ModelMuse does not support HYDRUS for MODFLOW, all data required by this package were prepared using spreadsheet software.

Sensitivity analysis

Additionally, a sensitivity analysis was performed by changing values of the van Genuchten-Mualem parameters of fine sand, one at a time, according to the following scheme: K_S was decreased or increased by one order of magnitude (K_S = 1 or 100 m/d), α was changed by +/– 50% (α = 7.25 and 21.75 m^{-1}), and n was changed by +/– 0.5 (n = 2.18 and 3.18). Such a range of parameter variability may reflect uncertainty in the unsaturated zone parameters as measured in the field or estimated from basic soil data via pedotransfer functions. For example, a study by Meyer et al. (1997) provides the following range of variability for α and n in the USDA sand textural group: K_S = 0.3 m/d to 16 m/d, α = 6.87 to 22.6 m^{-1}, and n = 1.95 to 3.62. According to other authors, the hydraulic conductivity of sands may vary in a wider range. For example, Freeze and Cherry (1979) gave values of K_S from about 1 to 1000 m/d for clean sands. These intervals are wider than those assumed in our study; combinations of hydraulic parameters that differ from the above intervals may still be considered physically admissible.

RESULTS AND DISCUSSION

Results obtained for the various scenarios described in the previous section are presented in Tables 2 and 3 and Figures 3 to 8. The different scenarios are compared in terms of the average yearly recharge rate during the 5-year simulation period, daily recharge values in the two HYDRUS regions, and evolutions of the groundwater table and the freshwater-saltwater interface in the center of the domain.

Influence of the soil hydraulic properties

The results of simulations performed using daily values of precipitation and reference evaporation for the three types of sand are presented in Table 2 and Figures 3 and 4. For these simulations we neglected the presence of vegetation. This means that the maximum evaporation flux at the soil surface was set to ET_0 as indicated in the previous section. Table 2 shows average annual values of recharge computed for the 5-year period. They varied from 476 mm/yr for medium sand to 416 mm/yr for loamy sand, which corresponds to a relative difference of about 13%. Figure 3 shows daily values of recharge in two regions, obtained using the fine sand hydraulic parameters. The distribution of recharge was found to be highly variable in time, generally following the pattern of precipitation. However, it can be seen that the depth of the vadose zone has a visible influence on the temporal distribution of recharge and its maximum daily values. In Region 2, where the depth to groundwater was larger than in Region 1, the recharge distribution was much smoother throughout the year, with peak values largely reduced. On the other hand, recharge rates between precipitation periods were larger in Region 2 because of longer redistribution time of soil moisture in deeper profiles.

Table 2. Average annual recharge rates [mm/yr] obtained for different simulation settings.

Scenario	Medium sand	Fine sand	Loamy sand
Daily weather data No vegetation	476	449	416
Daily weather data With vegetation	359	315	306
Weekly averaged weather data No vegetation	370	354	341
Weekly averaged weather data With vegetation	317	304	301
Monthly averaged weather data No vegetation	338	326	318
Monthly averaged weather data With vegetation	338	326	318

Table 3. Minimum (ζ_{min}) and maximum (ζ_{max}) elevations of the freshwater-saltwater interface and the average annual recharge rate for different values of the soil hydraulic parameters.

Scenario	ζ_{min} [m]	ζ_{max} [m]	Average recharge [mm/yr]
Fine sand (Basic case)	–28.96	–28.45	449
K_s =100 m/d	–29.02	–28.45	461
K_s = 1 m/d	–28.88	–28.45	432
α = 29 /m	–29.11	–28.45	474
α = 7.25 /m	–28.83	–28.45	423
n = 3.08	–29.07	–28.45	468
n = 2.08	–28.79	–28.45	405

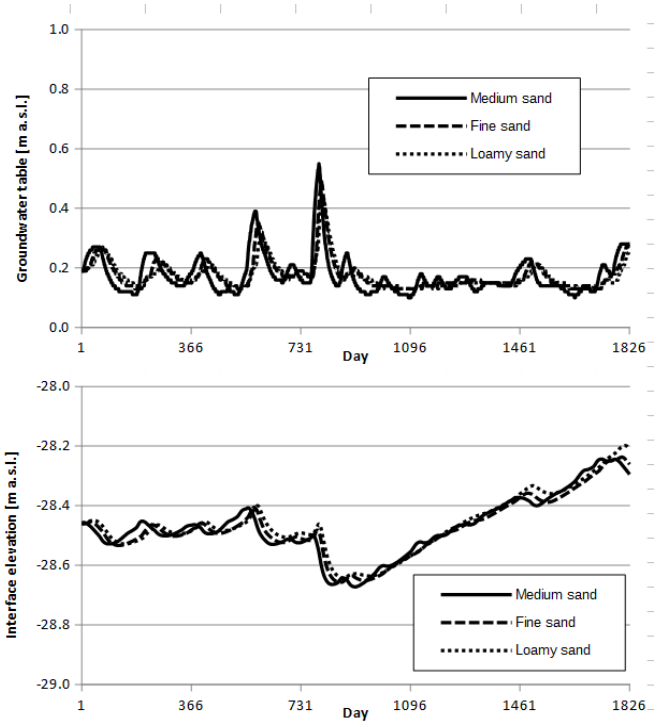

Fig. 8. Evolution of the water table position (top) and the freshwater/saltwater interface for different types of sand, using monthly weather data and assuming no vegetation.

As shown in Figure 4, the water table fluctuated following periods of high and low recharge, with a maximum amplitude of about 0.4 m. The freshwater-saltwater interface also showed seasonal fluctuations, with a general decreasing trend. The final position of the interface was about 0.5 m lower than the initial position. This can be explained by the fact that average yearly

recharge rates during the simulation period (from 416 mm/yr to 476 mm/yr) were significantly higher that the recharge rate used obtain the initial steady-state condition (300 mm/yr). The results shown in Figure 4 are similar for all three soil types, except that for loamy sand the interface elevation decreased at a lower rate than for medium and fine sand. We also note that recharge values were larger during the first 3 years of the simulations, resulting in a visible lower position of the interface. In contrast, the last 2 years were characterized by less recharge and more stable positions of the water table and the interface. The simulated position of the interface was generally higher than its elevation calculated using the Ghyben-Herzberg formula for a particular water table position. While the Ghyben-Herzberg approach assumes steady-state conditions, numerical simulations represent transient conditions. A notable time lag exists in the adjustment of the interface location for varying positions of the water table.

Results of the sensitivity analysis are presented in Table 3. The range of variability of average recharge rate and the final (minimum) position of the interface were consistent with the range of variability observed for the three sandy soils obtained earlier. An increase in any parameter (i.e., K_S, α, or n) produced an increase in recharge and a decrease in the final position of the interface. Modifying K_S by an order of magnitude produced a change of less than 4% in the average yearly recharge. Changing the van Genuchten parameter α by a factor of two resulted in variations in recharge of less than 6%. On the other hand, increasing or decreasing n by 19% produced a 4.2% increase and a 9.9% decrease in the average recharge rate, respectively. We hence conclude that, for our particular setting, the most sensitive parameter was n since relatively small changes of its value were found to have a significant effect on recharge.

Influence of water uptake by plant roots

The second series of simulations assumed that the evapotranspiration flux was distributed over a 2-m deep root zone. Results of these simulations are summarized in Table 2. The data show that root water uptake has a pronounced effect on recharge, and consequently also on the saltwater-freshwater interface position. Average yearly recharge rates decreased to values between 306 and 351 mm/yr, corresponding to a reduction of 24 to 30% compared to scenarios without vegetation. Relative differences in the average recharge rates of various soils were slightly larger than those for corresponding cases without vegetation (16% vs. 13%).

The reduction in recharge due to vegetation is also reflected in the daily values of recharge shown in Figure 5. In contrast to the previous case, the elevation of the freshwater-saltwater interface increased during the simulation period (Fig. 6) for all three soils. The increase was particularly visible during the last two years, characterized by smaller recharge rates, which is consistent with the results for the scenarios without vegetation. Also, in this case, one can see somewhat larger differences between soil types in terms of the interface position. The highest final elevation of the interface was obtained for medium sand.

Influence of the temporal resolution of weather data

In order to investigate the effects of the temporal resolution of weather data, simulations were carried out using weekly and monthly averaged precipitation and reference evapotranspiration rates. The resulting values of average annual recharge are reported in Table 2. For the bare soil scenarios with weekly and monthly averaged meteorological data, the recharge rate decreased by about 20 and 27% , respectively. Daily recharge values are shown in Figure 7 for the bare fine sandy soil and monthly averaged weather data. The plots show that the recharge patterns are distinctly different from those in Figure 3. As expected, fluctuations were smoothed to a large extent. The episodic nature of recharge, reported in the literature (e.g., Hunt et al., 2008; Smerdon et al., 2008), is lost when precipitation values are averaged over longer time periods. Similar conclusions on the influence of time averaging of the weather data were also presented by Batalha et al. (2018). These authors found that using long-term averages of precipitation and evapotranspiration will lead to severe underestimates of the recharge rates as compared to the use of daily data. Their results for semi-arid region in Brazil differed by a factor of 9 between simulations using daily and yearly averages of weather data. The discrepancy was found to be particularly significant for coarse-textured soils, which corroborates the results of our study.

The influence of the temporal resolution of weather data was found to be significantly smaller for the scenarios with vegetation. Table 2 shows that the maximum differences in average annual recharge were only about 13% for medium sand. In contrast to the case of bare soil (no vegetation), using monthly averaged weather data did lead to higher recharge rates than weekly averages. While this could be explained by a more complex pattern of water flow in the presence of a relatively deep root zone, these interactions remain to be investigated further. For the setting considered in this study, monthly averages of weather data produced nearly the same values of recharge for the cases with and without vegetation (differences were less than 1 mm/yr).

Table 2 also shows that the influence of soil hydraulic parameters on recharge decreases when weather data are averaged over longer time periods. While relative differences in recharge between the three types of sand for the daily data were about 13%, they were only about 8% and 6% for the weekly and monthly averaged data, respectively. Sensitivity analysis with respect to the hydraulic parameters K_S, α, and n were also carried out for the weekly and monthly weather data. While details are not further reported here, the obtained ranges of recharge values were similar to the ranges shown in Table 2 for the three types of sand. Similarly as for daily data, increasing K_S, α, or n produced a slightly higher recharge rates when weekly or monthly weather data were used, with the n parameter seemingly being the most sensitive parameter.

CONCLUSIONS

Based on preliminary evaluations carried out in this study, we consider the HYDRUS package for MODFLOW to be a promising tool for integrating vadose zone processes in a saturated groundwater flow model accounting for saltwater intrusion. This package allows calculations of spatially and temporally variable recharge rates using the physically-based Richards equation and an appropriate set of water retention and hydraulic conductivity functions characterizing vadose zone flow processes, and accounting for interactions with groundwater.

Our simulations indicated that for the particular system considered in this study, changes in soil hydraulic parameters had a moderate influence on the final position of the groundwater table and the freshwater-saltwater interface. This may explained by the fact that we considered only sandy soils, which are characterized by low water holding capacities and relatively high hydraulic conductivities. The sensitivity analysis showed that

the recharge rates are affected more by the α and n parameters of the van Genuchten function than by the hydraulic conductivity, which for our study was not the limiting factor for water infiltration. On the other hand, the results were influenced more significantly by the temporal resolution of the weather data and by the presence of vegetation (i.e., land use). The use of monthly and weekly averaged values of precipitation and potential evaporation led to recharge rates that were more than 20% smaller than those obtained using daily values. Similarly, when the potential evapotranspiration rate was distributed over the root zone instead of being assigned to the soil surface (i.e., vegetated versus unvegetated soil surfaces), the resulting recharge rates decreased by more than 24%. Differences in the recharge rate directly influenced the evolution of the saltwater-freshwater interface. For the scenarios with daily weather data and no vegetation, the position of the interface decreased with time due to relatively large recharge (larger than the initial steady-state value). The opposite trend was observed for scenarios with vegetation or for weekly and monthly averaged precipitation and evaporation data, which produced reductions in the recharge rate and upward displacement of the freshwater-saltwater interface.

Acknowledgements. This work has been supported by the National Science Centre, Poland, in the framework of project 2015/17/B/ST10/03233 "Groundwater recharge on outwash plain". Weather data were obtained from a station operated by the Department of Hydraulic Engineering, Faculty of Civil and Environmental Engineering, Gdańsk University of Technology.

The authors would like to thank two reviewers for their detailed and insightful remarks, which helped to improve the manuscript.

REFERENCES

Bailey, R.T., Morway, E.D., Niswonger, R.G., Gates, T.K., 2013. Modeling variably saturated multispecies reactive groundwater solute transport with MODFLOW-UZF and RT3D. Ground Water, 51, 5, 752–761. DOI: 10.1002/ird.1699.

Bakker, M., Schaars, F., Hughes, J.D., Langevin, C.D., Dausman, A.M., 2013. Documentation of the seawater intrusion (SWI2) package for MODFLOW. USGS Numbered Series “Techniques and Methods” 6-A46. US Geol. Survey, Reston, VA, USA.

Batalha, M.S., Barbosa, M.C., Faybishenko, B., van Genuchten, M.Th., 2018. Effect of temporal averaging of meteorological data on predictions of groundwater recharge. Journal of Hydrology and Hydrodynamics, 66, 2, 143–152.

Beegum, S., Šimůnek, J., Szymkiewicz, A., Sudheer, K.P., Nambi, I.M., 2018. Implementation of solute transport in the vadose zone into the 'HYDRUS package for MODFLOW'. Groundwater, (under review).

Carsel, R.F., Parrish, R.S., 1988. Developing joint probability distributions of soil water retention characteristics. Water Resources Research, 24, 5, 755–769.

Chang, S.W., Nemec, K., Kalin, L., Clement, T.P., 2016. Impacts of climate change and urbanization on groundwater resources in a barrier island. Journal of Environmental Engineering, D4016001.

Comte, J.C., Join, J.L., Banton, O., Nicolini, E., 2014. Modelling the response of fresh groundwater to climate and vegetation changes in coral islands. Hydrogeology Journal, 22, 8, 1905–1920.

Contractor, D.N., Jenson, J.W., 2000. Simulated effect of vadose infiltration on water levels in the Northern Guam Lens Aquifer. Journal of Hydrology, 229, 3, 232–254.

Dan, H.C., Xin, P., Li, L., Li, L., Lockington, D., 2012. Capillary effect on flow in the drainage layer of highway pavement. Canadian Journal of Civil Engineering, 39, 6, 654–666.

Dausman, A., Langevin, C., Bakker M., Schaars, F., 2010. A comparison between SWI and SEAWAT – the importance of dispersion, inversion and vertical anisotropy. In: Proceedings of the 21st Salt Water Intrusion Meeting, Azores, Portugal.

De Louw, P.G., Eeman, S., Siemon, B., Voortman, B.R., Gunnink, J., Van Baaren, E.S., Oude Essink, G., 2011. Shallow rainwater lenses in deltaic areas with saline seepage. Hydrology and Earth System Sciences, 15, 3659–3678.

Dyck, S., Chardabellas, P., 1963. Wege zur Ermittlung der nutzbaren Grundwasserreserven. Ber. Geol. Ges. DDR, 8, 245–262.

Eeman, S., Zee, S.V.D., Leijnse, A., De Louw, P.G.B., Maas, C., 2012. Response to recharge variation of thin rainwater lenses and their mixing zone with underlying saline groundwater. Hydrology and Earth System Sciences, 16, 10, 3535–3549.

Eeman, S., De Louw, P.G.B., Van der Zee, S.E.A.T. M., 2017. Cation exchange in a temporally fluctuating thin freshwater lens on top of saline groundwater. Hydrogeology Journal, 25, 1, 223–241.

Feddes, R.A., Kowalik, P.J., Zaradny, H., 1978. Simulation of Field Water Use and Crop Yield. John Wiley & Sons, New York, NY.

Foussereau, X., Graham, W.D., Akpoji, G.A., Destouni, G., Rao, P.S.C., 2001. Solute transport through a heterogeneous coupled vadose-saturated zone system with temporally random rainfall. Water Resources Research, 37, 6, 1577–1588.

Freeze, R.A., Cherry, J.A., 1979. Groundwater. Prentice Hall.

Grabarczyk, S., Żarski, J., 1992. Próba statystycznej weryfikacji niektórych wzorów określających ewapotranspirację potencjalną. [An attempt at statistical verification of selected formulae estimating potential evapotranspiration.] Zeszyty Naukowe Akademii Techniczno Rolniczej w Bydgoszczy (Rolnictwo). (in Polish.)

Hanson, R., Boyce, S., Schmid, W., Hughes, J., Mehl, S., Leake, S., Maddock III, Th., Niswonger, R., 2014. One-Water Hydrologic Flow Model (MODFLOW–OWHM), Techniques and Methods 6-A51. US Geological Survey, Reston, VA, USA. Available from: http://dx. DOI: org/10.3133/tm6A51.

Harbaugh, A.W., 2005. MODFLOW-2005, the US Geological Survey modular ground-water model: the ground-water flow process. US Department of the Interior, US Geological Survey, Reston, VA, USA, pp. 6-A16.

Healy, R.W., 2008. Simulating water, solute, and heat transport in the subsurface with the VS2DI software package. Vadose Zone Journal, 7, 632–639.

Healy, R.W., 2010. Estimating Groundwater Recharge. Cambridge University Press, Cambridge, UK, 245 p.

Holding, S., Allen, D.M., 2015. From days to decades: numerical modelling of freshwater lens response to climate change stressors on small low-lying islands. Hydrology and Earth System Sciences, 19, 2, 933–949.

Hölting, B., Coldewey, W.G., 2013. Hydrogeologie: Einführung in die allgemeine und angewandte Hydrogeologie. Springer-Verlag.

Houben, G., Post, V.E.A., 2016. How long does the recovery of a freshwater lens take after a massive saltwater inundation? Experiences from the island of Baltrum, Germany, after the 1962 flood disaster. In: Proceedings of 24th Salt Water Intrusion Meeting and the 4th Asia-Pacific Coastal Aquifer Management Meeting, 4 –8 July 2016, Cairns, Australia.

Hsieh, P.A., Wingle, A.W., Healy, R.W., 1999. VS2DI: A graphical software package for simulating fluid flow and solute or energy transport in variably saturated porous media. USGS Water-Resources Investigation Report 99-4130. US Geological Survey, Reston, USA.

Huang, M., Barbour, S.L., Elshorbagy, A., Zettl, J.D., Si, B.C., 2011. Water availability and forest growth in coarse-textured soils. Canadian Journal of Soil Science, 91, 2, 199–210.

Hunt, R.J., Prudic, D.E., Walker, J.F., Anderson, M.P., 2008. Importance of unsaturated zone flow for simulating recharge in a humid climate. Ground Water, 46, 4, 551–560.

Illangasekare, T., Tyler, S.W., Clement, T.P, .Villholth, K.G., Perera, A.P.G.R.L., Obeysekera, J., Gunatilaka, A., Panabokke, C.R, Hyndman, D.W., Cunningham, K.J., Kaluarachchi, J.J., Yeh, W.W-G., van Genuchten, M.Th., Jensen, K., 2006. Impacts of the 2004 tsunami on groundwater resources in Sri Lanka. Water Resour. Res., 42, W05201. DOI: 10.1029/2006WR004876.

Jocson, J.M. U., Jenson, J.W., Contractor, D.N., 2002. Recharge and aquifer response: northern Guam lens aquifer, Guam, Mariana Islands. Journal of Hydrology, 260, 1, 231–254.

Kamps, P.W.J.T., Nienhuis, P., Witte, J.P.M., 2008. Effects of climate change on the water table in the coastal dunes of the Amsterdam Water Supply. In: Proceedings MODFLOW.

Leterme, B., Gedeon, M., Jacques, D., 2013. Groundwater recharge modeling of the Nete catchment (Belgium) using the HYDRUS 1D - MODFLOW package. In: Šimůnek, J., M.Th. van Genuchten, Kodešová, R. (Eds.): Proc. of the 4th International Conference "HYDRUS Software Applications to Subsurface Flow and Contaminant Transport Problems, Prague, Czech Republic, pp. 235–244. ISBN: 978-80-213-2380-3

Leterme, B., Gedeon, M., Laloy, E., Rogiers, B., 2015. Unsaturated flow modeling with HYDRUS and UZF: calibration and intercomparison. In: Proc. MODFLOW and More 2015. Integrated GroundWater Modeling Center, May 31–June 3, 2015, Golden, CO.

Luoma, S., Okkonen, J., 2014. Impacts of future climate change and Baltic Sea level rise on groundwater recharge, groundwater levels, and surface leakage in the Hanko aquifer in southern Finland. Water, 6, 12, 3671–3700.

Mahmoodzadeh, D., Ketabchi, H., Ataie-Ashtiani, B., Simmons, C.T., 2014. Conceptualization of a fresh groundwater lens influenced by climate change: A modeling study of an arid-region island in the Persian Gulf, Iran. Journal of Hydrology, 519, 399–413.

Meyer, P.D., Rockhold, M.L., Gee, G.W., 1997. Uncertainty analyses of infiltration and subsurface flow and transport for SDMP sites. Rep. NUREG/CR-6565, PNNL-11705. U.S. Nuclear Regulatory Commission, Washington, DC.

Mollema, P.N., Antonellini, M., 2013. Seasonal variation in natural recharge of coastal aquifers. Hydrogeology Journal, 21, 4, 787–797.

Neitsch, S.L., Williams, J.R., Arnold, J.G., Kiniry, J.R., 2011. Soil and water assessment tool theoretical documentation version 2009. Texas Water Resources Institute, College Station, TX.

Neuman, S.P., Feddes R.A., Bresler, E., 1974. Finite element simulation of flow in saturated-unsaturated soils considering water uptake by plants. Third Annual Report, Project No. A10-SWC-77. Hydraulic Engineering Lab., Technion, Haifa, Israel.

Niswonger, R.G., Prudic, D.E., Regan, R.S., 2006. Documentation of the unsaturated-zone flow (UZF1) package for modeling unsaturated flow between the land surface and the water table with MODFLOW-2005 (No. 6-A19).

Oude Essink, G.H.P., Van Baaren, E.S., De Louw, P.G., 2010. Effects of climate change on coastal groundwater systems: a modeling study in the Netherlands. Water Resources Research, 46, 10.

Persson, M., Saifadeen, A., 2016. Effects of hysteresis, rainfall dynamics, and temporal resolution of rainfall input data in solute transport modelling in uncropped soil. Hydrological Sciences Journal, 61, 5, 982–990.

Prieto, C., Kotronarou, A., Destouni, G., 2006. The influence of temporal hydrological randomness on seawater intrusion in coastal aquifers. Journal of Hydrology, 330, 1, 285–300.

Sadurski, A., Borawska, J., Burczyk, T., 1987. Warunki hydrogeologiczne i hydrochemiczne Mierzei Helskiej [Hydrogeological and hydrochemical conditions of Hel Peninsula.] Kwartalnik Geologiczny, 31, 4, 767–782. (In Polish.)

Scanlon, B.R., Christman, M., Reedy, R.C., Porro, I., Šimůnek, J., Flerchinger, G.N., 2002. Intercode comparisons for simulating water balance of surficial sediments in semiarid regions. Water Resources Research, 38, 12, 1323. DOI: 10.1029/2001WR001233.

Schroeder, P.R., Dozier, T.S., Zappi, P.A., McEnroe, B.M., Sjostrom, J.W., Peton, R.L., 1994. The Hydrologic Evaluation of Landfill Performance (HELP) Model: Engineering Documentation for Version 3, EPA/600/R-94/168b. US. Environmental Protection Agency, Risk Reduction Engineering Laboratory, Cincinnati.

Seo, H.S., Šimůnek, J., Poeter, E., 2007. Documentation of the HYDRUS Package for MODFLOW-2000, the U.S. Geological Survey Modular Ground-Water Model, GWMI 2007-01. International Ground Water Modeling Center, Colorado School of Mines, Golden, Colorado, 96 p.

Šimůnek, J., Jarvis, N. J., van Genuchten, M.Th., Gärdenäs, A., 2003. Review and comparison of models for describing non-equilibrium and preferential flow and transport in the vadose zone. Journal of Hydrology, 272, 1, 14–35.

Šimůnek, J., Šejna, M., Saito, H., Sakai, M., van Genuchten, M.Th., 2008a. The HYDRUS-1D software package for simulating the one-dimensional movement of water, heat, and multiple solutes in variably-saturated media, Version 4.0. HYDRUS Software Series 3. Department of Environmental Sciences, University of California, Riverside, CA, USA, 315 p.

Šimůnek, J., van Genuchten, M.Th., Šejna M., 2008b. Development and applications of the HYDRUS and STANMOD software packages and related codes. Vadose Zone Journal, 7, 2, 587–600.

Šimůnek, J., van Genuchten, M.Th., Šejna, M., 2016. Recent developments and applications of the HYDRUS computer software packages. Vadose Zone Journal, 15, 7, 25 p. DOI: 10.2136/vzj2016.04.0033.

Sinclair, P., Galvis, S.C., Bosserelle, A.L., Post, V.E.A., Werner, A., 2016. Sustainability of freshwater lenses in atoll

environments. In: Proceedings of 24th Salt Water Intrusion Meeting and the 4th Asia-Pacific Coastal Aquifer Management Meeting, 4 –8 July 2016, Cairns, Australia.

Smerdon, B.D., Mendoza, C.A., Devito, K.J., 2008. Influence of subhumid climate and water table depth on groundwater recharge in shallow outwash aquifers. Water Resources Research, 44, W08427.

Stuyfzand, P.J., 2016. Formation and hydrogeochemistry of a freshwater lens on a sandbar island in saltwater lake Grevelingen, Netherlands. In: Proceedings of 24th Salt Water Intrusion Meeting and the 4th Asia-Pacific Coastal Aquifer Management Meeting, 4–8 July 2016, Cairns, Australia.

Sulzbacher, H., Wiederhold, H., Siemon, B., Grinat, M., Igel, J., Burschil, T., Günther, T., Hinsby, K., 2012. Numerical modelling of climate change impacts on freshwater lenses on the North Sea Island of Borkum using hydrological and geophysical methods. Hydrology and Earth System Sciences, 16, 10, 3621–3643.

Szymańska, P., Tisler, W., Schütz, C., Szymkiewicz, A., Neuweiler, I., Helmig, R., 2016. Experimental and numerical analysis of air trapping in a porous medium with coarse textured inclusions. Acta Geophysica, 64, 6, 2487–2509.

Therrien, R., McLaren, R. G., Sudicky, E. A., Panday, S. M., 2010. HydroGeoSphere: A three-dimensional numerical model describing fully-integrated subsurface and surface flow and solute transport. Groundwater Simulations Group, University of Waterloo, Waterloo, ON.

Thoms, R.B., Johnson, R.L., Healy, R.W., 2006. User's guide to the Variably Saturated Flow (VSF) process for MODFLOW. Techniques and Methods 6-A18. US Geological Survey, Reston, VA.

Trglavcnik, V., Robinson, C., Morrow, D., White, D., Paquin, V., Weber, K., 2016. Effect of tides, waves and precipitation on groundwater flow dynamics on Sable Island, Canada. In: Proceedings of 24th Salt Water Intrusion Meeting and the 4th Asia-Pacific Coastal Aquifer Management Meeting, 4–8 July 2016, Cairns, Australia.

Twarakavi, N.K.C., Šimůnek, J., Seo, H.S., 2008. Evaluating interactions between groundwater and vadose zone using HYDRUS-based flow package for MODFLOW. Vadose Zone Journal, 7, 2, 757–768.

Vandenbohede, A., Mollema, P.N., Greggio, N., Antonellini, M., 2014. Seasonal dynamic of a shallow freshwater lens due to irrigation in the coastal plain of Ravenna, Italy. Hydrogeology Journal, 22, 4, 893–909.

Vero, S.E., Ibrahim, T. G., Creamer, R. E., Grant, J., Healy, M. G., Henry, T., Kramers, G., Richards, K.G., Fenton, O. 2014. Consequences of varied soil hydraulic and meteorological complexity on unsaturated zone time lag estimates. Journal of Contaminant Hydrology, 170, 53–67.

Verruijt, A., 1968. A note on the Ghyben-Herzbeg formula. International Association of Scientific Hydrology Bulletin, 13, 4, 43–46. DOI: 10.1080/02626666809493624.

Voss, C.I., Provost, A.M., 2010. SUTRA: A model for saturated-unsaturated, variable-density groundwater flow with solute or energy transport. USGS Water- Resources Investigations Report, 02-4231, U.S. Geological Survey, Reston, VA

Werner, A.D., Lockinton, D.A., 2004. The potential for soil salinization above aquifers influenced by seawater intrusion. In: Proc. 13th International Soil Conservation Conference, Brisbane, paper No. 790.

Werner, A.D., Bakker, M., Post, V.E., Vandenbohede, A., Lu, C., Ataie-Ashtiani, B., Simmons, C.T., Barry, D.A., 2013. Seawater intrusion processes, investigation and management: recent advances and future challenges. Advances in Water Resources, 51, 3–26.

Winston, R.B., 2009. ModelMuse: a graphical user interface for MODFLOW-2005 and PHAST. US Geological Survey, Reston, VA.

Received 19 June 2017
Accepted 10 January 2018